A low-δ^{18}O intrusive breccia from the Koegel Fontein complex, South Africa

By : **Camille Olianti**

Supervised by : Prof. Chris Harris

Thesis presented for the degree of Masters of Science in the Department of Geological Sciences. University of Cape Town. December 2015.

DECLARATION

I declare that this dissertation is my own, unaided work. This work is being submitted for the degree of Masters of Science of Geochemistry at the University of Cape Town, in South Africa.

Camille Olianti

Tuesday the 8th of December 2015

Camille A. E. Olianti

ABSTRACT

The ~135 Ma Koegel Fontein complex, 350 km north of Cape Town, has rocks with abnormally low $\delta^{18}O$ values, as low as -5.2‰. The rocks with the lowest $\delta^{18}O$ values belong to an intrusive breccia and have a fine-grained, black matrix. The silica content of these breccia rocks ranges between 44-68 wt %, their whole-rock $\delta^{18}O$ values vary between -5.2‰ and +1.8‰, and their water content is between 0.2-1.1 wt %. The major and trace element composition of the breccia rocks is consistent with them containing variable proportions of bostonite, alkali basalt, gneiss, and epidote- and xenolith-rich material. Mapping indicates that the initial intrusion was an alkali basalt dyke and a bostonite dyke that were then intruded by two breccia plugs that extended along the planes of weakness created by the pre-existing dykes, forming two sub-parallel breccia dykes. The water content of the breccia rocks is low (average <1.0 wt %) and is consistent with interaction with fluids at a relatively high temperature (>300°C). These fluids interacted with the rocks from both dykes and are responsible for their ^{18}O-depletion. On the basis of the O- and H-isotope composition of the breccia rocks, the $\delta^{18}O$ value calculated for the fluids in equilibrium with the breccia rocks is approximately -10.8 ±0.2 ‰. This low $\delta^{18}O$ value of the meteoric fluids is too low for the low latitude and warm climate at ~135 Ma and indicates that ^{18}O-depletion at Koegel Fontein predates the intrusion of the complex in the Cretaceous. It is possible that low-$\delta^{18}O$ fluids circulated through the country rock during the Pan African when crustal reworking enabled deep circulation of surface water. This period of crustal reworking coincides with a 'Snowball Earth' event and would have been accompanied by ^{18}O-depleted meteoric water. In the Cretaceous, it is assumed that a mantle plume heated the crust, causing dehydration before partial melting of the crust. The initial low-$\delta^{18}O$ fluids are effectively metamorphic fluids in equilibrium with the rock. It is proposed that the initial loss of these fluids became explosive. These fluids migrated along the pre-existing alkali basalt and bostonite dykes, incorporating fragments of alkali basalt, bostonite, and country rock gneiss. This xenolith-rich fluidised material was then emplaced rapidly into the crust.

TABLE OF CONTENTS

LIST OF ILLUSTRATIONS

LIST OF FIGURES

LIST OF TABLES

ACKNOWLEDGEMENTS

My sincere thanks go to my supervisor Prof. Chris Harris who a year prior to my venture to Cape Town, while I was completing my BSc. at the University of Geneva, accepted my request to study with him for my Honours and Masters degrees. Not only did he assisted me as a supervisor but he also encouraged and directed me throughout these two years.

My thanks extend to the National Research Funding association for their generous scholarship, without which I could not have completed my Masters degree. I also thank Petrus le Roux, Fayrooza Rawoot, Christel Tinguely, and Kerryn Gray for their assistance in preparing and analysing my samples and Albie and Adele Pool, neighbouring landowners to the studied outcrop, for their hospitality.

GLOSSARY

Alteration: term referring to evidence for hydrothermal fluid-rock interaction, excluding low-temperature fluid-rock interaction. All the breccia rocks have undergone high-temperature (>300°C) hydrothermal alteration.

Bostonite: a fine-grained felsic rock with a trachytic texture (~microsyenite) that belongs to the bostonite suite (de Beer et al., 2002), which is a unit of the Koegel Fontein complex.

Breccia Outcrop: an outcrop made of two sub-parallel breccia dykes (the West Dyke and the East Dyke) that extend over an approximate total distance of 4 km. Along each breccia dykes there is a circular outcrop made of the same rock type.

Breccia Plug 1 and 2: two circular outcrops resembling intrusive plugs. The Breccia Plug 1 is ~10 m in diameter and situated on the East Dyke. This plug was previously thought to reflect the entire Breccia Outcrop (e.g. Curtis et al., 2013). The Breccia Plug 2 is ~5 m in diameter and located on the West Dyke. These two breccia plugs are about 80 m from each other.

The breccia rocks: dense, black rocks that make up the Breccia Outcrop. The breccia rocks consist mostly of groundmass, with variable quantities of xenoliths and sparse phenocrysts.

Low-$\delta^{18}O$ rock: igneous rock with $\delta^{18}O$ values below the composition of mantle-derived magmas (+5.7‰, e.g. Eiler, 2001). Low-$\delta^{18}O$ rocks dominate the Koegel Fontein complex.

Low-$\delta^{18}O$ magma: magma with $\delta^{18}O$ values <+5.7‰ (Taylor and Sheppard, 1986). Low-$\delta^{18}O$ magmas produced some of the rocks at the Koegel Fontein complex. Low-$\delta^{18}O$ magmas are uncommon worldwide (e.g. Bindeman, 2008) and none are known in the Damaraland complexes in Namibia, which formed contemporaneously with the Koegel Fontein complex (Harris, 1995; Trumbull et al., 2004).

Roof pendant: a ~25 km in diameter pluton made mostly of country rock gneiss. The roof pendant is in the middle of the complex and found immediately on top of the Rietpoort granite. The granite all around the roof pendant forms the highest topographic hills of the complex. The granite and the gneiss bring evidence for the granite intrusion to have been saucer-shaped (de Beer et al., 2002).

CHAPTER 1 INTRODUCTION

1.1 Project overview

Before the breakup of Gondwana, in the early Cretaceous, extensional forces on the crust led to the formation of the Paraná-Etendeka large igneous province in Brazil and northwest Namibia (e.g. Peate, 1997). Magma produced in Namibia formed the Damaraland ring complexes. The only large igneous complex south of Namibia and contemporaneous to the Damaraland complexes is the Koegel Fontein complex. This complex is found ~350 km north of Cape Town. The Koegel Fontein complex is the only early Cretaceous complex on the southwest African margin to be dominated by ^{18}O-depleted rocks and to have been produced by a small amount of low-δ^{18}O magmas (Curtis, 2010). These make the Koegel Fontein complex highly unusual and worth studying.

Within the ~35 km in diameter Koegel Fontein complex, there is a ~10 m in diameter circular outcrop made of rocks filled with fragments of other rocks supported in a black, fine-grained matrix. This outcrop is named in this work the Breccia Outcrop. The Breccia Outcrop is made of breccia rocks that resemble pseudotachylite, kimberlite, and Dwyka tillite, which are of impact, igneous, and sedimentary origin, respectively. One of the rocks (sample CCK21) from the Breccia Outcrop was sampled by accident and analysed for O-isotopes (Curtis, 2010). This rock was not expected to give an unusual δ^{18}O value (-4.1‰). Igneous rocks with δ^{18}O values below +5.7‰ are termed low-δ^{18}O rocks (e.g. Eiler, 2001) and are uncommon at low latitudes (<30°) and outside of a mountain range (e.g. Dansgaard, 1964), which is where the Koegel Fontein complex was situated at from the Cretaceous to present (Curtis et al., 2013).

Until the recent finding of the low-δ^{18}O rock CCK21 (Curtis, 2010), the Breccia Outcrop has only been studied to a limited extent. The Breccia Outcrop yields no emplacement model describing how it formed in the context of the emplacement of the complex and counts several disagreeing rock characterizations for the rocks it comprises. The breccia rocks were first interpreted as bostonite rocks (Jansen, 1960). These rocks were then described as olivine melilitites (de Beer and Armstrong, 1998). The latter classification was rejected after a preliminary geochemical study indicated that the breccia rocks contain no olivine or melilitite (Curtis, 2010). An Honours project was subsequently undertaken on the Breccia Outcrop (Olianti, 2014). The latter was upgraded into the present Masters project.

Overall, the lack of agreement on the type of rock that makes up the Breccia Outcrop, the absence of an emplacement model for the outcrop, and the finding of the lowest-δ^{18}O rock in the complex at the outcrop make the Breccia Outcrop an excellent study area. Detailed geochemical and petrographic work on this outcrop is carried out to investigate the characteristics of the rocks that make up the Breccia Outcrop and the distribution of the $\delta^{18}O$ values of the rocks over the area of the outcrop.

1.2 Aims of the study

The intent of this study is to define the range of rock types at and the spatial distribution of the rocks from the Breccia Outcrop and identify additional low-$\delta^{18}O$ rocks in the area of the outcrop. Ultimately, the aim is to suggest a model for the origin of the ^{18}O-depleted breccia rocks and to place the Breccia Outcrop in the context of the development of the complex.

The specific objectives are as follows:

1) Describe the breccia rocks and the surface outcrop expression that these rocks make up, 2) document the whole-rock and isotope composition of the rocks that make up the Breccia Outcrop, 3) determine the distribution of the $\delta^{18}O$ values of the breccia rocks over the area of the outcrop, and 4) explore the relationship between the Breccia Outcrop and the rest of Koegel Fontein complex.

CHAPTER 2 GEOLOGICAL SETTING

2.1 Regional geological setting

Three major events influenced the region of the Koegel Fontein complex since the mid-Proterozoic. The first event was the Namaqua-Natal metamorphic event. In second came the Pan African tectono-thermal event. The last event was the breakup of western Gondwana, which is the most significant event with respect to the Koegel Fontein igneous complex. All three events are described in the following sections.

2.1.1 Namaqua-Natal metamorphic province

The deformed and metamorphosed regional country rock at Koegel Fontein belongs to the Namaqua-Natal metamorphic province (Fig. 2.1), which formed between 1600-1000 Ma (e.g. Barton, 1983; Eglington et al., 1989; Thomas and Eglington, 1990). This region covers 100 000 km^2 of the west coast of southern Africa.

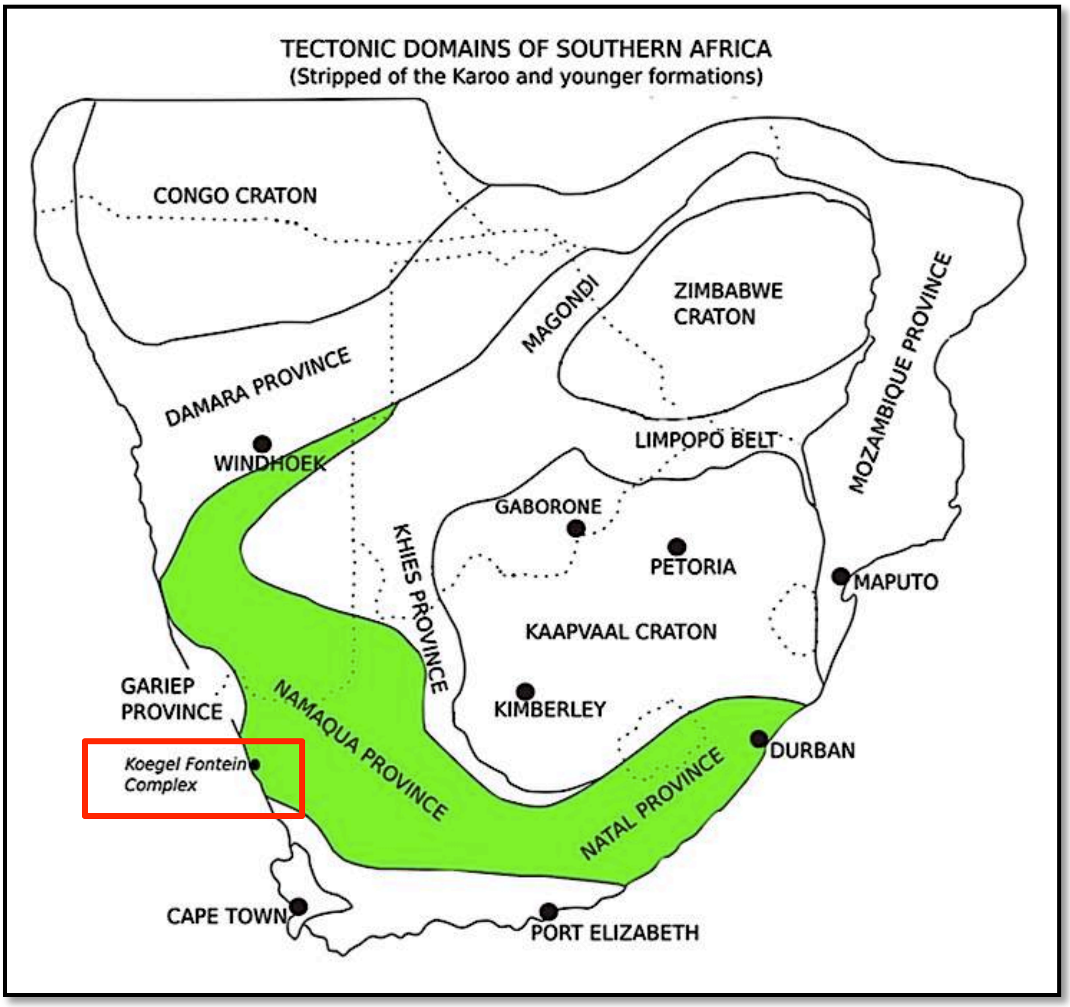

Fig. 2.1 Map of the tectonic domains of southern Africa. The map includes the present geographical situation of the Namaqua-Natal Belt and Koegel Fontein complex. After de Beer and Meyer (1984).

The Namaqua-Natal region underwent rifting between 1600-1300 Ma. The rifting was followed by the emergence of two oceans called Areachap and Tugela oceans. At 1300 Ma, the area experienced subduction along with arc magmatism. The regional country rock was then deformed and metamorphosed by the Namaqua-Natal orogenic event between 1220-1150 Ma. At 1080 Ma, an oblique strike-slip system developed across the region, forming major faults in the area (Fig. 2.2). (Cornell et al., 2006)

The Namaqua-Natal metamorphic province is divided into five domains, which are termed the Richtesveld Subprovince, the Bushmanland Terrane, the Kakamas Terrane, the Arachap Terrane, and the Kaaien Terrane. The Koegel Fontein complex intruded the Bushmanland Terrane. This terrane is made of Namaqua gneiss (2050-1700 Ma), supracrustal rocks metamorphosed to amphibolite (1600-1200 Ma), and granulite facies rocks and granitoids (1200-1000 Ma) (Cornell et al., 2006). These rocks make up the country rock at Koegel Fontein.

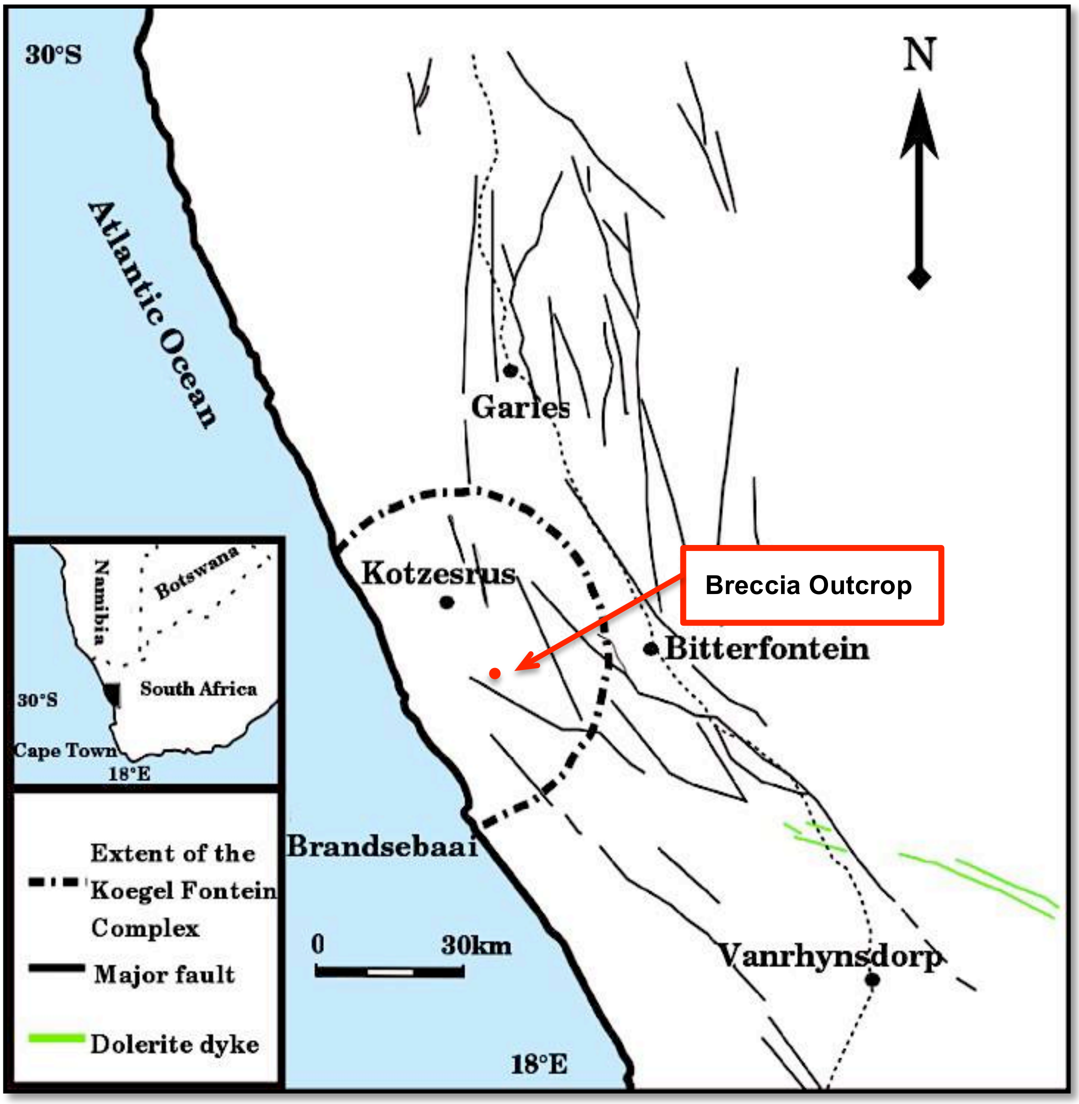

Fig. 2.2 Map showing major faults in the region, the size of the complex, and the geographical situation of the Breccia Outcrop. Modified after de Beer and Armstrong (1998) and Curtis (2010).

2.1.2 Pan African tectono-thermal event

The Pan African is a major tectono-thermal event that occurred in mobile belts throughout Africa. This tectono-thermal event took place ~500 Ma ago (Kennedy, 1964) and was associated with the development of metamorphic provinces that formed between African crustal blocks. These provinces (Fig. 2.3) sutured cratons and east and west Gondwana (Porada, 1989; Gresse et al., 2006).

Remnants of a mobile belt called the Gariep Belt are found at Koegel Fontein. The formation of the mobile belt started with the breakup of Rodinia and the creation of the Adamastor Ocean ~770 Ma ago (Gresse et al., 2006). Deposition of sediments in the Gariep basin evolved before subduction closed the Adamastor Ocean (Porada, 1989; Gresse et al., 2006). Subduction also caused tectono-metamorphic overprinting of the country rock found at Koegel Fontein (de Beer et al., 2002).

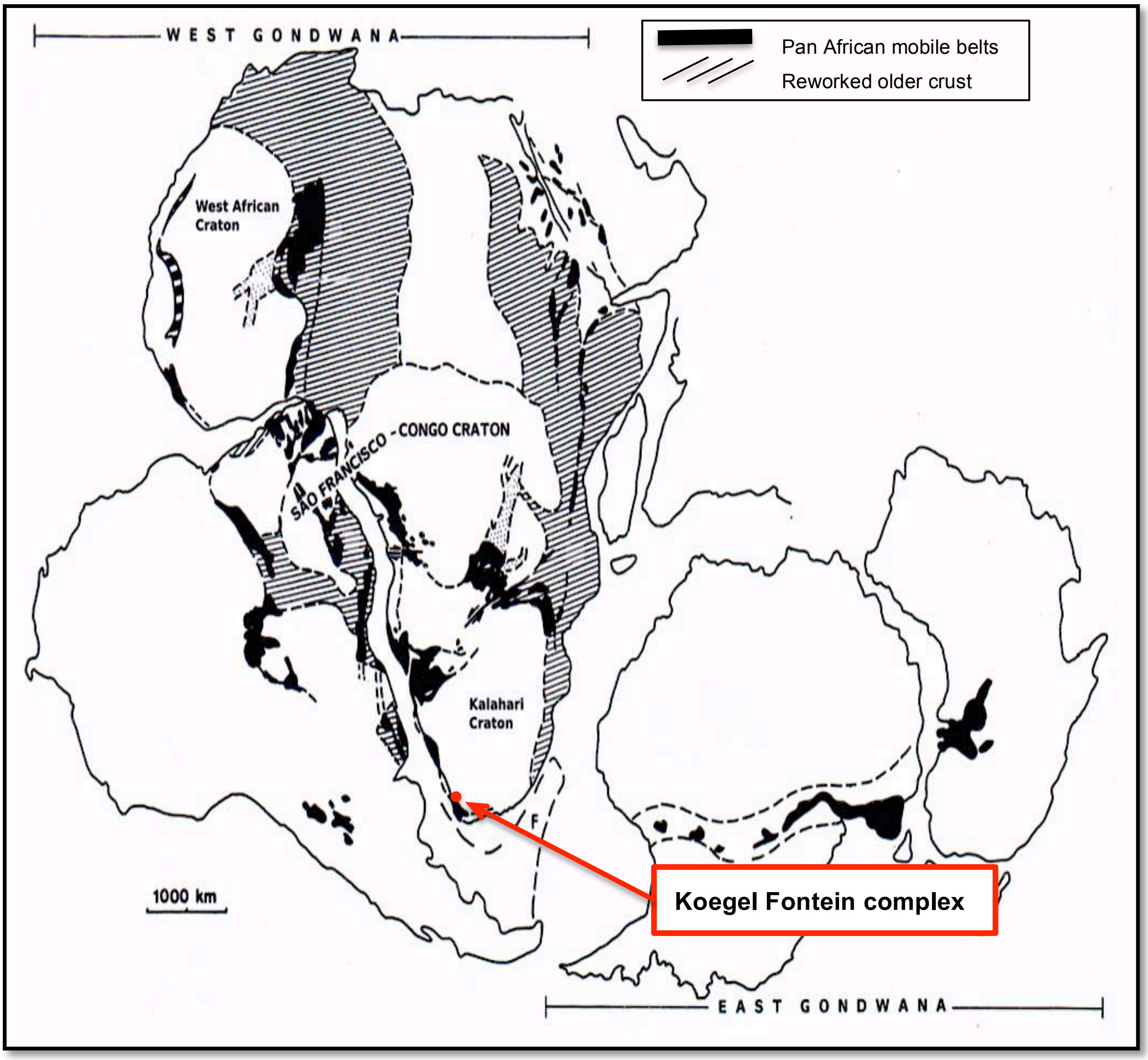

Fig. 2.3 Geological map of Gondwana showing the extent of the Pan African tectono-thermal event and the location of the Koegel Fontein complex. Modified after Porada (1989).

2.1.3 Breakup of western Gondwana

The supercontinent of Gondwana amalgamated at the beginning of the Palaeozoic and progressively fragmented from the Devonian to present. During the fragmentation, from the early Jurassic to the late Cretaceous (180-90 Ma), continents broke apart. The continental breakup has been divided into five stages by Watkeys (2006), starting with incipient rifting in eastern Gondwana and ending with the final separation of Africa from South America and Antarctica from Australia.

Initial rifting and magmatism of western Gondwana fall into the third and fourth stages at 155-135 Ma and 135-115 Ma, respectively. It is during these two stages, between 144 Ma and 133 Ma, that the Koegel Fontein complex was emplaced. In the third stage, motion along the Gastre Fault System and the Agulhas-Faulkand fracture zones led to northward propagation of fractures (Watkeys, 2006). These fractures migrated along pre-existing faults that formed during the Namaqua and Pan African orogenic events (Watkeys, 2006). The fractures were important for delineating the intrusion of the Koegel Fontein complex and dolerite dykes in the Cape Peninsula (Trumbull et al., 2007).

Substantial rifting began in the fourth stage. During this stage, the orientation of the tectonic plates changed. Tristan da Cunha mantle plume intersected weakened and thinned crust, which lead to the separation of Africa from South America (Watkeys, 2006). Great volumes of magma were produced and spread beyond the rift boundaries. Ten percent of the total magmatism formed the Damaraland complexes in northern Namibia (Ewart et al., 1998a). The intensity and the diversity of this breakup-related magmatism decreased south of the Damaraland complexes (Peate, 1997), with the exception of magmatism at the Koegel Fontein complex, which is situated >1000 km south of Damaraland.

2.2 South Atlantic magmatism

The South Atlantic is an early Cretaceous volcanic rifted zone. Approximately 130 Ma ago, magmatism along the South Atlantic margin formed the Paraná-Etendeka large igneous province (e.g. Peate, 1997; Marsh et al., 2001), plutonic ring complexes known as the Koegel Fontein complex and Damaraland complexes (Harris, 1995; Milner and le Roex, 1996; Trumbull et al., 2000; 2003, 2004a), the Walvis Ridge and Rio Grande Rise (O'Connor and le Roex, 1992), and mafic dykes swarms (e.g. Mohriak et al., 2002; Trumbull et al., 2002; 2007). Evidence for this South Atlantic magmatism is seen in the Paraná basin in eastern Brazil and the Etendeka basin in northern Namibia.

2.2.1 Paraná-Etendeka large igneous province

The Paraná-Etendeka large igneous province (Fig. 2.4) is a plume-related continental flood basalt that produced a volume >800 000 km^3 of erupted material and covers an area of ~170 000 km^2 over Brazil and Namibia. The large igneous province is related to a paired submarine volcanic chain, called the Rio Grande Rise and the Walvis Ridge (Peate, 1997). This volcanic chain is considered to mark Tristan da Cunha plume hotspot track and to have initiated the Paraná-Etendeka magmatism (O'Connor and le Roex, 1992).

Vigorous volcanic activity in the Paraná and Etendeka basins occurred between 138-128 Ma (Renne et al., 1996; Jerram et al.; 1999; Marzoli et al., 1999; Kirstein et al., 2001), with the onset of continental flood basalt magmatism in Namibia around 133 Ma (Ewart et al., 1998a; Jerram et al., 1999). The age of volcanism in the Paraná-Etendeka province coincides with that of Damaraland magmatism, which occurred between ~137-125 Ma (Wigand et al., 2004).

The volcanic rocks that make up the Paraná-Etendeka province consist of basalt, latite, and quartz latite or rhyodacite. The erupted material is thought to have come from one same source (Erlank et al., 1984; Harris et al., 1990; Ewart et al., 1998a,b), despite there being ~20 subvolcanic ring complexes and dykes associated with the province and thus no distinct eruptive centre (Trumbull et al., 2004a). Uncertainty prevails as to if the Koegel Fontein complex formed from the same source as the Damaraland complexes or not. Other potential mantle plumes in the South Atlantic were significantly closer to the Koegel Fontein complex at 135 Ma than Tristan da Cunha plume that produced the contemporaneous Damaraland complexes (O'Connor and Duncan, 1990). These mantle plumes presently associated with Bouvet Island and the Discovery and Shona seamounts could have initiated magmatism at Koegel Fontein (Curtis et al., 2013).

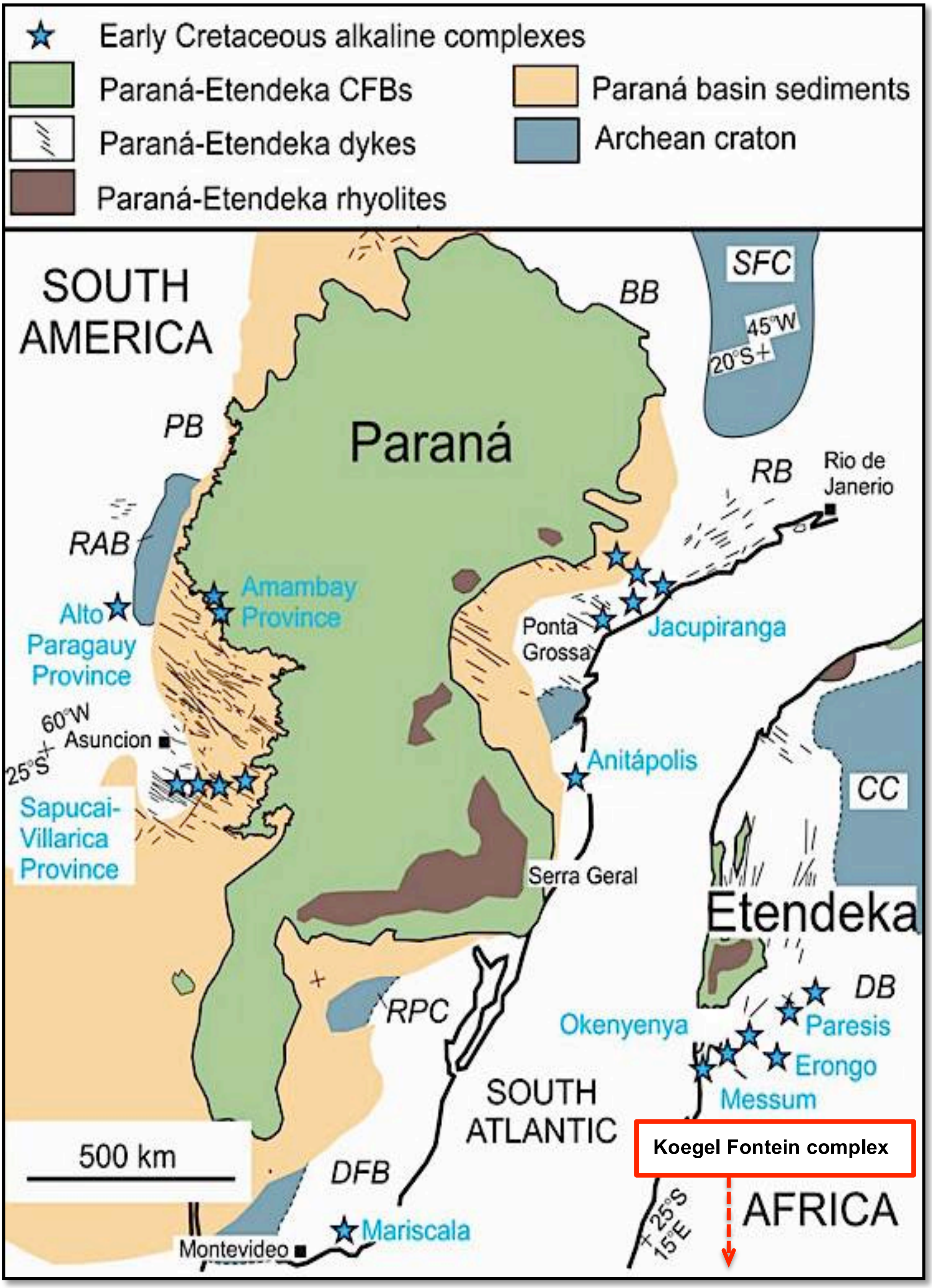

Fig. 2.4 Location sketch map of the Paraná-Etendeka large igneous province before continental breakup. Modified after Gibson et al. (2006). The distribution of the volcanics and the plate reconstruction at 128 Ma prior to the continental breakup are included. Abbreviations are as follows: BB: Brasilia Belt; DB: Damara Belt; DFB: Dom Feliciano Belt; PB: Paraguai Belt; RB: Ribeira Belt; CC: Congo Craton; LA: Luis Alves Craton; RAB: Rio Apa Block; RPC: Rio de la Plata Craton; SFC: São Francisco Craton.

2.2.2 West coast dyke swarms

Dykes along the west coast of southern Africa formed from early Cretaceous magmatism associated to the breakup of western Gondwana. These dykes extend from the Etendeka to the Cape Peninsula and form three main dyke swarm regions (Fig. 2.5), which are called Henties Bay-Outjo, Mehlberg, and False Bay (Trumbull et al., 2007). These west coast dykes are sub-parallel to the coast, excepting the Henties Bay-Outjo dykes that strike in a NE-SW direction (C. de Beer, unpublished data). Several of the dykes can be traced for tens of kilometres and range in width between ~1 m to >20 m (e.g. Botha and Hodgson, 1976; Reid and Rex, 1994; de Beer et al., 2002; Trumbull et al., 2007).

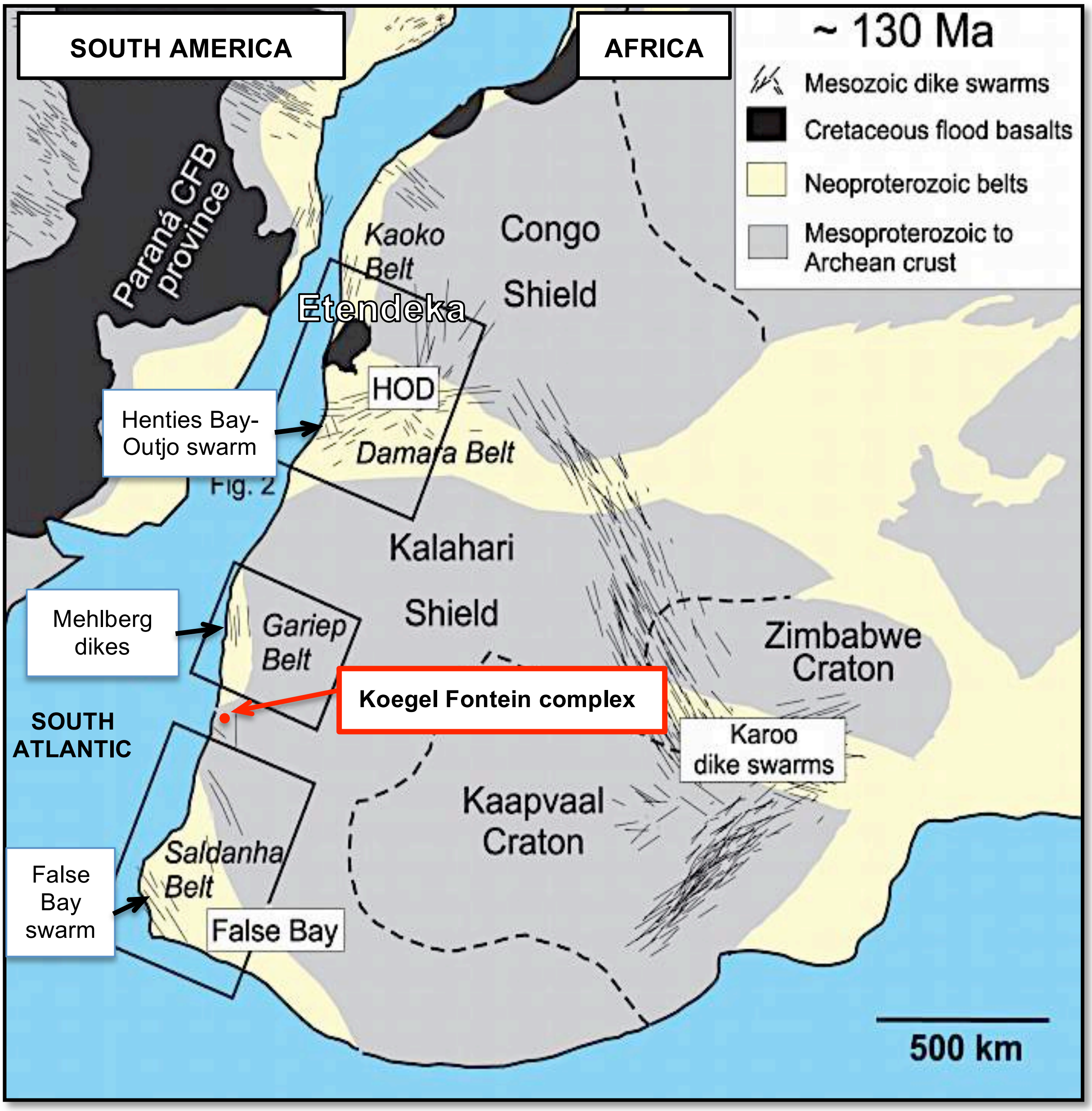

Fig. 2.5 Location sketch map indicating a pre-drift reconstruction of southern Africa and south-eastern South America. Approximated boundaries of basement provinces and the distribution of Mesozoic dike (~dyke) swarms and associated continental flood basalts are displayed on the map. Modified after Trumbull et al. (2007).

The dykes at Koegel Fontein are generally tholeiitic and alkaline (de Beer et al., 2002; Trumbull et al., 2007). The regional dolerite dykes cut the Namaqua-Natal bedrock (de Beer et al., 2002). Younger dykes than the regional dolerite dykes also cut the bedrock (Jansen, 1960; de Beer et al., 2002). These youngest dykes include dolerite dykes, bostonite (~microsyenite) and quartz porphyry dykes, and plugs and discontinuous dykes (de Beer et al., 2002).

The bostonite and quartz porphyry dykes form a suite of felsic and alkaline to sub-alkaline dykes. These dykes are spatially related to the early Cretaceous syenite and granite intrusions of the Koegel Fontein complex (de Beer et al, 2002). The bostonite dykes cut the mafic dykes, which indicates that the mafic dykes are the oldest (de Beer et al., 2002). The youngest of all these intrusions are plugs and discontinuous dykes, which are Tertiary in age and of alkaline and mafic to intermediate composition (McIver, 1981; Moore and Verwoerd, 1985; de Beer et al., 2002).

2.2.3 Damaraland complexes

The South Atlantic region yields one of the foremost examples of a large igneous province that formed along a volcanic rifted margin, known as the Damaraland complexes. The well-preserved and exposed Damaraland ring complexes are predominantly found in northern Namibia where they extend ~350 km inland in a northeast direction from the Atlantic coast to the margin of the Congo craton (Trumbull et al., 2000). These complexes range in age between ~137-125 Ma (Wigand et al., 2004) and in area from a few kilometres to tens of kilometres (Martin et al., 1960).

Rocks of the complexes range from alkaline and tholeiitic gabbro to carbonatite and to granite (Martin et al., 1960). These rocks formed contemporaneously with the Etendeka Group volcanics (Peate, 1997) and rocks from the Koegel Fontein complex (Trumbull et al., 2004a). Oxygen isotope work on rocks from the Damaraland complexes indicated that, overall, none of the complexes in Namibia have $\delta^{18}O$ values below +5.7‰ (Harris, 1995) unlike the Koegel Fontein complex.

2.3 Geology of the Koegel Fontein complex

2.3.1 Geology of the complex

The Koegel Fontein complex is as a sub-circular anorogenic intrusive complex (Fig. 2.6). This complex intruded at the junction of two major extensional faults striking north-south and east-west (de Beer et al., 2002). These two faults are crustal weaknesses that contain shear zones and associated fractures (de Beer et al., 2002). The largest of the shear zones is near the Breccia Outcrop (Curtis, 2010).

After single zircon U-Pb dating of rocks from the Koegel Fontein complex, suggestions of a young age (Jansen, 1960; McIver, 1981) were confirmed (de Beer and Armstrong, 1998). The magmatism that formed the felsic units at the Koegel Fontein complex occurred in two major pulses (de Beer and Armstrong, 1998). The first pulse took place during the third stage of the breakup of western Gondwana (Watkeys, 2006). This pulse involved the intrusion of 144.0 ± 2.0 Ma syenites, the Roovleitjie granite, and bostonite dykes (de Beer et al., 2002). This first pulse is older than the first intrusions observed in the Paraná-Etendeka large igneous province (138-128 Ma) (de Beer and Armstrong, 1998).

After a 10 Ma year hiatus, felsic magmatism was renewed. The second pulse began 133.9 ± 1.3 Ma ago (de Beer and Armstrong, 1998) with a swarm of quartz porphyry dykes that cut the bostonite dykes, both of which were subsequently truncated by the Rietpoort granite pluton (de Beer personal communication). The Rietpoort granite accounts for the greatest volume of material that intruded at Koegel Fontein (de Beer et al., 2002).

A late stage of magmatism occurred post continental rifting in the Late Cretaceous and Early Tertiary (e.g. Duncan et al., 1978; Hartnady and le Roex, 1985). Scattered dykes and plugs of alkaline to ultrabasic composition formed in the northern part of the Cape Peninsula (Janney et al., 2002). Small-sized olivine mellilitite and nephelinite plugs that form the Biesjesfontein suite also emerged at that time (McIver, 1981).

2.3.2 Koegel Fontein and Damaraland complexes

The major intrusive phase at Koegel Fontein occurred in the same time frame as the compositionally similar Damaraland complexes (Harris, 1995; Trumbull et al., 2004a). In spite of this concordant age, one plume per complex instead of one large plume for both complexes is thought to have initiated the magmatism (Curtis et al., 2013). Evidence for this is the >1000 km distance between the Damaraland and Koegel Fontein complexes, the low-$\delta^{18}O$ magmas that produced a small amount of rocks at Koegel Fontein (Harris, 1995), and observations of late Mesozoic South Atlantic plumes presently situated at Bouvet Island and Discovery and Shona seamounts, which were in closer proximity to Koegel Fontein at 135 Ma than the Tristan da Cunha plume (O'Connor and Duncan, 1990). In any case, Koegel Fontein has been suggested of being more strongly affected by crustal shear zones than by a thermal anomaly in the mantle (de Beer et al., 2002).

2.3.3 Koegel Fontein rock types

The Koegel Fontein complex intruded the Namaqua-Natal province. Rocks from the province are made of Mesoproterozoic felsic gneiss (1200-1000 Ma) and termed Namaqua gneisses (de Beer and Armstrong, 1998). The rocks that make up the Koegel Fontein complex are hyperbyssal and plutonic (Curtis, 2010). The hyperbyssal rocks are bostonites, quartz porphyries, and mafic dykes. The plutonic rocks include the Rietpoort granite, Rooivleitjie granite, syenites, and Zout River dyke. The host-rock and regional dolerite dykes are cut throughout the area by quartz veins, which are themselves cut by intrusions that form part of the complex, i.e. bostonite and mafic dykes (de Beer et al., 2002). These veins are thought to be older than the Koegel Fontein complex and younger than the country rock (Curtis et al., 2013).

In the ~35 km in diameter Koegel Fontein complex, there is a ~25 km in diameter pluton known as the Rietpoort granite. The Rietpoort granite forms the highest topographic hills of the complex and surrounds a well preserved, ~10 km in diameter roof pendant that lies directly on top the granite in the centre of the complex. This topographic variation between the roof pendant and the granite reflect that the granite intrusion was saucer-shaped (de Beer et al., 2002).

The roof pendant consists mostly of augen gneiss and is termed the late and post-tectonic Namaqua granite gneiss (de Beer and Armstrong, 1998) or the country rock gneiss (this study). The Breccia Outcrop (31°03’S; 17°54’E) is situated in the roof pendant (Fig. 2.6) close to the largest Pan African shear zone at Koegel Fontein (Curtis, 2010).

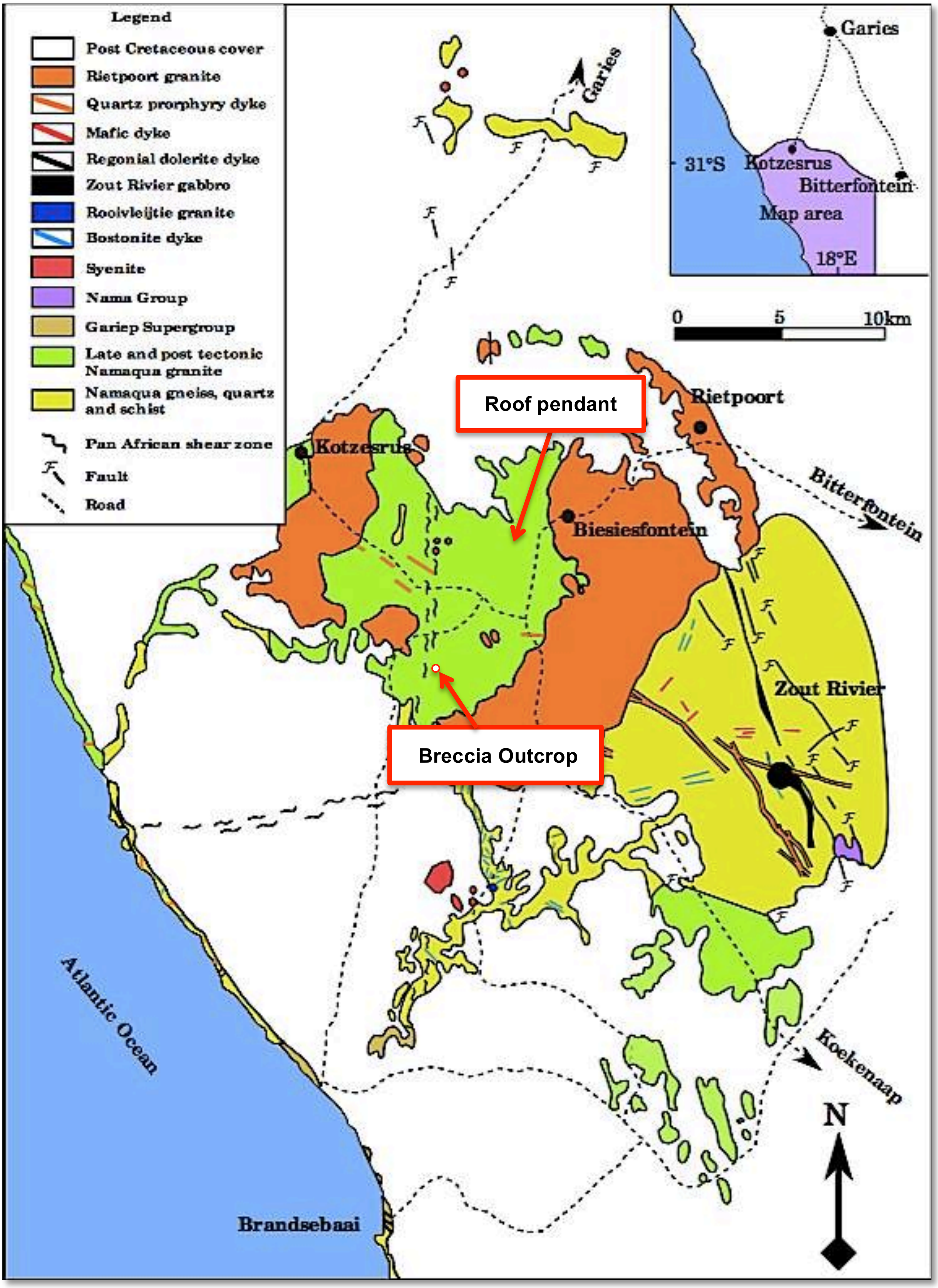

Fig. 2.6 Geology of the Koegel Fontein complex showing the location of the Breccia Outcrop. The roof pendant is shown on the map. Modified after de Beer and Armstrong (1998) and Curtis (2010).

2.4 Previous work on the complex

Over the last 5 years, rocks from the Koegel Fontein complex have been the subjects of increasingly detailed geochemical and petrographic studies (Curtis et al., 2011; Curtis et al., 2013) after Curtis (2010) discovered that the complex contained some low δ^{18}O-magmas and was dominated by low-δ^{18}O rocks.

A detailed geochemical and isotopic documentation of the complex, and a comparative study between the Koegel Fontein and Damaraland complexes was undertaken in 2011. This work counted a characterisation of the mafic and felsic intrusive units that make up the complex (Curtis et al., 2011). The bostonite suite and mafic dykes were two of the units analysed in Curtis et al. (2011). The bostonite suite is a series of bostonite dykes that consists of rocks similar to microsyenites (de Beer et al., 2002). Bostonite rocks have a felsic composition and trachytic texture made of subparallel laths of feldspar. These rocks are fine-grained and equigranular with >70 volume % feldspar and minor quartz, biotite, zircon, and opaque minerals. The secondary minerals in these rocks are generally epidote, carbonate, and chlorite.

The mafic dykes in Curtis et al. (2011) refer to tholeiitic and alkaline mafic dykes related to the Koegel Fontein complex. These tholeiitic and alkaline mafic dykes formed in the same time frame as the bostonite dykes. The mafic dykes intruded after the regional mafic dykes (also called dolerite dykes), which intruded before the Koegel Fontein complex. The tholeiitic mafic dykes are <2 m wide and consist of fine-grained rocks with ~5 volume % phenocrysts, which are mostly plagioclase (~70 volume % of the phenocrysts population), clinopyroxene (~30 volume %), and minor olivine. The alkaline mafic dykes are made of a fine-grained, porphyritic rock that contains ~10 volume % phenocrysts made of clinopyroxene, plagioclase, and hornblende. The secondary minerals in these alkaline and tholeiitic mafic rocks are frequently chlorite, epidote, and carbonate.

Curtis et al. (2013) described the widespread occurrence of low-δ^{18}O rocks at Koegel Fontein. These authors proposed that the abundance of low-δ^{18}O rocks results from high-temperature water-rock interactions. Fluids with low δ^{18}O values trapped in the pore space of the country rock, which had previously interacted with low-δ^{18}O meteoric fluids, were dehydrated in the Cretaceous when a mantle plume warmed the base of the crust (Curtis et al., 2013). Dehydration-melting reactions caused a range of low-δ^{18}O metamorphic fluids to exsolve from the country rock and migrate upwards through fractures and shear zones (Curtis et al., 2013). These metamorphic fluids, which had high temperatures and low δ^{18}O values, interacted with and depleted the rocks that make up the Koegel Fontein complex in ^{18}O.

The low $\delta^{18}O$ fluids dehydrated from the country rock when the Koegel Fontein complex was emplaced were meteoric in origin. Evidence for this is the low $\delta^{18}O$ value (-9.9‰) of the meteoric fluids calculated from quartz veins and hydrous minerals of the Koegel Fontein complex. Such a low $\delta^{18}O$ value is only found in meteoric fluids. These meteoric fluids interacted with and ^{18}O-depleted the country rock before the emplacement of the complex. This high-temperature fluid-rock interaction could have occurred in the Pan African, which was a time of crustal reworking. Deep fluid circulation could have taken place, trapping some of the meteoric fluids in the pore space of the country rock, and temperatures high enough could have been reached for the fluid to exchange ^{16}O with the country rock. (Curtis et al., 2013)

The ^{18}O-depletion in the meteoric fluids cannot easily be explained in the Cretaceous. Strongly ^{18}O-depleted meteoric fluids are normally found at high latitude, far inland, or high altitude, which is not the case of the complex at the time of its emplacement (e.g. Dansgaard, 1964). In the Cretaceous, reconstructed models of the Kalahari Craton on which is found the complex suggest that the Kalahari craton was at low latitude (<40°S) and remained constant over the last 130 Ma (e.g. Scotese et al., 1999). In addition, the complex was <1000 km from the nearest ocean and was not part of a mountain range (Curtis et al., 2013). Therefore, Curtis et al. (2013) suggest that the ^{18}O-depletion in the meteoric fluids happened prior in time, before the Pan African. Evidence for this are the paleo-latitude reconstructions of the Kalahari Craton (~60-20°S) between ~600-525 Ma (e.g. Tohver et al., 2006) and late Neoproterozoic global glaciations (e.g. Maruyama and Santosh, 2008), which can explain the calculated $\delta^{18}O$ value of -9.9‰ for the meteoric fluids.

In summary, rocks of the Koegel Fontein complex were ^{18}O-depleted by high-temperature metamorphic fluids with low $\delta^{18}O$ values (Curtis et al., 2013). These low-$\delta^{18}O$ metamorphic fluids were dehydrated from previously ^{18}O-depleted country rock when a Cretaceous mantle plume warmed the base of the crust (Curtis et al., 2013). These low-$\delta^{18}O$ metamorphic fluids were originally meteoric. Low-$\delta^{18}O$ fluids circulated through and ^{18}O-depleted the country rock gneiss, possibly in the Pan African when crustal reworking enabled deep fluid circulation (Curtis et al., 2013). The low-$\delta^{18}O$ meteoric fluids (-9.9‰) were most likely ^{18}O-depleted to such an extent before the Pan African (Curtis et al., 2013) when southern Africa was at high latitudes (e.g. Scotese et al., 1999) and/or the world a Snowball Earth (e.g. Maruyama and Santosh, 2008).

CHAPTER 3 GEOLOGY OF THE BRECCIA ROCKS

Chapter 3 addresses the first aim of this work by describing the breccia rocks and the shape that these rocks make up. This section includes a description of the gneiss and phonolite rocks sampled near the Breccia Outcrop.

3.1 Fieldwork

3.1.1 Mapping

The Koegel Fontein area is dominated by hills, which are generally farmed. The Breccia Outcrop is situated on one of the farmed lands, where farming machinery could have displaced rocks. The fieldwork was therefore carefully undertaken. Mapping revealed that the fine-grained (<0.5 mm), black breccia rocks are not only found amongst the single outcrop described by previous authors (e.g. Jansen, 1960; de Beer and Armstrong, 1998; Curtis, 2010; Curtis et al., 2013). More than fifteen poorly exposed additional outcrops were located, extending linearly over four of the farm hills. Instead of being limited to one single plug, these outcrops <1-2 m in diameter and <30-50 cm in height form a dyke-like structure that extends ~4 km lengthwise in a northwest-south direction (Fig. 3.1).

Two of the Breccia Outcrops are distinctly larger than the rest. These two, well-defined outcrops resemble intrusive plugs (Fig. 3.2.a). The outcrop described as a bostonite plug (Jansen, 1960) is named the Breccia Plug 1. This plug is ~10 m in diameter, >1 m in height, and 248 m above sea level. The second well-defined outcrop is called the Breccia Plug 2. This second plug (Fig. 3.2.b) is ~5 m in diameter, ~2-3 m in height, 244 m above sea level.

The rock that surrounds the Breccia Outcrop is made of the Mesoproterozoic country rock gneiss (~roof pendant). This gneiss outcrops in between the Breccia plug 1 and 2, which are ~80 m apart. The country rock gneiss also outcrops along the strike of the Breccia Outcrop, in between Breccia Outcrops, which are situated on either side of the gneiss outcrops. The gneiss brings evidence for the Breccia Plug 1 and 2 to form two separate plugs instead of one large intrusive plug and divides the Breccia Outcrop into two-sub-parallel dykes, which are called the West Dyke and the East Dyke.

Outcrops of gneiss form clusters of round boulders up to ~2-3 m in height and ~15-20 m in diameter. The most prominent outcrop of gneiss is next to the Breccia Plug 1 (Fig. 3.3.a). This outcrop is cut by a vein ~1-50 cm in width, which is filled with the breccia rock (Fig. 3.3.b). In several gneiss outcrops, the black matrix of the breccia rocks is mixed with the gneiss (Fig. 3.3.c).

Along the strike of the Breccia Outcrop, ~200 m south of the Breccia Plug 1, there is a pink to grey outcrop instead of black like the breccia rocks. This pink to grey outcrop resembles an intrusive plug <2 m in diameter and ~50 cm in height. The plug is henceforth referred to as the Phonolite Plug and the rocks it contains as phonolite rocks based on the geochemistry and petrography of these rocks, which are described in subsequent sections.

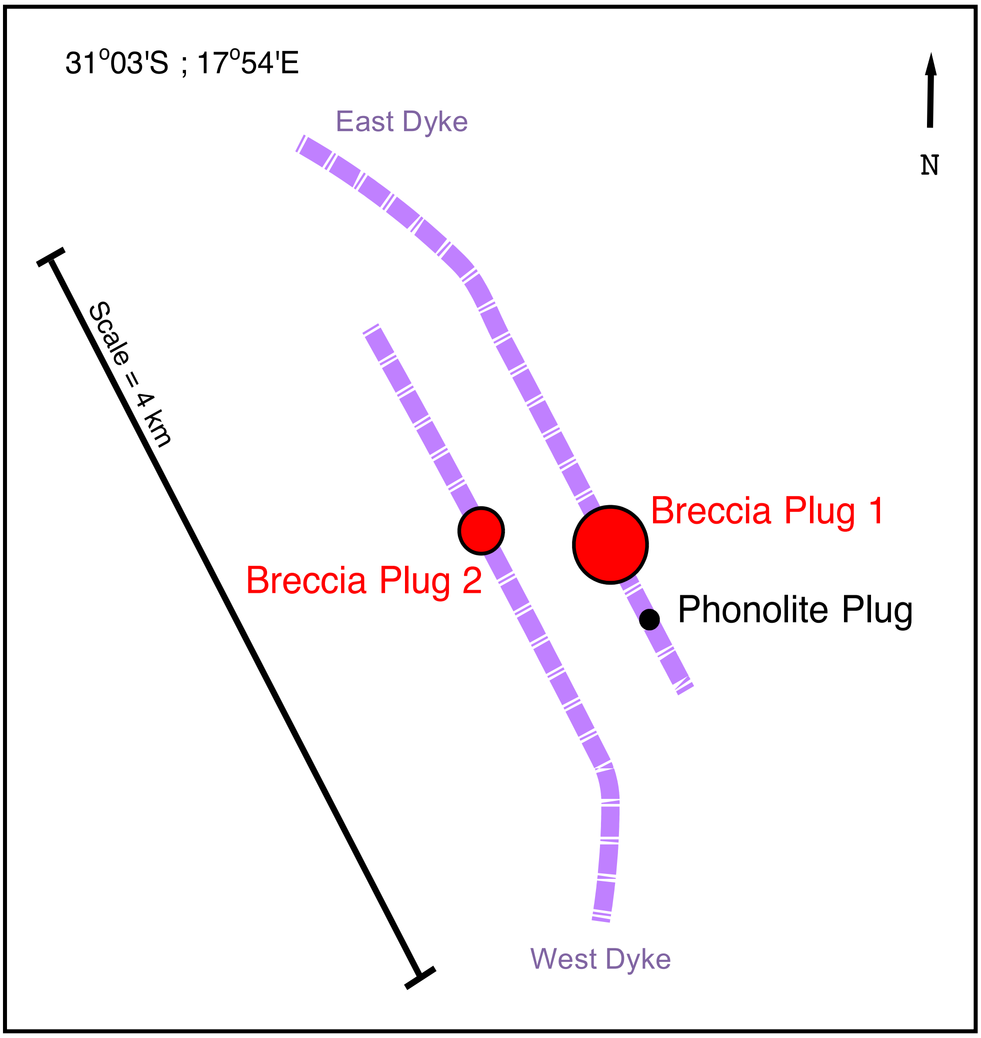

Fig. 3.1 Sketch showing the overall shape of the Breccia Outcrop. The outcrop includes the two sub-parallel dykes (the East Dyke and the West Dyke), the Breccia Plug 1, the Breccia Plug 2, and the Phonolite Plug.

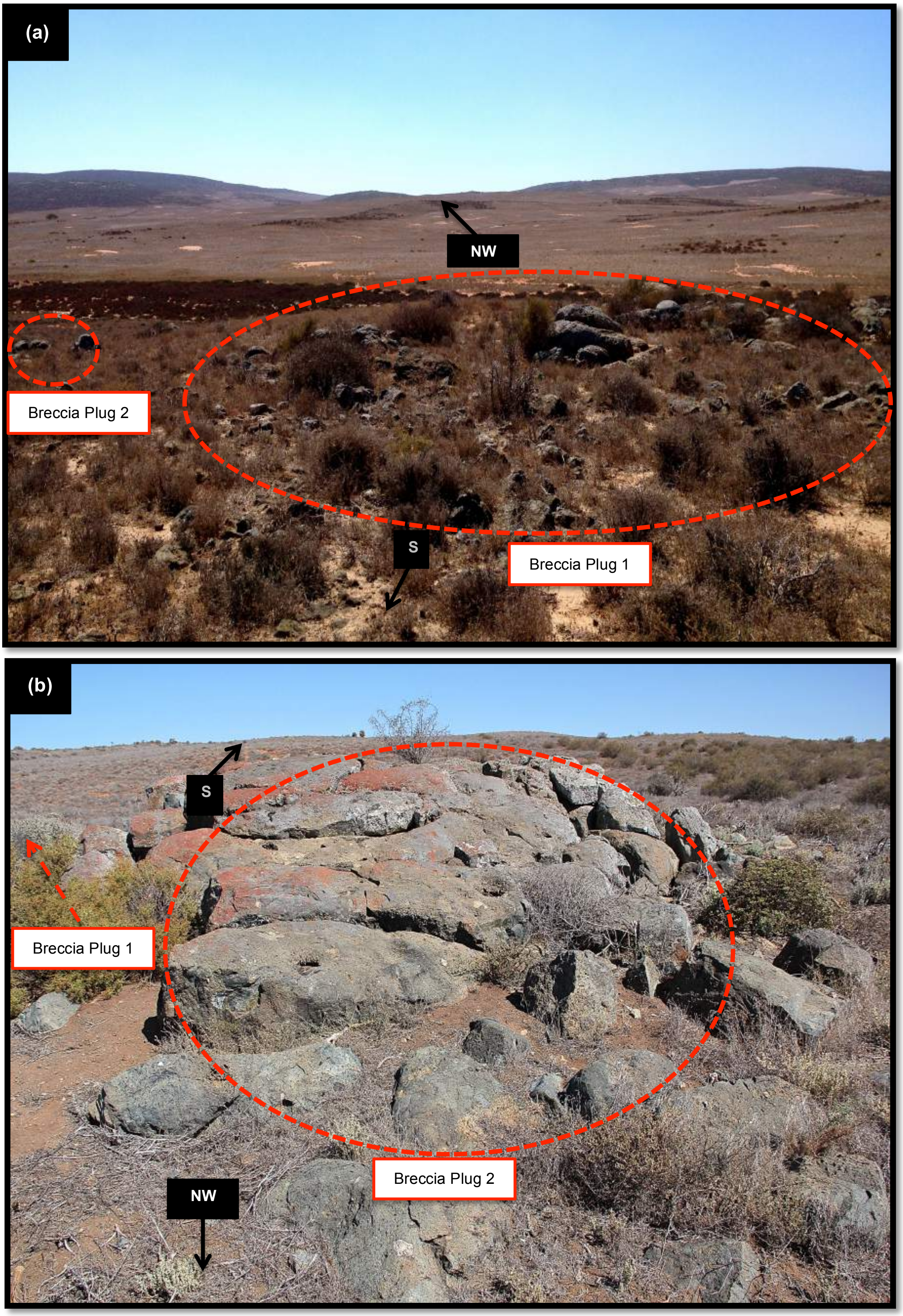

Fig. 3.2 Photographs of the two largest Breccia Outcrops. **(a)** Photograph showing the Breccia Plug 1 and 2. **(b)** Photograph of the Breccia Plug 2. NW and S are the strike direction of the Breccia Outcrop.

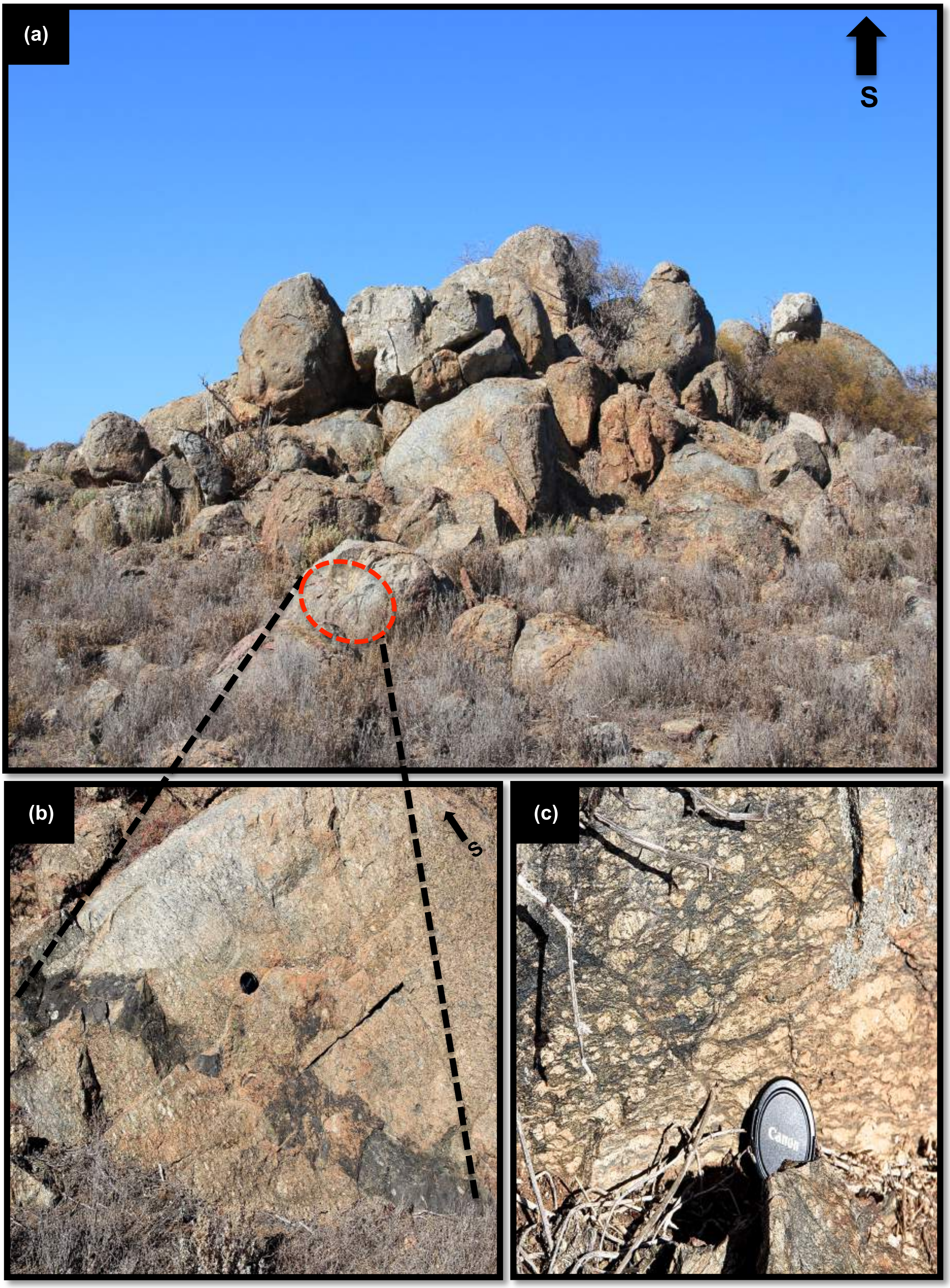

Fig. 3.3 Photographs of the gneiss near the Breccia Outcrop. **(a)** Photograph of a ~2 m in height and ~20 m in diameter gneiss outcrop. This outcrop consists of rounded boulders and loose pieces of gneiss. **(b)** A close up photograph of (a) showing a ~30 cm in width vein filled with breccia rock and cutting through the gneiss. **(c)** Photograph of an outcrop of gneiss mixed with the black matrix of the breccia rocks.

3.1.2 Sampling

Eleven breccia rocks and six gneisses were sampled in March 2014 (Fig. 3.4.a). These samples measured between ~5-10 cm in diameter. The samples were named COK (Camille Olianti Koegel Fontein) from 162 to 178, starting after CCK161 (Catherine Curtis Koegel, sample 161). In January 2015, thirteen breccia rocks, two phonolites, and five gneisses were sampled and numbered from COK189 to COK210 (Fig. 3.4.b). These samples measured ~5-10 cm in diameter, excepting five breccia rocks ~15-25 cm in diameter, which were used for rock and xenolith description. The field descriptions and the coordinates of all the samples are reported in Table 3.1.

One breccia rock was sampled at each outcrop, excepting three rocks that were collected from three locations at the Breccia Plug 1 and four rocks from four locations at the Breccia Plug 2. The eleven gneisses were collected from outcrops next to the Breccia Outcrop, in between the Breccia Plug 1 and 2, and in between the West and East Dykes. Two additional samples were collected from the Alkali-rich Plug.

Three of the breccia samples were treated differently than the rest of the rocks. Sample COK205, which consists of ~50% of black matrix and ~50% of green matrix, was divided into two sub-samples. The green and black types of matrix were removed from hand-specimen COK205 and named respectively COK205-A and COK205-B. Sample COK175 was analysed twice. The whole rock of sample COK175 was analysed first. A gneiss xenolith extracted from sample COK175 was analysed in second and called xenolith COK175. Sample COK208 was analysed once for a black xenolith it contained. The xenolith was extracted from COK208 and named xenolith COK208.

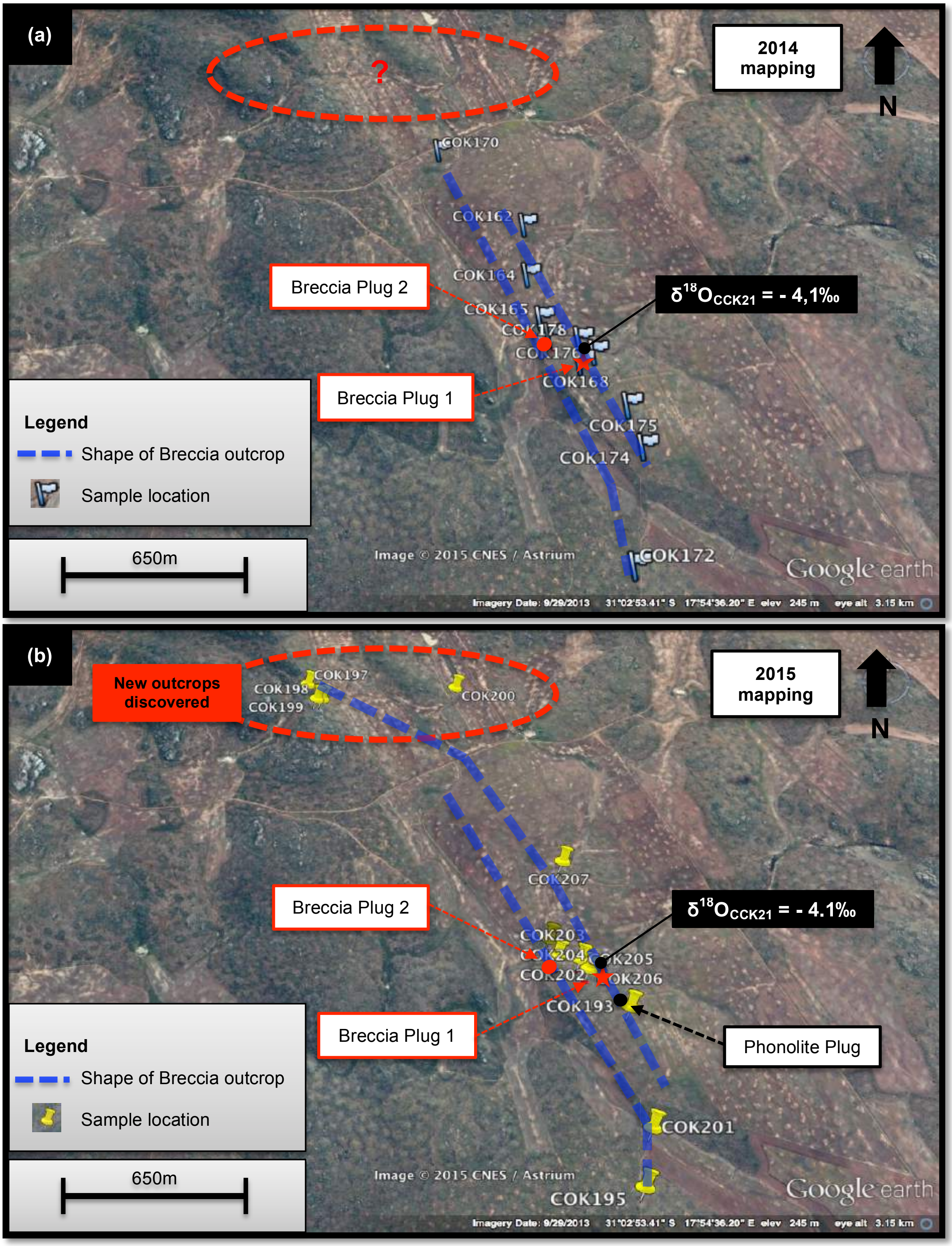

Fig. 3.4 Google Earth images showing the shape of the Breccia Outcrop. **(a)** Map showing COK162 to COK178, which were collected in 2014. **(b)** Map showing COK193 to COK208, which were sampled in 2015. A red star, a red sphere, and a black sphere show respectively the locations of the Breccia Plug 1, the Breccia Plug 2, and the Phonolite plug. Sample CCK21 displays the location of the rock with the lowest whole-rock δ^{18}O value in the complex discovered in 2010 (-4.1‰; Curtis, 2010).

Table 3.1 Sample name, coordinates, and field description for the breccia rocks, phonolite rocks, and gneisses. The term crystal is used for shiny grains observed in hand-specimens.

Sample name	Coordinates	Field description
Breccia rock		
COK162	31°02'41.14" S 17°54'44.70" E	The rock is strongly brecciated. The matrix is grey with abundant ~2 mm white xenoliths and fine-grained shiny crystals.
COK164	31°02'49.73" S 17°54'44.89" E	The matrix is black with abundant fine-grained xenoliths.
COK165	31°02'56.69" S 17°54'46.67" E	The rock shows a mixture between a black and green matrix with sparse medium-grained xenoliths.
COK166	31°02'59.45" S 17°54'47.81" E	The matrix is green and supports medium-grained xenoliths.
COK168	31°03'03.56" S 17°54'52.10" E	The rock is jointed on its surface and consists of a black matrix with a moderate amount of medium-grained, green xenoliths.
COK170	31°02'26.80" S 17°54'30.61" E	The matrix is black and supports sparse grey xenoliths.
COK172	31°03'30.17" S 17°54'57.18" E	The strike is 198°. The matrix is black with abundant fine-grained shiny crystals.
COK174	31°03'15.53" S 17°54.59.94" E	The strike is 198°. The rock has a green matrix with sparse medium-grained xenoliths.
COK175	31°03'09.90" S 17°54'58.40" E	The strike is 310°. The rock is strongly brecciated. The matrix is grey and has abundant coarse-grained, white xenoliths that resemble the gneiss sample COK171.
COK176	31°03'02.16" S 17°54'54.25" E	The matrix is black with abundant medium-grained, green xenoliths.
COK178	31°03'00.14" S 17°54'52.22" E	The matrix is black with sparse xenoliths and abundant fine-grained, shiny crystals.
COK193	31°03'06.96" S 17°54'57.84" E	The matrix is black with a moderate amount of fine-grained, round, green xenoliths.
COK195	31°03'30.18" S 17°54'57.18" E	The matrix is black with abundant fine-grained, shiny crystals.
COK197	31°02'09.12" S 17°54'05.34" E	The outcrop was discovered in 2015 on a hill north of the Breccia Plug 1 and 2. The outcrop has rocks with a black matrix that show abundant fine-grained, shiny crystals.
COK198	31°02'12.36" S 17°54'08.28" E	The outcrop was discovered in 2015 on a hill north of the Breccia Plug 1 and 2. The outcrop is made of rocks with a black matrix that show abundant fine-grained, shiny crystals.
COK199	31°02'12.48" S 17°54'07.32" E	The outcrop was discovered in 2015, on a hill north of the Breccia Plug 1 and 2. The outcrop has rocks with a black matrix that show fine-grained, shiny crystals and fine-grained, white to brown xenoliths.
COK200	31°02'09.18" S 17°54'31.98" E	Loose piece found in a dried up river bed in between two hills north of the Breccia Plugs. COK200 ressembles COK162. The rock has medium-grained, white and black xenoliths and fine-grained, shiny crystals.
COK201	31°03'23.10" S 17°54'59.04" E	The matrix is black, with abundant fine-grained, shiny crystals and sparse round, white xenoliths.

COK202	31°02'59.28" S 17°54'47.70" E	The matrix is fine-grained, green/grey, and has a waxy luster. The rock has fine-grained, shiny crystals.
COK203	31°02'59.28" S 17°54'47.70" E	Large hand-specimen n°1: the rock is strongly brecciated with a green matrix and has different types of medium-grained angular or round xenoliths.
COK204	31°02'59.28" S 17°54'47.70" E	Large hand-specimen n°2: the matrix is made of a green matrix with sparse, black xenoliths. There is a moderate amount of fine- to coarse-grained, white or brown xenoliths.
COK205	31°02'59.28" S 17°54'47.70" E	Large hand-specimen n°3: the rock is made of a mixture between a black and green matrix. There are fine- to coarse-grained, white xenoliths and coarse-grained gneiss xenoliths.
COK206	31°03'01.32" S 17°54'52.32" E	Large hand-specimen n°4: the matrix is a mixture between a black and green matrix. There are fine- to coarse-grained, white to brown xenoliths and coarse-grained gneiss xenoliths.
COK207	31°02'43.86" S 17°54'49.44" E	The matrix is black and supports fine-grained, shiny crystals and green xenoliths.
COK208	31°02'56.69" S 17°54'46.67" E	Large hand-specimen n°5: the matrix is a mixture between a black and grey matrix. There is a moderate amount of coarse- to fine-grained white xenoliths and coarse-grained gneiss xenoliths.
Phonolite rock		
COK191	31°03'06.12" S 17°54'57.72" E	The rock is made of a grey matrix, which supports round, mafic minerals. The outcrop is situated along the strike of the Breccia Outcrop.
COK192	31°03'06.12" S 17°54'57.72" E	The rock is made of a pink matrix, which supports fine-grained, round mafic minerals and feldspar phenocrysts. The outcrop is situated along the strike of the Breccia Outcrop.
Gneiss		
COK163	31°02'40.97" S 17°54'44.92" E	The gneiss is a coarse-grained, white to pink/brown rock.
COK167	31°03'02.64" S 17°54'48.55" E	The rock is deformed, sheared, and black. The gneiss shows fine layering.
COK171	31°02'23.91" S 17°54'31.66" E	The outcrop has a strike of 350°. The rock is strongly sheared and shows fine layreing. The gneiss is grey/black.
COK169	31°03'05.38" S 17°54'53.68" E	The gneiss is a white and green/brown, coarse-grained rock. The rock has coarse-grained phenocrysts of feldspar. This rock is green from the green mineral along the fine-grained mafic minerals.
COK173	31°03'16.68" S 17°54'59.05" E	The gneiss is a white to pink/brown, coarse grained rock with porphyroblastic feldspar.
COK177	31°03'00.06" S 17°54'52.96" E	The rock is made of a grey matrix. This gneiss is sheared.
COK189	31°03'02.40" S 17°55'00.54" E	The rock is grey and shows coarse-grained xenoliths.
COK190	31°03'05.28" S 17°55'10.61" E	The rock is grey and shows coarse-grained xenoliths.
COK194	31°03'23.10" S 17°54'59.04" E	The gneiss is grey to black. The rock is sheared and shows fine layering.
COK209	31°02'43.38" S 17°54'49.02" E	The outcrop is situated in a dried up river bed. This outcrop has strongly sheared gneisses.
COK210	31°04'07.86" S 17°55'26.58" E	This rock was collected south of the Breccia Outcrop. The gneiss is altered and sheared.

3.1.3 Hand-specimen description

The hand-specimens have been grouped into three types, which are the breccia rocks, phonolite rocks, and gneisses (Table 3.1). These groups of rock are summarised in this section.

The breccia rocks

The breccia rocks typically have a black matrix (Fig. 3.5.a). These rocks are hard, dense, and comprise ~0-80 volume % of fragments of other rocks. Most of the breccia rocks have between ~80-100 volume % matrix, excepting two intensely brecciated samples (COK162 and COK175). Despite the similar matrix percentage in most of the breccia rocks, these rocks can look entirely different because of the size, shape, quantity, and composition of their xenoliths and the colour and composition of the matrix.

Matrix. The breccia hand-specimens often show a mixture of two types of matrix, i.e. COK205 (Fig. 3.5.b). The one matrix is fine-grained, black and contains shiny crystals. The other matrix is green, too fine-grained to identify any constituents and has no crystals. These two types of matrix are different in thin section petrography. The green rock shows no evidence for what the origin of the rock might be, whereas the shiny crystals in the black matrix indicate the rock is likely igneous. The designation of the two distinct types of matrix is simplified by calling the green rock the green 'matrix' and the black rock the black 'groundmass'.

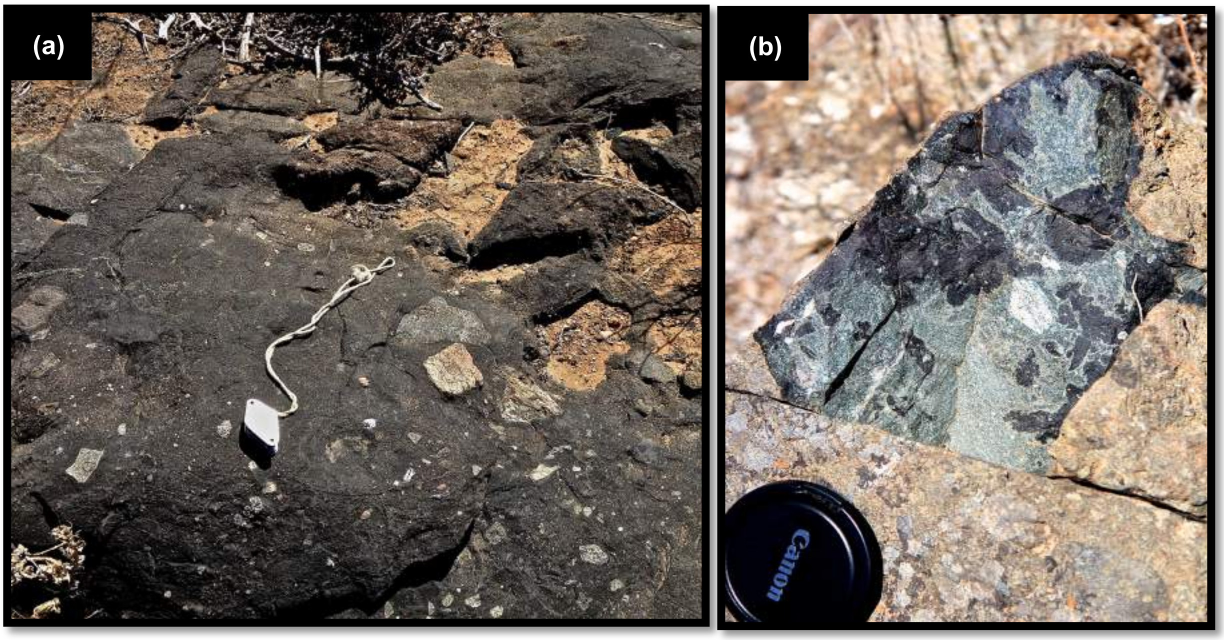

Fig. 3.5 Photographs of breccia rock outcrops. **(a)** Photograph showing the fine-grained, black groundmass of a Breccia Outcrop with abundant xenoliths (Breccia Plug 2). **(b)** Photograph of a fresh piece of breccia rock showing the black groundmass mixed with the green matrix (sample COK205).

Xenoliths. The xenolith fraction in the breccia rocks varies between ~0-80 volume %. The angular to round rock fragments resemble gneiss or are fine-grained, black rock. The size of the xenoliths varies between <1 mm to ~50 cm (Fig. 3.6.a). The brecciation can be intense (Fig. 3.6.b) or absent (Fig. 3.9).

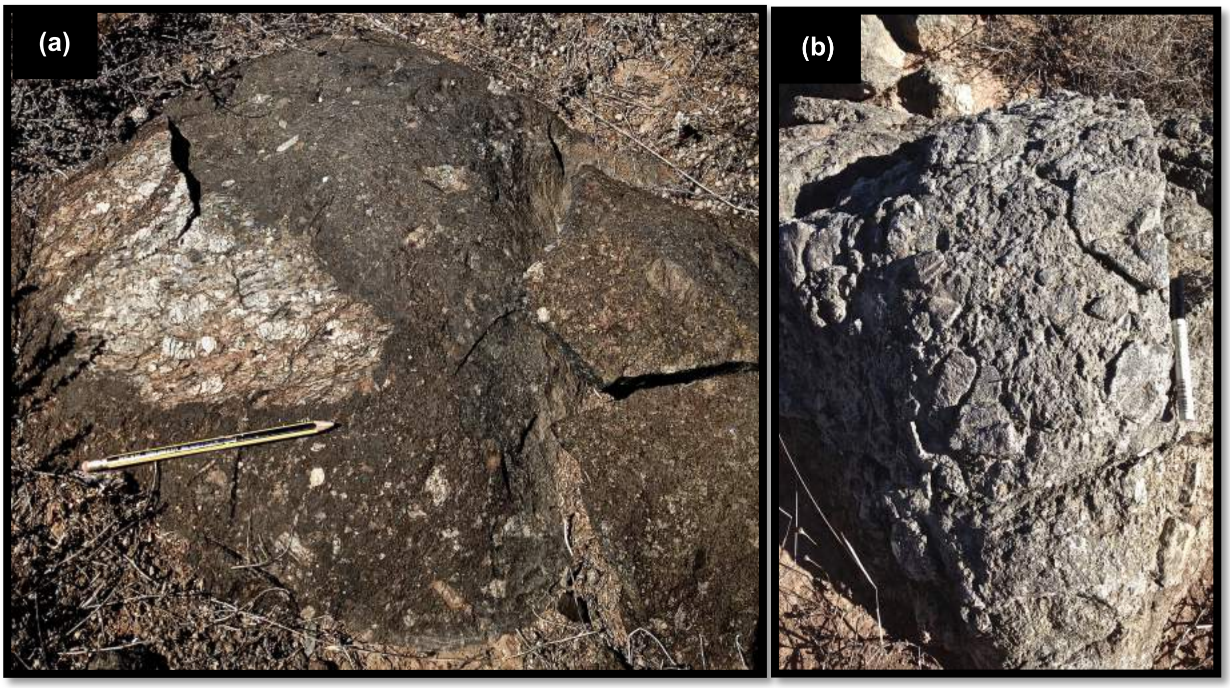

Fig. 3.6 Photographs showing breccia xenoliths. **(a)** Photograph showing an outcrop (COK174) with a ~50 cm gneiss xenolith and abundant <5 cm xenoliths in the black groundmass. **(b)** Photograph showing intense brecciation on the surface of the outcrop from which COK175 was sampled.

There are four types of xenoliths in the breccia rocks. The first type of xenoliths is called the gneiss xenoliths (Fig. 3.7.a). These xenoliths resemble the roof pendant augen gneiss (Fig. 3.7.b). The gneiss xenoliths are fine- (<0.5 mm) to coarse-grained (>2 mm) with well-defined angular or round edges. These rock fragments show mostly quartz. Only a few of the breccia rocks have layers of mafic minerals between quartz and feldspar (e.g. COK164) (Fig. 3.7.c). The size of the gneiss xenoliths ranges between ~1 cm and ~50 cm. These gneiss xenoliths are more frequently found in the green matrix than the black groundmass.

The second group of xenoliths is made of fine-grained, black groundmass (Fig. 3.8.a,b). These xenoliths are often round and between ~1 mm and ~5 cm in diameter. The black xenoliths are in the green matrix. These black rock fragments are more abundant than the gneiss xenoliths; both xenolith types can be found in the same rock (Fig. 3.7.a).

The third and fourth types of xenoliths consist of round, green xenoliths, which are rare compared to the black and gneiss xenoliths. The third type (Fig. 3.8.c) is made of pale green, round inclusions. These pale green xenoliths are ~1-2 cm in diameter and made of a fine-grained matrix too fine-grained to identify any mineral constituents.

The fourth type of xenolith is made of light to bottle green minerals, which are ≤8 mm in diameter. The light and bottle green xenoliths are only seen in two rock samples (COK165 and COK166). Depending on the grain size, the xenoliths are light green or bottle green. The light green xenoliths are too fine-grained to identify any constituents (Fig 3.8.d). The bottle green xenoliths (COK166) are ~2-8 mm in diameter, and resemble epidote, olivine, or pyroxene (Fig. 3.8.e).

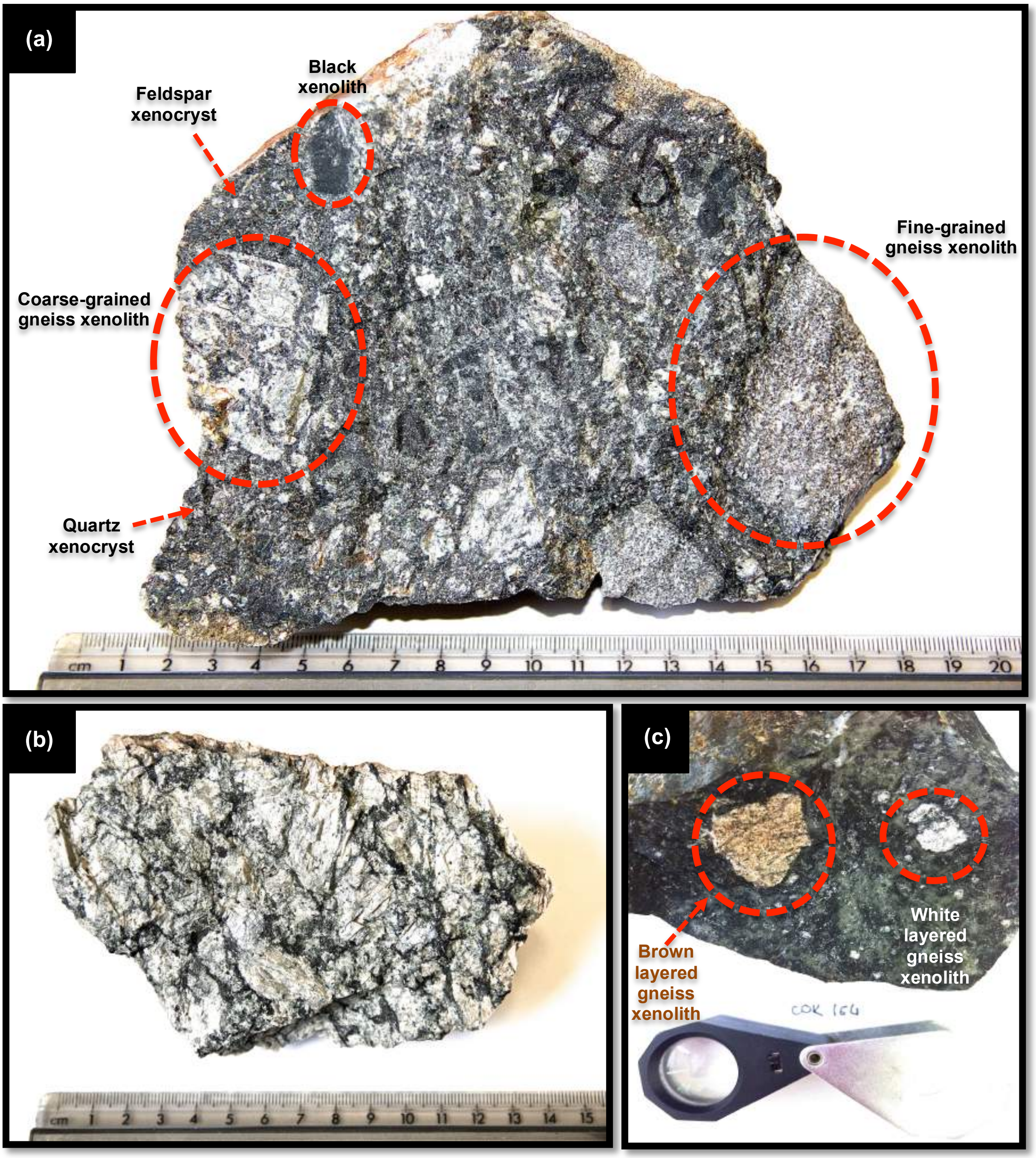

Fig. 3.7 Photographs of two xenolith-rich breccia rocks and one-augen gneiss. **(a)** Photograph showing two gneiss xenoliths, one quartz xenocryst, one feldspar xenocryst, and one black xenolith (sample COK175). **(b)** Photograph of gneiss COK169 collected <200 m from breccia COK175. The gneiss photograph is shown for comparison with the coarse-grained xenoliths in (a). **(c)** Photograph of two gneiss xenoliths in sample COK164. One of the gneiss xenoliths is brown and the other is white. Layers of mafic minerals between layers of quartz and feldspar are visible in both xenoliths.

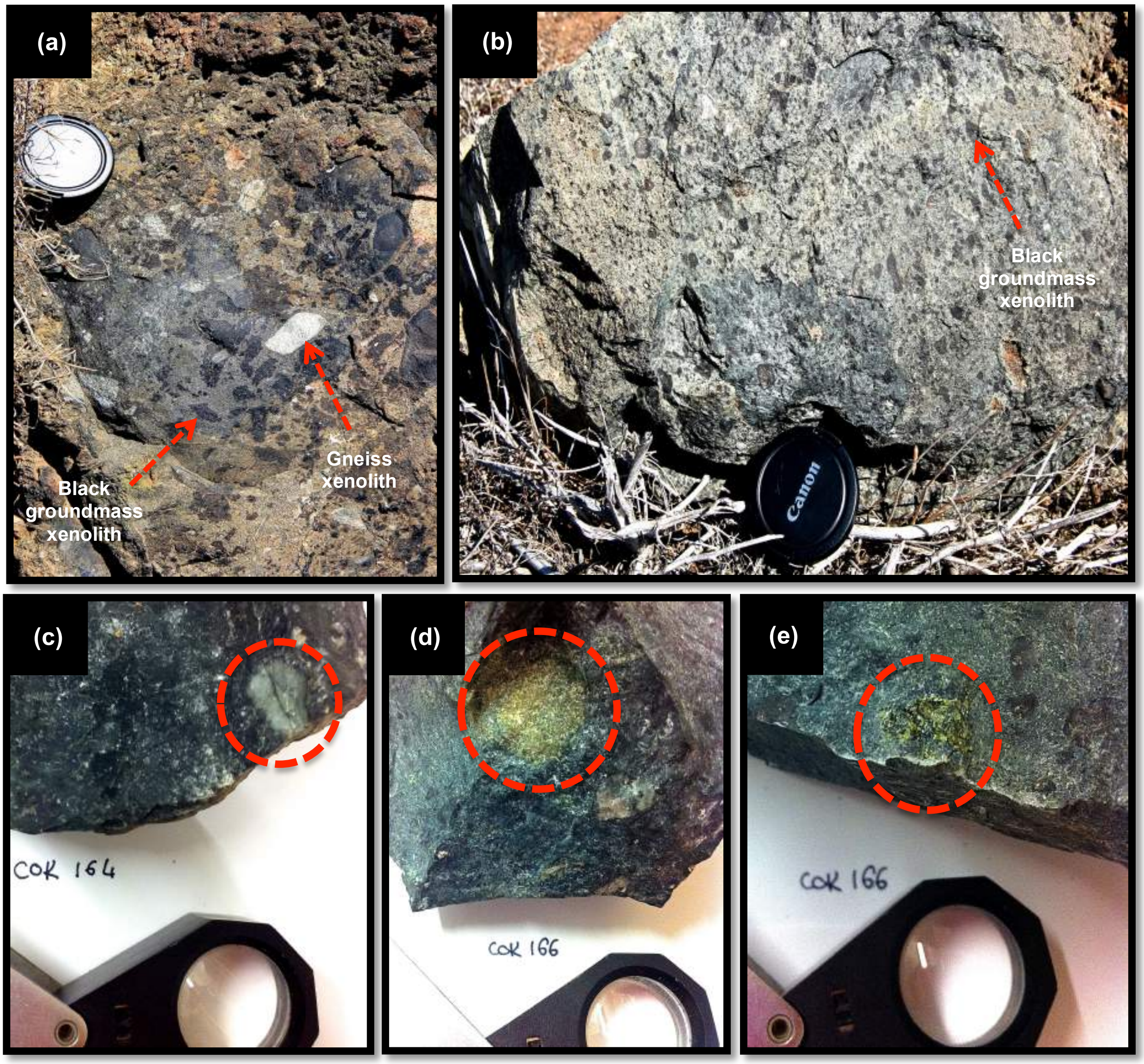

Fig. 3.8 Photographs showing the four xenolith types identified in the breccia rocks. **(a)** Photograph of an outcrop showing black and gneiss xenoliths. **(b)** Photograph showing abundant ≤1 cm black xenoliths in the green matrix of the breccia rocks. **(c)** Photograph of a fine-grained, pale green xenolith in COK164. **(d)** Photograph of a fine-grained, light green xenolith (COK166). **(e)** Photograph of a bottle green xenolith (COK166). This bottle green xenolith is coarser-grained than the light green xenolith in photograph (d).

Xenocrysts. The xenocrysts are crystals ≤5 mm in diameter made of quartz or alkali feldspar. These xenocrysts resemble crystals of the quartz and alkali feldspar found in the gneiss xenoliths. The most xenocrysts are found in the xenolith-rich breccia rocks (Fig. 3.7.a).

Xenolith-poor breccia rocks. The breccia rocks can have a small amount of xenoliths with a xenolith fraction <15 volume % (Fig. 3.9.a). These xenolith-poor breccia rocks consist mostly of the black groundmass (~85-95 %) and ≤5 mm in diameter shiny crystals (<15 %). The xenolith-poor breccia rocks often have veins filled with fine-grained epidote (Fig. 3.9.b).

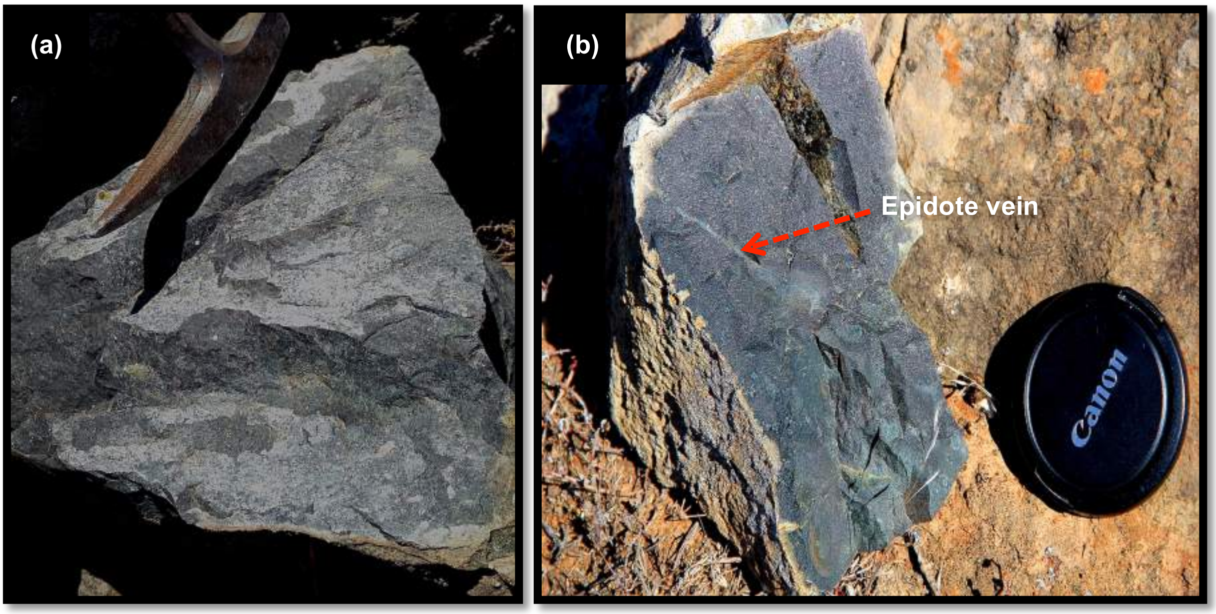

Fig. 3.9 Photographs of two xenolith-poor breccia samples. **(a)** Sample COK178 and **(b)** sample COK195 showing a vein filled with a epidote.

The phonolite rocks

Two samples from the Phonolite Plug were collected and numbered COK191 and COK192 (Fig. 3.10.a,b). These rocks are pink or grey, fine-grained, and consist of >90 volume % alkali feldspar. The phenocrysts assemblage (<20 volume %) is made of <2 mm in diameter magnetite and sparse porphyroblastic alkali feldspar. No xenoliths are visible in these rocks.

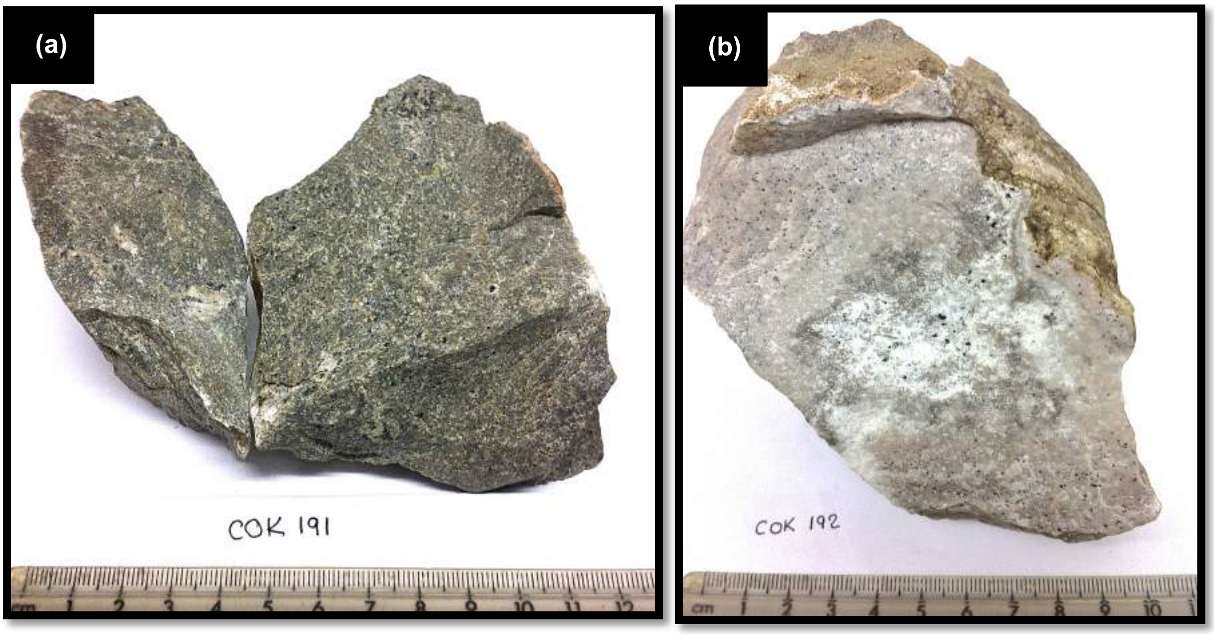

Fig. 3.10 Photographs of the phonolite rocks. **(a)** Sample COK191 with its grey groundmass and **(b)** sample COK192 with its pink groundmass. Both samples have abundant fine-grained magnetite dispersed in the groundmass.

The gneisses

The gneiss surrounding the Breccia Outcrop is augen gneiss. This gneiss is porphyritic, fine- to coarse-grained with porphyroblastic feldspar (Fig. 3.11.a), quartz, mafic minerals, and green alteration minerals. The gneiss near the Breccia Outcrop can be white/pink to brown (Fig. 3.11.b), excepting two gneiss samples, which are grey/black (Fig. 3.11.c,d).

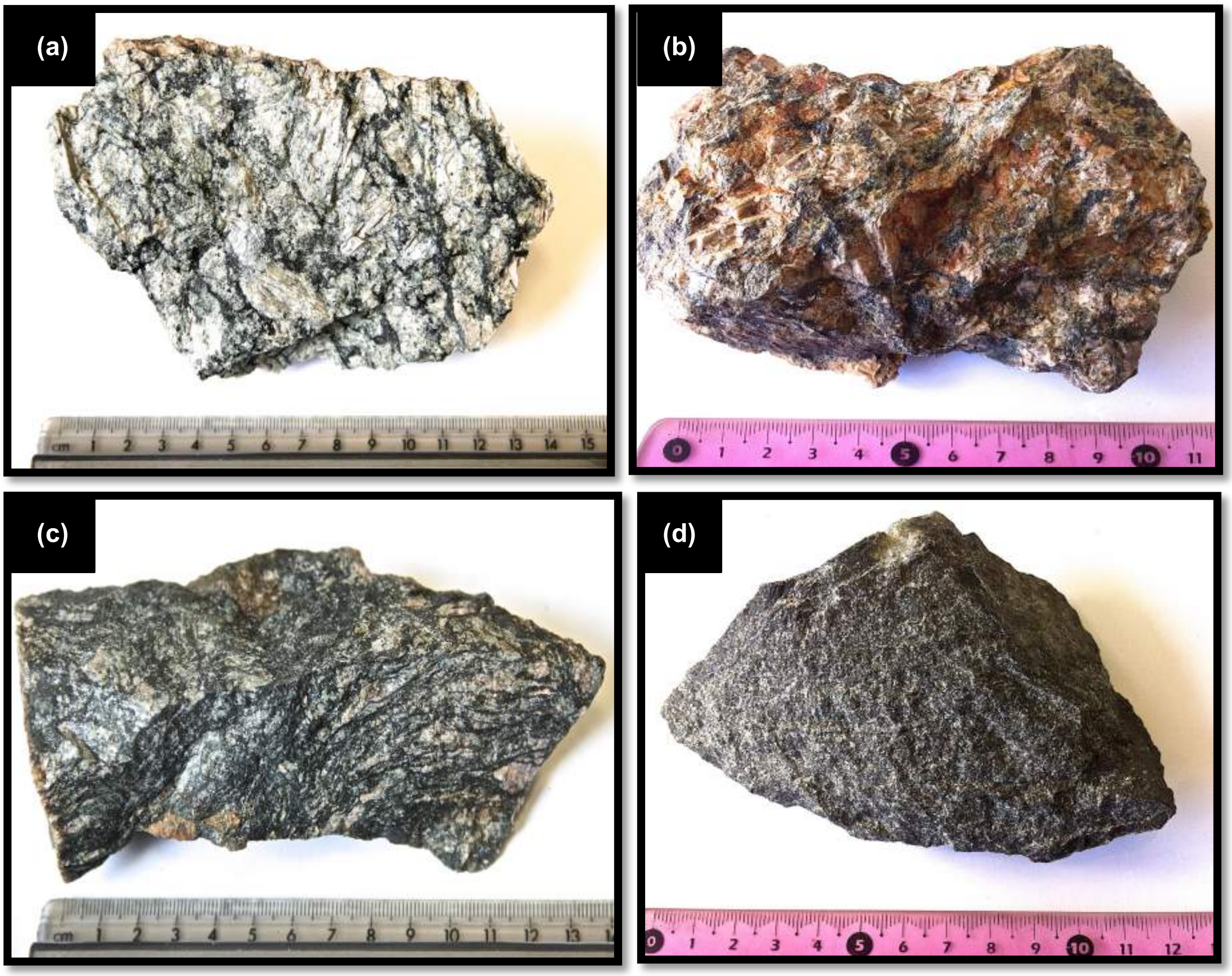

Fig. 3.11 Photographs of four gneisses. **(a)** Photograph of COK169 with porphyroblastic feldspar and green minerals replacing the mafic minerals. **(b)** Photograph of a pink/brown augen gneiss (COK163). **(c)** Photograph of COK177 with abundant layered mafic minerals. **(d)** Photograph of sheared gneiss COK171.

3.2 Thin section petrography

The thin section petrography of selected breccia rocks, phonolites, and gneisses is summarised in Table 3.5. This table includes the matrix, xenolith, and phenocryst fraction in each sample and their petrographic description. Thin section microphotographs and hand-specimen photographs of the selected samples are given in Appendix A. The thin section petrography for all the sampled rocks is described in Appendix B.

3.2.1 The breccia rocks

The breccia rocks consist of ~20-98% matrix component, ~0-79% xenoliths, and ~0-20% phenocrysts (Table 3.5). The wide range in matrix, xenolith, and phenocryst percentages in the breccia rocks reflects the degree of dissimilarity these rocks can have. The breccia rocks are divided into four groups to show the petrographic variability of these rocks (Table 3.2).

Table 3.2 Grouping of the breccia rocks using a binocular microscope.

Breccia rock			
Most matrix (~98%)	Most xenoliths (~40-79%)	Most phenocrysts (≥15%)	Black + green matrix (respective %)
COK192	**COK162**	COK174	**COK165 (~50-50)**
COK197	**COK175**	**COK195**	COK166 (~20-80)
	COK205	**COK198**	**COK168 (~80-20)**
		COK199	**COK170 (~40-60)**
			COK174 (~40-60)
			COK205 (~50-50)
Thin section petrography (Table 3.5 and Appendix B) and photomicrographs (Appendix A)			

Matrix

The two types of matrix observed in the breccia hand-specimens have been called in this work the black 'groundmass' and the green 'matrix'. The designation 'matrix' for the green rock and 'groundmass' for the black rock used for the hand-specimen description is kept for thin section petrography. This terminology is applied because the green rock is notably different to the black rock in thin section petrography. The green matrix shows no evidence for the origin of the green rock, whereas the black groundmass shows igneous groundmass textures, which bring evidence for the origin of the black rock. The black rock can be one of three types of groundmass, whereas the green matrix is one type of matrix. These four types of matrix are described hereafter.

To simplify the matrix description of the breccia rocks, the four types of matrix were indexed from A to D (Table 3.3). The first type of matrix, which is the green matrix in the breccia rocks, is called matrix (A). The three other types of matrix, which are black rock, are called groundmass (B), groundmass (C), and groundmass (D).

Green matrix. Matrix (A) is fine-grained, too fine-grained to identify any primary minerals, and strongly altered by epidote and chlorite (Fig. 3.12.a). This matrix does not show phenocrysts; there are however abundant xenoliths made of groundmass (B), gneiss xenoliths made of granoblastic quartz, and quartz xenocrysts.

Black groundmass. The first type of groundmass that is black in the hand-specimens is groundmass (B) (Fig. 3.12.b). This groundmass is generally too fine-grained or too altered to identify any constituents. Groundmass (B) contains abundant opaque minerals and is partly to entirely coated by a brown alteration mineral identified using the binocular microscope as biotite in two samples. Abundant alkali feldspar and/or plagioclase phenocrysts are supported in this groundmass. Fissures cutting through groundmass (B) are filled with matrix (A).

Groundmass (B) shows in two breccia samples a mixture between a groundmass with a basaltic texture similar to groundmass (D) and a groundmass with a trachytic texture similar to groundmass (C). Even though these two samples seem to show that groundmass (B) is a mixture between groundmass (C) and groundmass (D), the intense alteration of the breccia rocks and the fine-grain size of the groundmasses make it difficult to specify if groundmass (B) is a mixture between groundmass (C) and groundmass (D) or if groundmass (B) is another constituent in the breccia rocks.

Groundmass (C) (Fig. 3.12.c) is fine-grained with a trachytic texture similar to that of bostonites. This groundmass consists of oriented needle-like crystals of alkali feldspar coated by a brown alteration mineral. This groundmass contains alkali feldspar phenocrysts, quartz xenoliths, and groundmass (B) xenoliths.

The last matrix type is groundmass (D) (Fig. 3.12.d). Groundmass (D) has a basaltic texture. This groundmass is fine-grained and contains abundant phenocrysts of plagioclase and sparse phenocrysts of pyroxene, alkali feldspar, and amphibole.

Overall, the breccia rocks consist either of groundmass (C), groundmass (D), or a mixture of groundmass (B) and matrix (A) (Table 3.5). Matrix (A) forms most of sample COK205-A and groundmass (B) most of sample COK205-B. Groundmass (C) is reflected by COK178 and COK198 and groundmass (D) by COK172 and COK195. The geochemistry these types of matrix reflected by these samples is examined in the Results Chapter.

Table 3.3 Summarising table describing the four types of matrix in the breccia rocks.

Matrix	Description of the types of matrix in the breccia rocks
Matrix (A)	Fine-grained matrix partly to entirely replaced by epidote and chlorite. Matrix (A) often has abundant groundmass (B) xenoliths, gneiss xenoliths, and quartz xenocrysts. No phenocrysts are visible.
Groundmass (B)	Fine-grained groundmass coated by a brown (PPL and XPL) alteration mineral. The groundmass supports abundant phenocrysts of alkali feldspar and/or plagioclase. Groundmass (B) resembles to a mixture between groundmass (C) and (D) in two breccia samples.
Groundmass (C)	Fine-grained groundmass with a trachytic texture made of needle-like crystals of alkali feldspar. The trachytic texture ressembles that of bostonite rocks. Groundmass (C) is coated by a brown (PPL and XPL) alteration mineral.
Groundmass (D)	Fine-grained groundmass with a basaltic texture. The groundmass has abundant phenocrysts of plagioclase feldspar and sparse phenocrysts of pyroxene, alkali feldspar, and amphibole.

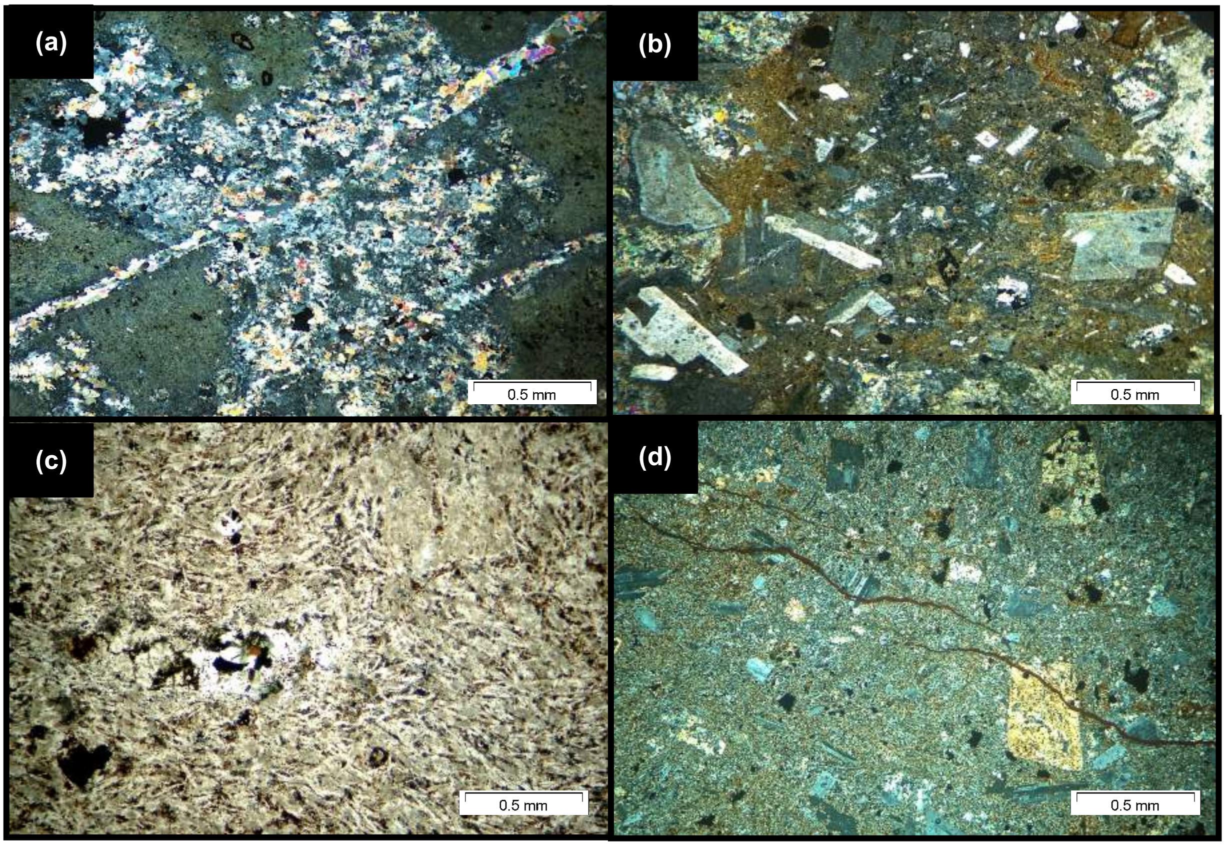

Fig. 3.12 Photomicrographs of the four types of matrix in the breccia rocks. **(a)** Photomicrograph in cross-polarised light (XPL) of matrix (A) in sample COK165. Veins filled with epidote cut through groundmass (B). **(b)** Photomicrograph (XPL) of groundmass (B) in sample COK165, which shows feldspar phenocrysts (~10 %) supported in groundmass (B). A brown alteration mineral covers groundmass (B). **(c)** Photomicrograph in plain-polarised light (PPL) of groundmass (C) in sample COK178, showing a trachytic groundmass texture. **(d)** Photomicrograph (XPL) of groundmass (D) in sample COK195. Plagioclase and pyroxene phenocrysts are supported in this groundmass.

Xenoliths

The breccia rocks contain up to ~79% of xenoliths (i.e. COK175). The xenoliths are round to angular and fine- to coarse-grained. Three of the four types of xenoliths are examined in thin section petrography. The fourth type, which is made of the light to bottle green xenoliths, was not visible on the thin section. This fourth type was most likely too thin for thin section and polished away when the thin section was prepared. Microprobe analysis was used instead to identify the minerals that make up this fourth type of xenoliths.

The first xenolith type, which is the gneiss xenoliths, is in most of the breccia rocks. This xenolith type is made of fine- to coarse-grained quartz with a granoblastic texture (Fig. 3.13.a). Two xenoliths in COK164 and COK166 show layers of sheared mafic minerals in between coarse-grained quartz and alkali feldspar (Fig. 3.13.b). These gneiss xenoliths are abundant in matrix (A) and sparse in groundmass (B), groundmass (C) (trachytic texture), and groundmass (D) (basaltic texture).

The second xenolith type (Fig. 3.13.c), which is the black xenoliths, resembles groundmass (B). These xenoliths are henceforth called groundmass (B) xenoliths. The groundmass (B) in these xenoliths occasionally contains strongly altered phenocrysts of alkali feldspar and/or plagioclase. These phenocrysts in the groundmass (B) xenoliths are partly to entirely altered by epidote, chlorite, or a brown (PPL and XPL) mineral, which was recognised as biotite in COK172 and COK195. Relict phenocrysts recrystallised by a fine-grained groundmass can also be seen in groundmass (B) xenoliths. Groundmass (B) xenoliths often have coronas of opaque minerals and can be partially replaced by epidote or chlorite.

The third type of xenoliths, which is the pale green xenoliths, is made of epidote (Fig. 3.13.d). This alteration mineral reflects that this third type is a cumulate of epidote instead of a rock fragment. This epidote is fine-grained, has a distinctive yellow birefringence in plain-polarised light, and forms glomeroporphyritic masses.

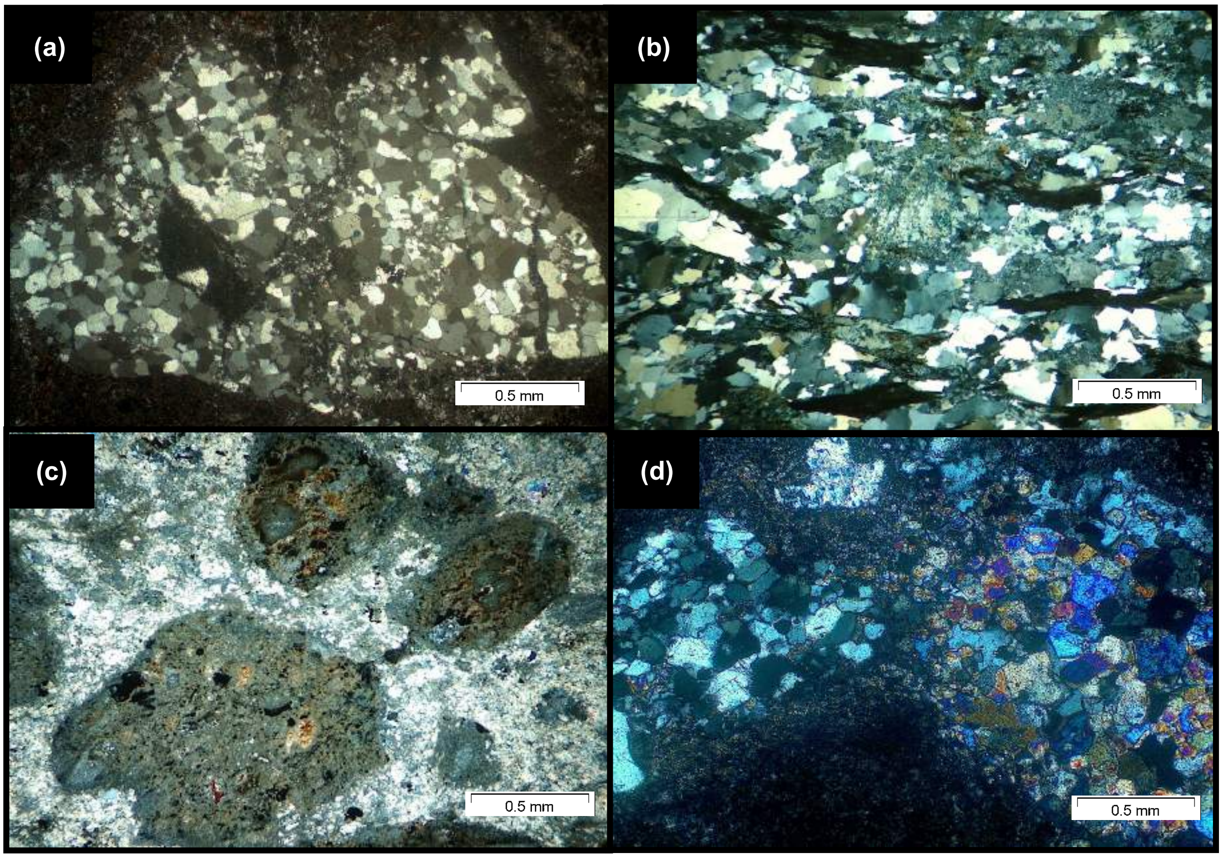

Fig. 3.13 Photomicrographs showing breccia rocks xenoliths. **(a)** Photomicrograph (XPL) of a gneiss xenolith made of granoblastic quartz (COK176). **(b)** Photomicrograph (XPL) of a xenolith resembling the roof pendant gneiss. Sheared mafic minerals are layered in between quartz and feldspar (COK164). **(c)** Photomicrograph (XPL) of round xenoliths made of groundmass (B) observed in matrix (A) (COK166). **(d)** Photomicrograph (XPL) of a gneiss xenolith made of granoblastic quartz next to a pale green xenolith made of fine-grained epidote (COK164).

Phenocrysts

The phenocryst assemblage in the breccia rocks consists predominantly of alkali feldspar and/or plagioclase (Fig. 3.14.a) with minor pyroxene and amphibole. Feldspar phenocrysts are common in groundmass (B), groundmass (C), and groundmass (D) and absent in matrix (A). These feldspar phenocrysts are subhedral to anhedral and mainly >0.5 mm in length. Feldspar can be tabular to prismatic and has sparse to abundant fine-grained opaque mineral inclusions. Alkali feldspar is medium- (0.5-2 mm) to coarse-grained (>2 mm) and shows Carlsbad twinning, whereas plagioclase is fine- (<0.5 mm) to coarse-grained and shows a polysynthetic twinning. The feldspar phenocrysts are often turbid and show perthitic and sieve textures.

Pyroxene and amphibole phenocrysts are only found in groundmass (D) (Fig. 3.14.b). These phenocrysts are sparse, strongly altered by chlorite, epidote, or biotite, and show poikilitic and resorption textures. Amphibole and pyroxene show perfect cleavages intersecting at 60°/120° and right angles, respectively.

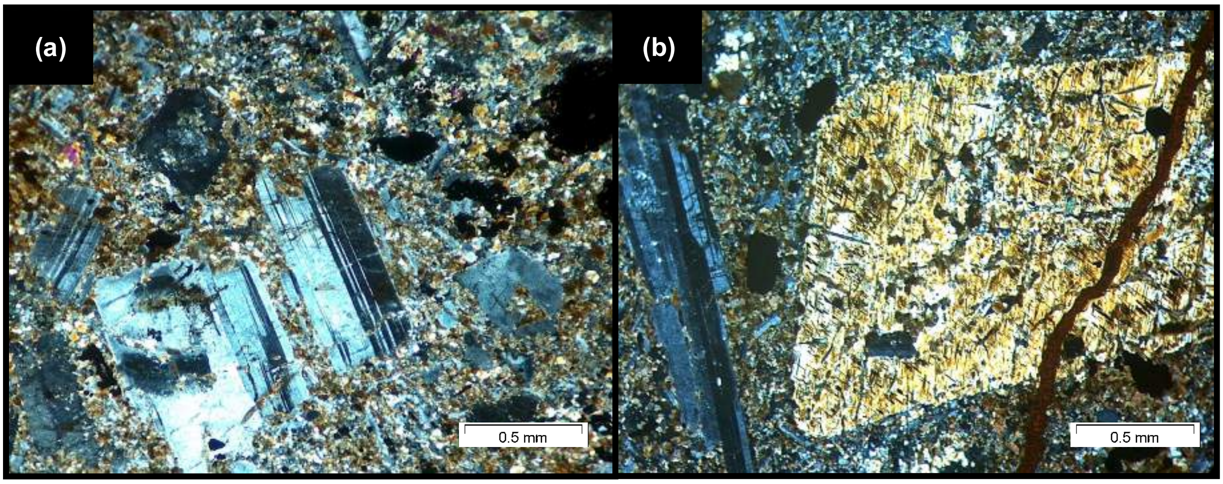

Fig. 3.14 Photomicrographs of phenocrysts. **(a)** Photomicrograph (XPL) of plagioclase feldspar in groundmass (B) showing polysynthetic twinning (COK172). **(b)** Photomicrograph (XPL) of an amphibole in groundmass (B) showing a cleavage intersecting at 60°/120° angles (COK195). A vein of biotite cuts through the amphibole.

3.2.2 Alteration of the breccia rocks

Brown alteration mineral

A brown (PPL and XPL) alteration mineral (Fig. 3.15.a) coats parts of groundmass (B), groundmass (C), groundmass (D), and groundmass (B) xenoliths. The brown (PPL and XPL) alteration mineral is recognised as biotite in sample COK172 and COK195. In the rest of the breccia rocks, the brown mineral product is too altered or too fine-grained to identify.

Epidote and chlorite

The fine- to medium-grained epidote is the main alteration phases in all of the breccia rocks (Fig. 3.15.c,d,e). Chlorite is less common than the epidote. Epidote and chlorite partly replace groundmass (B), groundmass (C), groundmass (D), groundmass (B) xenoliths, and gneiss xenoliths. Epidote and chlorite are the only alteration minerals recognised in matrix (A). Epidote is most abundant in sample COK165, COK168, COK170, and COK205-A.

Alteration textures

The xenoliths, xenocrysts, and phenocrysts have coronas and sieve textures. Sample COK162 contains two quartz xenocrysts with a flow texture (Fig. 3.15.b). The rims of xenoliths and feldspar phenocrysts are often replaced by epidote or less commonly by chlorite. Phenocrysts of feldspar are often turbid. The quartz is strained and shows trails of fluid inclusions. Several phenocrysts are relict and were recrystallised by a fine-grained groundmass (Fig. 3.15.f). Groundmass (B) is often too fine-grained and altered to identify any constituents (Fig. 3.15.g) and is mixed with matrix (A) (Fig. 3.15.h).

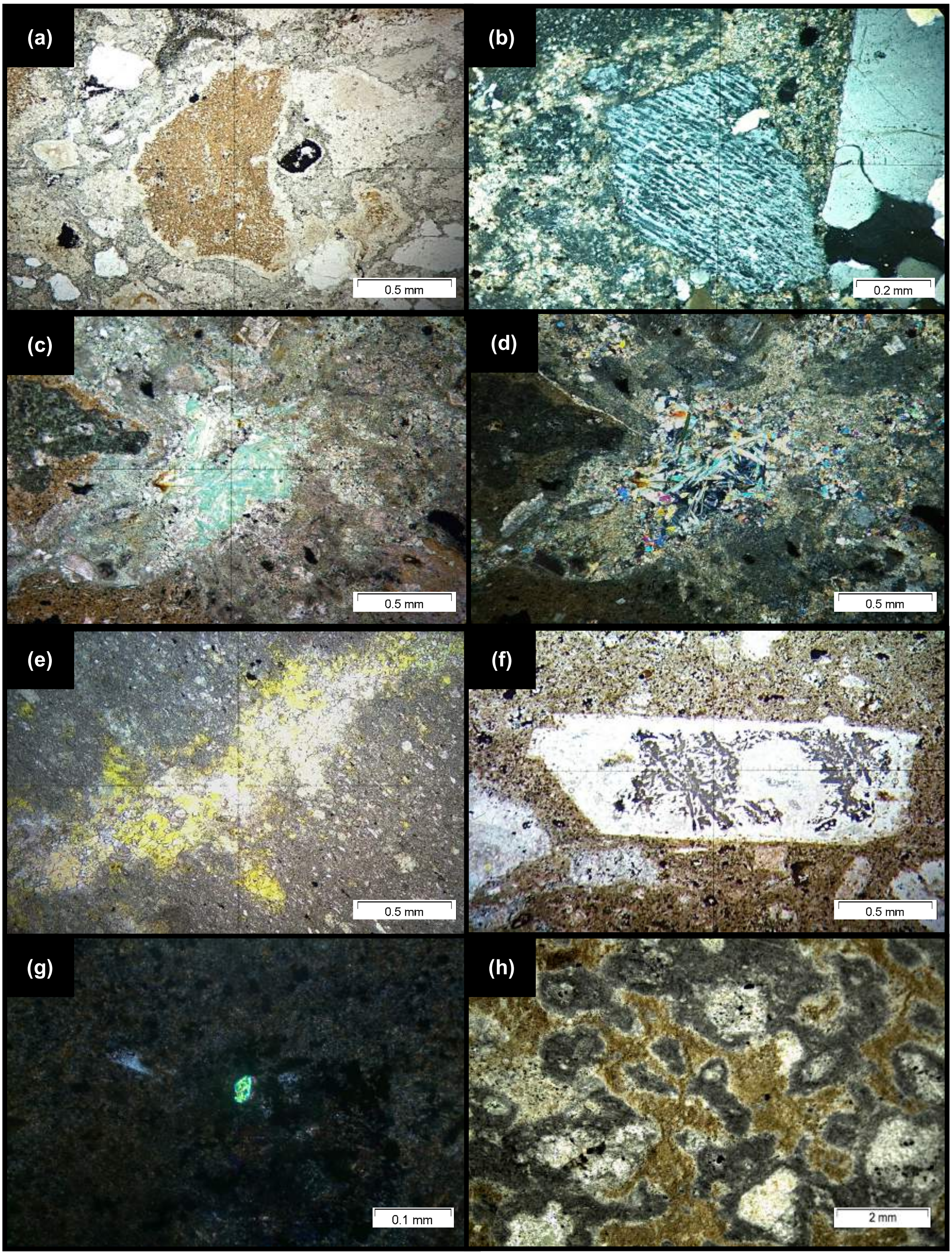

Fig. 3.15 Photomicrographs showing alteration of the breccia rocks. **(a)** Photomicrograph (PPL) of groundmass (B) xenoliths coated by a brown alteration phase and of **(b)** a flow texture (XPL) in a quartz grain (COK162). **(c)** Photomicrograph (COK164) showing chlorite with a green birefringence and epidote in PPL and **(d)** in XPL. **(e)** Photomicrograph of epidote showing a yellow birefringence in COK202 (PPL). **(f)** Photomicrograph (PPL) of COK165 showing a relict phenocryst of feldspar. **(g)** Photomicrograph (XPL) of a zircon mineral in the fine-grained, strongly altered groundmass (B) (COK168). **(h)** Photomicrograph (XPL) showing a mixture between matrix (A) (in green), groundmass (B) (in grey/black), and gneiss xenoliths (COK170).

3.2.3 The phonolite rocks

The rocks described in this section are called phonolite based on the compositional field they plot in on the TAS diagram and their nepheline content proven later on in this study.

Despite the fact that the Phonolite Plug is found along the strike of the Breccia Outcrop, this plug is made of rocks with a different mineral composition. The matrix in the phonolites is called groundmass (E). This designation follows that of the four types of matrix of the breccia rocks, which were indexed from A to D. In addition, the phonolites show an igneous groundmass texture, hence the terminology ‘groundmass’. Groundmass (E) is made of >90 volume %, fine-grained alkali feldspar (Fig. 3.16.a,b). This groundmass supports <20 volume % phenocrysts, which are made of opaque minerals and alkali feldspar. There is no evidence of xenoliths in the phonolites.

A brown mineral product in PPL and XPL coats parts of groundmass (E). The alkali feldspar that makes up groundmass (E) is strongly altered by epidote and chlorite; this feldspar has a dusty alteration. These feldspar phenocrysts show perthitic and resoption textures.

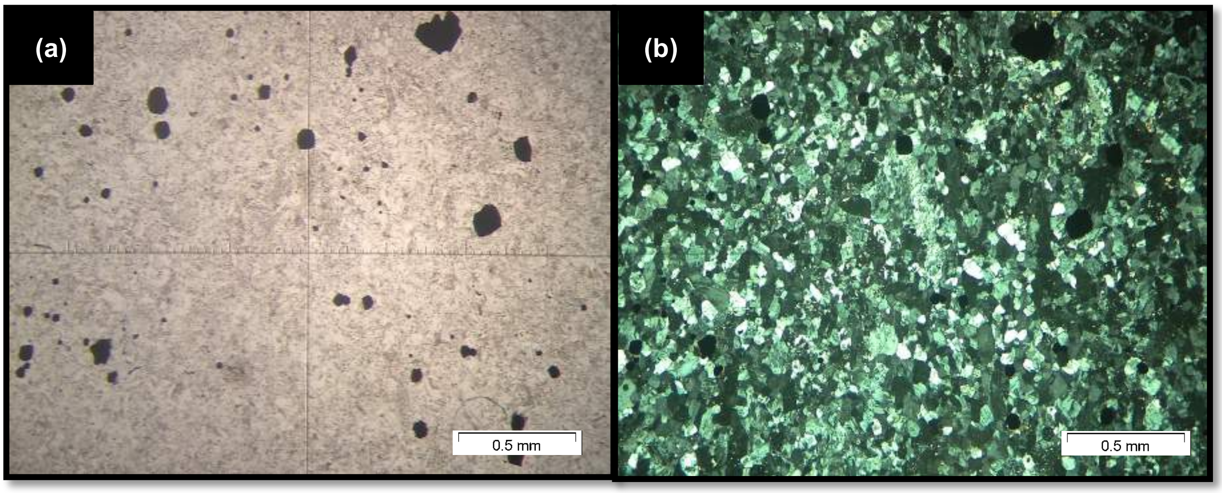

Fig. 3.16 Photomicrographs of phonolite COK192. **(a)** (PPL) and **(b)** (XPL).

3.2.4 The gneisses

The gneiss from the roof pendant has previously been described (Curtis et al., 2011). The rock is a porphyritic, fine- to coarse-grained augen gneiss consisting of anhedral to subhedral inequigranular grains with a granoblastic texture. The mineralogy includes porphyroblastic feldspar (~45%) within layered quartz (30-40%), biotite (~20%), plagioclase (≤10%), and traces of amphibole, chlorite, and opaque minerals. Feldspar has simple twining and is often perthitic and altered.

Two of the gneisses collected in this work are dissimilar to the rest of the gneisses. The first unusual rock is COK171 (Fig. 3.17.a), which is black in hand-specimen. In thin section, COK171 shows mostly quartz with sparse sheared feldspar, which is elongated. Sample COK171 comprises sparse mafic minerals, which are altered by chlorite and epidote. The second distinctive rock is COK169 (Fig. 3.17.b). This sample contains significantly more chlorite and epidote than the rest of the gneisses, which explains the green colour of the hand-specimen.

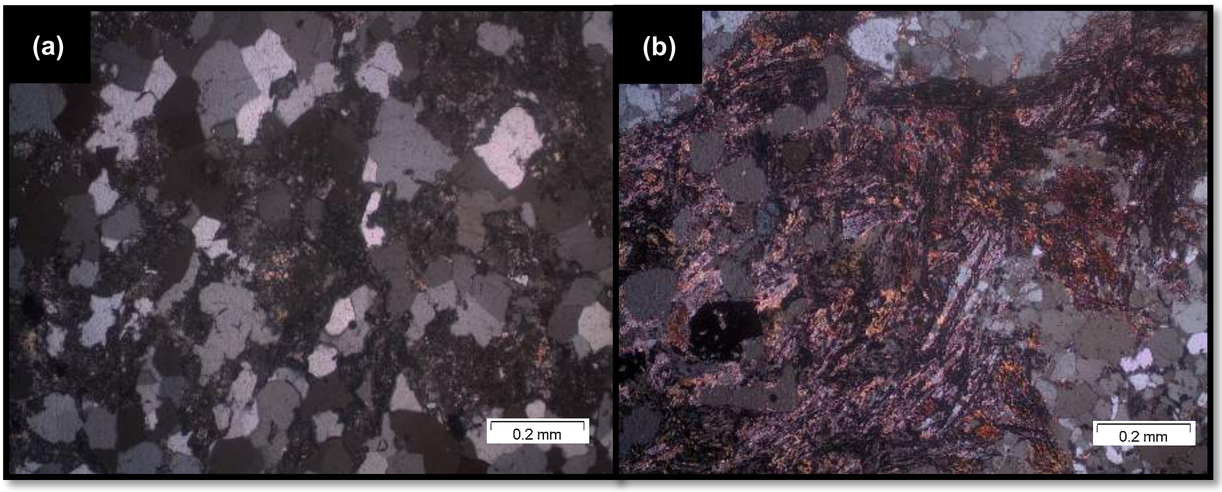

Fig. 3.17 Photomicrographs of two gneiss samples. **(a)** Sample COK171 (XPL) showing sheared altered mafic minerals and **(b)** COK169 (XPL) showing mafic minerals altered by epidote and chlorite.

3.2.5 Sample grouping

The rocks are separated into two groups. Group 1 consists of rocks found along the strike of the Breccia Outcrop (Table 3.4.a). This group is subdivided into two subgroups, which are rocks with an 'igneous texture' and rocks with a 'mixture of igneous and metamorphic textures'. Group 2 consists of all the rocks collected next to the Breccia Outcrop. The samples in group 2 are the rocks with a metamorphic texture (Table 3.4.b).

The subgroup 'igneous texture' contains five breccia rocks and the two phonolite rocks. Sample COK172 and COK195 are in the sub-category 'basalt' because these two samples have a basaltic igneous texture in petrography. Sample COK178, COK198, and COK199 are in the sub-category 'bostonite' because of their trachytic groundmass texture that resembles that of bostonite rock. Sample COK191 and COK192 are the two phonolites in the 'phonolite' sub-category.

The subgroup 'mixture of igneous and metamorphic textures' contains sixteen breccia rocks. These rocks are generally made of matrix (A), groundmass (B), and gneiss and groundmass (B) xenoliths. The group 2 includes ten rocks, which show a metamorphic texture and are country rock gneiss.

Table 3.4 Grouping of rocks found along and next to the Breccia Outcrop. **(a)** Rocks sampled along the strike of the Breccia Outcrop. **(b)** Rocks collected next to the Breccia Outcrop. The breccia rocks either have an igneous texture or a mixture of an igneous and metamorphic texture. Two phonolites found along the strike of the Breccia Outcrop have an igneous texture. Rocks next to the Breccia Outcrop are metamorphic augen gneisses.

(a) Rocks along the Breccia Outcrop				**(b) Rocks next to the Breccia Outcrop**
Igneous texture			**Mixture of igneous and metamorphic textures**	**Metamorphic texture**
Breccia rock		Phonolite rock	Breccia rock	Augen gneiss
Basalt	Bostonite			
COK172	COK178	COK191	COK162	COK163
COK195	COK198	COK192	COK164	COK167
	COK199		COK165	COK169
			COK166	COK171
			COK168	COK177
			COK170	COK189
			COK174	COK190
			COK175	COK194
			COK176	COK209
			COK193	COK210
			COK197	
			COK200	
			COK201	
			COK202	
			COK205	
			COK207	

3.2.6 Summary

Firstly, the breccia rocks show two types of igneous groundmass textures. Groundmass (C) in COK178 and COK198 has a trachytic groundmass texture similar to that in bostonites. Groundmass (D) in COK172 and COK195 shows a basaltic groundmass texture similar to that in basalts. Secondly, groundmass (B) is phenocryst-rich (≤20%). Thirdly, matrix (A) consists mostly of epidote and chlorite, shows no evidence of phenocrysts, and supports abundant xenoliths. Fourthly, the most breccia xenoliths are made of groundmass (B). Fifthly, the gneiss xenoliths are abundant in the breccia rocks. These xenoliths are generally only made of granoblastic quartz. Finally, the phonolites contain mostly alkali feldspar with sparse microphenocrysts of opaque minerals, some nepheline in the groundmass, and show no evidence of xenoliths (Table 3.5).

Table 3.5 Summarised petrography of selected breccia rocks, phonolite rocks, and gneisses. Photographs of these samples are shown in Appendix A. The summarised petrography for all the rocks sampled in this work is found in Appendix B.

Size classification: <0.5mm=fine-grained; 0.5-2mm=medium-grained; >2mm=coarse-grained

1) Igneous textures

Breccia rock - bostonite

Sample name	Comment	Rock type	Matrix	Phenocryst	Xenolith / xenocryst	1ry mineralogy	2ry mineralogy	Description	Alteration
COK178	Trachytic texture	Igneous (bostonite)	95%	5%	0%	**Matrix:** groundmass (C); opaque minerals **Phenocryst:** alkali feldspar; relict feldspar	Epidote, brown mineral	Groundmass (C) is fine-grained, with a trachytic texture made of oriented, elongate crystals of alkali feldspar. Alkali feldspar phenocrysts are medium- to coarse-grained, and show Carlsbad twinning. Some feldspars are relict phenocrysts, recrystallised by a fine-grained matrix, too fine to identify. Relict phenocrysts show intergrowth textures. There are no visible xenoliths.	There is an abundant fine-grained, brown (PPL) mineral in between aligned alkali feldspar crystals. The groundmass is strongly altered by epidote. Phenocrysts are embayed, and partially to entirely replaced by epidote.
COK198	Trachytic texture	Igneous (bostonite)	75%	20%	5%	**Matrix:** groundmass (C); opaque minerals **Phenocryst:** alkali feldspar **Xenolith:** groundmass (B)	Epidote, brown mineral	The groundmass is fine-grained, with a trachytic texture made of oriented, elongate crystals of alkali feldspar. Alkali feldspar phenocrysts are coarse-grained, and show Carlsbad twinning.	Fissures are filled with epidote. A moderate amount of a brown (PPL, XPL), round mineral spreads over the groundmass. Xenoliths are coated by a fine-grained, brown (PPL, XPL) mineral. Phenocrysts show resorption textures, and have a dusty alteration. Epidote partially replaces the xenoliths.

Breccia rock - basalt

Sample name	Comments	Rock type	Matrix	Phenocryst	Xenolith / xenocryst	1ry mineralogy	2ry mineralogy	Description	Alteration
COK172	Basaltic texture	Igneous (basalt)	85%	13%	2%	**Matrix:** groundmass (D) coated by biotite; opaque minerals **Phenocryst:** plagioclase; amphibole; pyroxene **Xenolith:** quartz	Epidote, biotite	The groundmass is fine-grained, with elongate microcrystals of plagioclase. Plagioclase phenocrysts are fine- to medium-grained, and show polysynthetic twinning. Plagioclase laths are euhedral to subhedral, clustered in glomeroporphyritic masses. There are sparse amphibole and pyroxene, with their perfect cleavage intersecting respectively at 60°/120° and right angles. Gneiss xenoliths show fine-grained, granoblastic quartz.	Groundmass (D) is coated by elongate, brown pleochroic (PPL) biotite. The phenocrysts and xenoliths are altered by fine-grained epidote. Amphiboles and pyroxenes show poikilitic and resorption textures. Plagioclase has a dusty alteration.
COK195	Basaltic texture	Igneous (basalt)	85%	15%	0%	**Matrix:** groundmass (D) coated by biotite; opaque minerals **Phenocryst:** plagioclase; pyroxene; amphibole; alkali feldspar	Epidote, biotite	The groundmass is too fine-grained to identify. There are abundant medium- to fine-grained plagioclase phenocrysts. There are pyroxene and amphibole phenocrysts with their perfect cleavage intersecting respectively at right angles and at 60°/120°. There are no visible xenoliths.	The groundmass is coated by biotite. Epidote and biotite fill fissures in phenocrysts. Plagioclase is partially replaced by epidote. Phenocrysts show resorption textures.

Phonolite rock

Sample name	Comments	Rock type	Matrix	Phenocryst	Xenolith / xenocryst	1ry mineralogy	2ry mineralogy	Description	Alteration
COK192	Pink hand-specimen	Igneous	95%	5%	0%	**Matrix:** groundmass (E) **Phenocryst:** opaque minerals; alkali feldspar	Epidote, chlorite	The groundmass is fine-grained (coarser-grained than COK191), and mostly made of alkali feldspar (>90 volume %). Opaque minerals are round, fine-grained phenocrysts. Alkali feldspar phenocrysts are medium-grained. There are no visible xenoliths.	Parts of the groundmass (E) is altered by fine-grained epidote. Alkali feldspar in groundmass (E) has a dusty alteration. Feldspar phenocrysts are strongly altered by epidote, and show perthitic textures. Opaque minerals have coronas of epidote.

Continued…

2) Mixture of igneous and metamorphic textures

Breccia rock

Sample name	Comments	Rock type	Matrix	Phenocryst	Xenolith / xenocryst	1ry mineralogy	2ry mineralogy	Description	Alteration
COK162	Flow texture in two quartz xenocrysts	Igneous and metamorphic	39%	0%	60%	**Matrix:** matrix (A) **Xenolith:** groundmass (B) with abundant opaque minerals; quartz	Epidote, brown mineral	Xenoliths are mostly made of groundmass (B). There are sparse, fine- to medium-grained disseminated quartz xenocrysts. Gneiss xenoliths consist of granoblastic quartz. The xenoliths and xenocrysts are round, or angular, and found in matrix (A). Two quartz xenocrysts show a flow texture. Quartz has a wavy extinction. There are no visible phenocrysts.	Matrix (A) is strongly altered by fine-grained epidote. Groundmass (B) xenoliths are coated by a brown (PPL, XPL) alteration product.
COK165	Xenolith with the lowest δ18O value (-5.6‰)	Igneous and metamorphic	85%	10%	5%	**Matrix:** groundmass (B); matrix (A); opaque minerals **Phenocryst:** feldspar in groundmass (B) **Xenolith:** groundmass (B); quartz	Epidote, chlorite, brown mineral	Groundmass (B) and matrix (A) are mixed together. Relict phenocrysts of feldspar are fine- to medium-grained, and strictly found in groundmass (B). Groundmass (B) xenoliths, and gneiss xenolith made of granoblastic quartz are found in matrix (A).	The matrices and the phenocrysts are strongly altered. Matrix (A) is replaced by fine- to medium-grained epidote, and chlorite. Groundmass (B) is coated by a fine-grained, brown (PPL, XPL) mineral. Feldspar phenocrysts are strongly altered by epidote. The phenocrysts are embayed, and show sieve textures.
COK168	Lowest δ18O value (-5.2‰)	Igneous and metamorphic	85%	10%	5%	**Matrix:** groundmass (B); matrix (A); zircon **Phenocryst:** plagioclase and alkali feldspar in groundmass (B); opaque minerals **Xenolith:** groundmass (B)	Epidote, chlorite, brown mineral, calcite	Plagioclase and alkali feldspar phenocrysts are fine- to medium-grained, and subhedral. Xenoliths of groundmass (B) in matrix (A) contain abundant medium-grained opaque minerals.	Fine- to medium-grained epidote and chlorite replace matrix (A). Sparse calcite is found in matrix (A). Groundmass (B) is partly coated by a fine-grained, brown (PPL and XPL) mineral. Phenocrysts show sieve and resorption textures, and have altered rims.
COK170	Lowest δ18O value (-5.2‰)	Igneous and metamorphic	86%	0%	15%	**Matrix:** groundmass (B); matrix (A); opaque minerals **Xenolith:** quartz; groundmass (B)	Epidote, brown mineral	Groundmass (B) and matrix (A) are mixed together. The gneiss xenoliths consist of granoblastic quartz. There are no visible phenocrysts.	Matrix (A) is strongly altered by epidote. Parts of granoblastic quartz and groundmass (B) xenoliths are replaced by epidote.
COK175	Contains the most xenoliths	Igneous and metamorphic	20%	1%	79%	**Matrix:** groundmass (B) **Phenocryst:** alkali feldspar **Xenolith:** quartz; groundmass (B)	Brown mineral, epidote	Groundmass (B) contains sparse phenocrysts of alkali feldspar. There are abundant gneiss xenoliths made of granoblastic quartz, and disseminated, quartz xenocrysts. Groundmass (B) xenoliths have abundant fine-grained, opaque minerals in them.	The groundmass is coated by a brown (PPL, XPL) mineral. The xenoliths and xenocrysts of quartz are strained, and show trails of fluid inclusions. Phenocrysts are turbid, with altered rims. The alkali feldspar shows perthitic and sieve textures.
COK205	Mixture of green matrix and black groundmass	Igneous and metamorphic	45%	10%	45%	**Matrix:** groundmass (B); matrix (A) **Phenocryst:** feldspar; relict feldspar **Xenolith:** groundmass (B); quartz	Epidote, chlorite, brown mineral	Groundmass (B) and matrix (A) are mixed together. Groundmass (B) contains the feldspar phenocrysts. Matrix (A) has abundant disseminated quartz xenocrysts and granoblastic quartz xenoliths. The xenoliths of groundmass (B) are well-defined, round or angular, and fine- to coarse-grained. <2% of the feldspar phenocrysts are relict, replaced by a groundmass that is too fine-grained to identify.	Both matrices are strongly altered. Matrix (A) is replaced by abundant epidote, and chlorite. Groundmass (B) is coated by a brown (PPL, XPL) mineral. Groundmass (B) xenoliths have coronas of opaque minerals, and chlorite.

3) Metamorphic texture

Gneiss

Sample name	Comments	Rock type	Matrix	Phenocryst	Xenolith / xenocryst	1ry mineralogy	2ry mineralogy	Description	Alteration
COK167	Sheared	Augen gneiss	-	-	-	Alkali feldspar, quartz, biotite, opaque minerals, zircon	Chlorite	The texture is medium- to coarse-grained, with sutured grain boundaries. Quartz and feldspar are elongate, showing preferred orientation towards shearing. Biotite is sheared. There is evidence of recrystallization by fine-grained quartz showing 120° grain boundaries.	Quartz and feldspar have altered rims, and are embayed. The feldspar rims and biotite grains are chloritised.
COK169	Greenish rock	Augen gneiss	-	-	-	Alkali feldspar, quartz, biotite, opaque minerals, zircon	Chlorite, epidote	The texture is medium- to coarse-grained, with abundant coarse-grained porphyroblastic alkali feldspar. Feldspar is inequigranular, anhedral to subhedral.	Alkali feldspar rims are chloritised. Alkali feldspar is perthitic, and embayed. Biotite is replaced by epidote and chlorite.

CHAPTER 4 METHODOLOGY

The data of the thirty-seven samples collected on two field trips, one in March 2014 and the other in January 2015, were produced at the University of Cape Town (UCT). The samples were split into three parts using a hydraulic splitter. One part from each sample was saved as a hand-specimen and the other was used to make thin sections. The last part was crushed into a Sturtevant Laboratory jaw crusher. Half the material from the jaw crusher was sieved (200-600 µm) and used for mineral separation. The other half was placed into a SeibTechnik carbon steel swing mill and ground to fine powder. The powder was used in all following analytical analyses.

4.1 Whole-rock geochemistry

4.1.1 X-ray fluorescence

Twenty-eight samples (18 breccia rocks, 2 phonolite rocks, 2 breccia xenoliths, and 6 gneisses) were analysed for whole-rock major element compositions and 12 samples (8 breccia rocks, 2 phonolite rocks, 2 breccia xenoliths) for whole-rock trace element concentrations.

Major elements

Following the method described by Willis and Duncan (2008), ~2 g of powdered samples were weighed, dried at 110°C, and ashed overnight at 950°C to determine the loss on ignition (LOI) and convert all Fe to oxidised Fe^{3+}. The ashed samples were then mixed with LiT-LiM flux (57:43 respectively), with LiBr used as releasing agent, and fused in a Claisse gas burner to make fusion disks. Natural standards from the USGS and SARMS (South African producers of Metallurgical and Geological Certified Reference Materials) were prepared following the same method and used to calibrate the data. The matrix was corrected using the Fundamental Parameter method (Rousseau et al., 1996; Willis and Duncan, 2008).

A Panalytical Axios wavelength-dispersive x-ray fluorescence (XRF) spectrometer (acquired in 2010) with a sample-changer (56 sample capacity) and rhodium end-window X-ray tube measured the major element concentrations from fusion disks. The intensity data was processed with SuperQ software. The XRF instrument detection limits were calculated based on the sample matrix and the specific analytical conditions used for the analysis. The detection limit values were between 0.003 wt % and 0.016 wt % (Table 4.1.a). The analytical uncertainties for major elements were in the order of 1-2%.

Trace elements

The samples were analysed for trace elements as powder briquettes. A flux bound ~6 g of whole-rock powder, which was then supported in a boric acid base and prepared using a ten-ton hydraulic cold press. The Panalytical Axios wavelength-dispersive XRF spectrometer measured the trace element concentrations and data were refined using SuperQ software. The lower limits of detection for trace elements were between 1 ppm and 5 ppm for all the trace elements, excepting S (10 ppm) and F (40 ppm) (Table 4.1.b).

Table 4.1 Lower limits of detection (LLD). LLD for (**a**) major and **(b)** trace element concentrations in the breccia rocks from XRF data.

(a) Major elements (measured on fused disk)			
Element	LLD (ppm)	Oxide	LLD (wt.% oxide)
Si	50	SiO2	0.011
Ti	20	TiO2	0.003
Al	80	Al2O3	0.015
Fe	20	Fe2O3	0.003
Mn	20	MnO	0.003
Mg	50	MgO	0.008
Ca	40	CaO	0.006
Na	120	Na2O	0.016
K	30	K2O	0.004
P	30	P2O5	0.007
S	60	SO3	0.015
Cr	20	Cr2O3	0.003
Ni	20	NiO	0.003
(b) Trace elements (measured on powder briquettes)			
Element	LLD (ppm)	Element	LLD (ppm)
Zn	3	Pb	2
Cu	3	Co	3
Ni	5	Mn	3
Mo	1	Cr	2
Nb	1	V	3
Zr	1	F	40
Y	1	S	10
Sr	1	Cl	5
Rb	1	Sc	1
U	2	Ba	5
Th	2		

4.1.2 Inductively coupled plasma mass spectrometer

Trace element compositions were obtained for 22 xenoliths, which include 15 breccia rocks, 1 phonolite rock, 6 gneisses, and BHVO-2 certified reference materials (CRM). These concentrations were obtained using solution inductively coupled plasma mass spectrometer (ICP-MS). A 4:1 concentrated HF-HNO_3 acid mixture was added to 50 mg rock powders in sealed Teflon beakers. After the samples were left for 48h at ±140°C and brought to dryness, 2 ml of concentrated HNO_3 were added to the samples. The final product was dried and mixed with 5% HNO_3 solution that included 10 ppb Bi, In, Re, and Rh internal standards. The samples were standardised against artificial multi-element standard solutions. The concentrations of these samples were determined on a Thermo-Fisher X-Series II Quadrupole ICP-MS (installed in 2009). Errors throughout the concentration range were <3%. The accuracy and procedural blank levels were consistent with those reported by le Roex et al. (2001).

The trace element data for the CRM BHVO-2 are shown against the recommended values from GeoReM (Table 4.2). The trace element Ni, which is an important element in this work used to distinguish rock components in the breccia rocks, is typically not well resolved by ICP-MS. The ICP-MS Ni value does not show good agreement with the Ni value from GeoReM. The concentration of Ni in the samples obtained by ICP-MS analysis is therefore not considered further. The only Ni data included in the subsequent chapters are results from XRF analysis.

Zirconium does not show a strong agreement with the Zr value from GeoReM. Similarly to Ni, Zr is generally not well resolved by ICP-MS. The difference in the observed and calculated Zr concentrations from ICP-MS analysis likely reflects the incomplete dissolution of zircon minerals in the digestion process. This difference should, however, be negligible due to the minor quantities of zirconium present in the breccia rocks. The Zr data of the breccia rocks from ICP-MS analysis are therefore used for further interpretation.

Table 4.2 Trace element concentrations (ppm) of the standard BHVO-2 against the internationally accepted values of BHVO-2 from GeoReM. Nickel differs significantly from the accepted values of GeoReM and is highlighted in yellow. Nickel from ICP-MS analysis is not considered further.

Element	BHVO-2 GeoReM (ppm)	BHVO-2 UCT (ppm)
7Li	4.8	4.3
45Sc	32	32
51V	317	317
52Cr	280	266
59Co	45	39
62Ni	119	190
65Cu	127	145
66Zn	123	131
85Rb	9.11	9.00
88Sr	396	393
89Y	26	23
90Zr	172	159
93Nb	18.1	17.1
137Ba	131	130
139La	15.2	14.6
140Ce	37.5	36.3
141Pr	5.35	5.07
144Nd	24.5	23.9
152Sm	6.07	6.12

Continued…

153Eu	2.07	2.08
159Tb	0.92	0.93
160Gd	6.24	6.12
163Dy	5.31	5.18
165Ho	0.98	1.00
166Er	2.54	2.47
169Tm	0.33	0.35
174Yb	2	2
175Lu	0.274	0.300
178Hf	4.36	4.30
181Ta	1.14	1.57
208Pb	1.60	1.65
232Th	1.22	1.14
238U	0.403	0.357

XRF and ICP-MS data

Five breccia rocks and 1 phonolite were analysed using both XRF and ICP-MS methods to compare Zr trace element data of these rocks (Fig. 4.1). Niobium and Ba data from ICP-MS and XRF analysis are also compared. The data are taken from COK172 and COK195 (basaltic texture), COK198 (trachytic texture), COK205-A (green matrix), COK205-B (black groundmass), and COK192 (phonolite rock).

Niobium data show the best correlation between XRF and ICP-MS data with a near ~1:1 ratio line. The Ba data are not as strongly correlated as the Nb data. Sample COK172, COK195, and COK205-B have ~200 ppm more Ba by XRF analysis than ICP-MS analysis. Only COK192 and COK198 plot immediately on the Ba 1:1 ratio line. The Zr data of COK198 and COK205-B are strongly correlated and have a ~1:1 ratio. Sample COK172, COK195, and COK205-A have ~200 ppm more Zr by XRF analysis than ICP-MS analysis. The main inconsistency in the Zr results is seen in the phonolite COK192. Sample COK192 has over 3500 ppm Zr when analysed by XRF methods.

The Nb data is strongly correlated and the data for Zr and Ba are moderately correlated. The main discrepancy in the results is in the Zr data of COK192. This inconsistent Zr data possibly results from incomplete dissolution of a Zr-bearing mineral and the difference in the quantity of sample analysed using the two methods. Zr-bearing minerals, which are generally harder to dissolve than other minerals, must have been incompletely dissolved when the samples were prepared for ICP-MS analysis. Alternatively, in ICP-MS analysis, only 50 mg of sample is prepared, while 5 g of sample is used for XRF analysis. The Zr-bearing minerals could have been incompletely dissolved and thus not counted using the ICP-MS method. The high XRF value is most probably right because of the high Nb value, which is in perfect agreement between the ICP-MS and XRF results.

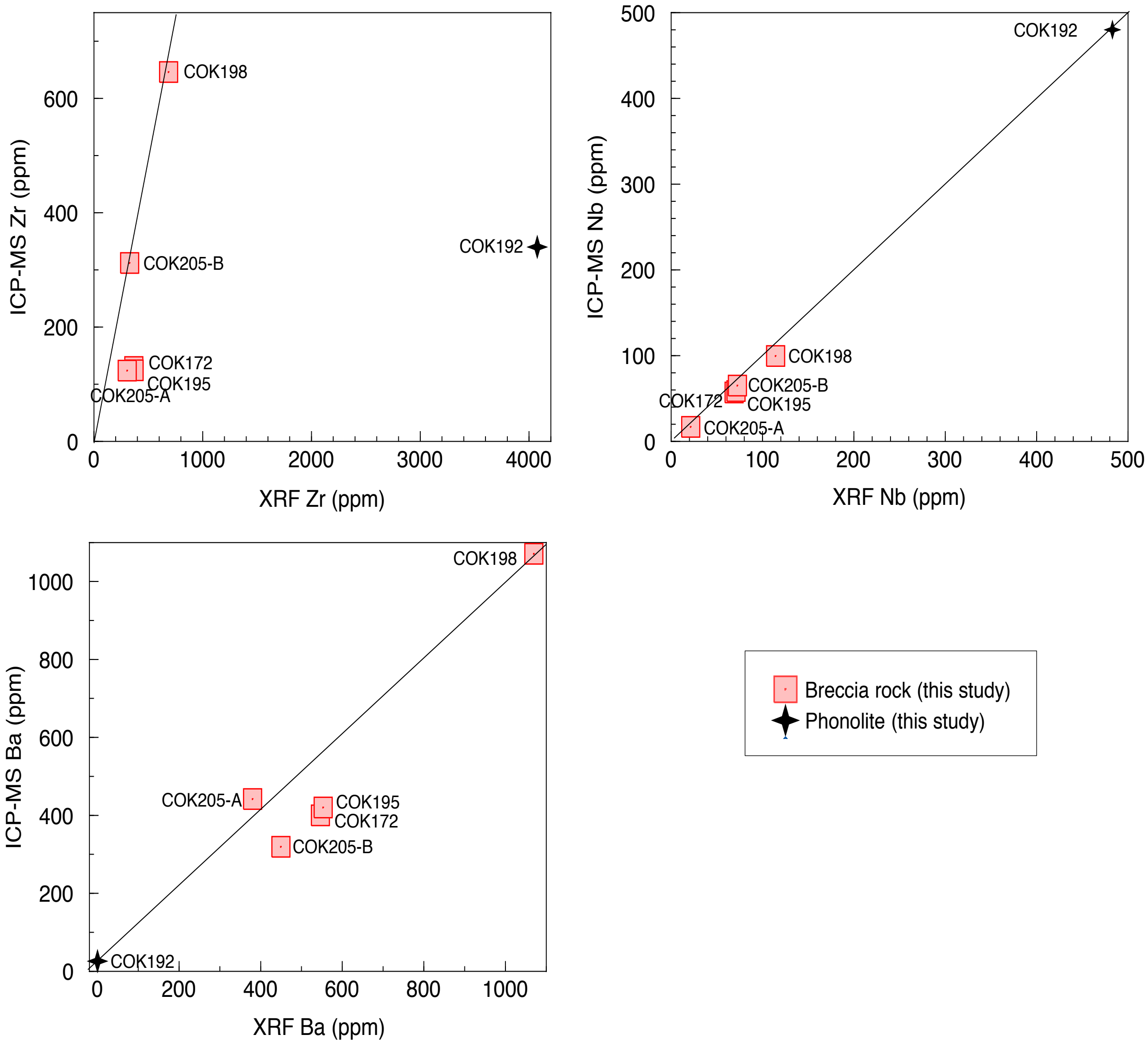

Fig. 4.1 Plots comparing the ICP-MS and XRF data of 5 breccia rocks and 1 phonolite. The black line represents the 1:1 ratio between ICP-MS and XRF data.

4.2 Mineral chemistry

4.2.1 Electron microprobe

The aim of using the probe was to try and confirm the presence of nepheline. This investigation was not a full-on probe study.

Two grains (one mineral phase) from the groundmass of COK191, five grains (one mineral phase) from the groundmass of COK192, and one bottle green xenolith from COK166 were chosen for electron microprobe analysis. Thin sections of the phonolite samples were made and 36 grains were picked out from xenolith COK166 and prepared on an epoxy mount. The thin sections and epoxy mount were polished and carbon coated before analysis to avoid charge build up.

Before inserting the thin sections into the instrument, minerals to analyse were circled with a pen. The minerals from the groundmass of sample COK191 and COK192 were then probed. The mineral in the groundmass of COK192 was probed five times to have a compositional range of this mineral. The measurements of groundmass phases are the compositions of those phases and not the mixture of different crystals.

The samples were analysed with an acceleration voltage of 15 kV, a current of 20 µA, and a beam diameter of 3 µm. Counting times for all elements were five seconds for backgrounds and ten seconds per peak. Minerals in the phonolites were analysed 2-4 times to get an average estimate. Thirty-six grains from the bottle green xenolith were analysed to have a compositional range of the mineral analysed.

Mineral compositions were acquired using JEOL Superprobe JXA-8100 Electron Probe Microanalyser (EPMA), which is equiped with four wavelength dispersive spectrometers and a range of crystals for x-ray detection (LDE1, LDE2, PETJ, PETH, TAP, LIF, and LIFH). Amphibole was used as a standard. Data were corrected and reduced with CITZAF (Armstrong, 1995).

4.3 Stable isotope analysis

Oxygen and hydrogen isotopes of whole-rock samples and selected grains were analysed in the Stable Isotope Laboratory, at UCT. For oxygen isotopes, both conventional and laser fluorination methods were employed. A Finnegan Mat Delta XP mass spectrometer in dual-inlet mode measured the oxygen and hydrogen ratios in the samples. All data were reported in the standard δ-notation relative to Standard Mean Ocean Water (SMOW): $\delta = ((R_{sample}/R_{standard}) - 1) \times 1000$, with R being the measured ratio (i.e. $^{18}O/^{16}O$, $D/^{1}H$).

4.3.1 Oxygen isotopes

In 2014, four xenoliths were picked out of the breccia rocks with the lowest $\delta^{18}O$ values (COK165, COK168, COK170, and COK175). In 2015, three xenoliths were chosen for their type (COK162, COK164, and COK166). The first type of xenoliths was extracted from COK162. This first type was white and <5 mm in diameter. The second type of xenoliths was taken from COK164. This xenolith resembled the pink/brown gneiss. The third type was extracted from COK166. This xenolith was the fine-grained, light green xenolith type.

Conventional methods

Twenty-nine whole-rock samples (18 breccia rocks, 2 phonolite rocks, 6 gneisses, and 3 breccia xenoliths from COK162, COK164, and COK166) were analysed using conventional oxygen isotope methods described by Harris and Erlank (1992). About 10 mg of each sample was reacted with ClF_3 at 550°C for 3h to free oxygen gas from the silicate sample. The liberated O_2 was then converted to CO_2 using a hot platinized carbon rod. The CO_2 was stored in break seal tubes.

Duplicate splits of quartz standard MQ were run with each batch of 8 samples to monitor analytical precision and convert the raw data to the SMOW scale using the $\delta^{18}O$ value of 10.1‰ for MQ. The MQ gave a 2σ error of 0.16‰.

Laser Fluorination methods

Mineral separates extracted from four breccia rocks (COK165, COK168, COK170, and COK175) were analysed for oxygen isotopes using laser fluorination methods described by Harris and Vogeli (2010). The mineral separates (2-3 mg) were cleaned and placed in four holes of a polished nickel sample holder along with chips (2-3 mg) of the internal standard Monastery Garnet (MON GT). To avoid absorption of moisture, the sample holder was dried in a 110°C oven for >2 h before direct insertion into the reaction chamber. The purified O_2, formed from each sample reaction with 10 kPa BrF_5, were collected onto a 5Å molecular sieve embodied in a glass storage bottle.

Oxygen isotope ratios were measured on O_2 gas in the Archaeology Department at UCT. The isotope composition of the O_2 reference gas was determined by converting an aliquot of O_2 to CO_2 using the carbon convertor on the conventional extraction line. This oxygen isotope value was used to calculate raw (δ) values of each sample relative to the SMOW scale. MON GT was calibrated on the UCT laser system against UWG-2 garnet standard ($\delta^{18}O$ = 5.80‰) from Valley et al. (1995). An average $\delta^{18}O$ value of 5.38‰ obtained for MON GT was used to normalise the raw data to the SMOW scale (Harris and Vogeli, 2010). The average difference in $\delta^{18}O$ values of 2 MONT GT standards run with each batch of 10 samples was 0.12‰ (n = 175), corresponding to a 2σ value of 0.15‰.

4.3.2 Hydrogen isotopes

Five whole-rock powder samples (COK165, COK169, COK170, COK174, and COK175) with the lowest $\delta^{18}O$ values (2014 samples) were analysed for hydrogen isotopes. The hydrogen was extracted using the Zn-reduction method described by Vennemann and O'Neil (1993). About 1-2 mg of water and 100 mg or 200 mg of powder were weighed. The LOI values of the five samples were used to determine the amount of sample powder required (100 mg or 200 mg). Three kaolinite standards were prepared. The samples and the standards were inserted into quartz glass tubes and dried overnight at 110°C before they were degassed at

200°C on a vacuum line. Water extracted by pyrolysis at 1200°C was then collected into a liquid N_2 trap.

Water was reduced to hydrogen gas by using low blank "Indiana zinc" (Schimmelmann and DeNiro, 1993). The reduced water was trapped in break seal tubes and then sent for analysis on the Archaeology Department mass spectrometer. Raw sample data were calibrated to the SMOW scale using CTMP internal water standard with a δD value of -7.4‰. The scale compression was corrected with CTMP and the measured value for Rocky Mountain Water (RMW) with a δD value of -134‰. The precision for the hydrogen isotope ratios and water content based on repeated analysis of the kaolinite internal standard of the Stable Isotope Laboratory were respectively 2‰ (1σ) and 0.10 wt % (1σ).

4.4 Radiogenic isotope analysis

Twenty-two samples (15 breccia rocks, 1 phonolite rock, and 6 gneisses) and one certified reference material (BHVO-2) were analysed for Sr and Nd isotopes using the solutions left after final sample dilutions for ICP-MS analysis. Samples were selected to encompass a range in rock composition and $\delta^{18}O$ value.

4.4.1 Strontium and neodymium isotopes

Separation

The Rb/Sr ratios determined by quadrupole ICP-MS of several samples were high. High ratios can reduce the accuracy of the $^{87}Sr/^{86}Sr$ measurements and bias the age correction and errorchron when corrected for isobaric interference of ^{87}Rb and ^{87}Sr after routine strontium separation chemistry. To prevent this, an additional step was added to the routine chemistry for the removal of rubidium and retention of strontium before Sr.Spec and Ln.Spec chemistry, after Miková and Denková (2007).

PFA Teflon columns (6.4 mm ID) with 185 mm resin bed, and 125 ml column reservoir were filled with pre-washed AG50W-X8 100-200mesh cation exchange resin. The columns were calibrated with an incompatible element-rich ocean island basalt. The basalt sample was passed through the columns in 2.5M HCl with eluted acid solutions recovered every 2-3 ml. The elution intervals for strontium and REE were fixed to retain a maximum amount of strontium while excluding rubidium. Fractions of strontium and REE collected were dried and redissolved in 1.5mL of 2M HNO_3. The prepared solutions were then sent for routine processing, following methods described by Miková and Denková (2007).

The separation process used chromatographic material Sr.Spec ion exchange resin for strontium, TRU.Spec resin for Light Rare Earth Elements (LREE), and Ln.Spec resin for neodymium. Sr.Spec and Tru.Spec columns were conditioned with 2 ml of 2 M HNO_3. Sr.Spec columns were then positioned directly above Tru.Spec columns, and were conditioned with 1 ml of 2 M HNO_3 and the dissolved sample loaded. The strontium was retained in the upper Sr.Spec column, while the LREE were retained in the lower column filled with the TRU.spec resin. The resins were then separated and used individually.

The strontium fractions were collected in clean beakers after elution in water, brought to dryness, and redissolved with 2 ml of 0.2% HNO_3. After 20 minutes in an ultrasonic bath, the solutions were ready for Multi-Collector ICP-MS (MC-ICP-MS) analysis.

Tru.Spec and Ln.Spec resins were used to separate neodymium from the LREE. Ln.Spec were conditioned before placement below the Tru.Spec columns. Tru.Spec columns were washed with 3 ml of 0.05 M HNO_3, which eluted the LREE from the TRU.Spec columns onto the Ln.Spec columns. The racks were then separated.

The Ln.Spec columns were washed with 1 ml of HNO_3, 7 ml of 0.2 M HCL, and another 7 ml of 0.2 M HCL. The neodymium fraction was collected with another 7 ml of 0.2 M HCL into clean beakers, brought to dryness, converted to nitrate, and redissolved in 2 ml of 0.2% HNO_3. After 20 minutes in an ultrasonic bath, the solutions were ready for MC-ICP-MS analysis.

Analysis

Strontium and neodymium isotope analyses were performed on a Nu Instruments NuPlasma HR MC-ICP-MS housed in the Department of Geological Sciences, at UCT. Strontium isotopes were analysed as 200 ppb 0.2% HNO_3 solutions and neodymium isotopes were analysed as 50 ppb 2 % HNO_3 solutions. Strontium solutions were introduced into the MC-ICP-MS by a micro-cyclonic spray-chamber and neodymium solutions by a DSN-100 desolvating nebuliser. Standard NIST SRM987 (reference value of 0.710255) was run for $^{87}Sr/^{86}Sr$ analysis. JNdi-1 (reference value of 0.512115) was used for $^{143}Nd/^{144}Nd$ analysis.

All strontium isotope data were corrected for rubidium interferences, using the measured signal for ^{85}Rb and the natural $^{85}Rb/^{87}Rb$ ratio. In addition, the data were corrected for instrumental mass fractionation, using the exponential law and the $^{86}Sr/^{88}Sr$ value of 0.1194.

All neodymium isotope data were corrected for Sm and Ce interferences, using the measured signal for ^{147}Sm and ^{140}Ce natural Sm and Ce isotope abundances. In addition, the data were corrected for instrumental mass fractionation using the exponential law and the ^{146}Nd/^{144}Nd values of 0.7219.

The ^{143}Nd/^{144}Nd analysis of the certified reference material BHVO-2 gave a value of 0.512988 ±10 (2σ, n = 2) within error of the value from Weis et al. (2006) of 0.512984 ±11 and the long-term UCT average value of 0.512987 ±17 (2σ, n = 86). The ^{87}Sr/^{86}Sr measured on BHVO-2 gave an average value of 0.703477 (2σ, n = 2) within error of the value from Weis et al. (2006) of 0.703479 ±20 and the long-term average value at UCT of 0.703480 ±23 (2σ, n = 74).

Equations

The equations to calculate the ^{87}Rb/^{86}Sr ratio from Sr and Rb concentrations (ppm) and the ^{147}Sm/^{144}Nd ratio from Sm and Nd concentrations (ppm) are given below.

$$\frac{^{87}Rb}{^{86}Sr} = \left(\frac{Rb}{Sr}\right)\left[2.6939 + 0.2832\frac{^{87}Sr}{^{86}Sr}\right]$$

$$\frac{^{147}Sm}{^{144}Nd} = \left(\frac{Sm}{Nd}\right)\left[0.53151 + 0.14252\frac{^{143}Nd}{^{144}Nd}\right]$$

The equations for determining the age-corrected values of ^{87}Sr/^{86}Sr and ^{143}Nd/^{144}Nd are as follows (with λ = decay constant, t = age, and x_0 = initial ratio of the isotopic system analysed):

$$\frac{^{87}\mathrm{Sr}}{^{86}\mathrm{Sr}} = \left(\frac{^{87}\mathrm{Sr}}{^{86}\mathrm{Sr}}\right)_0 + \frac{^{87}\mathrm{Rb}}{^{86}\mathrm{Sr}}(e^{\lambda t} - 1) \qquad \frac{^{143}Nd}{^{144}Nd} = \left(\frac{^{143}Nd}{^{144}Nd}\right)_0 + \frac{^{147}Sm}{^{144}Nd}(e^{\lambda t} - 1)$$

The εNd and εSr values were obtained using the following equations:

$$\varepsilon_{\mathrm{Nd}} = 10^4 * \frac{(^{143}\mathrm{Nd}/^{144}\mathrm{Nd})_{\mathrm{sample}}}{(^{143}\mathrm{Nd}/^{144}\mathrm{Nd})_{\mathrm{CHUR}} - ((^{147}\mathrm{Sm}/^{144}\mathrm{Nd})_{\mathrm{CHUR}} * (e^{(EA*6.54*10\text{-}6)} - 1))} \quad -1$$

$$\varepsilon_{\mathrm{Sr}} = 10^4 * \frac{(^{87}\mathrm{Sr}/^{86}\mathrm{Sr})_{\mathrm{sample}}}{((^{87}\mathrm{Sr}/^{86}\mathrm{Sr})_{\mathrm{BE}} - (^{87}\mathrm{Rb}/^{86}\mathrm{Sr})_{\mathrm{BE}} * (e^{(EA*1.42*10\text{-}5)} - 1))} \quad -1$$

(^{143}Nd/^{144}Nd)$_{\mathrm{CHUR}}$: present day ratio of an undifferentiated Chondrite Uniform Reservoir (CHUR) (as measured in chondrites) and assumed to reflect the undifferentiated Bulk Earth.
(^{147}Sm/^{144}Nd)$_{\mathrm{CHUR}}$: present day ^{147}Sm/^{144}Nd ratio of undifferentiated CHUR.

(^{87}Sr/^{86}Sr)$_{\mathrm{BE}}$: present day ^{87}Rb/^{86}Sr ratio of the Bulk Earth.
(^{87}Rb/^{86}Sr)$_{\mathrm{BE}}$: present day ^{87}Rb/^{86}Sr ratio of the Bulk Earth.

EA: estimated age e.g. 135 Ma.
* All values for the present day CHUR and Bulk Earth ratios are taken from White (2007).

CHAPTER 5 RESULTS

This chapter addresses the second and third aims of this study, which are to document the whole-rock and isotope compositions of the breccia rocks and examine the distribution of the $\delta^{18}O$ values of the breccia rocks over the Breccia Outcrop area. These aims are investigated by carrying out geochemical work on the rocks sampled in this study.

Three sets of samples are discussed in this chapter. The first set of samples consists of the COK samples. The two other sets of samples are rocks from the Koegel Fontein complex that were previously analysed (Curtis et al., 2011). The one sample set includes bostonite rocks (n = 4), which are termed CCK and CDB (CDB, originally from the Council for Geoscience). The other sample set consists of alkaline and tholeiitic mafic rocks (n = 21). When the data are available, the bostonite and mafic rock sample sets are included in the figures and used for comparison with the breccia rock sample set.

5.1 Whole-rock geochemistry

5.1.1 Major elements

On average, the breccia rocks have high concentrations in Al_2O_3, Fe_2O_3, CaO, K_2O, and TiO_2 and low concentrations in MnO, Na_2O, and P_2O_5 (Fig. 5.1 and Table 5.1). The oxide concentrations of MgO, Fe_2O_3, TiO_2, CaO, MnO, Al_2O_3, Na_2O, and P_2O_5 in the breccia rocks decrease with increasing SiO_2, excepting K_2O (Pearson product-moment correlation coefficient of the breccia rocks ($r_{breccia}$), $r_{breccia} = 0.30$). The strongest negative correlation in the breccia rocks is between Fe_2O_3 and SiO_2 ($r_{breccia} = -0.85$). Other major elements with strong correlations coefficients are P_2O_5 ($r_{breccia} = -0.81$), TiO_2 ($r_{breccia} = -0.76$), and MnO ($r_{breccia} = -0.72$).

The SiO_2 content of the breccia rocks ranges between 44-68 wt % (average = 53 wt %), extending from the SiO_2 content field of the mafic rocks (45-53 wt %, average = 50 wt %) across to the SiO_2 content field of the bostonites (61-67 wt %, average = 65 wt %) (Fig. 5.1). The average concentration of silica in the breccia rocks is closer to that in the mafic rocks than that in the bostonites. The bostonite and mafic rocks each have quite uniform major element compositions, which differ significantly from each other. The mafic rocks have higher MgO, Fe_2O_3, TiO_2, CaO, MnO, and P_2O_5 than the breccia rocks and lower Na_2O, and K_2O. By contrast, the bostonites have higher Al_2O_3, Na_2O, and K_2O than the breccia rocks and lower MgO, Fe_2O_3, TiO_2, CaO, MnO, and P_2O_5.

The two phonolite rocks have the highest MnO, Al_2O_3, Na_2O, and K_2O and the lowest MgO, Fe_2O_3, TiO_2, CaO, and P_2O_5 of all the samples (Fig. 5.1). Both phonolites (COK191 and COK192) have a silica content of 59 wt %.

The SiO_2 content of the gneisses varies between 56-76 wt % (average = 69 wt %). These gneisses have the highest average SiO_2 content of all the types of COK rocks. Two of these gneisses are compositional outliers (COK169 and COK171). Sample COK169 has a lower concentration in SiO_2 than the five other gneisses and a higher concentration in Al_2O_3 and K_2O. Sample COK171 has a higher concentration in SiO_2 than the five other gneisses and a lower concentration in Al_2O_3, Na_2O, and K_2O.

The two xenoliths analysed differ mostly from each other in SiO_2 and CaO (Table 5.1). Xenolith COK175 has 64 wt % SiO_2 and 1 wt % CaO, whereas xenolith COK208 has 53 wt % SiO_2 and 8 wt % CaO. Xenolith COK175 has a compositionally similar concentration in SiO_2 and CaO to that of the bostonite and gneiss, whereas xenolith COK208 has a similar SiO_2 and CaO concentration to the average breccia rock.

The main difference between xenolith COK175 and xenolith COK208 and the rest of the rocks lies in the average K_2O concentration, which is ~5 wt % higher in xenolith COK175 than in the average gneiss and >7 wt % higher in xenolith COK208 than in the average breccia rock.

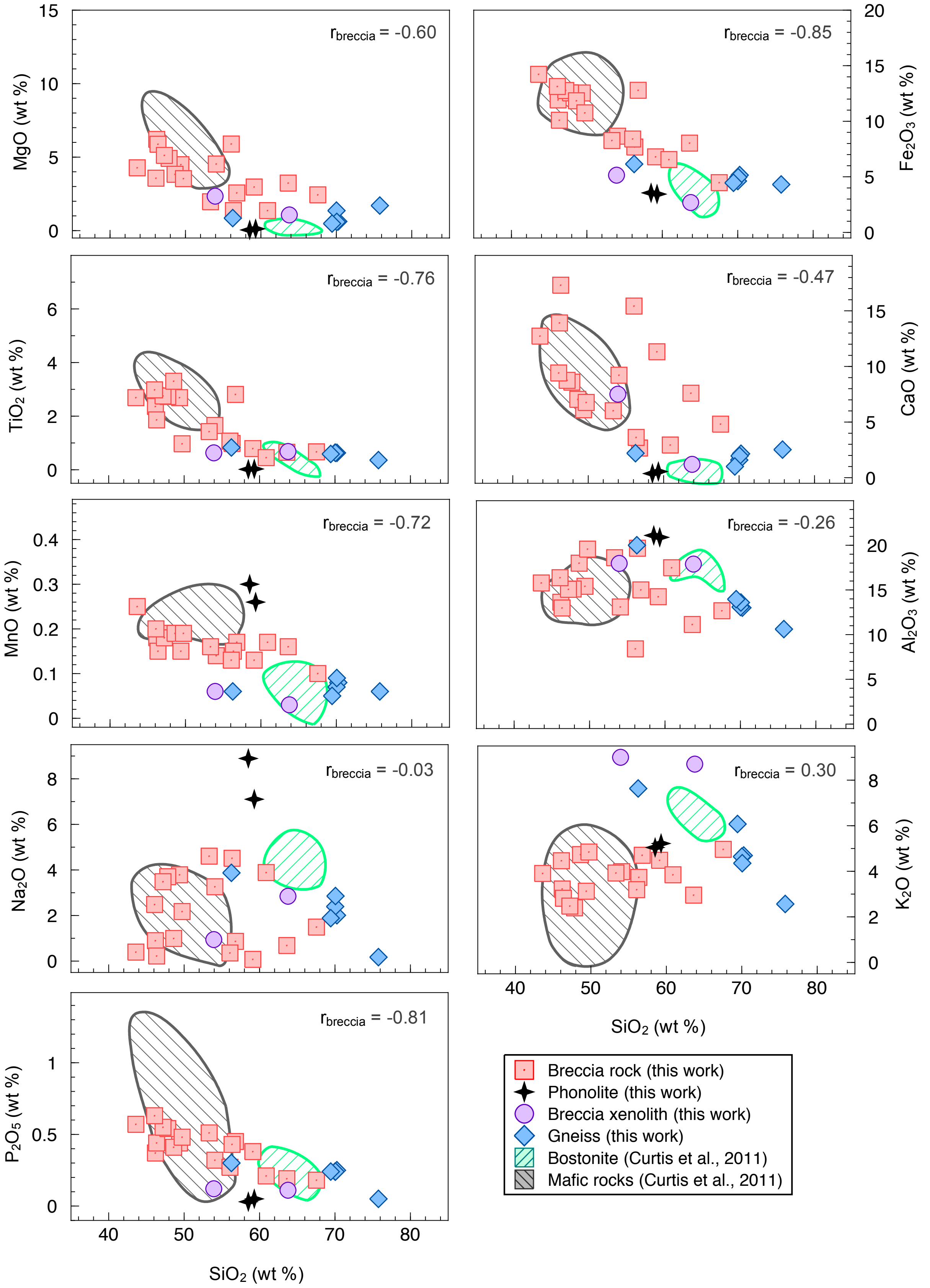

Fig. 5. 1 Major element concentrations plotted against silica content for 18 breccia rocks, 2 phonolite rocks, 2 breccia xenoliths, and 6 gneisses (this work). The bostonite and mafic rock data (Curtis et al., 2011) are used for comparison with the breccia rock data. r$_{breccia}$ is the Pearson product-moment correlation coefficient of the 18 breccia rocks.

Table 5.1 Major element oxides (wt.%) of the breccia rocks, phonolite rocks, breccia xenoliths, and gneisses (this work).

	SiO_2	TiO_2	Al_2O_3	Fe_2O_3	MnO	MgO	CaO	Na_2O	K_2O	P_2O_5	SO_3	Cr_2O_3	NiO	H_2O^-	LOI	Sum
	wt.%	wt.%	wt.%	wt.%	wt.%	wt.%	wt.%	wt.%	wt.%	wt.%	wt.%	wt.%	wt.%	wt.%	wt.%	%
Sample name	Breccia rock															
COK162	59.12	0.79	14.24	6.79	0.13	2.96	11.32	0.07	4.48	0.38	b.d.	b.d.	0.01	0.04	0.42	100.75
COK164	60.89	0.45	17.48	6.55	0.17	1.36	2.93	3.88	3.84	0.21	b.d.	b.d.	0.01	0.02	0.78	98.58
COK165	46.20	2.36	13.61	11.92	0.18	6.20	13.91	0.89	3.22	0.37	b.d.	b.d.	0.04	0.05	1.01	99.98
COK166	46.36	1.86	12.98	10.09	0.15	5.87	17.30	0.22	2.81	0.44	b.d.	b.d.	0.04	0.04	0.75	98.94
COK168	49.39	2.69	15.40	12.54	0.15	4.48	6.10	3.78	3.12	0.44	b.d.	b.d.	0.03	0.04	1.14	99.33
COK170	43.61	2.69	15.78	14.22	0.25	4.27	12.72	0.39	3.90	0.57	b.d.	b.d.	0.04	0.02	0.53	99.09
COK172	47.84	2.73	15.10	12.55	0.19	4.91	8.59	3.70	2.39	0.54	0.00	0.01	0.01	0.07	0.59	99.23
COK174	54.09	1.65	13.09	8.65	0.14	4.53	9.21	3.26	3.98	0.32	b.d.	b.d.	0.02	0.03	0.71	99.69
COK175	67.55	0.67	12.66	4.47	0.10	2.43	4.81	1.49	4.96	0.18	b.d.	b.d.	0.01	0.04	0.56	99.93
COK176	56.81	2.81	15.00	12.78	0.17	2.56	2.66	0.86	4.70	0.45	b.d.	b.d.	0.03	0.05	0.59	99.50
COK178	56.36	0.98	19.66	7.68	0.15	1.36	3.61	4.51	3.73	0.43	0.03	b.d.	0.01	0.04	0.68	99.24
COK195	47.21	2.75	15.06	12.76	0.18	5.11	8.75	3.48	2.47	0.55	0.00	0.01	0.01	0.01	0.69	99.07
COK198	53.33	1.42	18.60	8.26	0.16	1.96	6.01	4.60	3.92	0.51	0.00	0.00	0.01	0.03	0.71	99.54
COK201	46.09	2.98	16.36	13.12	0.20	3.56	9.41	2.48	4.46	0.63	0.00	0.01	0.01	0.02	0.19	99.52
COK202	56.08	1.07	8.40	8.40	0.13	5.89	15.43	0.35	3.19	0.27	0.00	0.01	0.02	0.05	0.28	99.56
COK205-A	63.62	0.65	11.13	8.03	0.16	3.23	7.59	0.68	2.95	0.19	0.00	0.01	0.01	0.09	1.06	99.40
COK205-B	48.63	3.30	17.99	11.84	0.19	3.83	7.04	0.99	4.73	0.41	0.03	0.01	0.03	0.01	0.33	99.37
COK207	49.74	0.97	19.56	10.75	0.19	3.53	6.76	2.17	4.84	0.48	0.00	0.00	0.01	0.12	0.35	99.47
Average	52.94	1.82	15.12	10.08	0.17	3.78	8.56	2.10	3.76	0.41	0.01	0.01	0.02	0.04	0.63	99.45
Sample name	Phonolite rock															
COK191	59.30	0.03	20.89	3.44	0.26	0.12	0.55	7.10	5.22	0.05	0.01	0.00	0.01	0.02	1.08	98.07
COK192	58.52	0.02	21.10	3.56	0.30	0.04	0.37	8.89	5.04	0.03	0.00	0.00	0.01	0.02	0.52	98.41
Average	58.91	0.03	20.99	3.50	0.28	0.08	0.46	7.99	5.13	0.04	0.00	0.00	0.01	0.02	0.80	98.24
Sample name	Breccia xenolith															
COK175-xenolith	63.77	0.68	17.89	2.68	0.03	1.06	1.19	2.84	8.70	0.11	0.00	0.01	0.01	0.01	0.74	99.71
COK208-xenolith	53.94	0.63	17.96	5.14	0.06	2.34	7.50	0.94	9.00	0.12	0.00	0.00	0.02	0.07	1.70	99.41
Average	58.86	0.65	17.92	3.91	0.04	1.70	4.35	1.89	8.85	0.11	0.00	0.00	0.01	0.04	1.22	99.56
Sample name	Gneiss															
COK163	70.26	0.63	13.02	5.15	0.08	0.62	2.15	2.01	4.69	0.25	b.d.	0.07	0.04	0.02	0.93	99.94
COK167	70.02	0.64	13.09	4.62	0.07	1.36	1.58	2.39	4.64	0.24	b.d.	b.d.	0.01	0.04	0.95	99.66
COK169	56.27	0.83	20.00	6.15	0.06	0.85	2.20	3.87	7.63	0.30	b.d.	b.d.	0.01	0.05	1.15	99.37
COK171	75.77	0.36	10.62	4.31	0.06	1.70	2.52	0.17	2.56	0.05	b.d.	b.d.	0.01	0.05	1.79	99.99
COK173	70.06	0.63	13.59	4.96	0.09	0.59	1.96	2.85	4.35	0.24	b.d.	b.d.	0.01	0.09	0.83	100.28
COK177	69.44	0.59	13.96	4.46	0.05	0.48	1.00	1.88	6.07	0.24	b.d.	b.d.	0.01	0.07	0.79	99.05
Average	68.64	0.61	14.05	4.94	0.07	0.93	1.90	2.20	4.99	0.22	-	0.07	0.01	0.05	1.08	99.71

Total alkali-silica diagram

A total alkali-silica (TAS) diagram (Fig. 5.2) has been used to assign volcanic rock names to analysed samples using the fields of Le Maitre (1989). The breccia rocks plot from the tephrite or basanite field (COK170) and the basalt field (COK165, COK166) to the trachyandesite field (COK164, COK178) and the dacite field (COK175, COK205-A). Nine breccia rocks plot in the mafic rock field. The other nine breccia rocks plot in between the bostonite field and the mafic rock field.

Sample COK172 and COK195, which have a basaltic texture in thin section petrography, plot in the mafic rock field (Fig. 5.2). Sample COK178 and COK198, which have a trachytic texture, plot in between the bostonite field and the mafic rock field. Sample COK175, which contains the most gneiss xenoliths, plots next to the average gneiss, in the dacite field. The two sub-samples of COK205 have a 15 wt % silica difference. Sample COK205-B (black groundmass) plots in the mafic rock field between the trachybasalt and basalt fields. Sample COK205-A (green matrix) plots in the dacite field.

Sample COK191 and COK192 have respectively 12 wt % and 14 wt % total alkali and both phonolites have 59 wt % silica. Sample COK191 and COK192 plot respectively in the trachyte field and the phonolite field (Fig. 5.2). The phonolite rocks have an average total alkali content 7 wt % higher than the average breccia rock.

The total alkali content in the gneiss rocks varies between 3-11 wt % (average = 6 wt %). Outlier COK169 has 11 wt % total alkalis, whereas outlier COK171 contains only 3 wt % total alkalis. Five of the gneisses plot in the granite field (Fig. 5.2), including COK171. Sample COK169 is the only of the six gneisses to plot in the tephriphonolite field.

The two xenoliths, which were separated from the matrix and analysed individually, are not as compositionally close to the whole rock data of the breccia rocks as anticipated. Xenolith COK175 and xenolith COK208 have a total alkali content of 12 wt % and 10 wt % respectively. Xenolith COK175 has 6 wt % more total alkalis than the whole rock COK175. Xenolith COK175 plots in the trachydacite field near the bostonite field (Fig. 5.2). In comparison, xenolith COK208 plots in the tephriphonolite field with gneiss COK169.

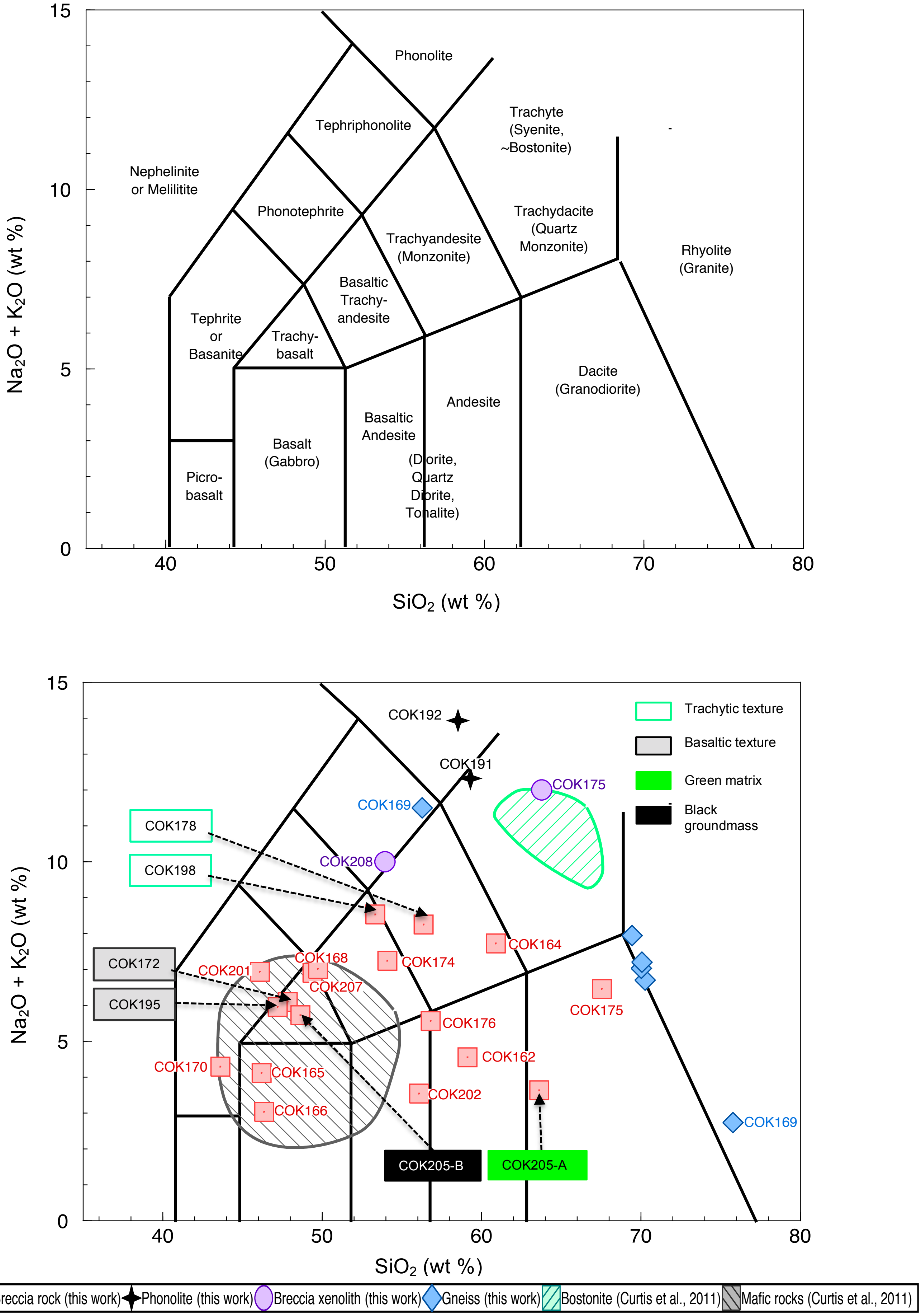

Fig. 5.2 TAS diagram (Le Maitre, 1989). Diagram showing **(a)** the labels for each field and **(b)** the compositions of the COK samples (this study) and fields for the bostonite and mafic rocks (Curtis et al., 2011).

Variation of the silica content of the breccia rocks along the Breccia Outcrop

The West and East Dykes are compositionally different (Fig. 5.3). The eight breccia rocks with the lowest silica content are situated along the West Dyke. These eight breccia samples have a silica content that ranges between 44-56 wt % (average = 48 wt %, n = 8). Seven of these eight breccia rocks plot in the mafic rock field on the TAS diagram (Fig. 5.2).

The ten breccia rocks on the East Dyke have a silica content that ranges between 50-68 wt % (average = 58 wt %, n = 10), which is on average 10 wt % higher than for the average breccia rock on the West Dyke (Fig. 5.3). None of these ten breccia rocks plot in the mafic rock field (Fig. 5.2), excepting COK205-B.

The two rocks with a basaltic texture (COK172 and COK195) have an average silica content of 48 wt % and are situated on the West Dyke, south of the Breccia Plug 2 (Fig. 5.3). Sample COK170, which has the lowest silica content of all the breccia rocks (44 wt %), is situated north of the Breccia Plug 2. Sample COK202, which has the highest silica content (56 wt %) on the West Dyke is the only rock on this dyke to have a silica content >50 wt %.

The two rocks with a trachytic texture (COK178 and COK198) are situated on the East Dyke (Fig. 5.3). Sample COK198 contains 53 wt % silica and is located northwest of the Breccia Plug 1. Sample COK178 has 56 wt % silica and is situated at the Breccia Plug 1. Sample COK175, which comprises the most gneiss xenolith, was also sampled along the East Dyke. This sample has the highest silica content of all the breccia rocks (68 wt %) and is situated south of the Breccia Plug 1.

The phonolite rocks are situated along the East Dyke (Fig. 5.3). The silica content (59 wt %) in these two phonolites is consistent with the higher silica content of the breccia rocks situated on the East Dyke than on the West Dyke.

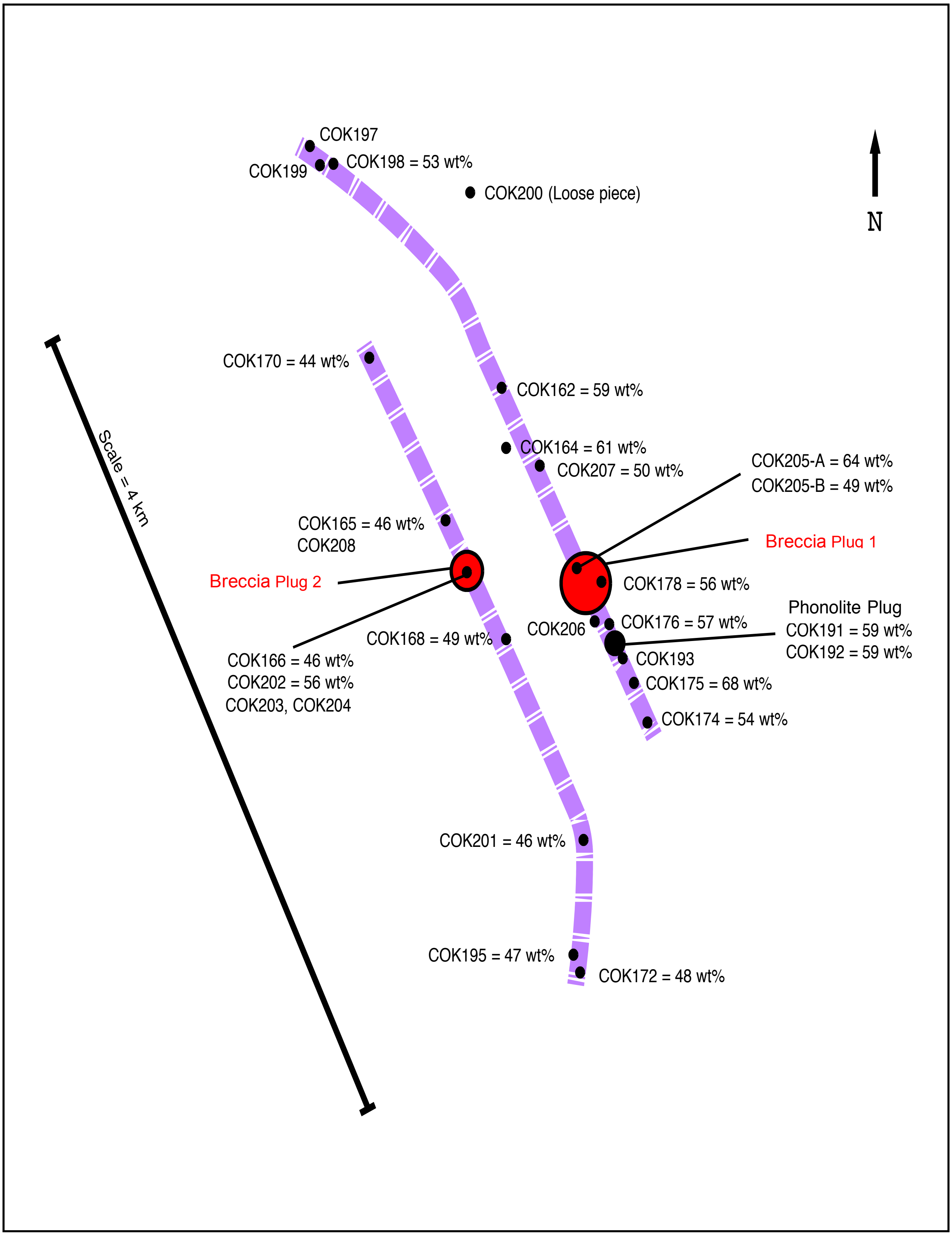

Fig. 5.3 Schematic map showing the distribution of the silica content of the breccia rocks and phonolites along the Breccia Outcrop. The representation is not to scale.

Loss on ignition

The water content and LOI values of the breccia rocks show good agreement and vary by less than 0.6 wt % (Table 5.2). The LOI values of the breccia rocks show no statistically significant correlation with any major or trace element concentrations. The LOI values of these breccias are low, ranging between 0.2-1.1 wt % (average = 0.6 wt %, n = 18) (Fig. 5.4). The LOI values of the gneisses and the breccia xenoliths are also low (<2.0 wt %). Overall, the types of rock analysed in this work all have LOI values below those of bostonites and mafic rocks.

Table 5.2 LOI values (by mass difference after ashing at 1000°C) and water content (H-isotope procedure) of five breccia samples (COK165, COK168, COK170, COK174, and COK175). The samples were selected for their low whole-rock $\delta^{18}O$ values.

Breccia rock	**LOI (wt %)**	**Water (wt %)**	**$\delta^{18}O_{WR}$ (‰)**
COK165	1.0	1.0	-4.9
COK168	1.1	0.7	-5.2
COK170	0.5	1.1	-5.2
COK174	0.7	0.6	-4.0
COK175	0.6	0.5	-4.0

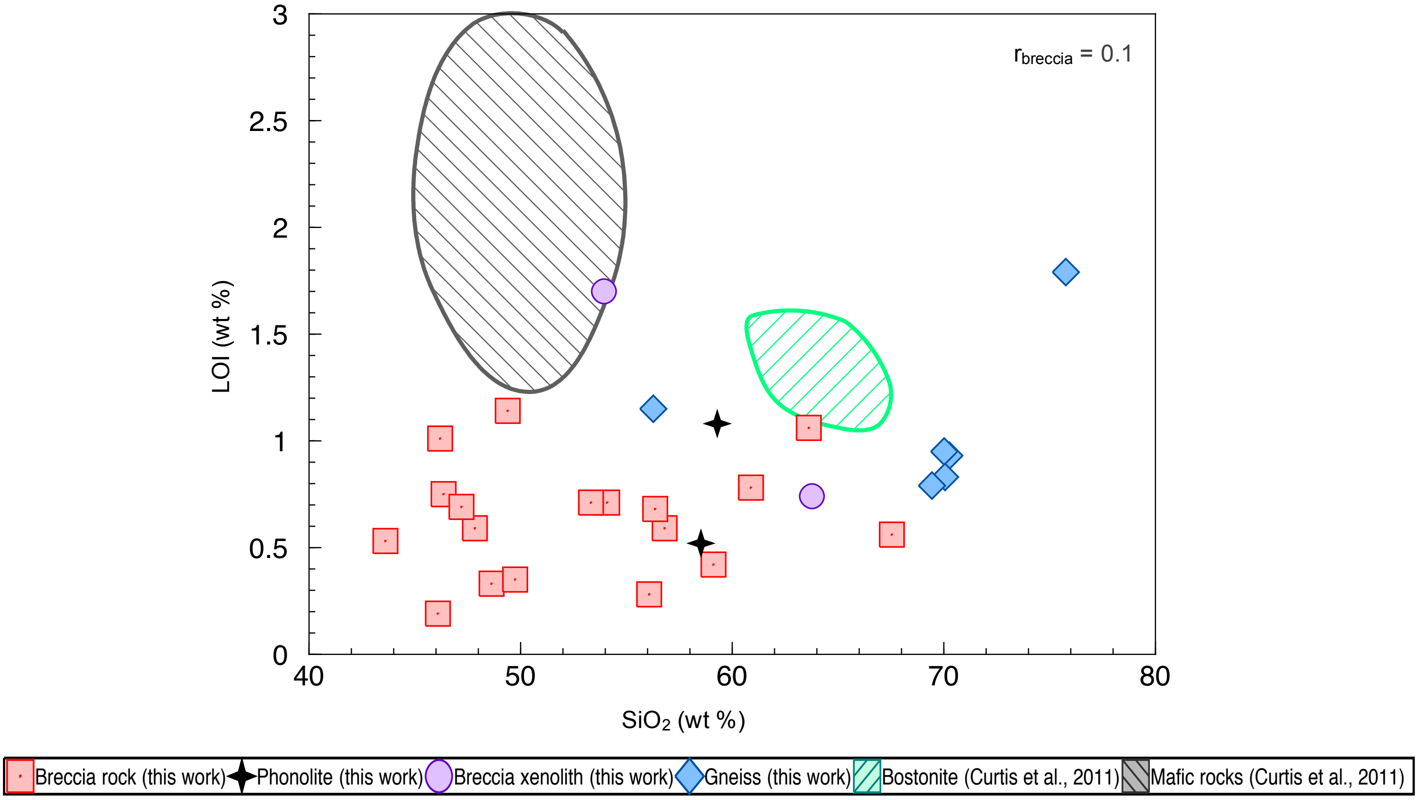

Fig. 5.4 Plot of LOI values versus silica content of the COK samples (this study) and the bostonite and mafic rocks (Curtis et al., 2011). $r_{breccia}$ is the Pearson product-moment correlation coefficient of the 18 breccia rocks.

5.1.2 Trace elements

The trace elements concentrations in the breccia rocks are poorly correlated with their silica content (Fig. 5.5). Nickel, Sr, and Cr, which have the strongest negative correlation coefficients of these trace elements, have a correlation coefficient between 0.00 and -0.50. Niobium, Rb, Sr, Cr, and Ni trace elements are negatively correlated with the increase of silica content in the breccia rocks ($r_{breccia}$ between -0.02 and -0.46); Zr is the only trace element positively correlated ($r_{breccia}$ = 0.18), however, this correlation is weak.

Large ion lithophile elements

Rubidium and Sr concentrations in the breccia rocks range respectively between 57-526 ppm and 163-964 ppm (Table 5.3 and Table 5.4). Sample COK172 and COK195 contain the most Sr and the least Rb of the breccia rocks, with on average 963 ppm Sr and 57 ppm Rb. These two samples plot in the mafic rock field on both plots (Fig. 5.5). Sample COK178 and COK198 have less Sr and more Rb than COK172 and COK195, with on average 427 ppm Sr and 176 ppm Rb. Sample COK178 and COK198 plot in between the bostonite and mafic rock fields.

Barium concentrations in the breccia rocks range between 155-1070 ppm. The Ba concentration in the breccia rocks with a low silica content are on average higher than for the breccia rocks with a high silica content, excepting COK198 and COK175, which have a high silica content and high Ba concentrations (Fig. 5.5). The Ba concentration between COK169 and COK171 (gneiss) and between COK191 and COK192 (phonolites) varies by >800 ppm.

Siderophile elements

Chromium and Ni concentrations in the breccia rocks vary respectively between 13-739 ppm and 31-180 ppm. The highest Cr concentration is found in COK170, which has a concentration significantly higher than the rest of the breccia rocks (739 ppm). The rocks with the least Cr are the gneiss and phonolite rocks (<50 ppm). Nickel is the most abundant in sample COK205-B (180 ppm) (Table 5.3). Nickel and Cr are more abundant in COK205-B (180 ppm Ni and 79 ppm Cr) than in COK205-A (35 ppm Ni and 38 ppm Cr). Similarly, Ni and Cr are more abundant in COK172 and COK195 than in COK178 and COK198, which contain on average ~50 ppm less Cr and Ni.

The Cr data discriminates two groups of rocks, one of which contains COK172 and COK195 and plots in the mafic rock field, and the other includes COK178 and COK198 and plots close to the bostonite field (Fig. 5.5). Two less obvious series can be distinguished on the Ni plot. One series of data of the breccia rocks has a lower concentration in Ni (<50 ppm) than the other. This group contains COK178, COK198, and COK205-A. The other group, which includes the two rocks with a basaltic texture in petrography, shows a higher concentration in Ni (>50 ppm) than the first group of breccia rocks, especially COK205-B (180 ppm).

High field strength elements

Niobium and Zr concentrations in the breccia rocks vary respectively between 21-137 ppm and 187-897 ppm. The concentrations of these two trace elements are higher in COK178 and COK198 than in COK172 and COK195. On both diagrams, COK178 and COK198 plot near the bostonite field, whereas COK172 and COK195 plot in the mafic rock field (Fig. 5.5). Sample COK175 has Nb and Zr concentrations close to those of the gneisses. This sample and these gneisses have the lowest average Nb and Zr concentrations. The rocks with the highest Nb and Zr concentrations are the phonolite rocks, which have on average 498 ppm Nb and 3939 ppm Zr.

An interesting feature of the breccia rocks is the apparent division of the data into two groups on the Nb and Zr diagrams (Fig. 5.5). One group of breccia rocks, which includes COK172 and COK195, has lower concentrations in Nb and Zr than the other group of breccia rocks, which comprises COK178 and COK198. The group with the lowest Zr and Nb concentrations for a given silica content plot in the mafic rock field, whereas the group with the highest Zr and Nb concentrations plot the closest to the bostonite field. Both groups of rocks on both plots have a difference in concentration that decreases with increasing silica.

Incompatible trace elements Y, Nb, and Zr

Further comparison of the breccia rocks and the bostonite and mafic rocks are made on Y/Nb and Zr/Nb plots (Fig. 5.6). The breccia rocks plot near or in the alkaline mafic dyke field (Y/Nb = 0.1) (Curtis et al., 2011) on the Y/Nb plot, excepting COK205-A and COK175, which plot in the tholeiitic mafic dyke field (Y/Nb = 3) (Curtis et al., 2011) (Fig. 5.6.a). On the Nb/Zr plot, the breccia rock data vary between the alkaline (Zr/Nb = 5) and tholeiitic (Zr/Nb = 10) mafic dyke fields (Curtis et al., 2011) (Fig. 5.6.b). Ten breccia rocks, including COK172 and COK195, plot in the alkaline mafic dyke field or in between the tholeiitic and alkaline mafic dyke fields. Sample COK205-A plots in the tholeiitic dyke field. Sample COK178 and COK198 plot near the bostonite trend on which the average bostonite plots.

In summary, there are more breccia rocks that plot in or near the alkaline mafic rock field on the incompatible trace element plots than the tholeiitic mafic rock field. However, overall, the breccia rock data are more spread out on the Y/Nb and Zr/Nb plots than the well distinguished alkaline and tholeiitic mafic rock data.

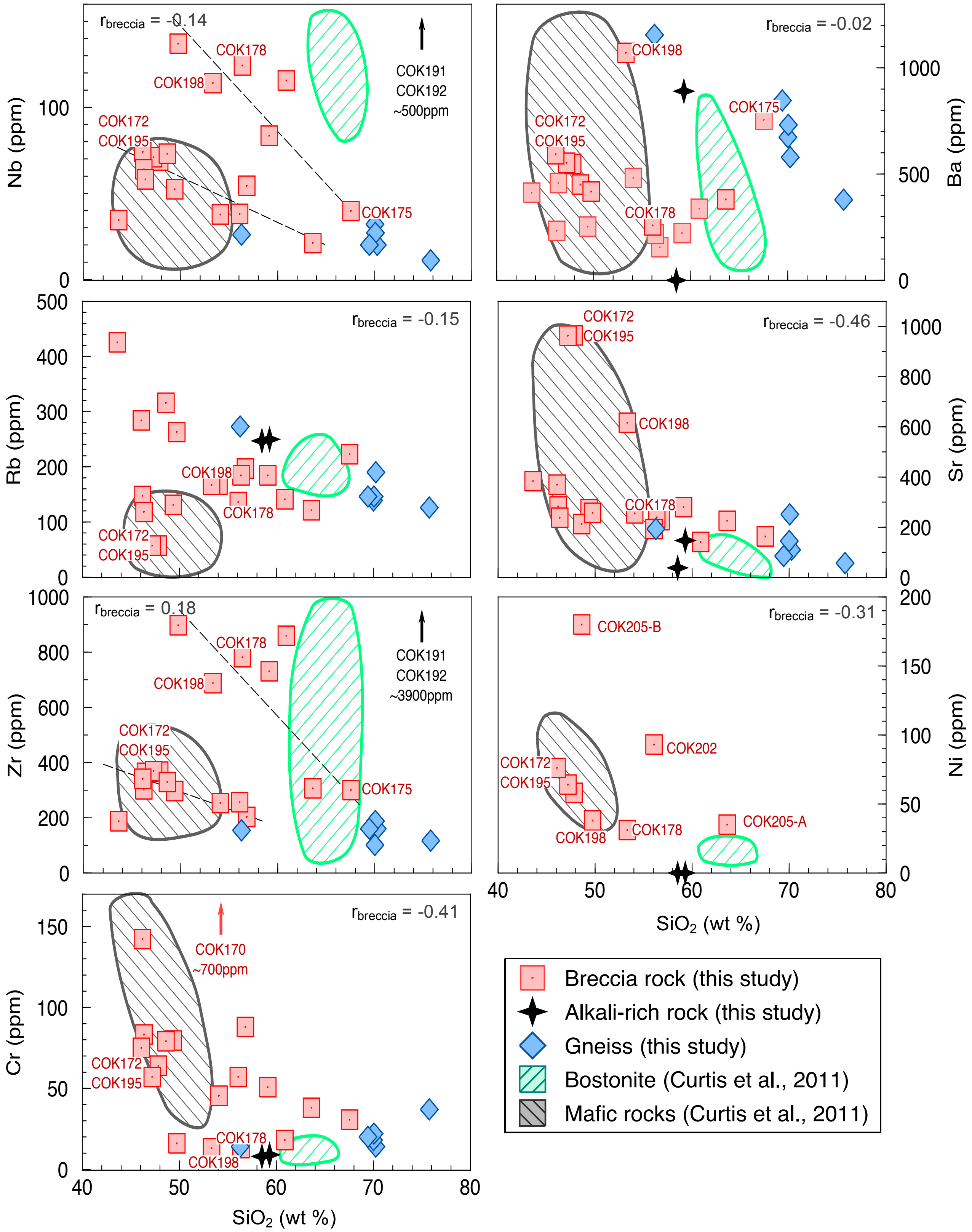

Fig. 5.5 Selected trace element concentrations plotted against silica content for 18 breccia rocks (XRF and ICP-MS data), 2 phonolite rocks (XRF data), and 6 gneisses (ICP-MS data). The XRF data were used instead of the ICP-MS data for the breccia rocks analysed using both analytical methods. Only Ni data from XRF analysis are included (see Chapter 4). The trace element data of the bostonite and mafic rocks from XRF analysis were used for abundances >10 ppm and from ICP-MS analysis for concentrations <10 ppm (Curtis et al., 2011). $r_{breccia}$ is the Pearson product-moment correlation coefficient of the 18 breccia rocks only.

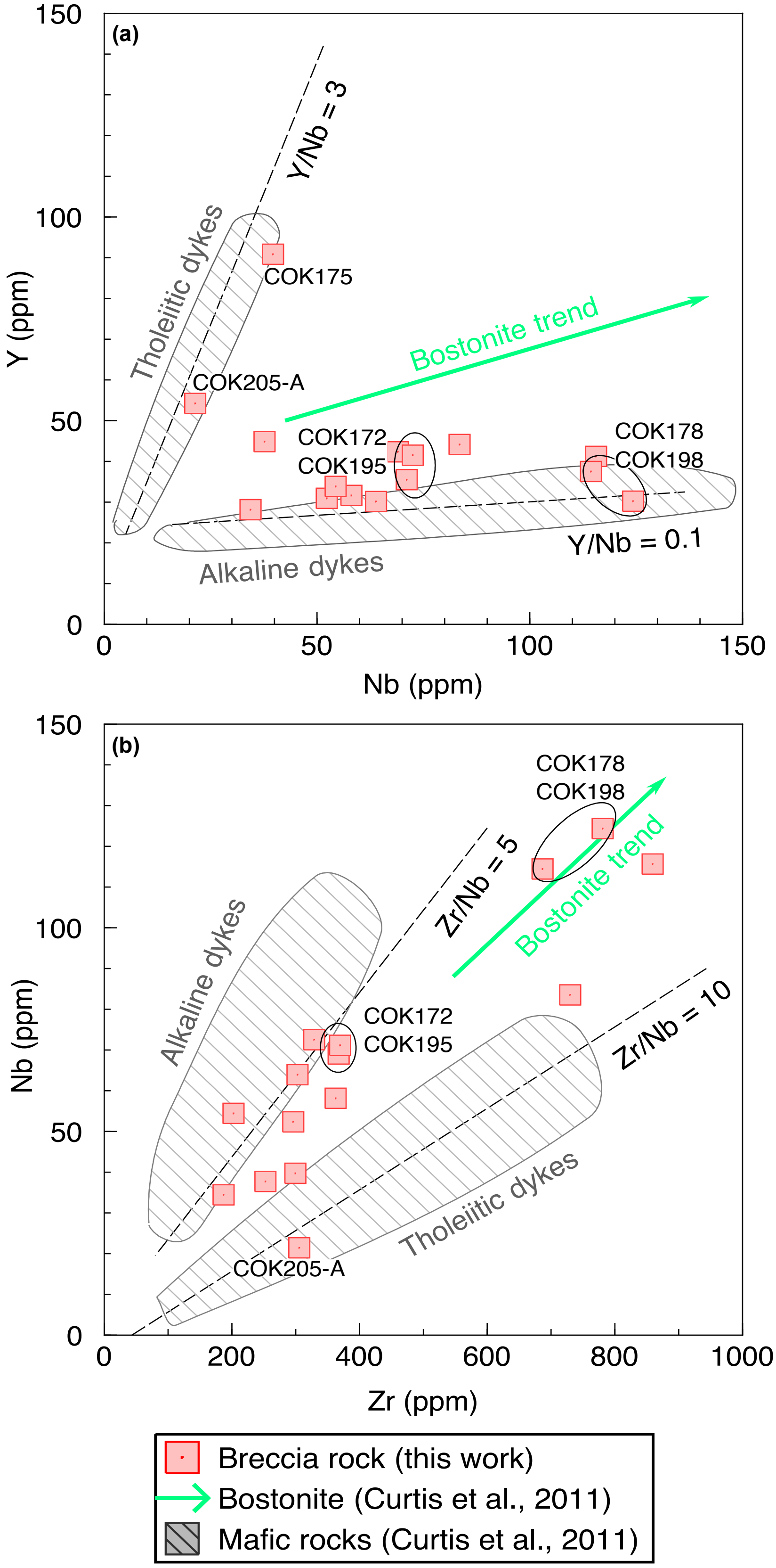

Fig. 5.6 Variation in Y, Nb, and Zr contents for the breccia rocks (this study) and the bostonite and mafic rocks (Curtis et al., 2011). The tholeiitic and alkaline mafic rocks are shown in two separate fields (excluding outliers). The bostonite data are significantly more scattered than the mafic rocks because Y, Zr, and Nb are less incompatible in high silica-granitic magmas; a trend on which the average bostonite plots is thus drawn instead of a field. **(a)** Y/Nb and **(b)** Nb/Zr plots.

Table 5.3 Trace element concentrations (ppm) of COK samples (XRF data).

	Zn	Cu	Ni	Mo	Nb	Zr	Y	Sr	Rb	U	Th	Pb	Co	Mn	Cr	V	F	S	Cl	Sc	Ba
	ppm	ppm	ppm	ppm	ppm	ppm	ppm	ppm	ppm	ppm	ppm	ppm	ppm	ppm	ppm	ppm	ppm	ppm	ppm	ppm	ppm
Sample name	**Breccia rock**																				
COK172	99.8	47.6	58.3	b.d.	69.0	367	42.3	964	56.8	2.62	b.d.	5.29	34.1	1343	64.4	183	1279	317	197	18.1	547
COK195	103	39.0	64.4	b.d.	71.1	369	35.5	963	57.5	2.06	b.d.	3.73	37.6	1315	57.1	189	1336	285	179	18.4	553
COK198	93.6	27.5	31.1	12.2	114	687	37.5	616	167	b.d.	4.81	10.9	12.3	1207	12.7	71.1	1386	303	522	10.5	1070
COK201	113	71.0	76.4	2.43	74.3	341	26.0	369	284	b.d.	b.d.	6.39	42.3	1568	74.7	201	1921	281	452	20.5	593
COK202	76.3	18.4	92.8	b.d.	37.6	256	22.8	192	136	b.d.	3.96	8.33	17.1	977	56.8	85.6	500	267	116	16.1	258
COK205-A	76.3	9.87	34.9	b.d.	21.4	306	54.2	225	121	b.d.	16.8	14.5	12.1	1218	37.7	68.0	1247	276	189	14.2	380
COK205-B	118	56.0	180.2	3.70	72.5	329	41.5	212	316	b.d.	4.09	19.2	59.8	1416	78.5	222	3330	401	380	21.9	450
COK207	97.0	16.2	38.2	12.8	137	897	48.3	257	263	b.d.	10.1	7.47	13.2	1473	16.0	49.8	2170	324	215	10.6	416
Average	97.0	35.7	72.0	7.79	74.7	444	38.5	475	175	2.34	7.96	9.48	28.6	1315	49.7	134	1646	307	281	16.3	533
Sample name	**Phonolite rock**																				
COK191	279	6.17	b.d.	34.1	513	3802	138	147	250	25.7	71.5	56.0	b.d.	1832	9.08	3.40	247	353	138	b.d.	890
COK192	227	2.30	b.d.	38.5	483	4076	107	37.5	247	25.5	57.6	46.3	b.d.	1775	8.09	5.57	414	270	118	b.d.	b.d.
Average	253	4.23	-	36.3	498	3939	122	92.3	249	25.6	64.5	51.2	-	1803	8.59	4.48	330	312	128	-	-
Sample name	**Breccia xenolith**																				
COK175-xenolith	47.4	29.7	7.5	b.d.	42.7	197	29.8	148	356	b.d.	13.4	49.9	b.d.	204	78.2	69.3	861	323	191	6.60	1055
COK208-xenolith	110	11.5	70.9	b.d.	38.2	474	5.16	308	251	b.d.	7.19	18.2	12.3	457	16.4	62.3	747	295	276	9.80	405
Average	78.6	20.6	39.2	-	40.4	336	17.5	228	304	-	10.3	34.0	12.3	331	47.3	65.8	804	309	233	8.20	730

Table 5.4 Trace element concentrations (ppm) of COK samples (ICP-MS data).

	Li	Sc	V	Cr	Co	Cu	Zn	Rb	Sr	Y	Zr	Nb	Ba	La	Ce	Pr	Nd	Sm	Eu	Gd	Dy
	ppm	ppm	ppm	ppm	ppm	ppm	ppm	ppm	ppm	ppm	ppm	ppm	ppm	ppm	ppm	ppm	ppm	ppm	ppm	ppm	ppm
Sample name	**Breccia rock**																				
COK162	19.5	0.74	36.5	50.7	5.24	21.4	168	185	279.8	44.1	730	83.5	221	67.4	131	14.2	51.7	9.65	1.97	8.88	8.35
COK164	20.7	< d.l.	17.7	18.0	4.20	18.4	196	141	140.8	41.2	859	116	336	76.9	161	15.0	51.7	8.84	1.58	8.02	8.02
COK165	35.0	16.7	150	142	29.3	65.4	189	147	282.5	30.1	303	63.9	233	30.7	66.0	8.02	32.7	7.05	2.16	7.38	6.16
COK166	17.4	11.1	118	83.2	30.9	132	168	118	237.5	31.6	363	58.1	457	44.4	88.9	10.2	39.2	7.55	2.11	7.50	6.41
COK168	34.0	13.6	143	79.5	38.7	134	160	131	271.6	30.9	296	52.3	252	42.4	94.7	10.9	43.5	8.48	2.57	8.53	7.03
COK170	13.7	24.7	237	739	66.9	27.4	206	426	383.0	28.1	187	34.4	412	27.0	60.4	7.69	32.5	7.24	2.50	7.20	5.84
COK172	34.5	15.7	128	71.3	29.4	76.6	195	55.3	924.6	29.7	130	57.0	400	41.8	87.8	10.3	42.1	8.70	2.44	7.86	6.42
COK174	28.5	10.4	86.4	45.4	20.1	91.1	130	168	254.6	44.8	253	37.7	481	61.9	135	16.0	61.4	12.2	2.15	10.8	9.17
COK175	25.1	7.98	41.4	30.6	4.7	26.5	157	223	163.4	90.8	300	39.7	754	76.5	164	19.1	71.9	14.4	1.92	15.2	16.5
COK176	16.2	14.1	119	87.9	48.1	128	291	197	227.9	33.8	203	54.4	155	42.3	90.8	10.6	42.1	8.93	2.47	9.05	7.58
COK178	17.3	< d.l.	21.6	13.1	5.8	26.2	109	185	239.0	30.2	781	124	218	84.2	161	15.3	50.9	8.46	1.77	7.00	6.26
COK195	39.8	16.7	136	70.7	32.9	59.9	175	56.7	933.4	30.3	124	58.6	420	41.1	87.3	10.2	41.8	8.58	2.52	7.86	6.59
COK198	31.2	1.89	44.2	17.6	12.5	45.7	237	164	599.6	32.6	646	99.5	1071	74.8	145	14.5	52.6	9.30	2.34	7.65	6.75
COK205-A	9.49	9.65	55.0	39.7	10.5	24.8	244	121	225.0	44.7	124	16.7	442	52.3	111	13.2	52.5	10.8	1.69	8.79	8.29
COK205-B	13.3	20.0	167	93.6	55.7	84.7	153	336	207.1	43.3	312	64.9	319	58.9	116	14.9	60.4	12.7	2.37	11.2	9.49
Average	23.8	12.8	99.9	124	25.7	67.9	179	179	309.5	39.6	400	65.5	356	54.1	113	12.5	47.2	9.22	2.15	8.86	7.98
Sample name	**Phonolite rock**																				
COK192	40.9	< d.l.	1.00	4.34	0.11	8.77	514	217	34.2	96.3	341	480	25.9	216	394	35.2	110	20.3	1.61	17.3	20.2
Sample name	**Gneiss**																				
COK163	18.0	14.8	22.7	13.6	4.01	19.8	297	190	110	83.2	160	20.2	579	91.8	223	26.4	103	20.7	2.24	19.9	19.2
COK167	35.0	8.33	32.7	18.4	4.98	49.0	137	139	145	65.1	101	31.7	673	73.1	170	19.3	75.3	14.9	2.09	14.2	13.1
COK169	21.4	10.0	35.7	14.5	5.72	7.62	135	273	193	52.7	154	25.5	1155	110	295	32.0	123	24.4	2.93	18.1	13.5
COK171	53.6	9.13	32.0	37.3	3.69	9.76	104	126	57.1	68.5	117	10.5	379	55.0	122	15.3	64.0	14.1	1.35	12.0	12.5
COK173	26.4	7.57	31.1	22.2	4.71	16.5	180	146	251	49.9	188	27.1	731	82.7	195	22.5	86.6	16.9	2.01	14.2	11.1
COK177	10.0	3.49	27.9	19.5	3.81	12.4	251	146	85.0	30.9	160	20.4	846	51.5	132	16.3	63.0	10.5	1.12	8.47	8.57
Average	27.4	8.88	30.3	20.9	4.48	19.2	184	170	140	58.4	146	22.6	727	77.4	190	22.0	85.8	16.9	1.95	14.5	13.0

Continued…

Table 5.4 Trace element concentrations (ppm) of COK samples (ICP-MS data).

	Ho	Er	Tm	Yb	Lu	Hf	Ta	Pb	Th	U
	ppm	ppm	ppm	ppm	ppm	ppm	ppm	ppm	ppm	ppm
Sample name					Breccia rock					
COK162	1.65	4.79	0.69	4.75	0.73	14.9	6.15	18.6	14.9	6.47
COK164	1.58	4.83	0.73	5.10	0.80	17.9	9.03	20.6	17.9	5.78
COK165	1.14	3.09	0.41	2.59	0.40	5.73	2.54	11.9	3.47	1.43
COK166	1.24	3.43	0.47	3.07	0.47	7.45	3.59	7.69	7.65	3.93
COK168	1.30	3.60	0.49	3.05	0.46	6.41	2.85	10.1	5.98	1.43
COK170	1.06	2.81	0.37	2.14	0.32	4.20	2.20	66.8	2.00	0.79
COK172	1.23	3.16	0.44	2.69	0.42	3.28	3.45	5.63	4.47	1.10
COK174	1.72	4.95	0.66	3.94	0.56	5.68	1.96	17.4	18.6	1.68
COK175	3.34	10.5	1.52	9.79	1.46	7.89	1.88	45.6	33.1	3.41
COK176	1.37	3.66	0.48	2.99	0.44	4.66	3.03	18.8	6.06	2.46
COK178	1.16	3.60	0.51	3.66	0.57	15.1	7.56	7.04	12.6	2.60
COK195	1.25	3.21	0.45	2.63	0.43	3.04	3.55	5.14	3.92	1.03
COK198	1.32	3.54	0.53	3.45	0.55	11.4	5.83	11.9	9.18	2.54
COK205-A	1.73	4.90	0.73	4.39	0.72	3.21	0.97	16.4	16.9	0.76
COK205-B	1.82	4.64	0.63	3.74	0.59	6.11	3.77	23.7	9.06	1.47
Average	1.53	4.40	0.62	3.98	0.60	8.47	4.02	20.9	11.5	2.83
Sample name					Phonolite rock					
COK192	4.05	11.0	1.60	9.07	1.25	6.27	44.6	51.9	57.9	23.4
Sample name					Gneiss					
COK163	3.66	10.1	1.27	7.12	0.95	4.46	1.27	43.6	31.3	2.51
COK167	2.55	7.61	1.09	7.13	1.04	2.86	0.93	36.6	20.8	1.16
COK169	2.38	6.33	0.82	4.92	0.77	4.76	1.07	47.8	38.8	3.52
COK171	2.49	7.30	1.00	6.42	0.92	3.75	0.57	21.7	12.7	1.26
COK173	2.02	5.76	0.75	4.34	0.60	4.82	0.90	36.2	30.7	2.24
COK177	1.62	4.39	0.55	3.30	0.46	4.63	0.86	13.9	15.6	1.44
Average	2.45	6.91	0.91	5.54	0.79	4.21	0.93	33.3	25.0	2.02

Rare earth elements

The rare earth element (REE) normalised abundances (Table 5.5) and the patterns of fifteen breccia rocks and one phonolite rock are shown on a chondrite-normalised diagram (Sun and McDonough, 1989) (Fig. 5.7). The breccia rocks have three different types of REE patterns. The first group of breccia rocks is reflected by the REE pattern (REE pattern 1) of seven breccia rocks (COK162, COK164, COK174, COK178 and COK198 (trachytic texture), COK205-A, and COK205-B). These seven breccia rocks are enriched in light REE (LREE) (up to 355 ppm La in COK178), depleted in heavy REE (HREE), and show a negative Eu anomaly.

A second group of breccia rocks (COK165 and COK166 (basalt field on TAS diagram), COK168, COK170, COK172 and COK195 (basaltic texture), and COK176) shows a second type of REE pattern (REE pattern 2) (Fig. 5.7). This second REE pattern is similar to the REE pattern 1, excepting the absence of a Eu anomaly. The REE pattern 2 is enriched in LREE, with up to 187 ppm in COK166, and depleted in HREE, with Lu abundances as low as 13 ppm in COK170.

One rock (COK175) reflects a third type of REE pattern (REE pattern 3) (Fig. 5.7). This sample has a similar REE pattern to the REE pattern 1, however, COK175 is enriched in HREE compared to the rest of the breccia rocks. This sample has 58 ppm Lu, whereas the breccia rocks with the REE pattern 1 and REE pattern 2 have on average 26 ppm Lu and 10 ppm Lu, respectively.

The phonolite shows a fourth type of REE pattern (Fig. 5.7). This rock has a REE pattern with a negative Eu anomaly like the REE pattern 1, however, the Eu anomaly of this phonolite is more pronounced than that shown by the REE pattern 1. The main difference between the REE pattern of the phonolite and the REE patterns of the breccia rocks is the LREE enrichment shown by the REE pattern of the phonolite. Sample COK192 contains significantly more LREE (912 ppm La) than the breccia rocks (355 ppm La).

The three REE patterns of the breccia rocks were compared to those of the bostonites and alkaline, tholeiitic, and regional mafic dykes from Curtis et al. (2011) (Fig. 5.8). There is an obvious correlation between the REE pattern 1 and REE pattern 3 of the breccia rocks with the REE pattern of the bostonites (Fig. 5.8.a). These three REE patterns show a Eu anomaly. The REE pattern 1 and 3 of the breccias are, however, uniformly below the REE pattern of the bostonites.

The REE pattern 2 of the breccia rocks and the REE patterns of the three types of mafic rocks (Curtis et al., 2011) show patterns without a Eu anomaly (Fig. 5.8.b). The REE pattern 2 resembles the most the REE pattern of the alkaline mafic rocks. Both REE patterns are the steepest of these four patterns without a Eu anomaly. Similarly to the REE pattern 1 and that of the bostonites, the REE pattern 2 is uniformly below the REE pattern of the alkaline mafic rocks.

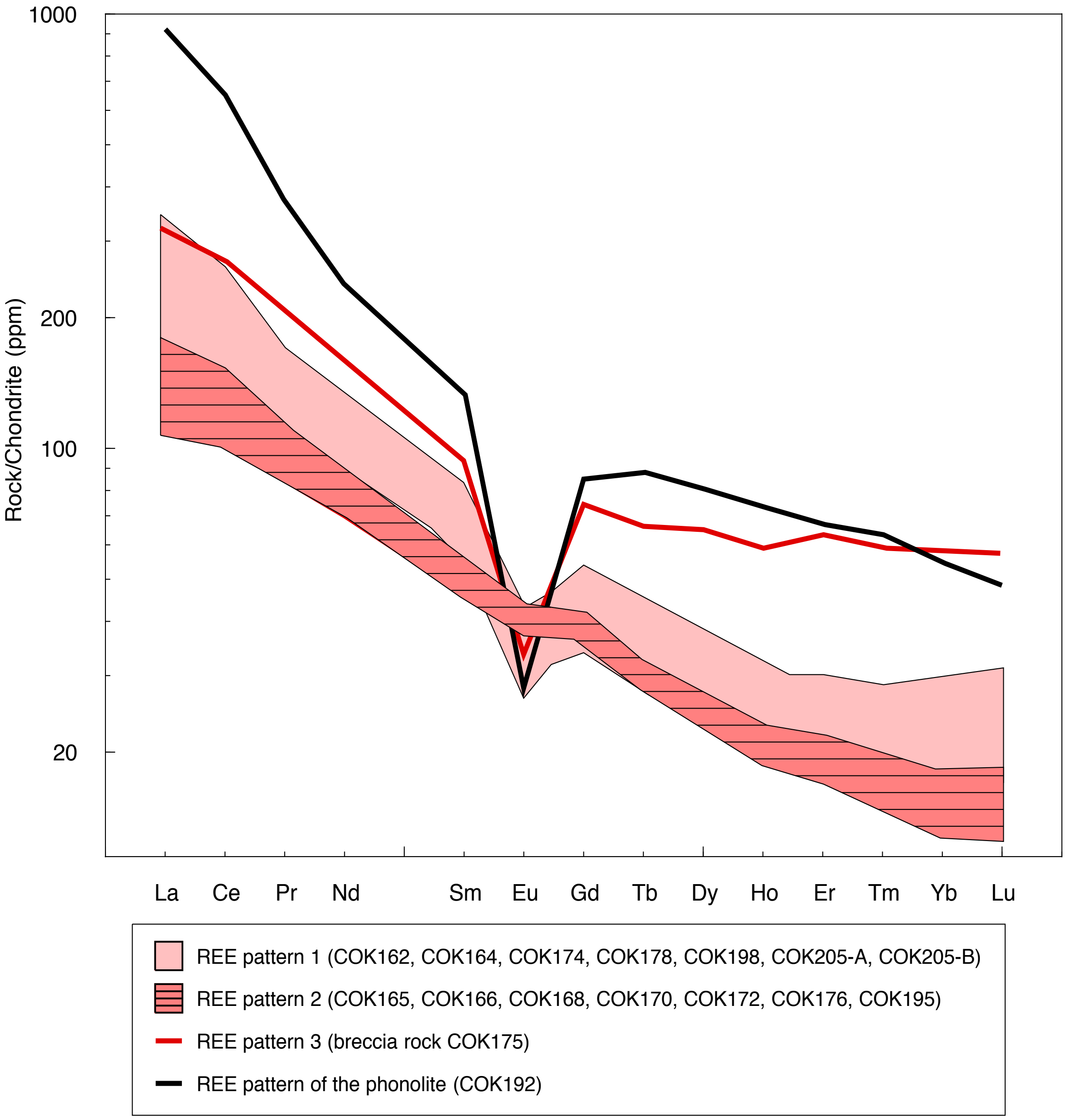

Fig. 5.7 Chondrite-normalised REE plot (Sun and McDonough, 1989) showing the three REE patterns of the breccia rocks and the REE pattern of phonolite COK192. The REE pattern 1 represents the pattern of a first group of breccia rocks, which includes COK162, COK164, COK174, COK178, COK198, COK205-A, and COK205-B. The REE pattern 2 reflects the pattern of a second group of breccia rocks, which consists of COK165, COK166, COK168, COK170, COK172, COK176, and COK195. The third REE pattern is shown by sample COK175, which has the most gneiss xenoliths. The last REE pattern is shown by the phonolite COK192.

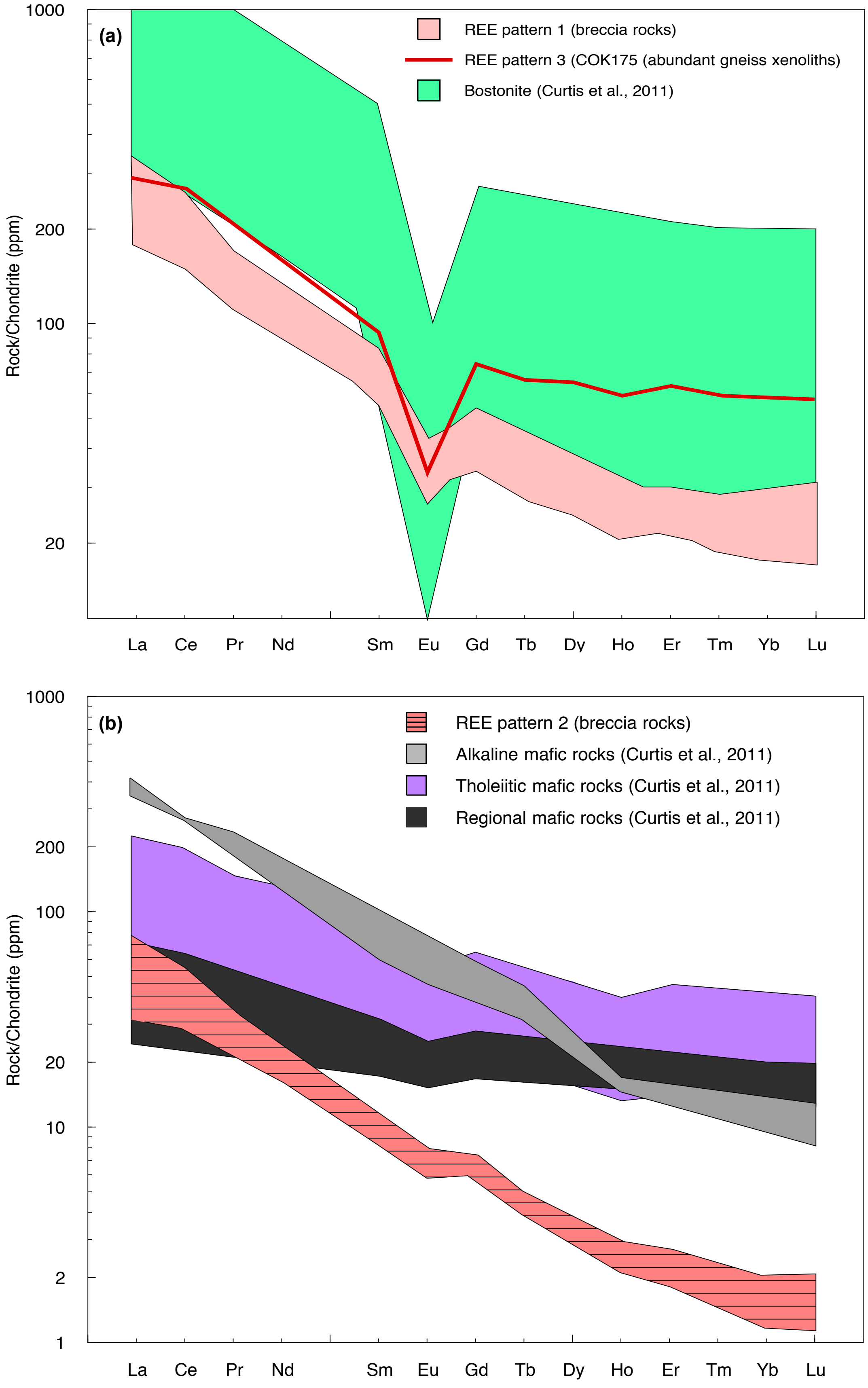

Fig. 5.8 Chondrite-normalised REE plots (Sun and McDonough, 1989). **(a)** The REE pattern 1 and REE pattern 3 (this study) compared to the REE pattern of the bostonites (Curtis et al., 2011). **(b)** The REE pattern 2 (this study) compared to the REE patterns of the alkaline, tholeiitic, and regional mafic rocks (Curtis et al., 2011).

5.2 Mineral chemistry of the phonolites and xenolith COK166

A microprobe study was made to determine if any of the fine-grained low-relief colourless minerals in the groundmass of COK191 and COK192 were nepheline. Nepheline would be expected in rocks of their composition.

The two grains from COK191 (Table 5.5.a) have a mineral composition consistent with the chemistry of anorthoclase (Deer et al., 1992) (Table 5.5.c). The five grains analysed from COK192 (Table 5.5.a) have a chemical composition consistent with nepheline (Deer et al., 1992) (Table 5.5c.c).

The microprobe data for 36 bottle green minerals picked out of xenolith COK166 show negligible variations. The average molecular oxides (wt %) and cation proportions (p.f.u) for the 36 grains from xenolith COK166 was calculated and is presented in the following table. These data are consistent (Table 5.5.b) with those of epidote (Deer et al., 1992) (Table 5.5.c).

Table 5.5 Microprobe data comparing oxide concentrations (wt %) and cation proportions (p.f.u) of grains of anorthoclase in groundmass COK191, grains of nepheline in groundmass COK192, and grains of epidote in xenolith COK166 with mineral data from Deer et al. (1992). **(a)** Data of grain 1 and 2 of possible anorthoclase in groundmass COK191 and average data of five grains of nepheline in groundmass COK192. **(b)** Average microprobe data of 36 grains of epidote from xenolith COK166. **(c)** Microprobe data of anorthoclase, nepheline, and epidote (Deer et al, 1992). FeO* is the total iron oxide concentration in the sample (Fe_2O_3+FeO).

Sample material	**(a)** Thin section			**(b)** Grain mount
Rock type	Phonolite			Breccia rock
Sample name	COK191	COK191	COK192	Xenolith COK166
Grain n°	1	2	3	-
Comment	Possible anorthoclase	Possible anorthoclase	Average for 5 grains Possible nepheline	Average for 36 green grains Possible epidote
Oxide (wt %)				
SiO_2	66.69	66.47	44.70	38.86
TiO_2	0.00	0.00	0.00	0.13
Al_2O_3	20.98	21.12	34.74	22.85
Cr_2O_3	0.00	0.00	0.03	0.04
FeO*	0.09	0.00	0.19	11.30
MnO	0.06	0.01	0.07	0.10
MgO	0.00	0.02	0.17	0.50
CaO	0.41	0.26	0.08	22.23
Na_2O	6.94	7.32	15.61	0.05
K_2O	5.63	5.71	6.01	0.01
Total	100.80	100.91	101.60	96.07
Cation (p.f.u)	Based on 32 O	Based on 32 O	Based on 32 O	Based on 12.5 O
Si	11.765	11.765	8.394	3.185
Ti	0.000	0.000	0.000	0.008
Al	4.363	4.363	7.691	2.208
Cr	0.000	0.000	0.000	0.003
Fe^{2+}	0.012	0.012	0.027	0.774
Mn	0.009	0.009	0.011	0.007
Mg	0.000	0.000	0.048	0.061
Ca	0.078	0.078	0.016	1.952
Na	2.374	2.374	5.683	0.008
K	1.267	1.267	1.440	0.001
	(c) Data from Deer et al. (1992)			
Mineral	Anorthoclase	Anorthoclase	Nepheline	Epidote
Locality	Grande Caldeira, Azores	Grande Caldeira, Azores	New Zealand	Sittampundi, Madras, India
Reference	Tuttle (1952)	Tuttle (1952)	Tilley (1954)	Subramaniam (1956)
Oxide (wt %)				
SiO_2	66.97	66.97	44.65	38.64
TiO_2	0.04	0.04	0.00	0.14
Al_2O_3	18.75	18.75	32.03	27.69
Cr_2O_3	0.00	0.00	0.00	0.00
Fe_2O_3	0.88	0.88	0.59	7.57
FeO			0.00	0.14
MnO	0.00	0.00	0.00	0.04
MgO	0.00	0.00	0.00	0.11
CaO	0.36	0.36	0.71	23.79
Na_2O	7.88	7.88	17.25	0.00
K_2O	5.39	5.39	3.66	0.00
$H2O^+$	0.01	0.01	0.96	1.84
$H2O^-$	0.03	0.03	0.21	0.00
Total	100.31	100.31	100.06	100.01
Cation (p.f.u)	Based on 32 O	Based on 32 O	Based on 32 O	Based on 12.5 O
Si	11.923	11.932	8.585	3.007
Ti	0.005	0.005	0.000	0.008
Al	3.938	3.938	7.361	2.540
Cr	0.000	0.000	0.000	0.000
Fe^{3+}	0.118	0.118	0.085	0.443
Fe^{2+}	0.000	0.000	0.000	0.009
Mn	0.000	0.000	0.000	0.003
Mg	0.000	0.000	0.000	0.013
Ca	0.069	0.069	0.147	1.984
Na	2.722	2.722	6.428	0.000
K	1.226	1.226	0.897	0.000

5.3 Stable isotopes

5.3.1 Oxygen isotopes

The breccia rocks

The whole-rock $\delta^{18}O$ values in the breccia rocks (Table 5.6) range from -5.2‰ to +1.8‰ (average = -2.6‰, n = 18). The lowest whole-rock $\delta^{18}O$ value of the breccia rocks (-5.2‰) is the lowest whole-rock $\delta^{18}O$ value of all the Koegel Fontein rocks. The $\delta^{18}O$ values of the breccia rocks have a moderate positive correlation with SiO_2 content ($r_{breccia}$ = 0.43) (Fig. 5.9.a). Although the average whole-rock $\delta^{18}O$ value of the breccia rocks with a SiO_2 content <50 wt % is about +2‰ lower than the average $\delta^{18}O$ value for the rocks with a SiO_2 content >50 wt %, the oxygen data of the breccia rocks are spread out and thus no correlation is drawn.

The average whole-rock $\delta^{18}O$ value of the gneisses (-0.6‰, n = 6) is lower than that of the mantle (+5.7‰). The bostonite and mafic rocks also have an average whole-rock $\delta^{18}O$ value <+5.7‰. The only rock type with an average whole-rock $\delta^{18}O$ value greater than +5.7‰ is the phonolite, which has a value of +8.0‰.

There is no correlation between whole-rock $\delta^{18}O$ values and LOI values in the breccia rocks, which have a weak positive correlation of 0.30 (Fig. 5.9.b). This absence of correlation is supported by results of xenolith and mineral separate analyses, which have comparable xenolith $\delta^{18}O$ values (+1.6‰ to -5.6‰, n = 7) to those of the whole rock.

The breccia xenoliths

The $\delta^{18}O$ values of three xenoliths extracted from three breccia rocks and the mineral separates from four breccia rocks are plotted against the whole-rock values of the samples they were taken from (Fig. 5.10). The white xenolith from COK162 has the same $\delta^{18}O$ value as the whole rock. The light to bottle green xenolith from COK166 and the gneiss xenolith from COK164 have $\delta^{18}O$ values higher than those of the whole rock they were extracted from.

The mineral separates from COK164, COK168, and COK170 have higher $\delta^{18}O$ values than the whole rock, whereas the mineral separates from COK165 and COK175 have lower $\delta^{18}O$ values than the whole rock (Fig 5.10). The mineral separates from COK165 give the lowest $\delta^{18}O$ value of all the analysed rocks, mineral separates, and xenoliths from the Koegel Fontein complex.

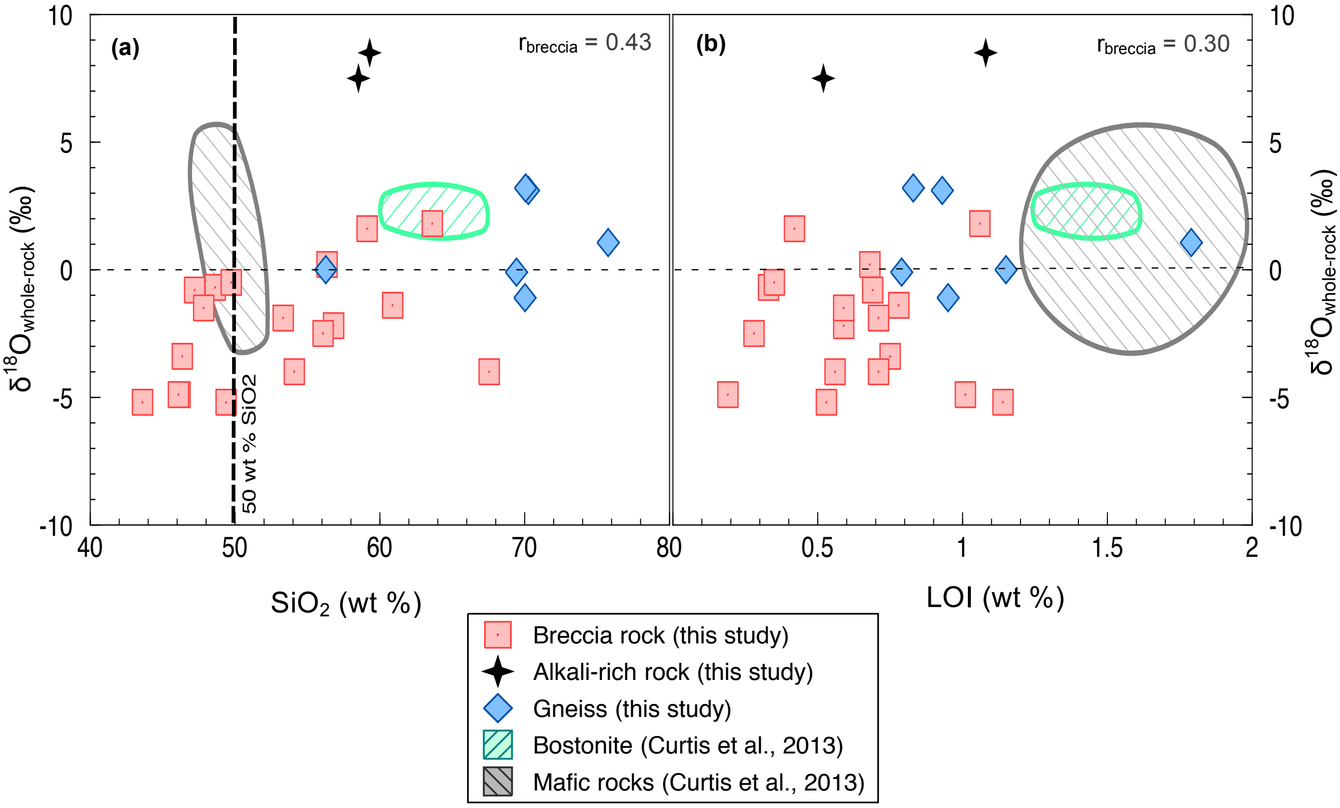

Fig. 5.9 Variation of whole-rock $\delta^{18}O$ with silica content and LOI values for the COK samples (this study) and the bostonite and mafic rocks (Curtis et al., 2013). Whole-rock $\delta^{18}O$ values vs. **(a)** SiO$_2$ content and **(b)** LOI values. $r_{breccia}$ is the Pearson product-moment correlation coefficient of the 18 breccia rocks only.

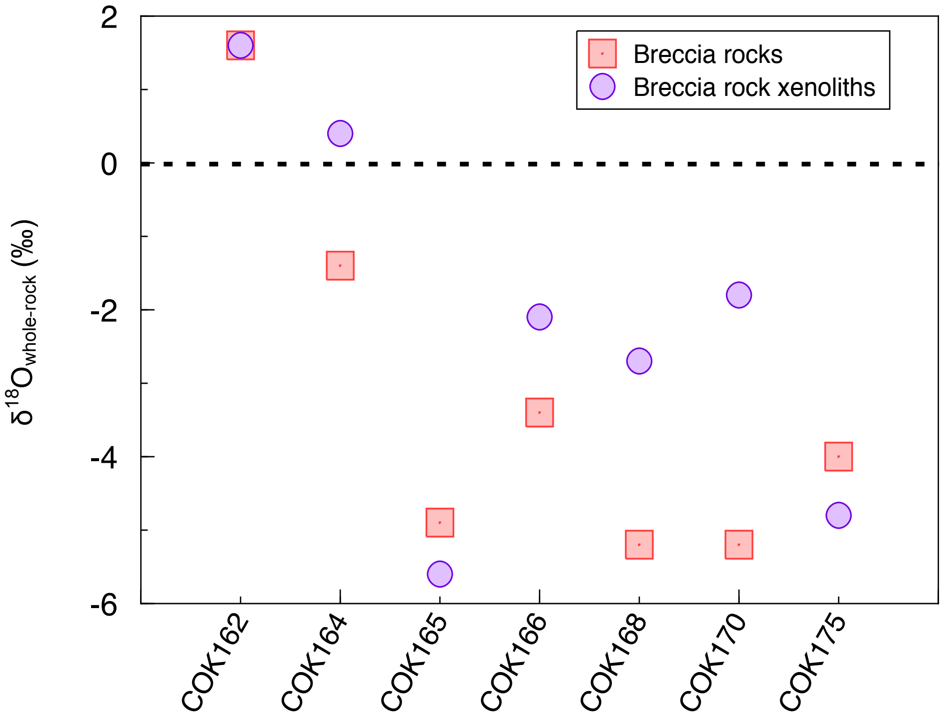

Fig. 5.10 Plot comparing the $\delta^{18}O$ values of the whole-rock with the $\delta^{18}O$ values of the xenoliths or mineral separates extracted from these rocks.

Table 5.6 Summary of the oxygen and hydrogen isotope ratios and the water content of the breccia rocks, phonolite rocks, and gneisses. The bostonites and mafic rock data are found in Curtis et al. (2013).

Breccia rock	**$\delta^{18}O_{Whole\text{-}rock}$ (‰)**	**$\delta D_{Whole\text{-}rock}$ (‰)**	**H_2O^+ (wt %)**	**$\delta^{18}O_{xenolith}$ (‰)**
COK162	1.6			1.6
COK164	-1.4			0.4
COK165	-4.9	-110	1.0	-5.6
COK166	-3.4			-2.1
COK168	-5.2	-123	0.7	-2.7
COK170	-5.2	-137	1.1	-1.8
COK172	-1.5			
COK174	-4.0	-113	0.6	
COK175	-4.0	-110	0.5	-4.8
COK176	-2.2			
COK178	0.2			
COK195	-0.8			
COK198	-1.9			
COK201	-4.9			
COK202	-2.5			
COK205-A	1.8			
COK205-B	-0.7			
COK207	-0.5			
Average	-2.6	-119	0.8	-2.1

Phonolite rock	**$\delta^{18}O_{Whole\text{-}rock}$ (‰)**	**$\delta D_{Whole\text{-}rock}$ (‰)**	**H_2O^+ (wt %)**	**$\delta^{18}O_{xenolith}$ (‰)**
COK191	8.5			
COK192	7.5			
Average	8.0			

Gneiss	**$\delta^{18}O_{Whole\text{-}rock}$ (‰)**	**$\delta D_{Whole\text{-}rock}$ (‰)**	**H_2O^+ (wt %)**	**$\delta^{18}O_{xenolith}$ (‰)**
COK163	3.1			
COK167	-1.1			
COK169	0.0			
COK171	1.1			
COK173	3.2			
COK177	-0.1			
Average	-0.6			

Variation of $\delta^{18}O$ values along the Breccia Outcrop

The $\delta^{18}O$ values of the breccia rocks show no systematic spatial variation (Fig. 5.11). Although the average $\delta^{18}O$ value of the breccia rocks on the West Dyke is about +2.0‰ lower than that of the breccia rocks on the East Dyke, both dykes have breccia rocks with some of the lowest oxygen isotope ratios (e.g. East Dyke: $\delta^{18}O_{COK174}$ = -4.0‰, West Dyke: $\delta^{18}O_{COK166}$ = -3.6‰).

West Dyke. The breccia rocks COK168 and COK170, which have the lowest whole-rock $\delta^{18}O$ values (-5.2‰) of all the COK samples analysed, are situated along the West Dyke of the Breccia Outcrop (Fig. 5.11). This side of the dyke also has breccia rocks with high whole-rock $\delta^{18}O$ values for the breccia rocks. The two rocks with the highest whole-rock $\delta^{18}O$ values on the West Dyke are sample COK172 and COK195 (basaltic groundmass texture in thin section petrography) with values of -1.5‰ and-0.8‰, respectively.

East Dyke. The breccia rock COK205-A, which has the highest $\delta^{18}O$ value (+1.8‰) of all the breccia rocks analysed, is located on the East Dyke, at the Breccia Plug 1 (Fig. 5.11). Sample COK178, which has a trachytic groundmass texture in thin section petrography, is also situated at the Breccia Plug 1 and has a $\delta^{18}O$ value of +0.2‰. Sample COK198, which is the second sample with a trachytic groundmass texture, is also located on the East Dyke. This sample is the furthest northwest from the Breccia Plug 1 and has a $\delta^{18}O$ value of -1.9‰. South of the Breccia Plug 1, there is COK174 and COK175, which both have the lowest $\delta^{18}O$ value on the East Dyke (-4.0‰). The $\delta^{18}O$ values of sample COK174 and COK175 are lower than the other rocks on the East Dyke.

The phonolites are situated on the East Dyke and have $\delta^{18}O$ values (average = +8.0‰) that are significantly higher than the $\delta^{18}O$ value of the breccia rocks (Fig. 5.11). These phonolites have a $\delta^{18}O$ value on average +9.5‰ higher than the average breccia rock on the East Dyke of the Breccia Outcrop.

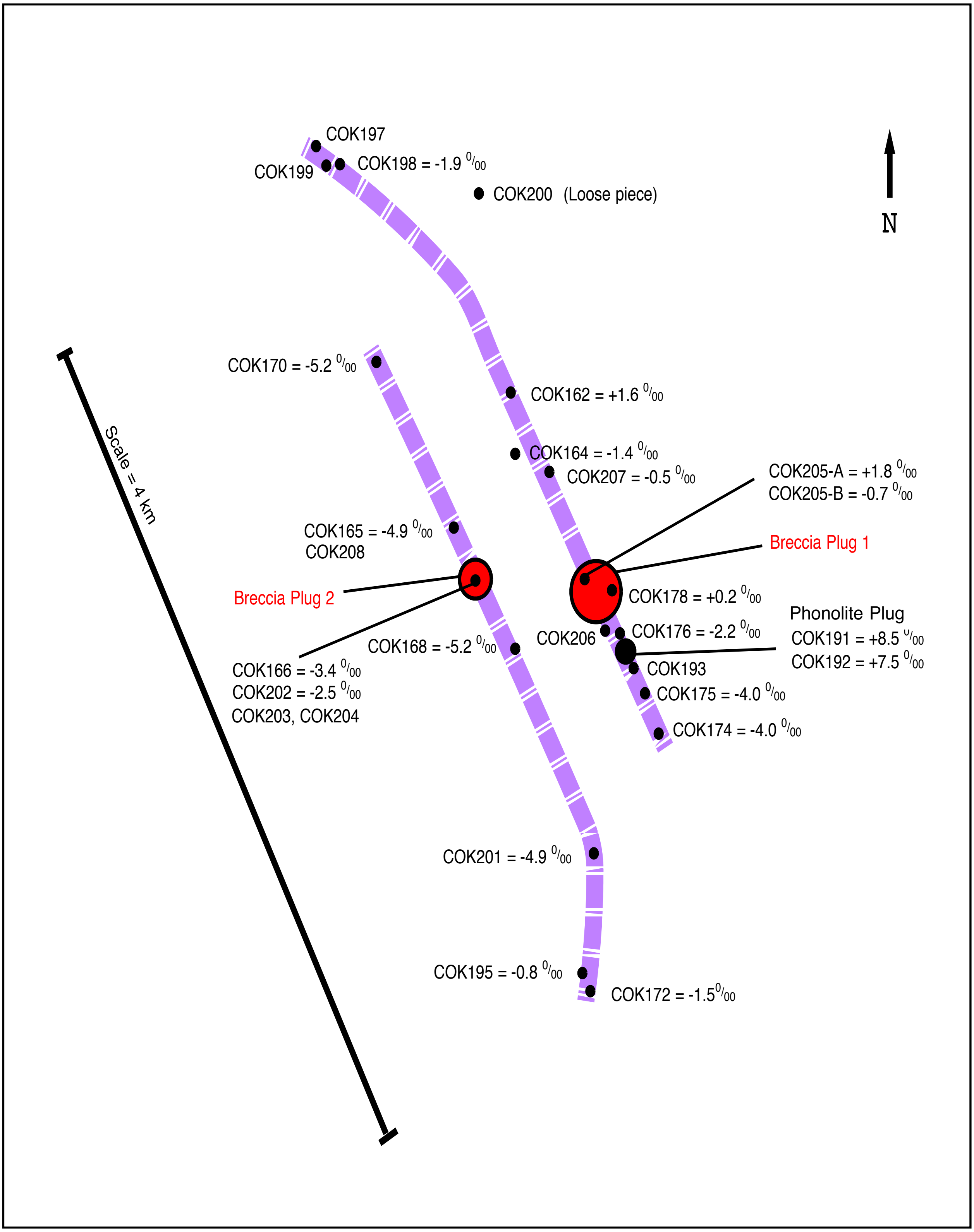

Fig. 5.11 Schematic map showing the distribution of the $\delta^{18}O$ values of the breccia rocks and phonolites along the Breccia Outcrop. The breccia rocks without an oxygen isotope ratio are rocks that were only studied petrographically. The representation is not to scale.

5.3.2 Hydrogen isotopes

Hydrogen isotope variation in the breccia rocks

The whole-rock δD values of all the Koegel Fontein igneous rocks range from -184‰ to -65‰ (average = -99‰, n = 67) (Curtis et al., 2013). The whole-rock δD values of five breccia rocks analysed in this study range from -137‰ to -110‰ (average = -119‰, n=5) (Table 5.6). The lowest whole-rock δD value of the five breccia samples (-137‰) is from COK170, which is one of the most altered breccia rocks. The highest whole-rock δD value (-110‰) is also from a strongly altered breccia rock (COK165). This shows there is no relationship between the hydrogen isotope data and the degree of alteration based on petrography.

The measured H_2O^+ concentrations vary between 0.5-1.1 wt % in the breccia rocks and respectively between 1.7-4.6 wt % and 0.6-1.0 wt % (Table 5.6) in the bostonite and mafic rocks (Curtis et al., 2013). The water concentrations in the bostonite and mafic rocks show no correlation with hydrogen isotope data (Curtis et al., 2013). In comparison, the water content in the five breccia rocks is moderately well correlated with the hydrogen isotope data ($r_{breccia} = -0.59$), apart from outlier COK165 that deviates from the linear correlation trend on which the four other breccia rocks plot (Fig. 5.12.a). The hydrogen and oxygen isotope data are more strongly correlated than the water content and hydrogen isotope data; these hydrogen and oxygen isotope data give a correlation coefficient of 0.69 (Fig. 5.12.b).

Regardless of the moderately strong correlations between the water content and whole-rock δD values and between the hydrogen and oxygen isotope compositions of the breccia rocks, the strength of these correlations is limited by the small dataset of breccia rocks (n = 5). Additional data would be required to draw any conclusions from these plots. This is kept in mind when the hydrogen and oxygen isotope data of the five breccia rocks is used in the discussion to estimate a δD and $\delta^{18}O$ value of a meteoric fluid.

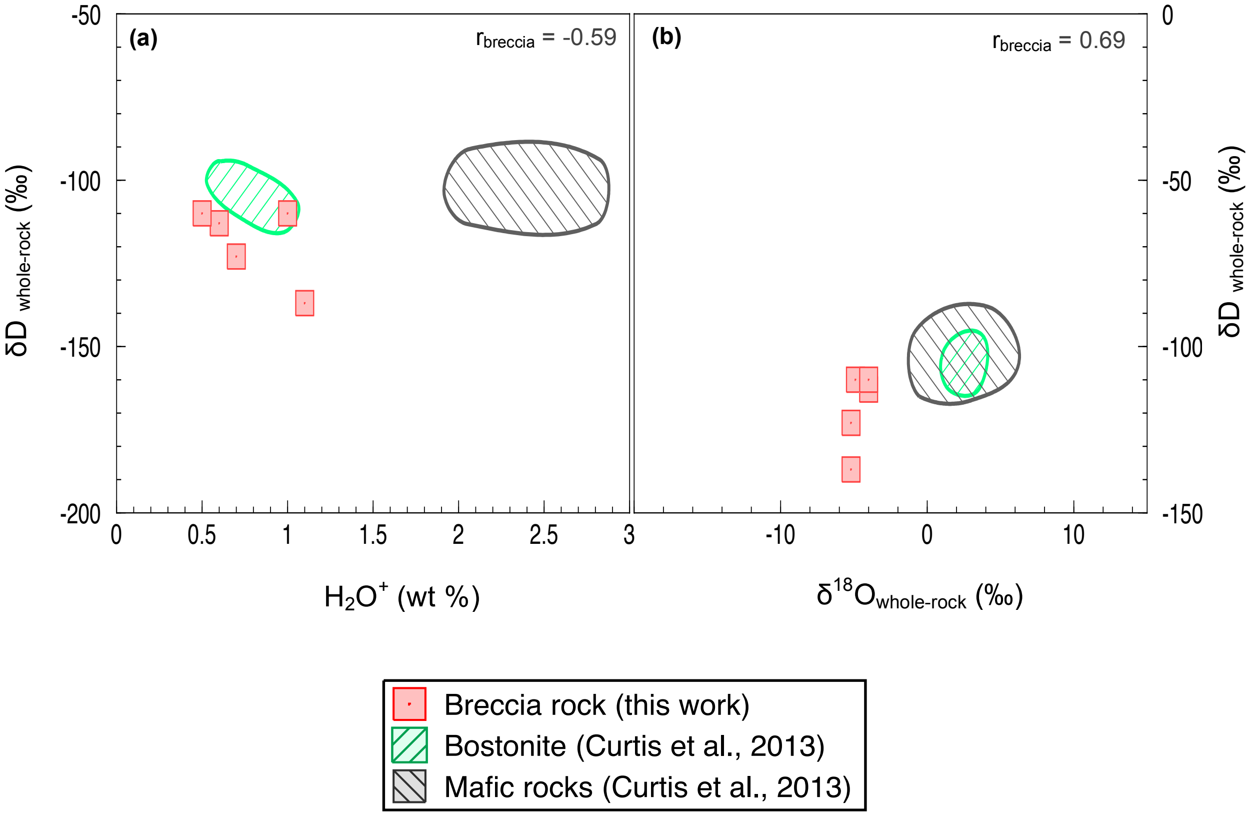

Fig. 5.12 Variation of δD values vs **(a)** measured weight % water and **(b)** $\delta^{18}O$ values of five breccia rocks (this study) and the bostonite and mafic rocks (Curtis et al., 2013). $r_{breccia}$ is the Pearson product-moment correlation coefficient of the five breccia rocks.

5.4 Radiogenic isotopes

5.4.1 Strontium and neodymium isotopes

The initial Sr isotope ratios ($^{87}Sr/^{86}Sr_{initial}$) and initial Nd epsilon values (εNd) for the breccia rocks are significantly variable, ranging respectively from 0.71050 to 0.74517 and -8.3 to +1.7 (Table 5.7). These data show a moderately strong negative correlation ($r_{breccia}$ = -0.57), excepting CO170, which deviates from the rest of the breccia rock dataset (Fig. 5.13). Sample COK170 has the highest εNd value of all the analysed rocks (+1.7) and a $^{87}Sr/^{86}Sr_{initial}$ ratio of 0.74162.

The $^{87}Sr/^{86}Sr_{initial}$ ratios and εNd values, age-corrected to 135 Ma, distinguish three groups of breccia rocks (Fig. 5.17). The first group of breccia rocks has low $^{87}Sr/^{86}Sr_{initial}$ ratios and high εNd values. This group consists of COK172 and COK195, which have the lowest $^{87}Sr/^{86}Sr_{initial}$ values (0.71050 and 0.7182, respectively) and the second and third highest εNd values (+0.9 and +1.2, respectively). The second group comprises most of the breccia rocks (n = 9). This second group has εNd values that range between -2.8 and +0.2 and $^{87}Sr/^{86}Sr_{initial}$ ratios that vary between 0.73334 and 0.72233. The third group consists of rocks with high $^{87}Sr/^{86}Sr_{initial}$ ratios and low εNd values. This third group includes samples COK175 and COK205-A, which have respectively the highest and third highest $^{87}Sr/^{86}Sr_{initial}$ values (0.74517 and 0.73356) and the lowest εNd values of the breccia rocks (-8.3 and -8.2).

The phonolite COK192, which was analysed for radiogenic isotopes, is the only rock that plots away from the rest of the samples (Fig 5.13). This rock has a $^{87}Sr/^{86}Sr_{initial}$ value of 0.79432 and εNd value of +0.5. This sample COK192 has an unexpectedly high $^{87}Sr/^{86}Sr_{initial}$ value for the εNd value it has. The εNd values in the six gneisses are uniform and on average equal to -9. The $^{87}Sr/^{86}Sr_{initial}$ ratios of the gneisses are more variable than the Nd isotope data and range from 0.73809 to 0.77352.

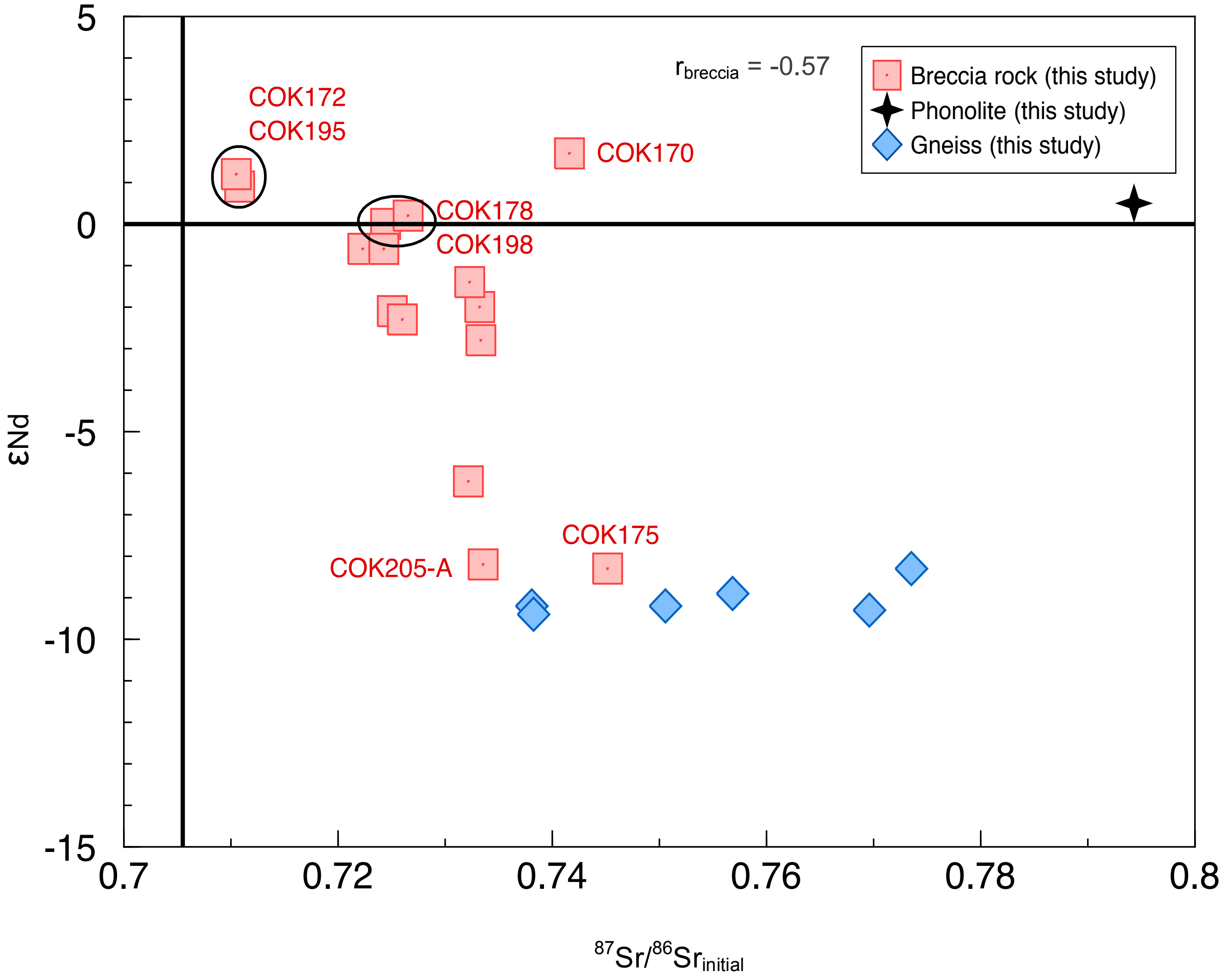

Fig. 5.13 Initial Sr isotope ratios and initial Nd epsilon values for 15 breccia rocks, 1 phonolite rock, and 6 gneisses, all three of which are age-corrected to 135 Ma. $r_{breccia}$ is the Pearson product-moment correlation coefficient of the 15 breccia rocks.

Table 5.7 Radiogenic isotope compositions of 15-breccia rocks, 1-phonolite rock, and 6-gneisses.

sample name	age Ma	$^{87}Sr/^{86}Sr_{measured}$ measured	±2σ internal ppm	Rb ppm	Sr ppm	$^{87}Rb/^{86}Sr$	$^{87}Sr/^{86}Sr_{initial}$ initial	εSr initial	$^{143}Nd/^{144}Nd_{measured}$ measured	±2σ internal ppm	Sm ppm	Nd ppm	$^{147}Sm/^{143}Nd$	$^{143}Nd/^{144}Nd_{initial}$ initial	εNd initial
Breccia rock															
COK162	135	0.72875	14	184.5	279.8	1.912	0.72508	291.6	0.51246	11	9.65	51.73	0.113	0.51236	-2.1
COK164	135	0.73881	12	141.0	140.8	2.907	0.73323	407.3	0.51246	13	8.84	51.68	0.103	0.51236	-2.0
COK165	135	0.72523	8	147.2	282.5	1.511	0.72233	252.5	0.51255	11	7.05	32.67	0.130	0.51244	-0.6
COK166	135	0.72703	10	117.8	237.5	1.438	0.72427	280.1	0.51254	12	7.55	39.22	0.116	0.51243	-0.6
COK168	135	0.72869	12	131.0	271.6	1.399	0.72601	304.7	0.51246	14	8.48	43.49	0.118	0.51235	-2.3
COK170	135	0.74781	11	425.5	383.0	3.228	0.74162	526.3	0.51267	7	7.24	32.46	0.135	0.51255	1.7
COK172	135	0.71116	9	55.3	924.6	0.173	0.71082	89.2	0.51262	12	8.70	42.08	0.125	0.51251	0.9
COK174	135	0.73585	10	167.8	254.6	1.913	0.73218	392.3	0.51225	9	12.15	61.41	0.120	0.51215	-6.2
COK175	135	0.75277	12	222.6	163.4	3.960	0.74517	576.7	0.51215	10	14.35	71.92	0.121	0.51204	-8.3
COK176	135	0.73711	15	196.7	227.9	2.505	0.73230	394.1	0.51251	13	8.93	42.10	0.128	0.51239	-1.4
COK178	135	0.73086	10	184.5	239.0	2.239	0.72656	312.6	0.51257	10	8.46	50.90	0.100	0.51248	0.2
COK195	135	0.71083	12	56.7	933.4	0.176	0.71050	84.6	0.51264	10	8.58	41.82	0.124	0.51253	1.2
COK198	135	0.72596	12	163.7	599.6	0.792	0.72444	282.5	0.51256	10	9.30	52.64	0.107	0.51247	0.0
COK205-A	135	0.73656	13	121.1	225.0	1.562	0.73356	412.0	0.51215	10	10.76	52.53	0.124	0.51204	-8.2
COK205-B	135	0.74237	14	335.8	207.1	4.709	0.73334	408.8	0.51244	7	12.65	60.39	0.127	0.51232	-2.8
Phonolite rock															
COK192	135	0.82995	14	216.8	34.2	18.567	0.79432	1274.4	0.51259	8	20.28	110.40	0.111	0.51249	0.5
Gneiss															
COK163	135	0.78318	12	190.2	110.2	5.032	0.77352	979.2	0.51215	8	20.69	102.50	0.122	0.51204	-8.3
COK167	135	0.74343	11	138.9	145.0	2.782	0.73809	476.3	0.51210	12	14.93	75.34	0.120	0.51200	-9.2
COK169	135	0.76471	12	272.7	193.4	4.104	0.75684	742.4	0.51211	9	24.42	123.30	0.120	0.51201	-8.9
COK171	135	0.78196	11	126.0	57.1	6.435	0.76961	923.6	0.51211	11	14.12	63.99	0.133	0.51199	-9.3
COK173	135	0.74148	11	145.7	251.0	1.686	0.73825	478.5	0.51209	12	16.86	86.59	0.118	0.51198	-9.4
COK177	135	0.76015	11	145.7	85.0	4.988	0.75058	653.5	0.51208	11	10.50	62.98	0.101	0.51199	-9.2

S-r and Nd-isotope initial ratios for all the rocks are calculated to 135 Ma based on U-Pb zircon dates.

5.4.2 Radiogenic and oxygen isotopes

The O and Sr isotope data of the breccia rocks are poorly correlated ($r_{breccia}$ = -0.23) (Fig. 5.14.a). Sample COK170 and COK175, which have some of the lowest δ^{18}O values of the breccia rocks (-5.2‰ and -4.0‰, respectively), have the highest ^{87}Sr/^{86}Sr$_{initial}$ ratios of these rocks (0.74162 and 0.74517). By contrast, COK165 and COK168, which also have some of the lowest δ^{18}O values of the breccia rocks (-4.9‰ and -5.2‰, respectively), have lower ^{87}Sr/^{86}Sr$_{initial}$ ratios (0.72233 and 0.72601, respectively) than COK170 and COK175. These data indicate that breccia rocks with low δ^{18}O values do not necessarily have high concentrations in Sr isotopes. The oxygen isotope composition of the breccia rocks shows no relationship with the Nd isotope data ($r_{breccia}$ = -0.10) (Fig. 5.14.b). These data indicate that the breccia rocks with high and low εNd values can have high and low δ^{18}O values.

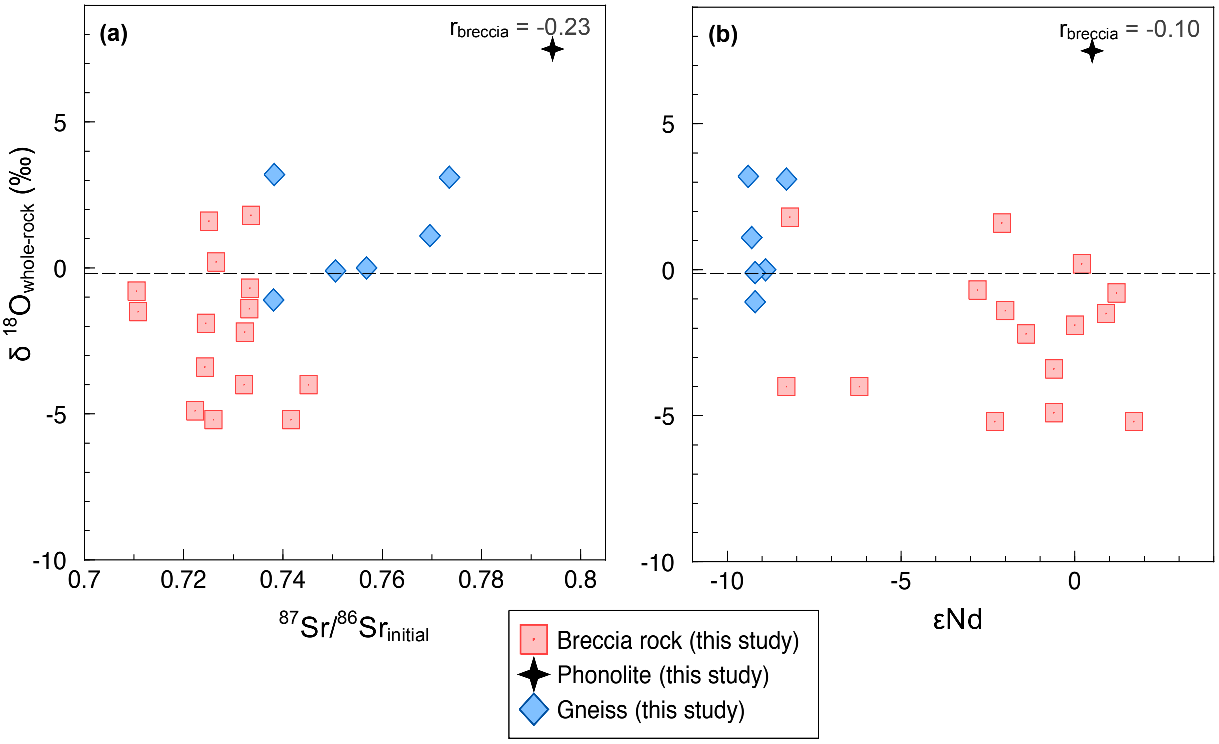

Fig. 5.14 Oxygen isotope data of the 15 breccia rocks, 1 phonolite rock, and 6 gneisses versus **(a)** initial Sr isotope ratios and **(b)** initial Nd epsilon values. $r_{breccia}$ is the Pearson product-moment correlation coefficient of the 15 breccia rocks.

5.4.3 Radiogenic isotopes and element compositions

The radiogenic isotope data plotted in Figure 5.15 to Figure 5.18 are included for completion of this work. These diagrams are briefly described.

Strontium isotopes

The major element concentrations and $^{87}Sr/^{86}Sr_{initial}$ ratios of the breccia rocks have correlation coefficient values < ±0.5, excepting P_2O_5 and K_2O concentrations, which have correlation coefficients of -0.54 and 0.72, respectively (Fig. 5.15). The breccia rock data are especially well correlated in the K_2O diagram on which there are no distinct outliers.

The trace element concentrations and $^{87}Sr/^{86}Sr_{initial}$ ratios of the breccia rocks have correlation coefficients < ±0.5, excepting Sr and Rb trace element concentrations with strong correlation coefficient values of -0.76 and 0.72, respectively (Fig. 5.16). In this figure, the Sr trace element data are also strongly correlated with $^{87}Rb/^{86}Sr$ ratios ($r_{breccia}$ = -0.70). The Sr trace element concentrations versus $^{87}Sr/^{86}Sr_{initial}$ and $^{87}Rb/^{86}Sr$ ratios discriminate two groups of breccia rocks that plot along two negative trends sub-parallel to one another. The Rb trace element data versus $^{87}Sr/^{86}Sr_{initial}$ are more scattered than the Sr trace element data versus $^{87}Sr/^{86}Sr_{initial}$ and only discriminate one series of breccia rocks.

Neodymium isotopes

The major element concentrations against $^{143}Nd/^{144}Nd_{initial}$ ratios of the breccia rocks show well-defined correlations in the MnO and P_2O_5 plots, which have respective correlation coefficient values of 0.62 and 0.86 (Fig. 5.17). The seven other major element plots have weak correlation coefficients values, which are < ±0.5.

The trace element concentrations versus $^{143}Nd/^{144}Nd_{initial}$ ratios of the breccia rocks show weak correlations (Fig. 5.18). Strontium is the only trace element to have concentrations moderately well correlated with the $^{143}Nd/^{144}Nd_{initial}$ ratios, with a correlation coefficient value of 0.54.

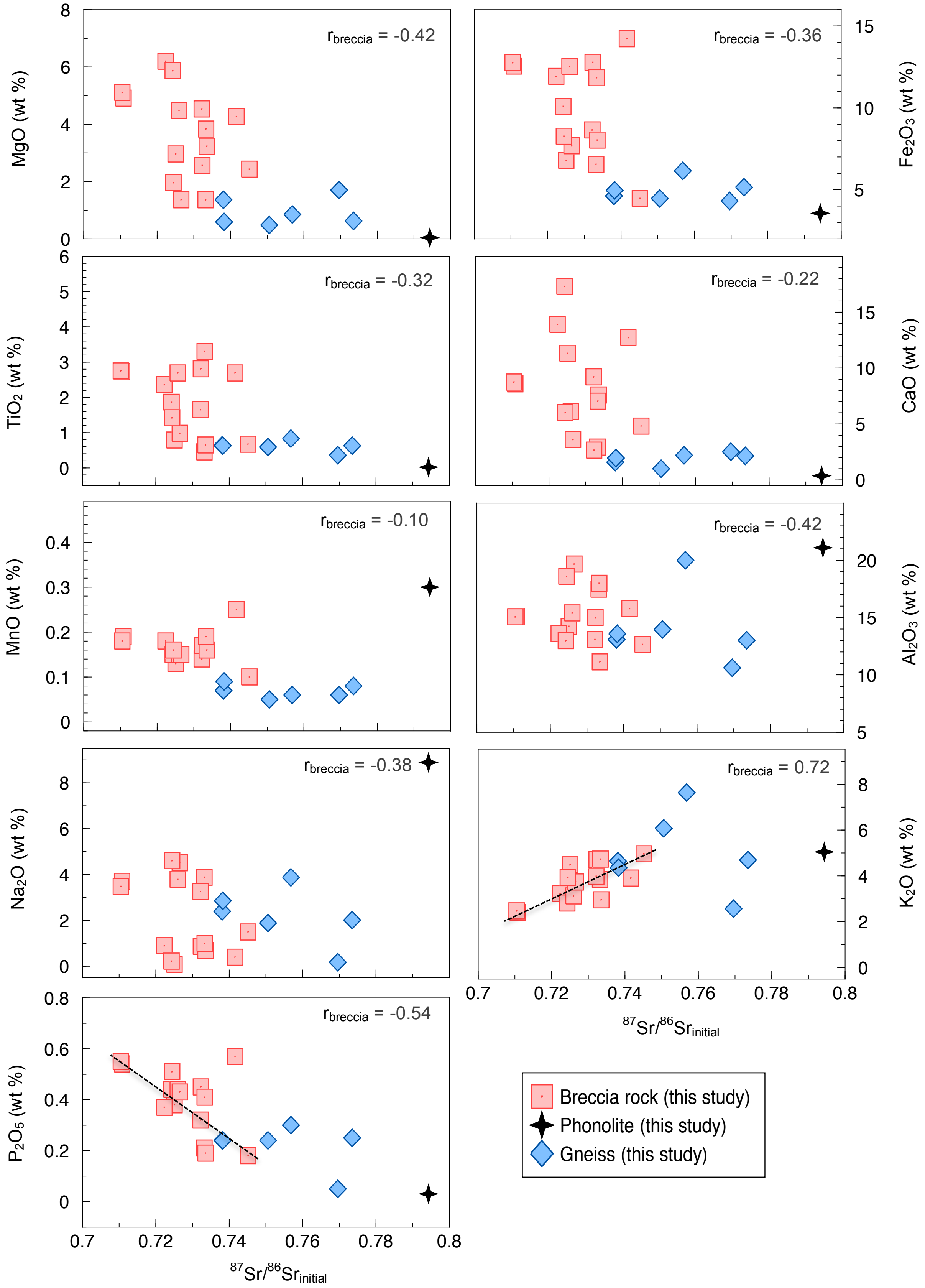

Fig. 5.15 Major element concentrations plotted against $^{87}Sr/^{86}Sr_{initial}$ values for 15 breccia rocks, 1 phonolite rock, and 6 gneisses. $r_{breccia}$ is the Pearson product-moment correlation coefficient of the 15 breccia rocks only.

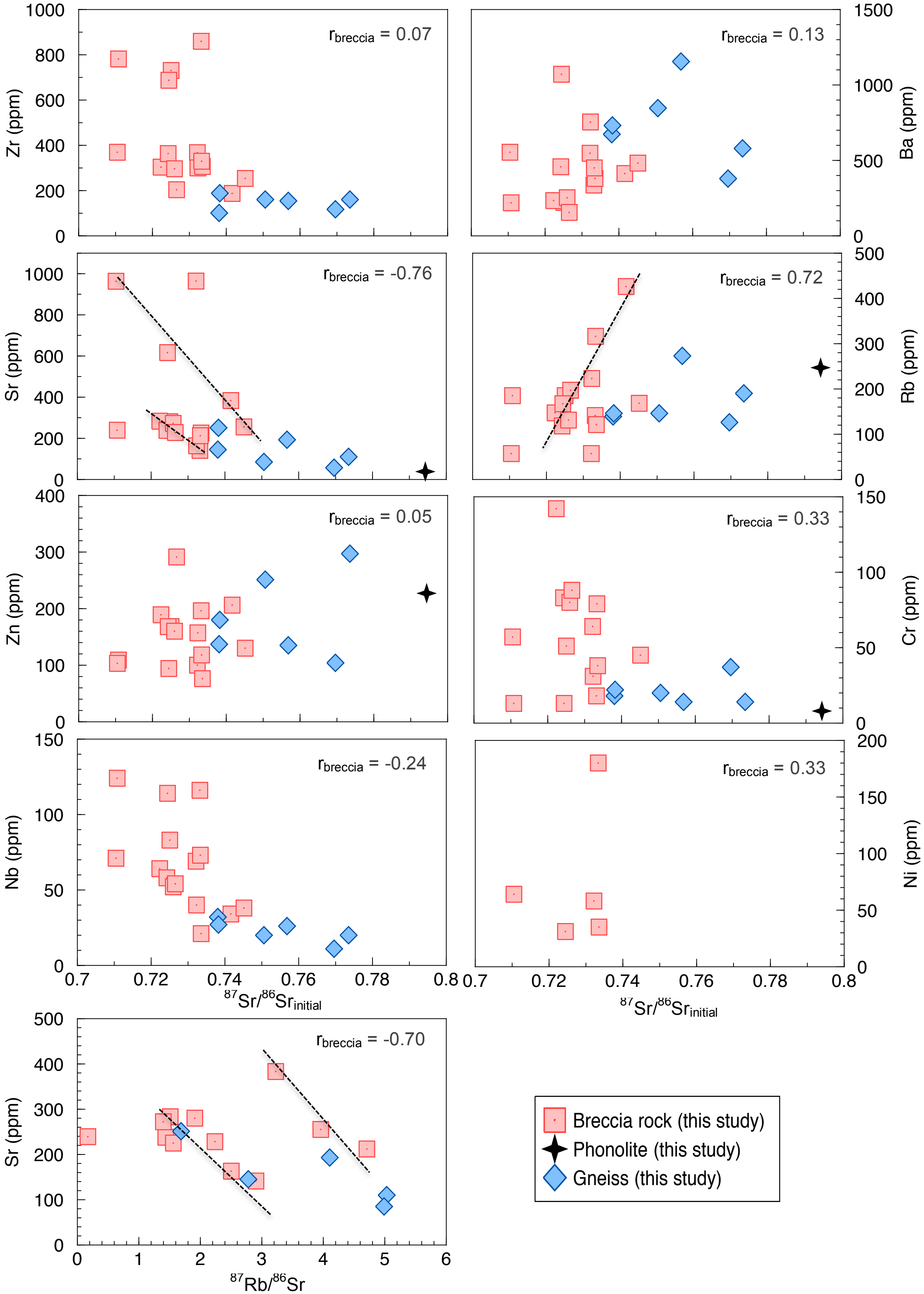

Fig. 5.16 Trace element concentrations plotted against $^{87}Sr/^{86}Sr_{initial}$ or $^{87}Rb/^{86}Sr$ values for 15 breccia rocks (XRF and ICP-MS data), 1 phonolite (XRF data), and 6 gneisses (ICP-MS data). The XRF data were used instead of ICP-MS data for rocks analysed using both methods. The phonolite is not included when its trace element concentration is significantly higher than that of the breccia rocks. Only Ni data from XRF analysis is included (see Chapter 4). $r_{breccia}$ is the Pearson product-moment correlation coefficient of the 15 breccia rocks.

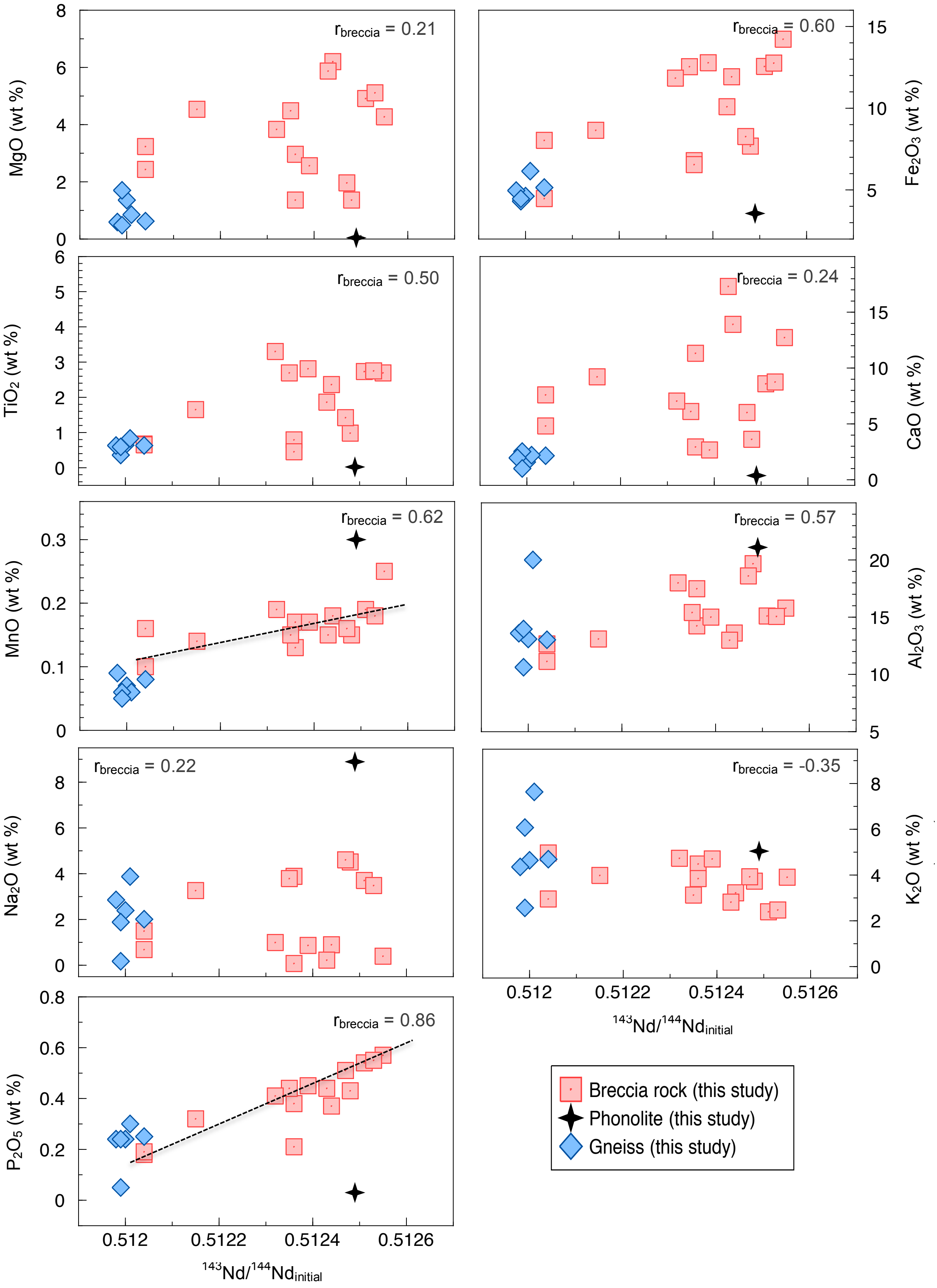

Fig. 5.17 Major element concentrations plotted against ^{143}Nd/^{144}Nd$_{initial}$ values for 15 breccia rocks, 1 phonolite rock, and 6 gneisses. $r_{breccia}$ is the Pearson product-moment correlation coefficient of the 15 breccia rocks only.

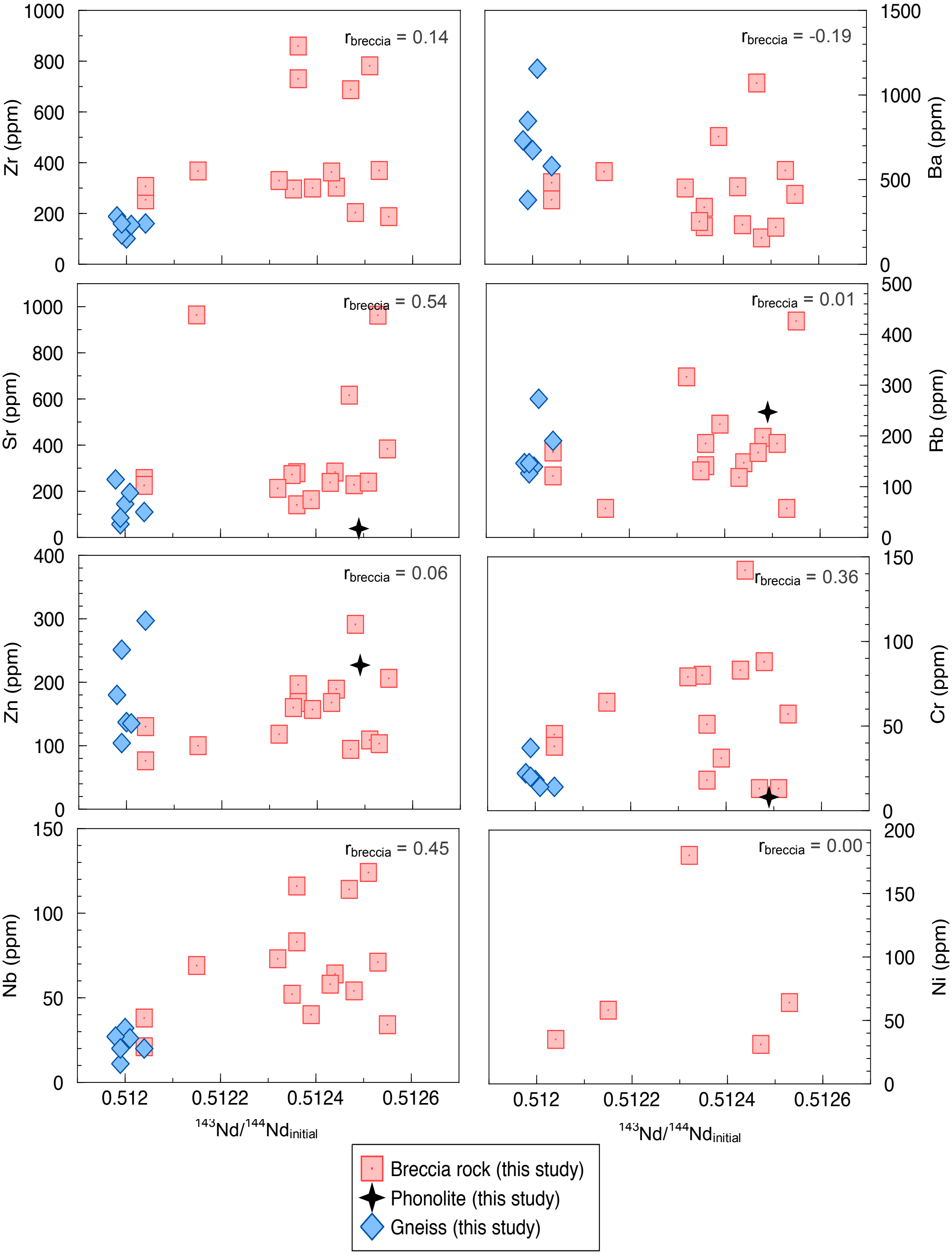

Fig. 5.18 Trace element concentrations plotted against ^{143}Nd/^{144}Nd$_{initial}$ values for 15 breccia rocks (XRF and ICP-MS data), 1 phonolite (XRF data), and 6 gneisses (ICP-MS data). The XRF data were used instead of ICP-MS data for the breccia rocks analysed using both methods. The phonolite is not included when its trace element concentration is significantly higher than that of the breccia rocks. Only Ni data from XRF analysis is included (see Chapter 4). $r_{breccia}$ is the Pearson product-moment correlation coefficient of the 15 breccia rocks only.

5.5 Summary of the key points

5.5.1 Whole-rock geochemistry

Major elements

Firstly, the breccia rocks have a wide major element compositional range that extends across from the mafic rock field to the bostonite field or from the mafic rock field to the gneisses (Fig. 5.1). And on average, the breccia rocks have a composition closer to that of the mafic rocks than that of the bostonites or gneisses (Fig. 5.1). Secondly, COK178 and COK198 (trachytic groundmass texture) have a major element composition close to that of the bostonites (Curtis et al., 2011) (Table 5.1). Thirdly, COK172 and COK195 (basaltic groundmass texture) have a composition similar to that of the mafic rocks (Curtis et al., 2011) and plot in or near the mafic rock compositional field (Fig. 5.1 and Fig. 5.2). Fourthly, COK205-B (black matrix) has a composition similar to that of mafic rocks, whereas COK205-A (green matrix) has a composition closer to that of bostonites or gneisses than that of mafic rocks (Fig. 5.1 and Fig. 5.2). Fifthly, COK175, which has the most gneiss xenoliths, has a composition close to that of gneiss (Table 5.1 and Fig. 5.2). Sixthly, the breccia rocks situated on the West Dyke of the Breccia Outcrop have an average silica content lower than that of the breccia rocks on the East Dyke (Fig. 5.3). Finally, the LOI values and water content in all of the breccia rocks are low (average <1.0 wt %) (Table 5.2 and Fig. 5.4).

Trace elements

Firstly, the breccia rocks have a wide trace element compositional range that extends across from the mafic rock field to the bostonite field or from the mafic rock field to the gneisses (Fig. 5.5). And on average, the breccia rocks have a chemical composition closer to that of the mafic rocks than that of the bostonites or gneisses (Fig. 5.5). Secondly, Y and Nb data distinguish two groups of breccia rocks (Fig. 5.6.a). The first group (Y/Nb = 0.1) contains most of the breccia rocks, which plot with the alkaline mafic dykes. The second group (Y/Nb = 3) includes two of the breccia rocks, which plot with the tholeiitic mafic dykes. Finally, the breccia rocks show three types of REE patterns (Fig. 5.7). The REE pattern 1 shows a pattern with a negative Eu anomaly. This first REE pattern is similar to that of the bostonites from Curtis et al. (2011) (Fig. 5.8.a). The REE pattern 2 shows a pattern without a Eu anomaly. This second pattern is similar to that of the alkaline mafic rocks from Curtis et al. (2011) (Fig. 5.8.b). The REE pattern 3 shows a pattern enriched in HREE compared to the rest of the REE patterns of the breccia rocks (Fig. 5.8.a).

5.5.2 Mineral chemistry

Firstly, the two grains (Table 5.5.a) in the groundmass of COK191 have a mineral composition consistent with the chemistry of anorthoclase. Secondly, the five grains (Table 5.5.a) from COK192 have a mineral composition consistent with nepheline. Finally, the 36 grains (Table 5.5.b) picked out from xenolith COK166 show negligible chemical variability and have a mineral composition consistent with epidote.

5.5.3 Stable isotopes

Firstly, all the COK samples have $\delta^{18}O$ value below the mantle value of +5.7‰, excepting the phonolites (COK191 and COK192) (Table 5.6). Secondly, COK168 and COK170 have the lowest whole-rock $\delta^{18}O$ value (-5.2‰) of the Koegel Fontein complex (Table 5.3 and Fig. 6.3). Thirdly, mineral separates from COK165 have a lower $\delta^{18}O$ value (-5.6‰) than all the whole-rocks, xenoliths, and mineral separates analysed at Koegel Fontein (Table 5.6). Finally, the variation of $\delta^{18}O$ values along the Breccia Outcrop is not systematic (Fig. 5.11).

5.5.4 Radiogenic isotopes

Firstly, the breccia rocks have a wide radiogenic isotope composition (Table 5.7) on the εNd value versus $^{87}Sr/^{86}Sr_{initial}$ ratio diagram (Fig. 5.13). Secondly, the radiogenic and oxygen isotope data of the breccia rocks are poorly correlated (Fig. 5.14). Thirdly, the Sr isotope data are strongly correlated with the $^{87}Sr/^{86}Sr_{initial}$ ratios and $^{87}Rb/^{86}Sr$ ratios of the breccia rocks ($r_{breccia}$ = -0.76 and $r_{breccia}$ = -0.70, respectively) (Fig. 5.16). Finally, the P_2O_5 concentrations is strongly correlated with the $^{143}Nd/^{144}Nd_{initial}$ ratios of the breccia rocks ($r_{breccia}$ = 0.86) (Fig. 5.17).

CHAPTER 6 DISCUSSION

The four aims of this study are discussed in this chapter. The first aim was to describe the breccia rocks and the shape that these rocks make up. The second objective was to document the whole-rock and isotope composition of the rocks that make up the Breccia Outcrop. The third aim was to determine the variation of the $\delta^{18}O$ values of the breccia rocks over the mapped area. The last objective was to explore the relationship between the Breccia Outcrop and the rest of the complex. This last aim is addressed after comparing the Breccia Outcrop to an intrusive hydrothermal breccia from another locality in the world and suggesting three emplacement models for the Breccia Outcrop.

6.1 The breccia rocks and the Breccia Outcrop

6.1.1 Characteristics of the breccia rocks

Matrix

Despite the breccia rocks having a variable fraction of groundmass, xenolith, and phenocryst and showing strong alteration, which makes the identification of individual components somewhat difficult, the breccia rocks are recognised as one rock type that is singular in the complex. These breccia rocks are commonly fine-grained and black, with gneiss and black xenoliths. These rocks can also be black and green with the green representing epidote alteration, or less frequently, chlorite alteration.

In thin section petrography, two types of groundmass reflecting the black rock in the breccia rocks show evidence that this black rock is igneous in origin and either basalt or bostonite. Groundmass (C) reflects that bostonite is one of the rock constituents that make up the breccia rocks. This groundmass was identified in COK178 and COK198, which have the distinct trachytic groundmass texture that defines the bostonite rocks at Koegel Fontein (de Beer et al., 2002). Groundmass (D) indicates that basalt is another rock component in the breccia rocks. This groundmass (D) was recognized in COK172 and COK195, which have a basaltic groundmass texture supporting phenocrysts of plagioclase, alkali feldspar, pyroxene, and amphibole.

There is a third type of groundmass (groundmass (B)) that reflects the black rock of the breccia rocks. This groundmass (B) shows no apparent texture. Instead, groundmass (B) is strongly altered by biotite. This third groundmass is suggested to be a strongly altered mixture between bostonite and basalt rather than a third rock component of the breccia rocks. There is not enough evidence to say if this mixture is mechanical or chemical.

Matrix (A), which is the green rock in the hand-specimens, is thought to represent a third rock constituent of the breccia rocks. This third rock component is too fine-grained to identify any primary minerals but shows mostly epidote with some chlorite and has abundant gneiss and black xenoliths. This third rock constituent is suggested to have been an epidote- and xenolith-rich fluidised material that transported rock fragments made of basalt, bostonite, and country rock gneiss (see the emplacement model section).

Overall, three types of rock are recognised in the breccia rocks. The first two rock types, which are both black in the hand-specimens, are bostonite and basalt. The third type of rock that makes up the breccia rocks, which is green in the hand-specimens, is an epidote- and xenolith-rich rock that has a matrix that is too fine-grained to identify any primary constituents. This third rock constituent could either be a different rock type to the basalt and bostonite or a fine-grained, fragmented version of all the rocks components found in the breccia rocks.

Xenoliths and xenocrysts

There are two xenolith types in the breccia rocks. The most abundant xenolith type is made of black rock. This black rock is described as groundmass (B) in thin section petrography. These groundmass (B) xenoliths are round inclusions made of a strongly altered mixture between bostonite and basalt. The occurrence of these xenoliths in the breccia rocks brings evidence for the bostonite and basalt rocks to predate the breccia rocks.

The second type of xenolith in the breccia rocks is the gneiss xenoliths. These gneiss xenoliths are less abundant in the breccia rocks than the groundmass (B) xenoliths. These fragments of gneiss are round or angular and mostly made of granoblastic quartz and occasionally of quartz, feldspar, biotite, and mafic minerals. The gneiss xenoliths in the breccia rocks reflect a fourth rock constituent that makes up the breccia rocks. This gneiss is thought to be country rock gneiss, which is Mezoproterozoic in age (1200-1000 Ma) (de Beer and Armstrong, 1998).

The breccia rocks with the most gneiss xenoliths typically have a fraction of disseminated quartz xenocrysts. The quartz xenocrysts are interpreted as pieces of quartz that broke off from the gneiss xenoliths or directly from the country rock when the material that formed the Breccia Outcrop intruded through the crust. In one sample (COK162), there are two quartz xenocrysts that show a flow texture. This flow texture indicates that a fluidised type of material flowed over the xenocrysts. This supports the suggestion that a fluid-rich mass formed the breccia rocks.

Sample COK205

Sample COK205 contains a fragment of black rock (groundmass (B) xenolith) supported in the epidote- and xenolith-rich green rock (matrix (A)). The sub-sample COK205-B brings evidence for the black rock to predate the breccia rocks. The sub-sample COK205-A, which is xenolith-rich (gneiss and groundmass (B) xenoliths), brings support to this epidote- and xenolith-rich green rock to have been a fluidised type of mass that broke off pieces of wall rock and transported them towards the surface of the crust.

Alteration

The breccia rocks exhibit strong petrographic evidence for alteration, which includes turbid feldspar, chloritised feldspar and amphibole, and secondary epidote, biotite, and chlorite minerals. One of the two most abundant alteration minerals in these rocks is epidote. Epidote is the main constituent of matrix (A). This mineral is also found replacing parts of the three groundmasses ((B), (C), and (D)) and two types of xenoliths (gneiss and groundmass (B) xenoliths). Epidote in the breccia rocks brings evidence for the breccia rocks to have experienced fluid-rock interaction (Curtis et al., 2013) at a temperature between 300-400°C (Deer et al., 1992).

The second of the two most abundant alteration minerals in the breccia rocks is a brown alteration product that altered the black rock of the breccia rocks. This alteration product is recognised as biotite in COK172 and COK195. Assuming that the brown alteration product in the other breccia rocks is also biotite, then biotite reflects a final equilibration between the black rock and hydrothermal fluids that ceased at a temperature >400°C (Deer et al., 1992).

The third alteration mineral is the least abundant of the three predominant alteration minerals in these rocks. This mineral is chlorite. Chlorite is abundant in matrix (A) and scarce in the groundmasses ((B), (C), and (D)) and phenocrysts. The presence of chlorite in matrix (A) indicates that the breccia rocks experienced fluid-rock interaction. The small quantity of chlorite in the breccia rocks compared to that of epidote brings evidence for epidote being the mineral representing the temperature at which the fluid and the rock interacted.

Overall, the alteration minerals can indicate the temperatures at which the rock and hydrothermal fluids interacted. The prevalence of epidote and biotite in the breccia rocks indicate that these rocks underwent fluid-rock interaction at a relatively high temperature (>300°C).

6.1.2 The Breccia Outcrop

The Breccia Outcrop, which was thought to be one single intrusive plug until 2014 (Olianti, 2014), consists of two sub-parallel breccia dykes, extending in northwest and south directions over a distance of about 4 km lengthwise (Fig. 3.1). This outcrop is deviated in the north and in the south. This deviation is thought to result from faults cutting through the West and East Dykes, although there is a lack of field evidence because of poor outcrop exposure.

Two distinct intrusive breccia plugs ~80 m away from one another are situated along the two sub-parallel breccia dykes (Fig. 3.1). The Breccia Plug 1 on the East Dyke and the Breccia Plug 2 on the West Dyke reflect two focal points where a xenolith- and fluid-rich material broke through the crust before extending along the basalt and bostonite dykes and forming the two sub-parallel breccia dykes.

A third intrusive plug made of phonolites is located on the East Dyke, south of the Breccia Plug 1 (Fig. 3.1). The Phonolite Plug is made of the first silica-understaruated rocks identified in the Koegel Fontein complex.

6.2 Chemical composition of the breccia rocks

6.2.1 Whole-rock geochemistry

Major elements

The major element concentrations in the breccia rocks range in between the reverse major element fields of the mafic rocks and the bostonite or gneiss rocks (Fig. 5.1). This major element variation in the breccia rocks support the suggestion made based on petrography that these rocks consist of at least three components, two of which are igneous (basalt and bostonite) and one metamorphic (gneiss).

The breccia rocks have a large compositional range that plots in between the bostonite field and the gneisses on one side and the less evolved mafic rocks than the bostonite and gneiss on the other side (Fig. 5.1). The heterogeneous compositional range of the breccia rocks indicates that these rocks are made of more than one rock type, which could be fragments of mafic rocks, bostonites, and gneisses.

By combining the petrography with results shown on the TAS diagram (Fig. 5.2) of the breccia rocks, three types of rock can be distinguished. The first type of rock is a mafic rock and suggested to be basalt. Basalt is suggested based on the basaltic groundmass texture of two (COK172 and COK195) of the nine rocks that plot in the mafic rock field on the TAS diagram. Two (COK165 and COK166) of the nine rocks in the mafic rock field plot directly in the basalt field on the TAS diagram. The abundance of basalt dykes in the Koegel Fontein region described by de Beer et al. (2002) is also in favour for basalt to be one of the main rock constituents in the breccia rocks. In addition, all nine rocks, excepting COK205-B, which is a basalt xenolith of COK205 on the East Dyke, are situated on the West Dyke of the Breccia Outcrop (Fig. 5.3).

The second rock type proposed to make up the breccia rocks is bostonite, although the bostonite constituent is not as strongly reflected by the whole-rock geochemistry of the breccia samples as the basalt component. The bostonite is suggested based on the trachytic groundmass texture in two breccia rocks (COK178 and COK198) situated on the East Dyke, the abundance of bostonite dykes in the complex (de Beer et al., 2002), the situation of the breccia rocks from the East Dyke (Fig. 5.3) to plot outside of the mafic rock field on the TAS diagram (Fig. 5.2), and the whole-rock geochemistry of these samples (Fig. 5.1).

The third rock component thought to exist in the breccia rocks is gneiss, forming gneiss xenoliths in the breccia rocks. The gneiss rock type is reflected by the whole-rock geochemistry (Fig. 5.1), petrography, and TAS content of sample COK175 (Fig. 5.2). Sample COK175 has the closest composition to the gneiss analysed in this work (Table 5.1) and contains the most gneiss xenoliths of all the breccia rocks.

None of the breccia rocks on the East Dyke (Fig. 5.3) and outside of the mafic rock field on the TAS diagram (Fig. 5.2) plot in the bostonite field. The range in composition of the breccia rocks situated on the East Dyke is suggested to result from the presence of groundmass (B) and gneiss xenoliths in these breccia rocks. These xenoliths are also part of the rock; the chemical composition of these xenoliths is therefore also reflected in the whole-rock geochemistry.

The major element compositional difference between COK205-A and COK205-B confirms that COK205 is made of two distinct rock types. Sample COK205-B, which plots in the trachybasalt field on the TAS diagram (Fig. 5.2), has a mafic composition (Table 5.1). Sample COK205-A, which plots in the dacite field on the TAS diagram, is felsic in composition.

The two xenoliths extracted from the whole rock of COK175 and COK208 and analysed individually do not plot on the TAS diagram (Fig. 5.2) as anticipated. These two xenoliths have an overall alkali content higher than the breccia rocks and the Namaqua metamorphic gneisses. This concentration variation is unresolved. The raw whole rock data and field mapping are used instead to make more conclusions of the xenoliths.

The major element concentrations (Table 5.1) of the breccia xenoliths COK175 and COK208 reflect two different rock types. The composition of xenolith COK208 (black xenolith), which has a low silica content compared to COK175 and is situated on the West Dyke, is consistent with that of the breccia rocks on this West Dyke (Fig. 5.3). This xenolith COK208 is suggested to be basalt. The composition of xenolith COK175, which has a high silica content compared to COK208 and is situated on the East Dyke, agrees with that of the breccia rocks on the East Dyke. This composition supports the suggestion that xenolith COK175 is gneiss.

The high Na_2O concentration from Na-bearing minerals in the phonolites (Table 5.1) and their assigned plotted position on the TAS diagram (Fig. 5.2) are evidence for these rocks not being genetically related to any rock component in the breccia rocks, although these rocks are situated along the East Dyke. These Na-bearing minerals were identified by microprobe analysis.

Trace elements

Hydrothermal alteration affects fluid-mobile elements hosted in feldspar minerals (e.g. Rb and Ba) more than elements of high charge density present in less soluble mineral phases (e.g. Zr, Nb and REE). The compositional scatter (Fig. 5.5) of Rb and Ba versus silica of the breccia rocks brings evidence for the breccia rocks with high Rb and Ba concentrations to have been altered. Sample COK198 for example, which contains abundant feldspar minerals based on petrography, has significantly higher Ba concentrations than other breccia rocks due to alteration.

The distribution of Sr element (Fig. 5.5) in the breccia rocks is partly controlled by the extent to which Sr^{2+} substitutes Ca^{2+} in the calcium-bearing minerals (i.e. plagioclase feldspar) and the degree to which the potassium feldspar captured Sr^{2+} in the place of K^+ ions. The Sr concentration in the breccia rocks with a basaltic texture (COK172 and COK195) is significantly higher than in the average breccia rock, which is consistent with the observed abundance of plagioclase.

The siderophile trace element data distinguish two groups of breccia rocks (Fig. 5.5). These data bring support for at least two types of magma sources that produced the main rock constituents in the breccia rocks. The first group of breccia rocks with high Cr and Ni concentrations have a main rock component that must have originated from a primitive type of magma. The second group of breccia rocks with low Cr and Ni concentrations must contain a main rock component that originated from a more evolved and more differentiated type of magma than that of the first group of breccia rocks.

The distribution of the Cr and Ni data of the breccia rocks is systematic. The breccia rocks with high Cr and Ni concentrations (Fig. 5.5) are situated on the West Dyke, whereas the breccia rocks with low Cr and Ni are situated East Dyke. These results bring evidence for the breccia rocks to be compositionally different on each dyke of the Breccia Outcrop. A mantle-derived type of magma could have produced the rocks on the West Dyke, whereas a crustal-related type of magma could have produced the rocks on the East Dyke.

There is an apparent division of the breccia rocks into two groups on the Zr and Nb versus silica plots (Fig. 5.5). This confirms prior suggestions made in this work that these rocks are dominated by at least two rock components. The first group of breccia rocks, which plots along the trend on which rocks have the lowest concentrations in Nb and Zr, contains breccia rocks with a predominant mafic rock composition. The second group of breccia rocks, which plots on the trend on which the breccia rocks have the highest concentrations in Nb and Zr, is proposed to contain breccia rocks with a predominant bostonite composition, although this group consists of rocks that have lower concentrations than those of the bostonites. These lower concentrations than those of the bostonites are explained by the composition of groundmass (B) xenoliths. These black xenoliths, which are thought to be a mixture between bostonite and basalt, might have a composition closer to that of basalt than bostonite and this was reflected in the whole-rock geochemistry.

The division in Nb and Zr data (Fig. 5.5) is linked to the spatial distribution of the breccia rocks. The breccia rocks with a predominant mafic rock composition are situated on the West Dyke of the Breccia Outcrop, while the breccia rocks with a main bostonite composition are situated on the East Dyke. This relationship suggests that the two dykes are made of breccia rocks that have main rock constituents that are compositionally different. The West Dyke consists of breccia rocks with a main mafic rock component, while the East Dyke contains breccia rocks with a predominant bostonite constituent.

The spread of the breccia rock data on incompatible trace element plots of Zr, Nb, and Y (Fig. 5.6) shows these rocks are compositionally variable and made of more than one rock constituent. Nevertheless, although the data of the breccia rocks are significantly more spread out than those of the alkaline and tholeiitic mafic rocks, it is worth noting that there is a greater number of breccia rocks that plot close to the alkaline mafic dykes than the tholeiitic mafic dykes, especially on the Y/Nb plot (Fig. 5.6.a). This evidence reflects that one of the rock constituents that make up the breccia rocks is alkaline rather than tholeiitic.

The Ba concentration difference (Fig. 5.5) between sample COK191 and COK192 could be interpreted two ways. The first suggestion is that the absence of Ba concentration in COK192 is an erroneous result. The second suggestion is that sample COK191 was the only sample of the two to have been hydrothermally altered. The first interpretation is the most appealing because the Phonolite Plug is <2 m in diameter and, thus, if alteration caused the Ba concentration difference in the two samples, then the alteration would have equally affected the phonolite samples.

Rare earth elements

The REE patterns of the breccia rocks provide further evidence for the breccia rocks to be made of three different rock types (Fig. 6.1). The negative Eu anomaly shown by the REE pattern 1 of a first group of breccia rocks indicates that this group of breccia rocks has a predominant bostonite component (Fig. 5.8.a). The absence of a negative Eu anomaly shown by the REE pattern 2 of a second group of breccia rocks reflects that this second group of breccia rocks has a main alkaline mafic rock constituent (Fig. 5.8.b). The REE pattern 3 of COK175, which is enriched in HREE, shows a similar profile to that of the Koegel Fontein gneisses (Curtis et al., 2011), although with lower abundances. This REE pattern 3 confirms that COK175 contains more gneiss xenoliths than the other breccia rocks.

The breccia rocks without a Eu anomaly are located on the West Dyke, whereas the breccia rocks with a negative Eu anomaly are situated on the East Dyke. This relationship suggests that the two dykes are made of breccia rocks with main rock constituents that are compositionally different. The West Dyke consists of breccia rocks mostly made of alkaline mafic rocks, whereas the East Dyke contains breccia rocks mainly made of bostonites.

Although the REE patterns 1, 2, and 3 have respectively the same shape as the REE patterns of the bostonite, alkaline mafic rocks, and gneisses, the REE patterns of the breccia rocks are uniformly below those of the bostonite, alkaline mafic rocks, and gneisses. This is suggested to result from dilution by REE-poor rock or loss of REE via the fluid. The fluids that ^{18}O-depleted the breccia rocks could have diluted these rocks and remobilized some of the minerals carrying the REE, i.e. alkali feldspar.

The LREE enrichment of the phonolite compared to the LREE abundances of the breccia rocks reflects a compositional difference between these two rock types (Fig. 6.1). A mineral phase rich in LREE (i.e. nepheline) could have been the result of the LREE enrichment in the phonolite. This mineral is identified in the mineral chemistry section.

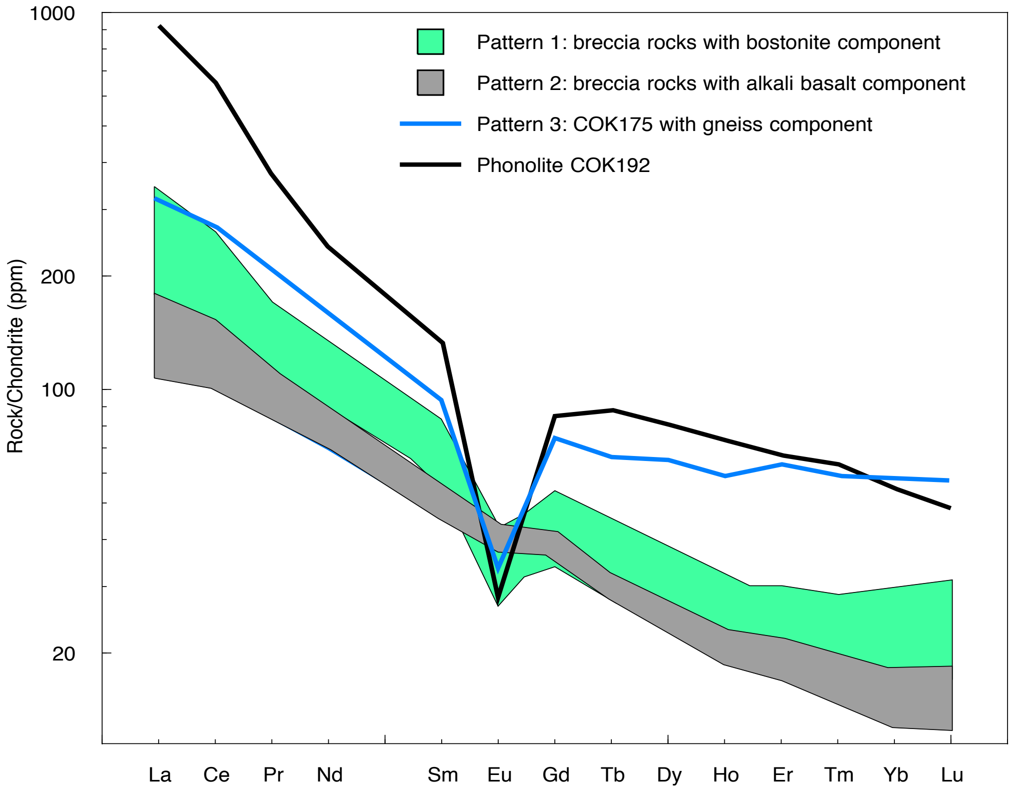

Fig. 6.1 Chondrite-normalised REE plot (Sun and McDonough, 1989) showing the REE pattern of breccia rocks with a main bostonite component, alkaline mafic rock component, or gneiss component and the REE pattern of phonolite COK192.

Composition of the West Dyke and East Dyke

It has been suggested above that there are three main rock constituents in the breccia rocks. The first and second rock components are bostonite and alkali basalt based on petrography, whole-rock compositions, REE patterns, and the abundance of bostonite and basalt dykes in the Koegel Fontein complex (de Beer et al., 2002). The bostonite and alkali basalt components are found in breccia rocks situated respectively on the East Dyke and West Dyke of the Breccia Outcrop. These results are used to suggest that the East Dyke and West Dyke used to be respectively a bostonite and alkali basalt dyke (Fig. 6.2) before the emplacement of the breccia (see 6.4 Emplacement models). The third rock constituent is made of fragments of the roof pendant gneiss (~country rock gneiss), which is found in breccia rocks on either dyke of the Breccia Outcrop.

The second xenolith type, which is the black xenoliths found in most of the breccia rocks, are not thought to be a fourth rock type but fragments of basalt and bostonite. These black xenoliths bring evidence for the basalt and the bostonite rocks to predate the eruption that formed the breccia rocks. It is difficult to say if these black xenoliths are only basalt or only bostonite or a mixture of both because these xenoliths are often too fine-grained to identify any constituents in thin section petrography. However, based on the mafic composition of xenolith COK208 and sample COK205-B and the more mafic than felsic composition of most of the breccia rocks on the East Dyke, the black xenoliths are proposed to contain more basalt than bostonite.

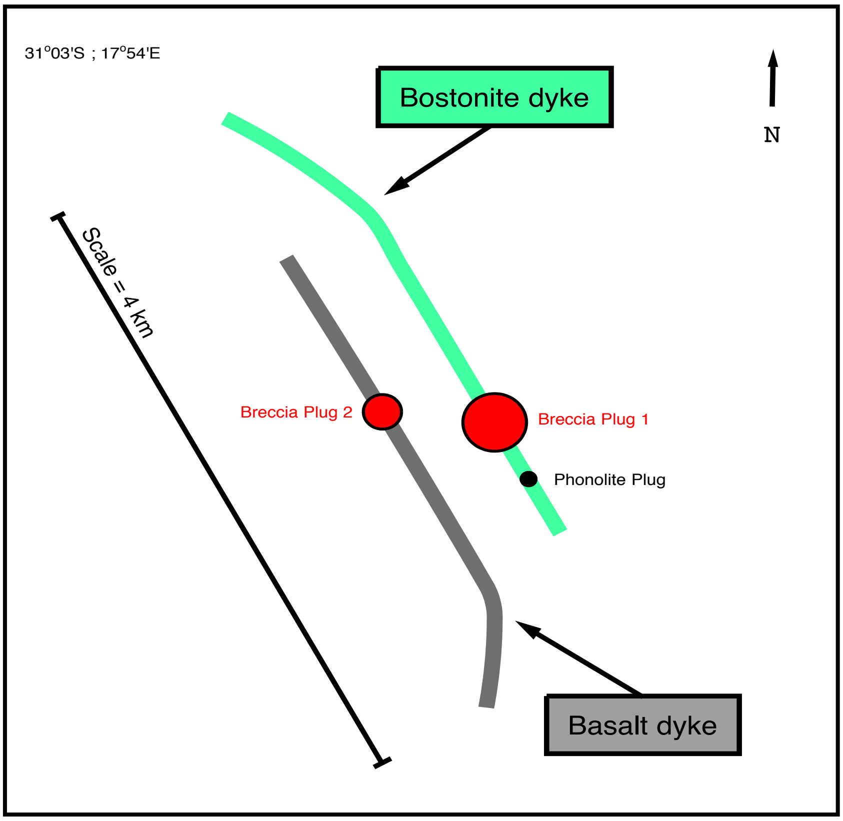

Fig. 6.2 Summarising sketch map describing the composition and shape of the Breccia Outcrop. The representation is not to scale.

6.2.2 Mineral chemistry of the phonolites and xenolith COK166

The microprobe results of grains in the groundmass of COK191 and COK192 indicate that the phonolites contain alkali feldspar and nepheline. The presence of nepheline brings support to silica-undersaturated rocks occurring in the complex, which are the first to have been recognised so far. The existence of nepheline in the phonolite and the absence of any such mineral in the breccia rocks bring evidence to the phonolite being unrelated to the breccia rocks.

The microprobe data of the bottle green grains in xenolith COK166 indicate that these grains are epidote. The green grains are suggested to reflect amygdales or fractures that have been filled with this alteration mineral. The presence of epidote supports the idea that fluid interaction in the breccia rocks was above 300°C (Deer et al., 1992).

6.3 Isotope composition of the breccia rock

6.3.1 Stable isotopes

An igneous rock has about 50 wt % oxygen and 0.18 wt % hydrogen per wt % water (Sheppard, 1986; Taylor and Sheppard, 1986). This means that O-isotopes are not susceptible to change whereas H-isotopes can change as a result of fairly limited interaction with external fluid.

Oxygen isotopes in the breccia rocks

The rocks analysed in this study, excepting the phonolites, have $\delta^{18}O$ values below that of the mid-ocean ridge basalt (MORB) value (+5.7‰) (e.g. Ito et al., 1987). Two breccia rocks (COK168 and COK170) (Fig 6.3.a) have lower $\delta^{18}O$ values than those of all the Koegel Fontein igneous rocks (Fig. 6.3.b) and country rock gneiss (Fig. 6.3.c) taken from Curtis et al. (2013). The low $\delta^{18}O$ values of the breccia rocks imply that the fluids that altered the Breccia Outcrop had some of the lowest $\delta^{18}O$ values of all the fluids that ^{18}O-depleted the complex.

The mineral separates, which are quartz and feldspar minerals from the gneiss xenoliths that were picked out of the rock powders, and the gneiss xenoliths have some of the lowest $\delta^{18}O$ values of all rocks in the complex (Fig. 6.3). One sample consisting of mineral separates from COK165 gives the lowest $\delta^{18}O$ values in the entire complex (-5.6‰, Table 5.6). The $\delta^{18}O$ values of the mineral separates and gneiss xenoliths are evidence that high-temperature fluids with low $\delta^{18}O$ values interacted with the country rock gneiss.

Unlike the breccia rocks, the phonolite rocks have normal $\delta^{18}O$ values around +8.0‰, which is above the MORB value of +5.7‰ (e.g. Ito et al., 1987). This difference in oxygen isotope composition between the breccia rocks and phonolites indicates that the high-temperature fluids that ^{18}O-depleted the Breccia Outcrop did not interact with the Phonolite Plug, possibly because the intrusion of the Phonolite Plug post-dated the intrusion that formed the Breccia Outcrop. This suggestion is supported by the absence of phonolite xenoliths in the breccia rocks.

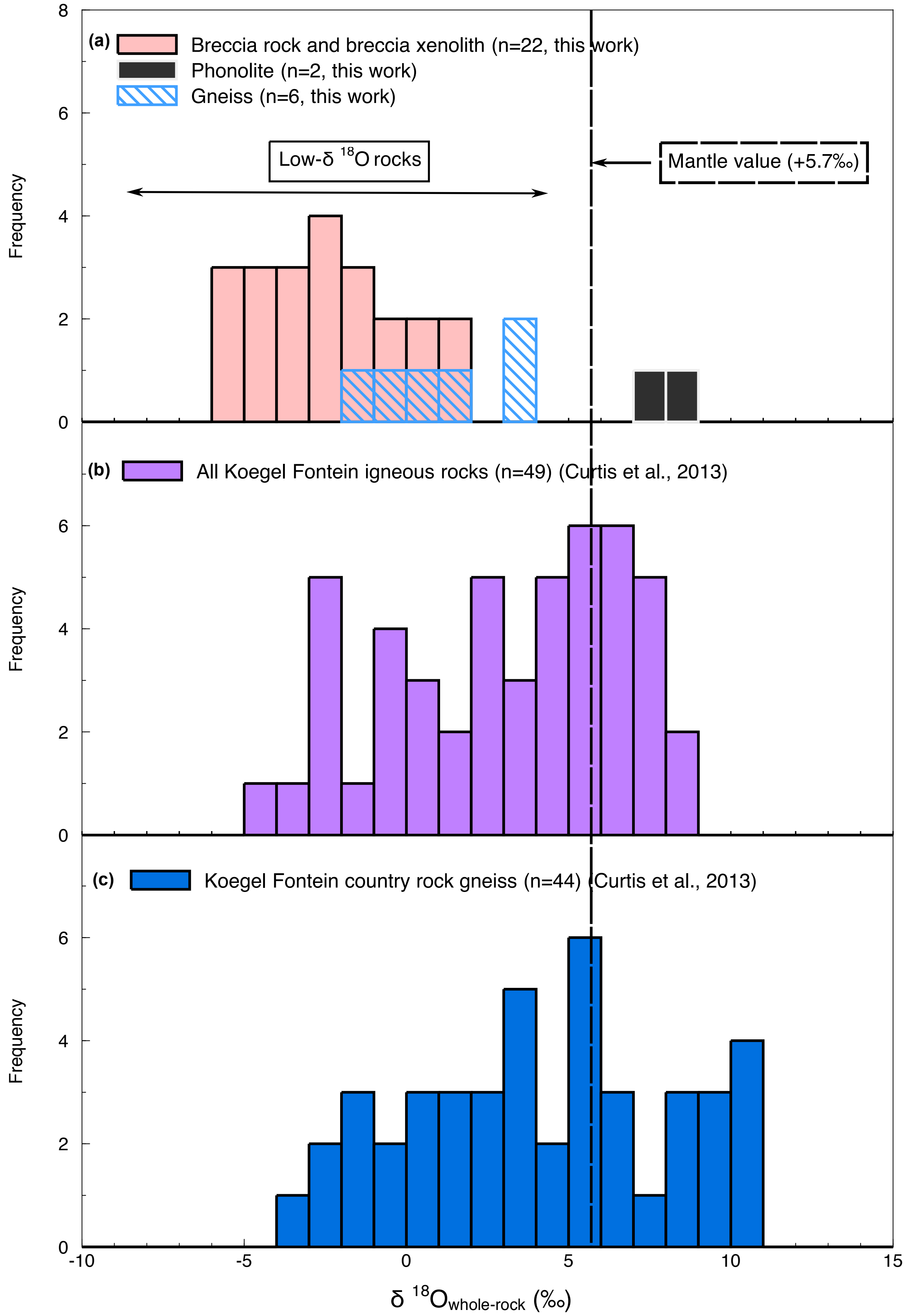

Fig. 6.3 Histograms summarising the oxygen isotope data. Data of **(a)** the breccia rocks and breccia xenoliths, phonolites, and gneisses (this work), **(b)** all the Koegel Fontein igneous rocks (Curtis et al., 2013), and **(c)** the Koegel Fontein gneisses (Curtis et al., 2013).

Variation of $\delta^{18}O$ values along the Breccia Outcrop

Breccia rocks with the lowest $\delta^{18}O$ values are found on both the West and East Dykes. This implies that the breccia rocks did not interact with the fluid systematically along the Breccia Outcrop. The West and East Dykes may well have interacted with one single fluid and underwent different degrees of fluid-rock interaction. These two dykes could also have interacted with fluids with $\delta^{18}O$ values that varied with time and/or position.

Isotopic δD and $\delta^{18}O$ values of the meteoric fluid

The overall ^{18}O-depletion in the Koegel Fontein rocks is considered by Curtis et al. (2013) to result from exchange between rock and hydrothermal fluid. The low $\delta^{18}O$ values of the igneous rocks were suggested to come from interaction with ^{18}O-depleted metamorphic fluids dehydrated from the country rock, which was previously altered by meteoric fluids with low $\delta^{18}O$ values (Curtis et al., 2013) (see Chapter 2.4). Based on the isotope composition of quartz veins and hydrous minerals, Curtis et al. (2013) estimated that the fluid had $\delta^{18}O$ and δD values of -9.9‰ and -69‰, respectively.

The whole-rock δD and $\delta^{18}O$ values of the breccia rocks plot right of the global meteoric water line (MWL; Craig, 1961), which is the linear correlation between the δD and $\delta^{18}O$ values in natural terrestrial water expressed as a worldwide average. Assuming the alteration in the complex was meteoric in origin (Curtis et al., 2013), the isotopic δD value of the meteoric fluid should plot along the MWL before the onset of the fluid-rock exchange of the breccia rocks. The calculated isotopic δD value of the meteoric fluid could then be extrapolated onto the whole-rock $\delta^{18}O$ value axis to obtain the isotopic $\delta^{18}O$ value this fluid.

The fractionation factor used for the estimation of the isotopic $\delta^{18}O$ value of the meteoric fluid is between ambient meteoric water and epidote (Chacko et al., 1999). Epidote is selected over biotite for the following calculations because this mineral has altered to some degree all the types of matrix in the breccia rocks. Since epidote reflects a fluid temperature between 300°C and 400°C, the isotopic $\delta^{18}O$ value of the meteoric fluid is calculated for both temperatures.

The isotopic δD value of the meteoric fluid calculated from the average δD value of the five breccia rocks is -85‰ and -77‰, assuming that the O isotope fractionation factor between epidote and ambient meteoric water ($\delta^{18}O_{epidote\text{-}water}$) is -34‰ (300°C) and -42‰ (400°C), respectively (Chacko et al., 1999) (Fig. 6.4). By extrapolation from the global MWL onto the O isotope axis, the measured isotopic $\delta^{18}O$ value of the meteoric fluid is approximately -11.3‰ using $\delta^{18}O_{epidote\text{-}water}$ = -34‰ and -10.2‰ using $\delta^{18}O_{epidote\text{-}water}$ = -42‰ (average $\delta^{18}O$ value of the meteoric fluid = -10.8‰). These measured $\delta^{18}O$ values are consistent with the

$\delta^{18}O$ value for the meteoric fluid (-9.9‰, n = 67) calculated by Curtis et al. (2013). This consistency brings evidence for the breccia rocks to have interacted with metamorphic fluids at the same time as the rest of the complex, when a Cretaceous mantle plume heated the base of the crust (e.g. O'Connor and Duncan, 1990; Ewart et al., 1998a,b; Trumbull et al., 2003).

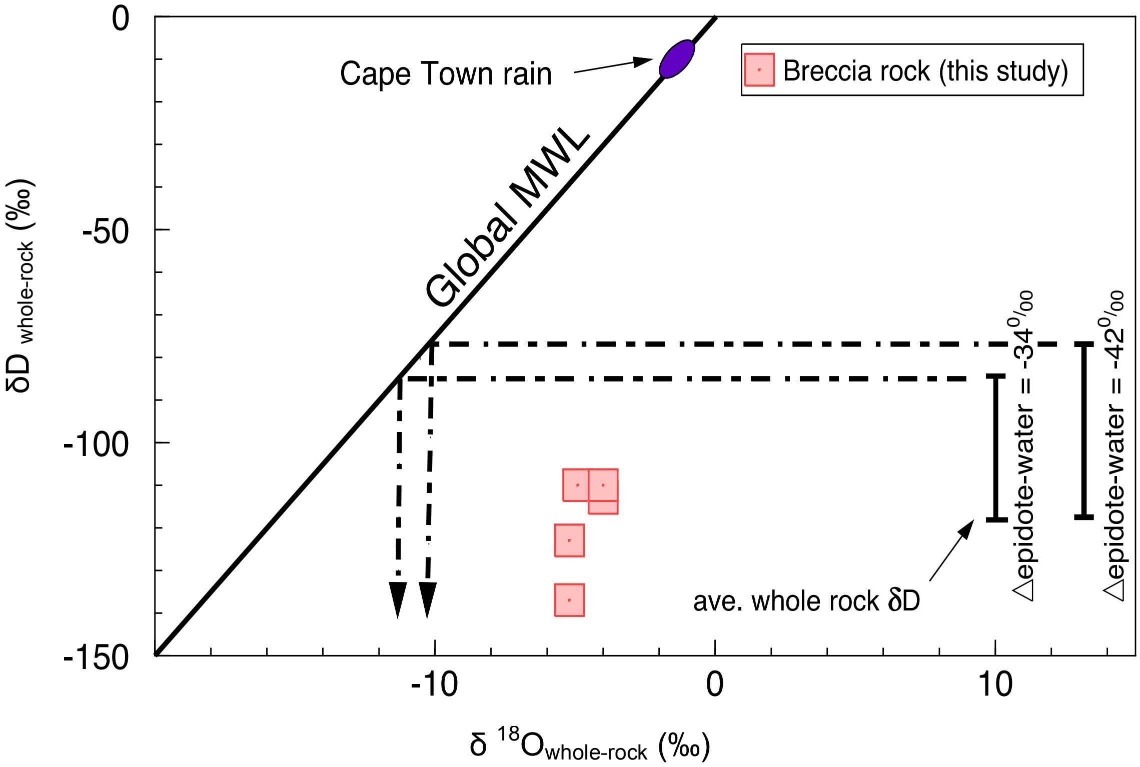

Fig. 6.4 Variation of the δD values versus the $\delta^{18}O$ values for five breccia rocks. The Cape Town rainwater (Harris et al., 2010) is used for reference of present day meteoric water in Southern Africa. The average whole-rock δD value of the five breccia rocks is -119‰. Assuming $\delta^{18}O_{epidote\text{-}water}$ = -34‰ (300°C) and $\delta^{18}O_{epidote\text{-}water}$ = -42‰ (400°C) (Chacko et al., 1999), the isotopic δD values of the meteoric fluid are respectively -85‰ and -77‰. These δD values correspond respectively to an isotopic $\delta^{18}O$ value for the meteoric fluid of approximately -11.3‰ and -10.2‰ (average = -10.8‰). These $\delta^{18}O$ values are >8‰ lower than that of Cape Town rainfall.

Water content and LOI values

The LOI is a proxy of the amount of carbonate and water present in a sample and hence the degree of alteration in the breccia rocks. The low LOI values of the breccia rocks (average <1.0 wt %) are consistent with a low water content. These LOI values agree with the water content obtained by H-isotope procedure (H_2O^+). The LOI and H_2O^+ data for COK168, COK174, COK170, and COK175 only show small differences (<0.6 wt %). These differences are suggested to represent small quantities of carbonates and/or small errors due to the high iron concentrations in the samples. Any Fe^{2+} in iron-rich rocks is converted to Fe^{3+} during the LOI determination, which adds weight to the sample.

The low quantities of water present in the rock and the low % hydrous minerals imply that the alteration minerals in these rocks also contain small quantities of water. The evidence of more epidote and biotite in the breccia rocks than chlorite confirms these results. Epidote and biotite contain respectively ~1.7 wt % H_2O^+ and ~3.6 wt % H_2O^+, whereas chlorite has ~12.1 wt % H_2O^+ (Deer et al., 1992).

The low LOI values and H_2O^+ content and the predominance of epidote and biotite in the breccia rocks indicate that the fluid that interacted with these rocks is not low-temperature groundwater but a hydrothermal fluid with a temperature >300°C. The temperature of this fluid is evidence that the breccia rocks underwent greenschist to amphibolite metamorphism.

6.3.2 Radiogenic isotopes

The Sr and Nd isotope data are compared with stable isotope data and whole-rock compositions to assess potential magmatic sources, better understand the fluid-rock interaction, and calculate the age of the breccia rocks and gneisses.

Strontium and neodymium isotopes

The resistance of Nd isotope ratios to change as a result of hydrothermal alteration in comparison to initial Sr isotope ratios makes Nd isotopes more suitable for recognising magma sources (e.g. Curtis et al., 2011). The overall range in εNd values of the breccia rocks brings evidence for these rocks to comprise variable quantities and types of rock fragments. This line of evidence is consistent with the observations of black and gneiss xenoliths in the breccia rocks based on petrography.

The breccia rocks have $^{87}Sr/^{86}Sr_{initial}$ ratios and εNd values that spread across from the Etendeka basalt field (Ewart et al., 1998a) to the Namaqua crust field (Reid, 1997, 1999) (Fig. 6.5). Two rock constituents of the breccia rocks can be distinguished from the Nd and initial Sr isotope data of four breccia rocks. The first rock component is mantle-derived and is suggest to be basalt. The basalt constituent is reflected by the radiogenic isotope data of COK172 and COK195, which have high εNd values, low initial Sr isotope ratios, plot close to the Bulk Earth, and overlap the Etendeka basalt field (Fig. 6.5).

The second rock component comes from a silica-rich crustal source and is suggested to be gneiss. This gneiss rock component is best reflected by the radiogenic isotope data of two breccia rocks (COK175 and COK205-A), which have the lowest εNd values of all the breccia rocks and plot the closest to the the Namaqua crust field (Fig. 6.5).

The rocks in between the breccia rocks with a prevalent basalt or gneiss component show a large compositional range (Fig. 6.5). This compositional variation supports the suggestion that the breccia rocks are made of several and different rock constituents, some of which are mantle-derived and the others from a silica-rich crustal source.

The complex has been subjected to strong alteration (Curtis et al., 2011) that could have lead ^{87}Sr to migrate into the system. The wide range in Sr initial ratios of the breccia rocks at near-constant Nd values (Fig. 6.5) is thus attributed to fluid interaction, which is consistent with the abundance of epidote and biotite in these rocks and the pervasive clouding of feldspar.

The radiogenic isotope data of the six gneisses are consistent with that of the Namaqua crust (Fig. 6.5). The phonolite rock is the only sample that plots nowhere near or directly in between the Etendeka basalt and Namaqua crust fields. However, this phonolite has the highest ^{87}Rb/^{86}Sr ratio (^{87}Rb/^{86}Sr = 19, whereas average breccia rocks: ^{87}Rb/^{86}Sr = 2) of all the analysed rocks. This high ratio must have imparted a significant error on the initial ratio.

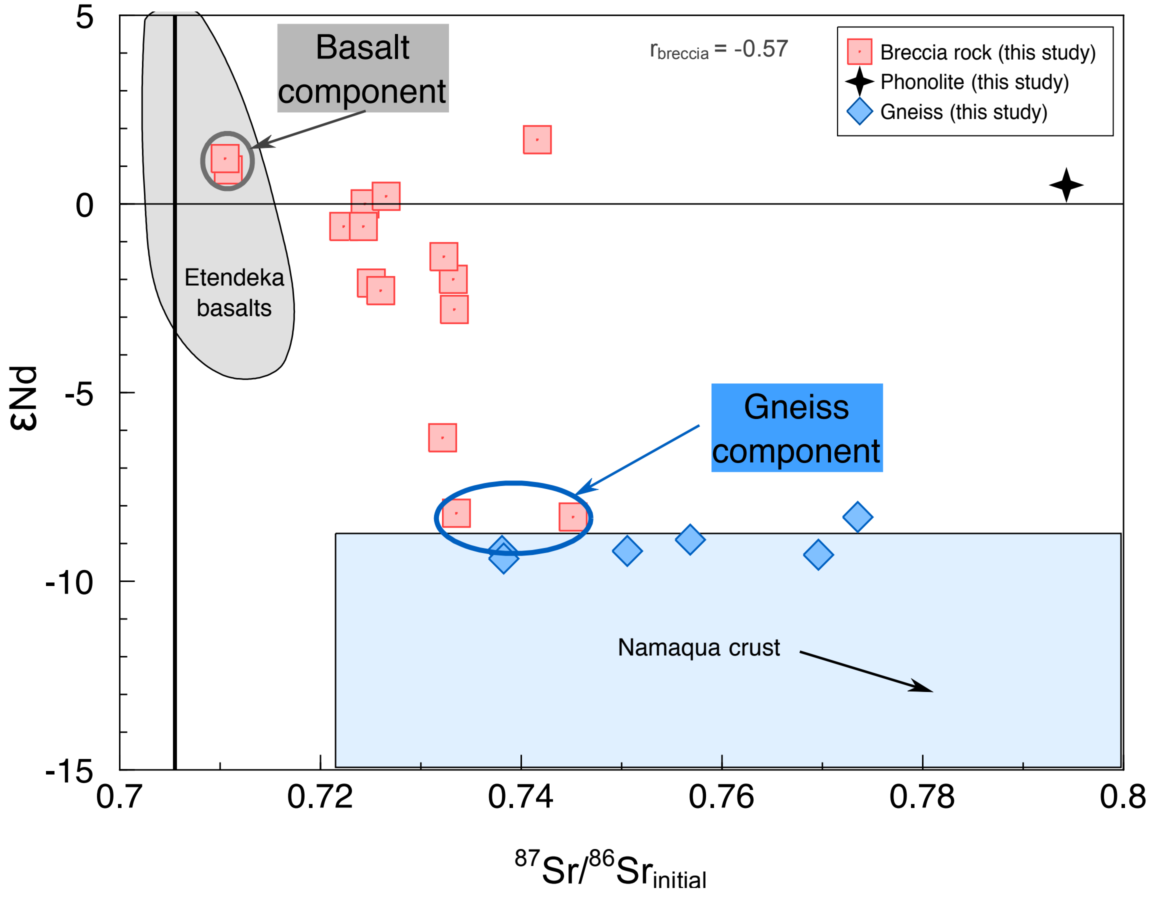

Fig. 6.5 Initial Sr isotope ratios and initial Nd epsilon values for 15 breccia rocks, 1 phonolite rock, and 6 gneisses, all three of which are age-corrected to 135 Ma. The measured data for the Namaqua crust is from Reid (1979, 1999). The field for the Etendeka basalts is from Ewart et al. (1998a,b). $r_{breccia}$ is the coefficient of correlation for the 15 breccia rocks.

Variation of the radiogenic isotope data along the Breccia Outcrop

The variation of the εNd values (Table 5.7) along the Breccia Outcrop is not systematic. This depends on the Nd concentration in each rock and the rock components in the breccia rocks. The εNd values of the breccia rocks with the most fragments of gneiss, which have lower εNd values than the alkali basalts and bostonites, are lower than the εNd values of the breccia rocks with the most fragments of basalt and bostonite, which have higher εNd values than the gneiss.

There is no systematic spatial variation in $^{87}Sr/^{86}Sr_{initial}$ ratios of the breccia rocks. For example, COK170 and COK195, which respectively have the highest and lowest $^{87}Sr/^{86}Sr_{initial}$ ratios (Table 5.7), are both situated on the West Dyke. There must have been variable fluid-rock interaction during ascent and emplacement of the breccia to explain this. The samples that interacted the least with fluids (basaltic and trachytic groundmass textures) have the lowest $^{87}Sr/^{86}Sr_{initial}$ ratios, whereas those that interacted the most with the fluid (COK170) have the highest $^{87}Sr/^{86}Sr_{initial}$ ratios.

Oxygen and major element composition versus radiogenic isotopes

The poor correlation of Sr element data with $\delta^{18}O$ values (Fig. 5.14.a) of the breccia rocks is consistent with the greater mobility of Sr and Rb versus Nd and Sm during fluid-rock interaction. This suggestion is supported by the absence of a relationship between εNd and $\delta^{18}O$ values (Fig. 5.14.b).

The major and trace element compositions versus the radiogenic isotope data show several correlations that indicate that the breccia rocks comprise mantle-derived and/or silica-rich crustal components. The group of breccia rocks with the highest Sr concentration for a given $^{87}Sr/^{86}Sr_{initial}$ or $^{87}Rb/^{86}Sr$ ratio reflect a crustal contribution, whereas the group with the lowest Sr concentration for the same given $^{87}Sr/^{86}Sr_{initial}$ or $^{87}Rb/^{86}Sr$ ratio indicate a mantle-derived source (Fig. 5.15 and Fig. 5.16).

The strong positive relationship ($r_{breccia}$ = 0.72) between the K_2O concentrations and the $^{87}Sr/^{86}Sr_{initial}$ ratios (Fig. 5.15) of the breccia rocks reflects variable amounts of gneiss xenoliths in these rocks. Breccia rocks with a high concentration in K_2O contain more gneiss xenoliths (high Sr-isotope ratios) than breccia rocks with low K_2O concentrations (low Sr-isotope ratios).

The strongest relationship ($r_{breccia}$ = 0.86) between major or trace element data and radiogenic isotope ratios is between P_2O_5 concentrations and $^{143}Nd/^{144}Nd_{initial}$ ratios (Fig. 5.17). This strong positive correlation is indicative of the abundance of P_2O_5 in the magma that produced the breccia rocks. The P_2O_5 concentrations are the lowest in the breccia rocks from a mantle-derived type of magma and the highest in the breccia rocks from a differentiated type of magma.

Rubidium-strontium "age"

The measured Sr isotope ratios ($^{87}Sr/^{86}Sr_{measured}$) and rubidium-strontium ratios ($^{87}Rb/^{86}Sr$) of fifteen breccia rocks are strongly correlated ($r_{breccia}$ = 0.89). The lines of best fit on the isochron diagram suggest an age of 567 Ma (Fig. 6.6.a). The significance of this age is uncertain despite a calculated Pan African age. By virtue of the xenolith that the Breccia Outcrop contains, the outcrop must be Cretaceous in age (Koegel Fontein complex, ~135 Ma). The approximate calculated Pan African age is thought to result from the Rb-Sr system, which was not reset by the fluid-rock interaction that formed the breccia rocks.

The apparent calculated Pan African age of the breccia rocks most likely reflects the age of the gneiss xenoliths in the breccia rocks. Assuming so, this age (~567 Ma) is significantly younger than the age of the Namaqua country rock gneiss (1200-1000 Ma). The young age of the gneiss xenoliths could be explained by crustal reworking during the Pan African orogeny, which could have reset the age of the gneiss xenoliths to the Pan African (~500 Ma). This statement, however, is speculative and need further investigation.

The $^{87}Sr/^{86}Sr_{measured}$ and $^{87}Rb/^{86}Sr$ ratios of the 6 gneisses are well correlated ($r_{breccia}$ = 0.90). The age calculation for these gneisses is approximately ~666 Ma (Fig. 6.6.b), which is significantly younger than that of the Mesoproterozoic Namaqua gneiss (1000-1200 Ma). This age difference is attributed to the homogeneity of the gneiss xenoliths, which might be more heterogeneous than suggested (e.g. de Beer et al., 2002; Curtis et al., 2011).

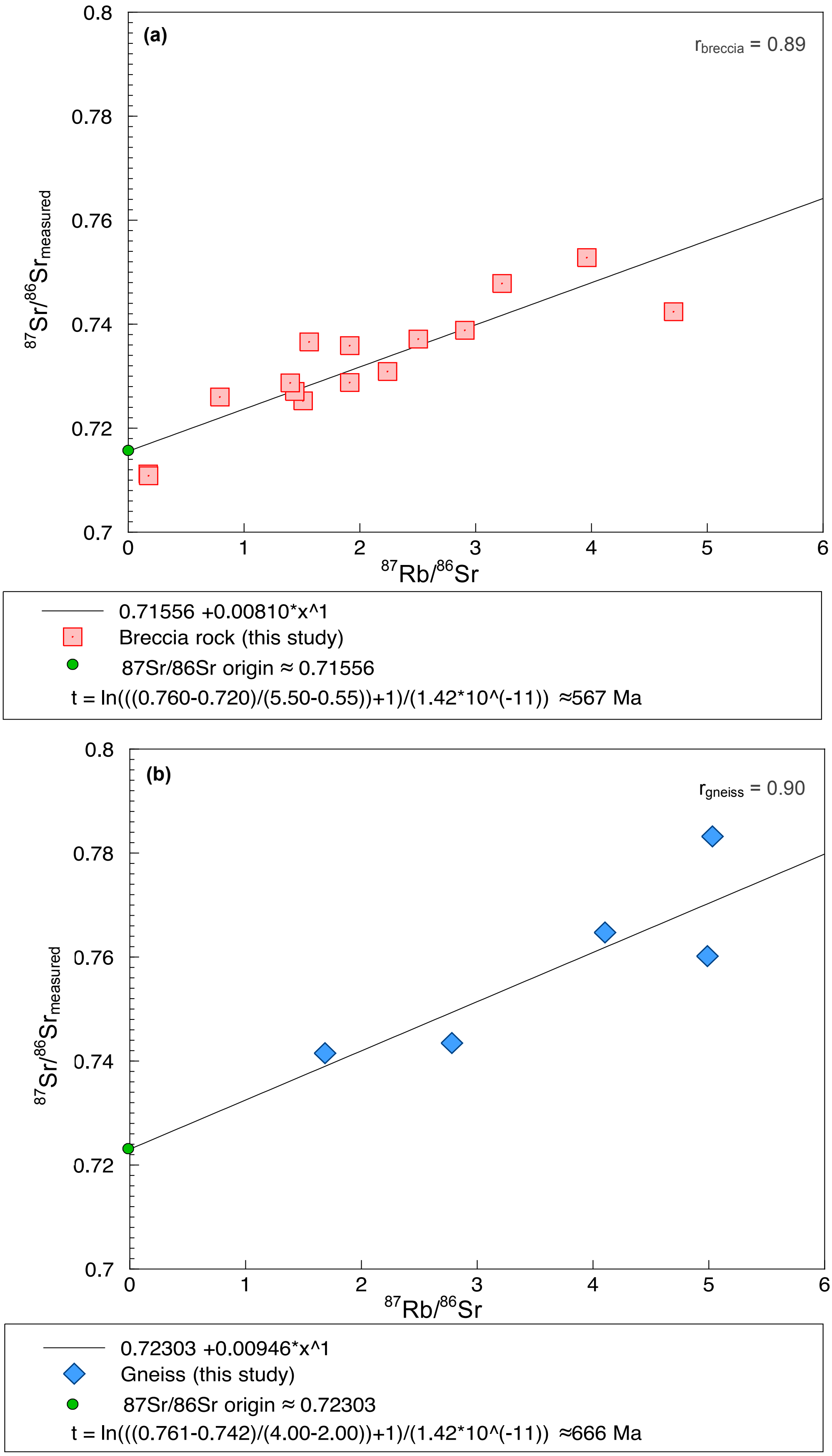

Fig. 6.6 Rubidium-strontium isochron for **(a)** 15 breccia rocks and **(b)** 6 gneisses. The regression equation, age calculation (t), and $^{87}Sr/^{86}Sr_{measured}$ value at the origin for the 15 breccia rocks and the 6 gneisses are included. $r_{breccia}$ is the Pearson product-moment correlation coefficient of the 15 breccia rocks and r_{gneiss} of the 6 gneisses.

6.4 Emplacement models

6.4.1 Emplacement model for the breccia rocks

Three emplacement models are proposed for the emplacement of the breccia rocks. In the first model, basalt and bostonite magmas both intrude through the crust at the same time, tearing off gneiss xenoliths from the wall rock. In this model, the bostonite and basalt intrusions make use of two separate fracture lines, breaking through the Breccia Plug 1 and the Breccia Plug 2, respectively. These intrusions then extend along two sub-parallel planes of weakness of the crust and form the Breccia Outcrop.

In the second model, a bostonite magma intrudes a pre-existing basalt dyke, tearing off gneiss and black xenoliths from the wall rock. In this model, the basalt magma intrudes first, breaking through the Breccia Plug 2 and extending along one plane of weakness of the crust. The bostonite intrusion carrying gneiss and black rock fragments only comes later in time, breaking through the Breccia Plug 1 and extending along a second plane of weakness of the crust.

In the third model, a fluidised mass intrudes two pre-existing dykes. In this model, the fluidised mass represents a volatile-rich type of fluidised material that incorporated gneiss and black rock fragments on its way up to the surface of the crust. In this third model, a basalt magma intrudes first and breaks through a plane of weakness of the crust. In second, a bostonite magma migrates upwards through the same pathway the basalt intrusion used. Near the surface of the crust, the bostonite intrusion separates from the main fracture line the basalt intruded through and breaks through a second plane of weakness sub-parallel to the basalt dyke. After both dykes are emplaced, a fluidised mass migrates upwards through the same crustal weakness the basalt and bostonite intrusions used, incorporating fragments of rock on its way up to the surface of the crust. This xenolith- and fluid-rich material intrudes through the Breccia Plug 1 on the bostonite dyke and the Breccia Plug 2 on the basalt dyke before extending along the two dykes.

Favoured model

The first model cannot explain the black xenoliths observed in the breccia rocks. The second model is more likely than the first model based on the succession of events described in the region, which suggests that basalt dykes were emplaced before the bostonite dykes (de Beer and Armstrong, 1998). The second model, however, does not explain the black xenoliths in the rocks along the basalt dyke or the epidote-rich green rock supporting black and gneiss xenoliths. These first two models are therefore not favoured.

The third model is the preferred one for the interpretation of the formation of the Breccia Outcrop. This model is favoured based on the suggested succession of events in the region (de Beer and Armstrong, 1998), the brecciation of the rocks, the shape and size distribution of the xenoliths, the mixing of lithologies in the breccia rocks, the flow texture in quartz xenocrysts, the black and gneiss xenoliths in the epidote-rich green rock, and the predominance of epidote in the breccia rocks.

The sequence of events can explain the more mafic than expected composition of the breccia rocks found on the bostonite dyke. If the bostonite magma intruded after the basalt dyke through the same fracture line, it could have incorporated a small amount of basalt rock on its way up towards the surface of the crust.

The intense brecciation of some breccia rocks and the mixing of rock types (basalt, bostonite, and gneiss) reflect a possible explosive type of eruption, which is caused by volatile-rich fluidsed masses (e.g. Weisheit et al., 2013). The shape and size distribution of the xenoliths are indicative of transport by turbulent fluidisation (McCallum, 1985; Olivier et al., 2006a).

The flow texture in quartz xenocrysts, the black and gneiss xenoliths in the epidote-rich green rock, and the intense alteration of the black xenoliths all support that a hydrothermal fluidised mass intruded through the pre-existing basalt and bostonite dykes. The abundance of epidote in most of the breccia rocks also brings evidence for a hydrothermal fluid to have altered the pre-existing rocks from both dykes.

6.4.2 Emplacement model for the phonolites

Three emplacement models for the phonolites are proposed. These suggested models are constructed using the third emplacement model for breccia rocks, which is the favoured model. In the first model, a phonolite magma intrudes the country rock before the Koegel Fontein complex was emplaced. In the Cretaceous, the bostonite magma intrudes through the same fracture line the phonolite magma used to intrude.

In the second model, the phonolite and bostonite magmas intrude at the same time through the pre-existing basalt dyke. In this model, the phonolite and bostonite magmas are genetically related.

In the third model, the phonolite magma intrudes after the bostonite dyke is emplaced. The phonolite magma makes use of the same fracture line used by the bostonite intrusion. In this model, the phonolite intrusion is not related to the Koegel Fontein complex.

Favoured model

The first model for the emplacement of the Phonolite Plug is not favoured. This model cannot explain the high O isotope ratios of the phonolite rocks (average= +8‰). If the Phonolite Plug was emplaced before the bostonite dyke, the plug should also have undergone high-temperature fluid-rock interaction and therefore have low $\delta^{18}O$ values. The first model cannot also explain the absence of phonolite xenoliths in the breccia rocks. If the Breccia Outcrop was emplaced after the Phonolite Plug, the fluidised mass that formed the Breccia Outcrop should have incorporated fragments of phonolite rock and thus some breccia rocks should contain phonolite xenoliths. This second argument is, however, treated carefully because the xenoliths in the breccia rocks are often strongly altered and hand-specimens and thin sections described petrographically cannot represent the whole outcrop they were sampled at. Further work on xenoliths classification and description would be useful to confirm this argument.

The second model is not the most likely model. The significant difference in O isotope values between the breccia rocks and the phonolites suggests that the Phonolite Plug could not have formed at the same time as the Breccia Outcrop. If the Phonolite Plug and the Breccia Outcrop formed at the same time, the high temperature fluidised mass should have altered and ^{18}O-depleted both rock types equally.

The third model is the preferred model. Evidence for this model is the normal $\delta^{18}O$ values of the phonolite rocks and the absence of phonolite xenoliths in the breccia rocks. The normal $\delta^{18}O$ values of the phonolites support the suggestion that the low-$\delta^{18}O$ fluids that altered the breccia rocks had already been dehydrated from the country rock when the Phonolite Plug formed. The absence of phonolite xenoliths is consistent with the Phonolite Plug post-dating the fluidised mass that migrated upwards through the basalt and bostonite dykes.

6.5 Example of a similar breccia intrusion

Hydrothermal breccias are uncommon rocks. These rocks form from variable processes such as phreato-magmatic explosions or mud diapir (Thorkelson et al., 2001), overpressure and volatile release in the mid-crust (Olivier et al., 2006a), and intrusions related to alkali magmatic activity (Bradbury and Baxter, 1992).

Examples of worldwide breccias that formed like the breccia rocks from Koegel Fontein are scarce and none of the examples found contain as detailed geochemistry as in this study. The most similar example to the intrusion of the breccia rocks found is of a hydrothermal mega breccia called the Hidden Valley breccia (Weisheit et al., 2013), which intruded the

Northern Flinders Ranges of South Australia. The emplacement of the Paleozoic Hidden Valley breccia is described and compared to mechanisms that formed the Breccia Outcrop.

6.5.1 Description of Hidden Valley breccias

Hidden Valley breccia is about 10 km^2 and consists of a mixture of lithologies of different provenance, varying in size from tens of microns to hundreds of metres. The breccia situated at the Mt. Painter Inlier formed during a >12 km exhumation, which started during the 500 Ma Delamerian Orogeny and lasted approximately 200 Ma (Weisheit et al., 2013).

The mechanism suggested for the formation of Hidden Valley breccia is hydraulic or fluid-assisted brecciation (Weisheit et al., 2013). Fluids released during exhumation with volumes between 5-30 km^3 could have extruded through Hidden Valley and caused extensive brecciation. A combination of four fluid sources is proposed to explain the required range of fluid volume (Weisheit et al., 2013). The fluids could have come from large-scale fluid convection, biotite dehydration, decompressional released of pore water trapped below Adelaidean unconformity, and fluids release by igneous intrusions. The model proposed describes fluids at depth that caused extensive pervasive alteration prior ascending through folds and Neoproterozoic faults to form K-feldspar alteration and brecciation (Weisheit et al., 2013).

6.5.2 Breccia rocks from Hidden Valley and Koegel Fontein

Although the Breccia Outcrop is significantly smaller than Hidden Valley mega breccia, contains smaller xenoliths than Hidden Valley breccia rocks, and occurs in a different tectonic region, both types of breccia rocks are thought to have formed from similar mechanisms. These mechanisms involved pressurised hydrothermal-fluids ascending through the country rock.

Fluids, initially trapped in pores or below unconformities, were most likely released by dehydration and decompression hydrothermal reactions, and migrated through crustal weaknesses. During ascension, the hydrothermal-fluids incorporated rock fragments from the wall rock. The deepest fragments were worn and became more rounded, while the fragments closest to the surface kept their sharp and angular clast shape. Once the hydrothermal-fluids reached an open space or a void in the rock layers intruded decompression caused these xenolith-rich fluids to erupt in an explosive manner, forming breccia rocks. (Curtis et al., 2013; Weisheit et al., 2013)

6.6 The relationship between the Breccia Outcrop and the complex

6.6.1 Suggested sequence of events

Before the Pan African, the high latitude of southern Africa (e.g. Tohver et al., 2006) and possible Neoproterozoic global glaciations on Earth (e.g. Maruyama and Santosh, 2008) caused surface water to be strongly ^{18}O-depleted (Curtis et al., 2013). The latitude and Snowball Earth arguments can explain the low δ^{18}O values of the meteoric fluids calculated in this work and in Curtis et al. (2013).

In the Pan African, which was a time of crustal reworking, surface water with low δ^{18}O values circulated through shear zones and associated fractures of the country rock gneiss (Curtis et al., 2013) (Fig. 6.7.a). These meteoric fluids interacted with the country rock at high temperatures and ^{18}O-depleted the country rock gneiss. During the Pan African, the Namaqua country rock gneiss (1200-1000 Ma) underwent intense reworking. Gneiss rocks were possibly mixed with other gneisses from various localities. Some of the gneisses were probably metamorphosed, which reset the age of these gneiss rocks to a younger age than 1000 Ma. The metamorphism and the gneiss heterogeneities explain the calculated age of the gneiss (~666 Ma), which is younger than the Namaqua gneiss and older than the Pan African.

In the Cretaceous, a South Atlantic mantle plume presently located at Bouvet Island and Discovery and Shona seamounts initiated magmatism at Koegel Fontein (Curtis et al., 2013). A shear zone where the complex is presently situated at started to melt due to the high water content it held from a previous fluid-rock interaction (Curtis et al., 2013). As the crust warmed, a premature alkali basalt magma intruded through a fracture line situated in one of the reactivated shear zone. The basalt intrusion broke through a plane of weakness of the crust and formed the alkali basalt dyke (Fig. 6.7.b).

As the crust was heated further, the crust became more differentiated than before. A bostonite magma forced its way out through the same fracture line that the basalt intrusion used (Fig. 6.7.b). Near the surface of the crust, the bostonite intrusion separated from the pathway the basalt used to intrude and broke through a second plane of weakness, forming the bostonite dyke. Evidence for the bostonite dyke to be younger than the basalt dyke is the more mafic than felsic composition of the bostonite rocks.

Once the crust is warm enough, low-δ^{18}O fluids trapped in the country rock since the Pan African were driven off by dehydration reactions (Curtis et al., 2013) (Fig. 6.7.c). These fluids, now metamorphic and with a temperature high enough to exchange their ^{16}O with the rock they migrate through (>300°C), rose towards the surface of the crust through the same pathway the basalt and bostonite magmas used to intrude. Given the occurrence of the reworked, retrogressed, and ^{18}O-depleted shear zones of the country rock, parts of the fluids must have had extremely low $\delta^{18}O$ values. The fluids with some of the lowest $\delta^{18}O$ values were the fluids that ^{18}O-depleted the breccia rocks. Evidence for this is the extremely low $\delta^{18}O$ values of the breccia rocks.

When the fluids were eventually dehydrated and migrated through the pre-existing fracture line the basalt and bostonite dykes used, the fluids incorporated variable amounts of materials on their way up to the surface of the crust. Some of the material was a mixture of fragments of alkali basalt and bostonite (groundmass (B) xenoliths), while other was country rock (gneiss xenoliths), which is the rock material that gives the older age (~567 Ma) of the breccia rocks than Cretaceous. The fluids eventually became xenolith-rich and burst out through the Breccia Plug 1 along the bostonite dyke and the Breccia Plug 2 along the basalt dyke, before extending along both dykes and forming the two sub-parallel breccia dykes (Fig. 6.7.d). Later in time, once the Breccia Outcrop and the rest of the complex were emplaced, a phonolite magma intruded the bostonite dyke and formed the Phonolite Plug.

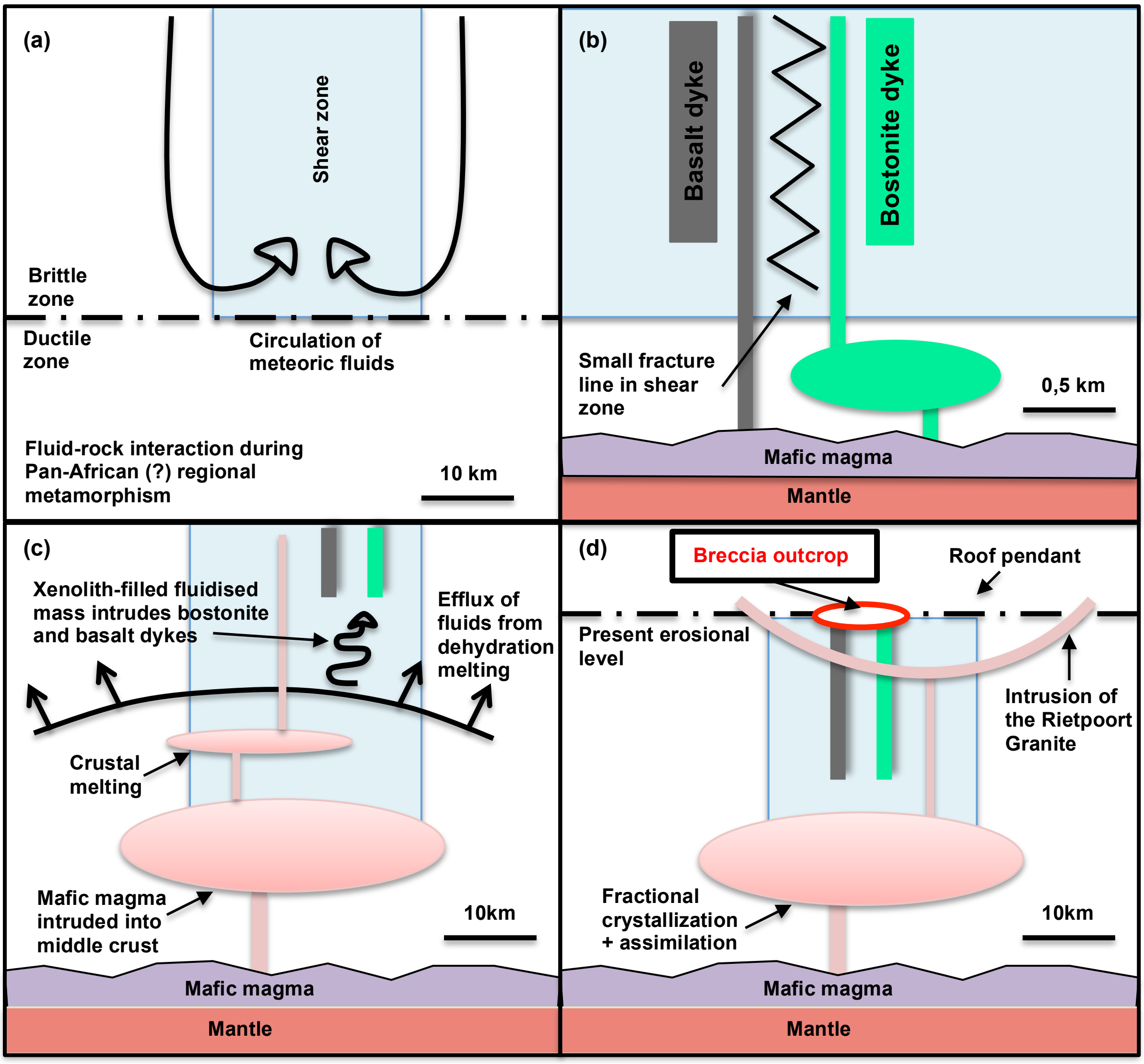

Fig. 6.7 Schematic cross-sections showing the proposed stages of development of the Breccia Outcrop within the Koegel Fontein complex. **(a)** Generation of low-δ^{18}O crust by meteoric-hydrothermal fluids and rock interaction along crustal shear zones during the Pan-African (?) regional metamorphism. **(b)** Emplacement of early igneous units in the Cretaceous: an alkali basalt dyke followed by a bostonite dyke intrude along a fracture line. **(c)** Growth of magma system at depth. Thermal metamorphism causes efflux of dehydration fluids from the altered crust. A xenolith-filled fluidised mass intrudes through the pre-existing bostonite and basalt dykes. **(d)** The Breccia Outcrop is now emplaced. The final stage of the complex is the intrusion of Rietpoort Granite, which cuts both the bostonite and basalt dykes.

CHAPTER 7 CONCLUSIONS

1. The Breccia Outcrop is made of two sub-parallel breccia dykes with a breccia plug on them. These dykes used to be an alkali basalt dyke and a bostonite dyke before a xenolith-rich fluidised mass intruded both dykes. This fluidised material broke through the Breccia Plug 1 on the bostonite dyke and the Breccia Plug 2 on the alkali basalt dyke before extending along both dykes and forming the breccia dykes.

2. The petrography, major and trace element compositions, and radiogenic isotope data reflect that three main rock components make up the breccia rocks, two of which are igneous (bostonite and basalt) and one metamorphic (gneiss).

3. A fourth rock constituent is an epidote-rich green rock supporting black and gneiss xenoliths. This green rock represents a xenolith- and fluid-rich material that migrated through the same crustal weakness through which pre-existing bostonite and alkali basalt dykes intruded. The xenoliths in this green rock are fragments of gneiss, alkali basalt, and bostonite that were broken off from the wall rock when the xenolith-rich fluidised mass migrated through the crustal weakness.

4. The phonolites are the first silica-undersaturated rocks described at Koegel Fontein. These rocks are made of alkali feldspar and nepheline and form the Phonolite Plug, which is an intrusive plug situated along the bostonite dyke. The absence of phonolite xenoliths in the breccia rocks and the normal $\delta^{18}O$ values of the phonolites are indicative that the Phonolite Plug intruded the bostonite dyke after the complex was emplaced.

5. The rocks with the lowest $\delta^{18}O$ values in the complex ($\delta^{18}O_{\text{whole-rock (COK168 and COK170)}}$ = -5.2‰ and $\delta^{18}O_{\text{mineral separates (COK165)}}$ = -5.6‰) are breccia rocks. The breccia rocks and adjacent gneisses are all low-$\delta^{18}O$ rocks with values below that of MORB (+5.7‰). Only the phonolites are normal-$\delta^{18}O$ rocks, with $\delta^{18}O$ values >+5.7‰ (average = +8.0‰).

6. The $\delta^{18}O$ value of the meteoric fluids (-10.8‰) calculated from the breccia rocks is inconsistent with the low latitude and warm climate of southern Africa in the Cretaceous. The ^{18}O-depletion of these fluids is proposed to have occurred in the late Proterozoic (Curtis et al., 2013) when there were global glaciations on Earth (e.g. Maruyama and Santosh, 2008) and when southern Africa was at high latitude (e.g. Tohver et al., 2006). These low-$\delta^{18}O$ fluids could then have ^{18}O-depleted the country rock during the Pan African orogeny, when crustal reworking enabled deep circulation of surface water (Curtis et al., 2013).

7. The Namaqua country rock gneiss (1200-1000 Ma) underwent intense reworking in the Pan African. Gneisses from various localities were mixed and some metamorphosed, resetting the age of these gneisses (calculated age of the gneisses: ~666 Ma).

8. Despite the calculated Pan African age (~567 Ma) of the breccia rocks, these rocks are suggested being ~135 Ma. This older age than Cretaceous indicates that the age of the breccia rocks was not completely reset by the Cretaceous breccia-forming event. This calculated age (~567 Ma) is suggested to reflect the age of the gneiss xenoliths in the breccia rocks, which was most likely reset during the Pan African orogeny (~500 Ma) due to crustal reworking.

9. The low water content and LOI values (0.2-1.1 wt %) and the dominance of epidote and biotite reflect a fluid temperature (>300°C) high enough for fluid-rock exchange. The fluids were dehydrated from the country rock when a Cretaceous mantle plume heated the base of the crust (e.g. Curtis et al., 2013). As the crust was heated further, a premature alkali basalt dyke intruded through a fracture line. The crust became more differentiated than before and a bostonite dyke intruded next through the same fracture line the alkali basalt dyke used to intrude. Near the surface, the bostonite magma separated from the fracture line and intruded near to the basalt dyke. Low-δ^{18}O fluids trapped in the country rock since the Pan African were eventually driven off by dehydration reactions and migrated through the alkali basalt and bostonite dykes. These fluids broke off fragments of alkali basalt, bostonite, and gneiss from the wall rock. The xenolith-rich fluidised material was decompressed rapidly and formed Breccia Outcrop.

10. The breccia rocks warrant more studies as they form an unusual rock type. The extremities of the Breccia Outcrop could use further mapping and sampling. Work on the composition of the breccia xenoliths could indicate if the bostonite and basalt dykes actually intruded through the same fracture line. The phonolites could be more extensively studied to further understand its emplacement model. Acquiring magnetic data and studying the magnetic anomaly at Koegel Fontein could help constrain the origin of the complex. A thorough comparative study between the Breccia Outcrop and other intrusive breccias worldwide could help better comprehend the emplacement of the outcrop. To end, the breccia rocks occur in an area where little igneous activity related to rifting is preserved onshore. Further exploration of the low-δ^{18}O rocks could add further understanding to geological processes occurring in the region and perhaps to the relationship between rifting and magmatism during the breakup of western Gondwana.

LIST OF REFERENCES

Armstrong, J. T. (1995). CITZAF – a package of correction programs for the quantitative Electron Microbeam X-Ray-Analysis of thick polished materials, thin-films, and particles. *Microbeam Analysis* **4**, 177-200.

Barton, J. M. (1983). Rb-Sr and U-Th-Pb isotopic studies of the Sand River Gneiss, Central Zone, Limpopo Mobile Belt. *Special Publication of the Geological Society of South Africa* **8,** 9-18.

Bindeman, I. N. (2008). Oxygen isotopes in mantle and crustal magmas as revealed by single crystal analysis. In: Putirka, K. D., Tepley, F. J., III (eds) *Minerals, Inclusions and Volcanic Processes. Mineralogical Society of America and Geochemical Society, Reviews in Mineralogy and Geochemistry* **69**, 445-478.

Botha, B. J. V., Hodgson, F. D. I. (1976). Karoo dolerites in northwestern Damaraland. *Transactions of the Geological Society of South Africa* **79**, 186-190.

Bradbury, J. C., Baxter, J. W. (1992). Intrusive breccias at Hicks Dome, Hardin County, Illinois. *Champaign, IL: Illinois State Geological Survey*, pp. 22-23

Cornell, D. H., Thomas, R. J., Moen, H. F. G., Reid, D. L., Moore, J. M., Gibson, R. L. (2006). The Namaqua–Natal Province In: Johnson, M. R., Anhaeusser, C. R., Thomas, R. J. (eds) *The Geology of South Africa*. Council for Geoscience, Pretoria, South Africa, pp. 325–379.

Craig, H. (1961). Isotopic variations in natural waters. *Science* **133**, 1702-1703.

Curtis, C. G., Harris, C., Trumbull, R. B., de Beer, C., Mudzanani, L. (2013). Oxygen Isotope Diversity in the Anorogenic Koegel Fontein Complex of South Africa: a Case for Basement Control and Selective Melting for the Production of Low-δ^{18}O Magmas. *Journal of Petrology* **54**, 1259-1283.

Curtis, C. G. (2010). Stable isotope and whole-rock geochemical study of the Cretaceous Koegel Fontein complex: magma characterisation, evidence for fluid-rock interaction and source constraints for low-δ^{18}O magmas, MSc thesis, University of Cape Town, 121 pp.

Curtis, C., G., Trumbull, R., B., de Beer, C., H., Harris, C., Reid, D., L., Romer, R., L. (2011). Geochemistry of the early Cretaceous Koegel Fontein anorogenic igneous complex, South Africa. *South African Journal of Geology* **114**, 353-378.

Dansgaard, W. (1964). Stable isotopes in precipitation. *Tellus* **16**, 436–468.

de Beer, C., H. (2010). The geology of the Garies area. Explanation 1:250 000 scale map 3017 Garies. Pretoria: Council for Geoscience.

de Beer, C. H., Armstrong, R. A. (1998). Age and tectonic setting of Mesozoic anorogenic Koegel Fontein complex west of Bitterfontein, Namaqualand, South Africa. *IAVCEI International Volcanological Congress, CapeTown, 11-16 July, 1998, Abstracts,* 15p.

de Beer, C. H., Gresse, P. G., Theron, J. N., Almond, J. E. (2002). The Geology of the Calvinia Area. Explanation of 1:250,000 scale sheet 3118 Calvinia. The Council for Geoscience, Pretoria, South Africa*,* 92pp.

de Beer, C. H., Meyer, R. (1984). Geophysical characteristics of the Namaqua-Natal Belt and its boundaries, South Africa. *Journal of Geodynamics* **1**, 473-494.

Deer, W. A., Howie, R. A., Zussman, J. (1992). An Introduction to the Rock–forming Minerals, 2nd Edition. *Pearson Education Ltd.* 696pp.

Duncan, R. A., Hargraves, R. B., Brey, G. P. (1978). Age, paleomagnetism and chemistry of melilite basalts in the Southern Cape, South Africa. *Geological Magazine* **115**, 317-327.

Eglington, B. M., Harmer, R. E., Kerr, A. (1989). Isotope and geochemical constraints on Proterozoic crustal evolution in southeastern Africa. *Precambrian Reseach* **45**, 159-174.

Eiler, J. M. (2001). Oxygen isotope variations of basaltic lavas and upper mantle rocks. In: Valley, J. W., Cole, D. (eds) *Stable Isotope Geochemistry. Mineral Society of America and Geochemical Society, Reviews in Mineralogy and Geochemistry* **43**, 319-364

Ewart, A., Milner, S. C., Armstrong, R. A., Duncan, A. R. (1998a). Etendeka volcanism of the Goboboseb Mountains and Messum Igneous complex, Namibia. Part i: Geochemical evidence of early Cretaceous Tristan Plume melts and the role of crustal contamination in the Paraná-Etendeka CFB. *Journal of Petrology* **39**, 191-225.

Ewart, A., Milner, S. C., Armstrong, R. A., Duncan, A. R. (1998b). Etendeka volcanism of the Goboboseb Mountains and Messum Igneous complex, Namibia. Part ii: Voluminous quartz latite volcanism of the Awahab Magma System. *Journal of Petrology* **39**, 227-253.

Gibson, S. A., Thompson, R. N., Day, J. A. (2006). Timescales and mechanisms of plume-lithosphere interactions: $^{40}Ar/^{39}Ar$ geochronology and geochemistry of alkaline igneous rocks from the Paraná-Etendeka large igneous province. *Earth and Planetary Science Letters* **251**, 1-17.

Gresse, P. G., von Veh, M. W., Frimmel, H. E. (2006). Namibian (Neoproterozoic) to Early Cambrian successions In: Johnson, M. R., Anhaeusser, C. R., Thomas, R. J. (eds) *The Geology of South Africa*. Council for Geoscience, Pretoria, South Africa, pp. 395–20.

Harris, C. (1995). Oxygen isotope geochemistry of the Mesozoic anorogenic complexes of Damaraland, northwest Namibia: evidence for crustal contamination and its effect on silica saturation. *Contributions to Mineral Petrology* **122**, 308-321.

Harris, C., Burgers, C., Miller, J., Rawoot., F. (2010). O- and H-isotope record of Cape Town rainfall from 1996 to 2008, and its application to recharge studies of Table Mountain groundwater. *South African Journal of Geology* **113**, 33-56.

Harris, C., Erlank., A. J. (1992). The production of large-volume, low $\delta^{18}O$ rhyolites during the rifting of Africa and Antartica: The Lebombo Monocline, southern Africa. *Geochimica et Cosmochimica Acta* **56**, 3561-3570.

Harris, C., Vogeli., J. (2010). Oxygen composition of garnet in the peninsula granite, Cape Granite Suite, South Africa: constraints of melting and emplacement mechanisms. *South African Journal of Geology* **113**, 401-412.

Harris, C., Whittingham, A. M., Milner, S. C., Armstrong, R. A. (1990). Oxygen isotope geochemistry of the silicic volcanic rocks of the Etendeka-Paraná province: Source constraints. *Geology* **18**, 1119-1121.

Hartnady, C. J. H., le Roex, A. P. (1985). Southern Ocean hotspot tracks and the Cenozoic absolute motion of the African, Antarctic, and South American plates. *Earth and Planetary Science Letters* **75**, 245-257.

Ito, E., White, W. M., Göpel, C. (1987). The O, Sr, Nd and Pb isotope geochemistry of MORB. *Chemical Geology* **62**, 157-176.

Janney, P. E., le Roex, A. P., Carlson, R. W., Viljoen, K. S. (2002). A chemical and Multi-Siotope Study of the Western Cape Olivine Melilitite Province, South Africa: Implications for the Sources of Kimberlites and the Origin of the HIMU Signature in Africa. *Journal of Petrology* **43**, pp. 2339-2370.

Jansen, H. (1960). The Geology of the Bitterfontein Area, Cape Province: Explanation of Sheet 253 (Bitterfontein). Pretoria: Geological Survey of South Africa, 97p.

Jerram, D., Mountney, N., Holzföster, F., Stollhofen, H. (1999). Internal stratigraphic relationships in the Etendeka Group in the Huab Basin, north west Namibia: understanding the onset of flood volcanism. *Journal of Geodynamics* **28**, 393-418.

Kennedy, W. Q. (1964). The structural differentiation of Africa in the Pan-African (±500my) tectonic episode. Univ. Leeds, Res. Inst. African Geol., Annu. Rep. **8**, 48-49.

Kirstein, L. A., Kelley, S., Hawkesworth, C., Turner, S., Mantovani, M., Wijbrans, J. (2001). Protracted felsic magmatic activity associated with the opening of the South Atlantic. *Journal of the Geological Society* **158**, 583-592.

Le Maitre, R. W. (1989). A Classification of Igneous Rocks and Glossary of Terms. *Oxford: Blackwell.*

le Roex, A. P., Späth, A., Zartman, R. E. (2001). Lithospheric thickness beneath the southern Kenya Rift: implications from basalt geochemistry, South Atlantic. *Journal of Petrology* **26**, 149-186.

Marsh, J. S., Ewan, A., Milner, S. C., Duncan, A. R., Miller, R., McG. (2001). The Etendeka Igneous Province: magma types and their stratigraphic distribution with implications for the evolution of the Paraná-Etendeka flood basalt province. *Bulletin of Volcanology* **62**, 464-486.

Martin, H., Mathias, M., Simpson, E. S. W. (1960). The Damaraland sub-volcanic ring complexes in South West Africa. In: Sorgenfrei, T. (eds) *Report of the International Geological Congress XXI Session 13. Conpenhagen: Norden,* pp. 156-174.

Maruyama, S., Santosh, M. (2008). Models on Snowball Earth and Cambrian explosion: A synopsis. *Gondwana Research* **14**, 22-32.

Marzoli, A., Melluso, L., Morra, V., Renne, P. R., Sgrosso, I., D'Antonio, M., Duarte Morais, L., Morais, E. A. A., Ricci, G. (1999). Geochronology and petrology of Cretaceous basaltic magmatism in the Kwanza basin (western Angola), and the relationships with the Paraná-Etendeka continental flood basalt province. *Journal of Geodynamics*, **28**, 341-356.

McCallum, M. E. (1985). Experimental evidence for fluidization processes in breccia pipe formation. *Econ Geol* **80**, 1523-1543.

McIver, J. R. (1981). Aspects of ultrabasic and basic alkaline intrusive rocks from Bitterfontein, South Africa. *Contributions to Mineralogy and Petrology* **78**, 1-11.

Miková, J., Denková, P. (2007). Modified chromatographic separation scheme for Sr and Nd isotope analysis in geological silicate samples. *Journal of Geosciences* **52**, 221-226.

Milner, S. C., le Roex, A. P. (1996). Isotope characteristics of the Okenyenya igneous complex, northwestern Namibia: constraints on the composition of the early Tristan plume and the origin of the EM 1 mantle component. *Earth and Planetary Science letters* **141**, 277-291.

Mohriak, W. U., Rosendahl, B. R., Turner, J. P., Valente, S. C. (2002). Crustal architecture of South Atlantic volcanic margins. In: Menzies, M. A., Klemperer, S. I., Ebinger, C. J., Baker, J. (eds) *Volcanic rifted margins. Geological Society of America Special Paper* **362,** 159-202.

Moore, A. E., Verwoerd, W. J. (1985). The olivine melilitite-"kimberlite"-carbonatite suite of Namaqualand and Bushmanland, South Africa. *South African Journal of Geology* **88**, 281-294.

O'Connor, J. M., Duncan, R. A. (1990). Evolution of the Walvis Ridge-Rio Grande Rise hot spot system: Implications for African and South American plate motions over plumes. *Journal of Geophysical Research* **95**, 17475-17502.

O'Connor, J. M., le Roex, A. P. (1992). South Atlantic hot spot-plume systems: 1. Distribution of volcanism in time and space. *Earth and Planetary Science Letters* **113**, 343-364.

Olivier, N. H. S., Rubenach, M. J., Fu, B., Baker, T., Blenkinsop, T. G., Cleverley, J. S., Marshall, L. J., Ridd, P. J. (2006a). Granite-related overpressure and volatile release in the mid crust: fluidized breccias from the Cloncurry District, Australia. *Geofluids* **6**, 346-353.

Peate, D., W. (1997). The Paraná-Etendeka Province. In: Mahoney, J. J., and Coffin, M. F. (eds) *Large Igneous Provinces: Continental, Oceanic and Planetary Flood Volcanism. American Geophysical Union, Geophysical Monograph* **100**, 217-231.

Porada, H. (1989). Pan–African rifting and orogenesis in southern to equatorial Africa and eastern Brazil. *Precambrian Research* **44**, 103–136.

Reid, D. L. (1979). Total rock Rb-Sr and U-Th-Pb isotopic study of Precambrian metavolcanic rocks in the lower Orange River region, Southern Africa. *Earth and Planetary Science Letters* **42**, 368-378.

Reid, D. L. (1999). Whole-rock radiometric age patterns in the Aggenys-Gamsberg, central Bushmanland, South Africa. *South African Journal of Geology* **100**, 11-22.

Reid, D. L., Rex, D. C. (1994). Cretaceous dykes associated with the opening of the South Atlantic; the Mehlberg Dyke, northern Richtersveld. *South African Journal of Geology* **97**, 135-145.

Renne, P. R., Ernesto, M., Paccia, I. G., Coe, R. S., Glen, J. M., Prevot, M., Perrin, M. (1992). The age of Paraná flood volcanism, rifting of Gondwanaland, and the Jurassic-Cretaceous boundary. *Science* **258**, 975-979.

Renne, P. R., Glen, J. M., Milner, S. C., Duncan, A. R. (1996). Age of Etendeka flood volcanism and associated intrusions in southwestern Africa. *Geological Society of America* **24**, 659-662.

Rousseau, R., Willis, J., Duncan, A. R. (1996). Practical XRF calibration procedures for major elements. *X-ray Spectrometry* **25**, 179-189.

Schimmelmann, A., DeNiro, M. J. (1993). Preparation of organic and water hydrogen for stable isotope analysis: effects due to reaction vessels and zinc. *Analytical Chemistry* **65**, 789-792.

Scotese, C. R., Boucot, A. J., McKerrow, W. S. (1999). Gondwanan palaeogeography and palaeoclimatology. *Journal of African Earth Sciences* **28**, 99-114.

Sheppard, S. M. F. (1986). Characterization and isotopic variation in natural waters. In: Valley, J. W., Taylor, Jr., H. P., O'Neil, J. R. (eds) *Stable Isotopes in High-temperature Geological Processes. Mineralogical Society of America, Reviews in Mineralogy* **16**, 165-183.

Subramaniam, A. P. (1956). Mineralogy and petrology of the Sittampundi complex, Salem district, Madras State, India. *Geological Society of America Bulletin* **67**, 317-390.

Taylor Jr., H. P., Sheppard, S. M. F. (1986). Igneous rocks: I. processes of isotope fractionation and isotope systematics. *Reviews in Mineralogy and Geochemistry* **16**, 227–271.

Thomas, R. J., Eglington, B. M. (1990). A Rb-Sr, Sm-Nd and U-Pb zircon isotopic study of the Mzumbe Suite, the oldest intrusive granitoid in southern Natal, South Africa. *South African Journal of Geology* **93**, 761-765.

Thorkelson, D. J., Mortensen, J. K., Creaser, R. A., Davidson, G. J., Abbott, J. G. (2001). Early Proterozoic magmatism in Yukon, Canada: constraints on the evolution of northwestern Laurentia. *Canadian Journal of Earth Sciences* **38**, 1479-1494.

Tilley, C. E. (1954). Nepheline-alkali feldspar parageneses. *American Journal of Science* **252**, 65-75.

Tohver, E., D'Agrella-Filho, M. S., Trindade, R. I. F. (2006). Paleomagnetic record of Africa and South America for the 1200-500 Ma interval, and evaluation of Rodinia and Gondwana assemblies. *Precambrian Research* **147**, 193-222.

Trumbull, R. B., Bühn, B., Romer, R. L., Volker, F. (2003). The petrology of basanite-tephrite intrusions in the Erongo complex and implications for a plume source of Cretaceous alkaline complexes in Namibia. *Journal of Petrology* **44**, 93-112.

Trumbull, R. B., Emmermann, Bühn, B., Gerstenberger, H., Mingram, B., Schmitt, A., Volker, F. (2000). Insights on the genesis of the Cretaceous Damaraland igneous complexes in Namibia from a Nd- and Sr-isotopic perspective. Communications of the *Geological Survey of Namibia* **12**, 313-324.

Trumbull, R. B., Harris, C., Frindt, S., Wigand, M. (2004a). Oxygen and neodymium isotope evidence for source diversity in Cretaceous anorogenic granites from Namibia and implications for A-type granite genesis. *Lithos* **73**, 21-40.

Trumbull, R. B., Sobolev, S. V., Bauer, K. (2002). Petrophysical modelling of high seismic velocity crust and the Namibian volcanic margin. In: Menzies, M. A., Klemperer, S. I., Ebinger, C. J., Baker, J. (eds) *Volcanic Rifted Margins, Geologic Society of America Special Paper* **362**, 221-230.

Trumbull, R. B., Reid, D. L., de Beer, C., van Acken, D., Romer, R. L. (2007). Magmatism and continental breakup at the west margin of southern Africa: a geochemical comparison of dolerite dikes from northwestern Namibia and the Western Cape. *South African Journal of Geology* **110**, 477-502.

Tuttle, O. F. (1952). Origin of the contrasting mineralogy of extrusive and plutonic salic rocks. *The Journal of Geology* **60**, pp. 107-124.

Valley, J. W., Kitchen, N., Kohn, M. J., Niendorf, C. R., Spicuzza, M. J. (1995). UWG-2, a garnet standard for oxygen isotope ratios: Strategies for high precision and accuracy with laser heating. *Geochimica et Cosmoschimica* **59**, 5223-5231.

Vennemann, T. W., O’Neil, J. R. (1993). A simple and inexpensive method of hydrogen isotope and water analyses of minerals and rocks based on zinc reagent. *Chemical Geology* **103**, 227-234.

Watkeys, M. (2006). Gondwana Breakup: A South African perspective. In: Johnson, M. R., Anhaeusser C. R., Thomas R. J. (eds) *The Geology of South Africa, Geological Society of South Africa/Council for Geoscience*, 531–539.

Weis, D., Kieffer, B., Maerschalk, C., Barling., J., de Jong, J., Williams, G. A., Hanano, D., Pretorius, W., Mattielli, N., Scoates, J. S., Goolaerts, A., Friedman, R. M., Mahoney, J. B. (2006). High precision isotopic characterization of USGS reference materials TIMS and MC-ICP-MS. *Geochemistry, Geophysics, Geosystems* **7**

Weisheit, A., Bons, P. D., Elburg A. (2013). Long-lived crustal-scale fluid flow: the hydrothermal mega-breccia of Hidden Valley, Mt. Painter Inlier, South Australia. *Gondwana Research* **24**, 700-712.

White, B. (2007). U-Th decay series dating.

Wigand, M., Schmitt, A. K., Trumbull, R. B., Villa, I. M., Emmermann, R. (2004). Short-lived magmatic activity in an anorogenic subvolcanic complex: ^{40}Ar-^{39}Ar and ion microprobe U-Pb zircon dating of the Erongo, Damaraland Province, Namibia. *Journal of Volcanology and Geothermal Research* **130**, 285-305.

Willis, J. P., Duncan, A. R. (2008). Understanding XRF spectrometry. *Almelo, PANalytical B. V.*

APPENDICES

APPENDIX A HAND-SPECIMEN PHOTOGRAPHS AND PHOTOMICROGRAPHS

A.1 **Breccia with strong alteration** - sample COK168

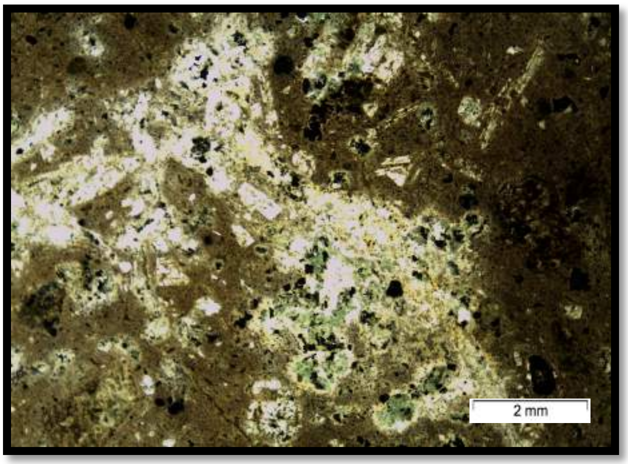

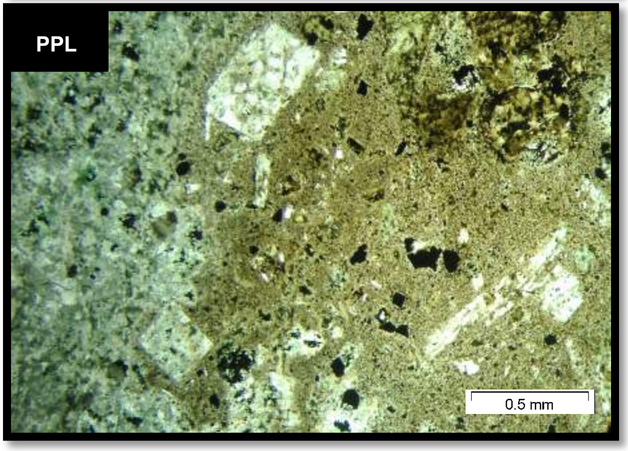

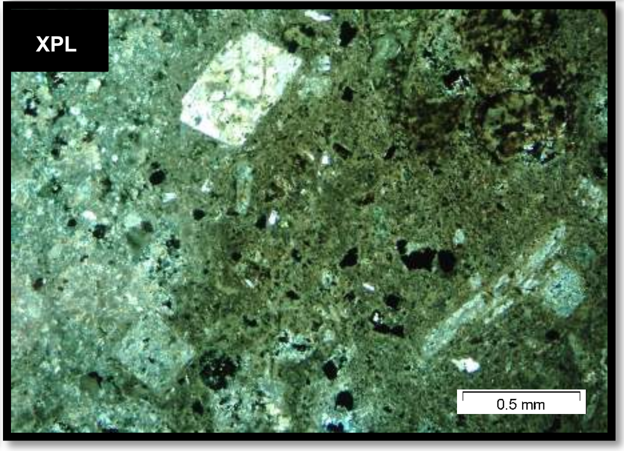

Sample COK168 consists of ~85% matrix, which is a mixture of groundmass (B) and matrix (A), and sparse zircon. The phenocryst assemblage makes up ~10% of the rock. The phenocrysts are made of fine- to medium-grained plagioclase and alkali feldspar and opaque minerals. Microphenocrysts of feldspar with a fibrous texture are occasional. Plagioclase and alkali feldspar phenocrysts are only found in groundmass (B). About 5% of the rock consists of xenoliths made of groundmass (B). Groundmass (B) xenoliths contain abundant medium-grained opaque minerals.

Fine- to medium-grained epidote and chlorite replace matrix (A). Groundmass (B) is partly coated by a fine-grained, brown (PPL, XPL) mineral. Phenocrysts have sieve textures, altered rims, and are embayed. Feldspar phenocrysts are strongly altered by epidote. Xenoliths are partly to entirely chloritised.

A.1 **Breccia with strong alteration** - sample COK170

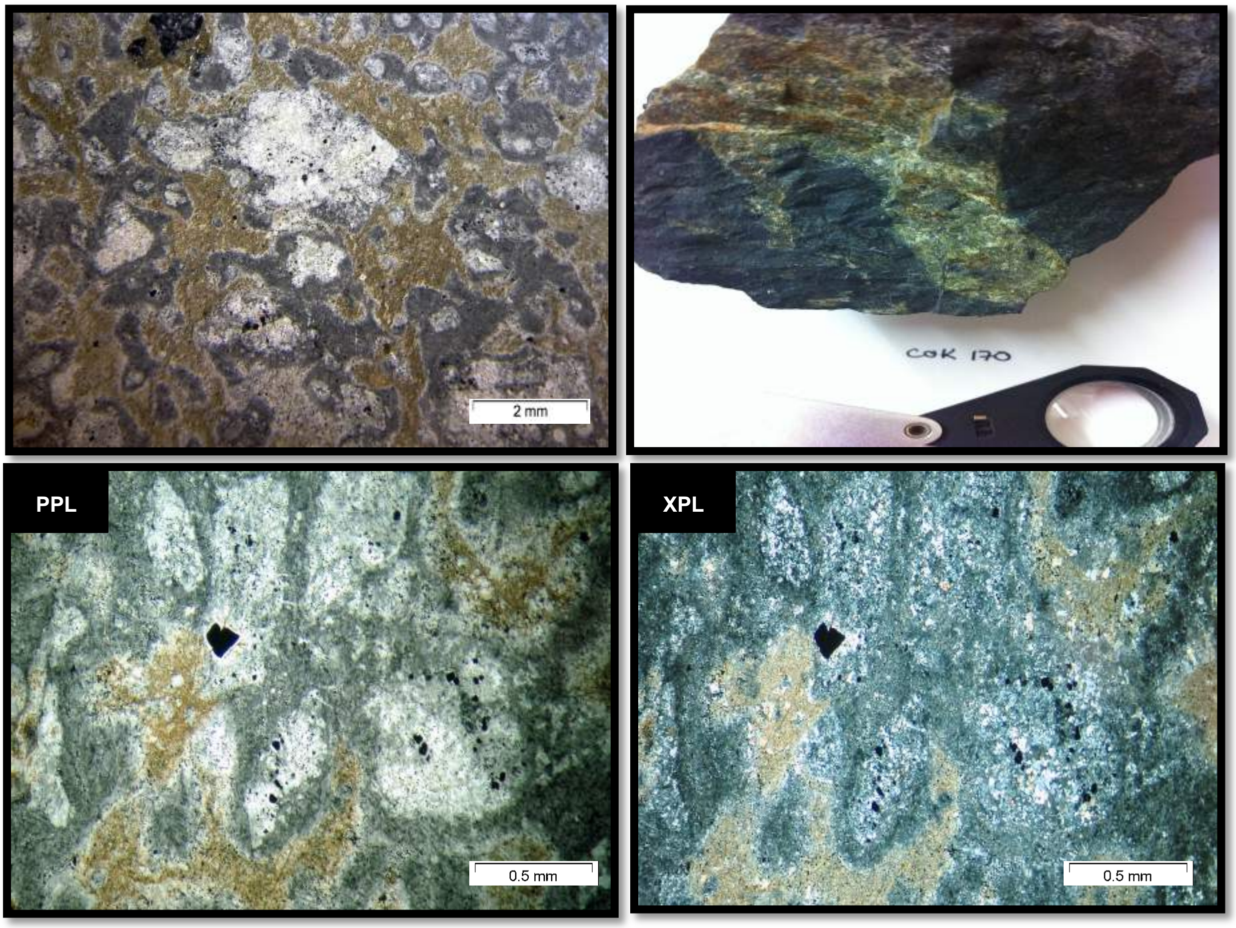

Sample COK170 consists of ~86% matrix, which is a mixture of groundmass (B) (in grey) and matrix (A) (in brown/yellow), and opaque minerals. Phenocrysts are not visible in this rock. About 15% of the rock consists of xenoliths made of granoblastic quartz or groundmass (B).

Fine- to medium-grained epidote replaces matrix (A). Groundmass (B) is partly coated by a fine-grained, brown (PPL, XPL) mineral. The granoblastic quartz and groundmass (B) xenoliths are partly replaced by epidote.

A.2 Breccia with the most xenoliths - sample COK162 (~60% xenoliths)

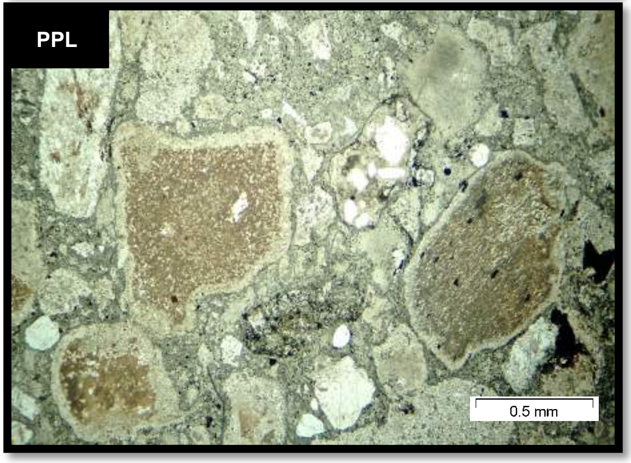

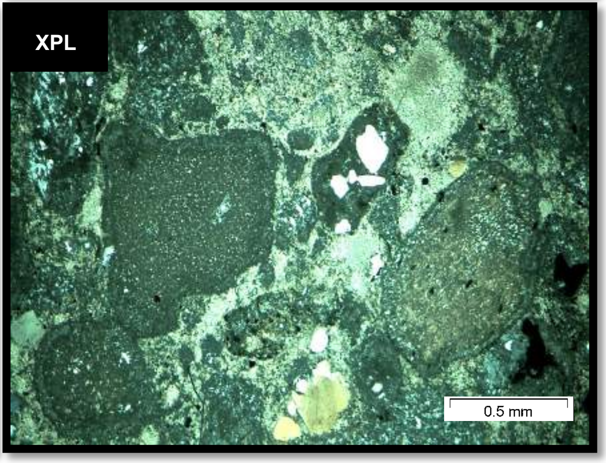

COK162 has ~39% matrix, which is described as matrix (A). No phenocrysts are visible in this rock. About 60% of the rock consists of xenoliths. The xenoliths are made of granoblastic quartz and groundmass (B). Sparse, fine- to medium-grained quartz xenocrysts are disseminated in the rock. Two of the quartz xenocrysts show a flow texture.

Fine-grained epidote replaces matrix (A). Groundmass (B) xenoliths are partly coated by a fine-grained, brown (PPL, XPL) alteration product. The xenoliths show coronas of a fine-grained mineral, which is too fine to identify any constituents. The quartz in the xenoliths has a wavy extinction.

A.2 Breccia with the most xenoliths - sample COK175 (~79% xenoliths)

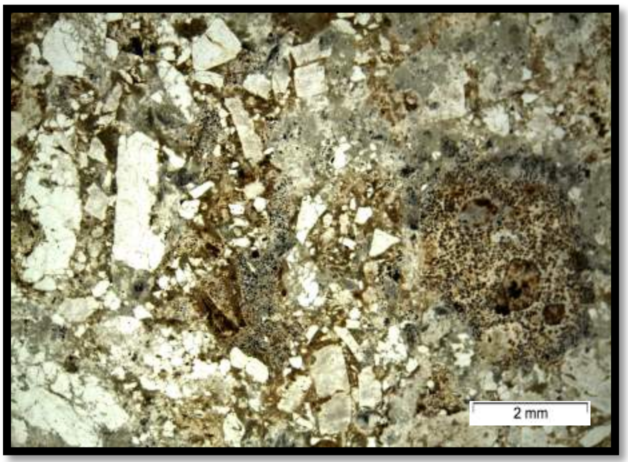

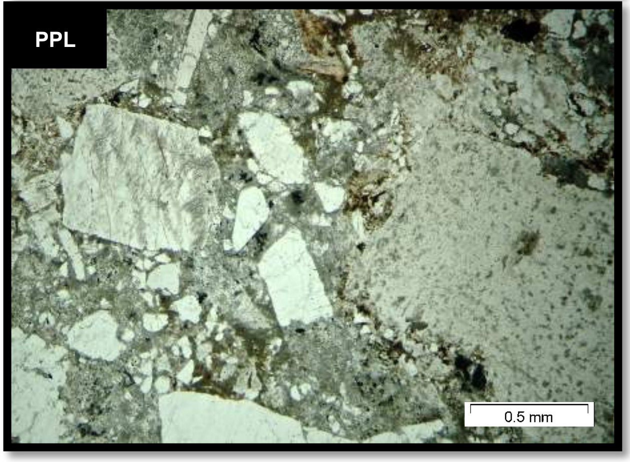

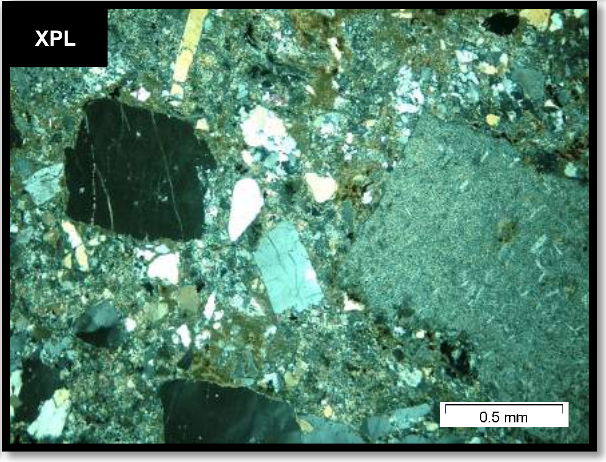

Sample COK175 consists of ~20%, which is described as groundmass (B). The phenocryst assemblage makes up ~1% of the rock. The phenocrysts are fine- to medium-grained alkali feldspar. About 79% of the rock is made of xenoliths of quartz, and groundmass (B). Groundmass (B) xenoliths contain abundant opaque minerals. There are abundant fine- to medium-grained quartz xenocrysts disseminated in the rock.

A brown (PPL, XPL) mineral coats groundmass (B). The xenoliths and xenocrysts of quartz are strained and show trails of fluid inclusions. Phenocrysts are turbid and have altered rims. The alkali feldspar shows perthitic and sieve textures. The brown mineral is chloritised and feldspar is replaced by a fine-grained groundmass along rims and cracks.

A.3 Breccia with a black and green matrix - sample COK165 (~50-50%)

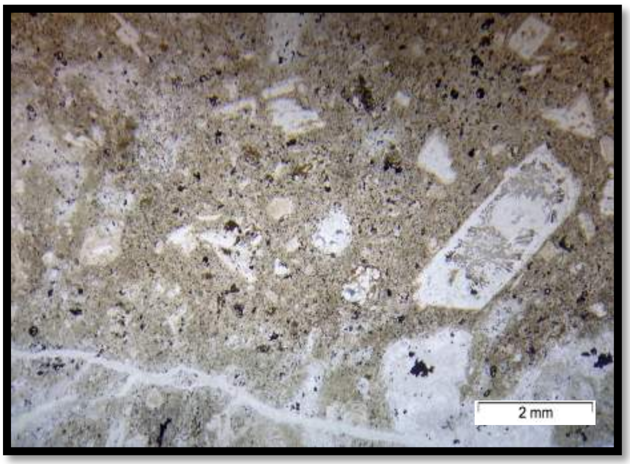

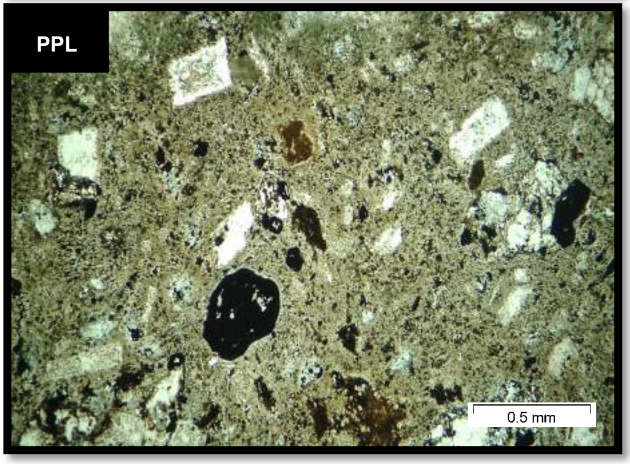

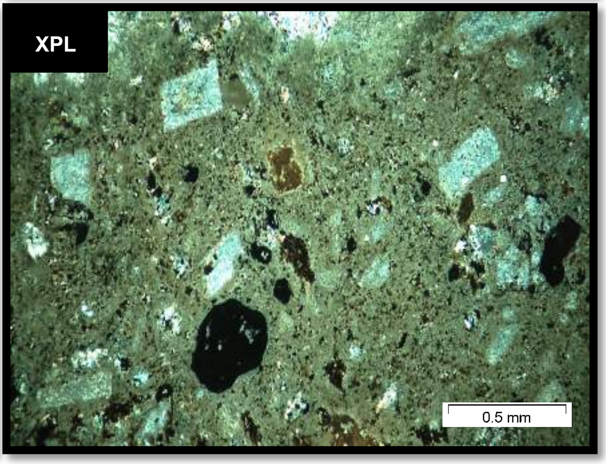

Sample COK165 consists of ~85% of matrix, which is described as a mixture of groundmass (B) and matrix (A), and opaque minerals. The phenocryst assemblage makes up ~10% of the rock. The phenocrysts are feldspar, which isx found in groundmass (B). About 5% of the rock consists of xenoliths of groundmass (B).

The matrices and the phenocrysts are strongly altered. Fine- to medium-grained epidote and chlorite replace matrix (A). A brown (PPL, XPL) mineral coats groundmass (B). The feldspar is turbid, embayed, and shows perthitic and sieve textures. Feldspar phenocrysts are chloritised.

A.3 **Breccia with a black and green matrix** - sample COK205 (~50-50%)

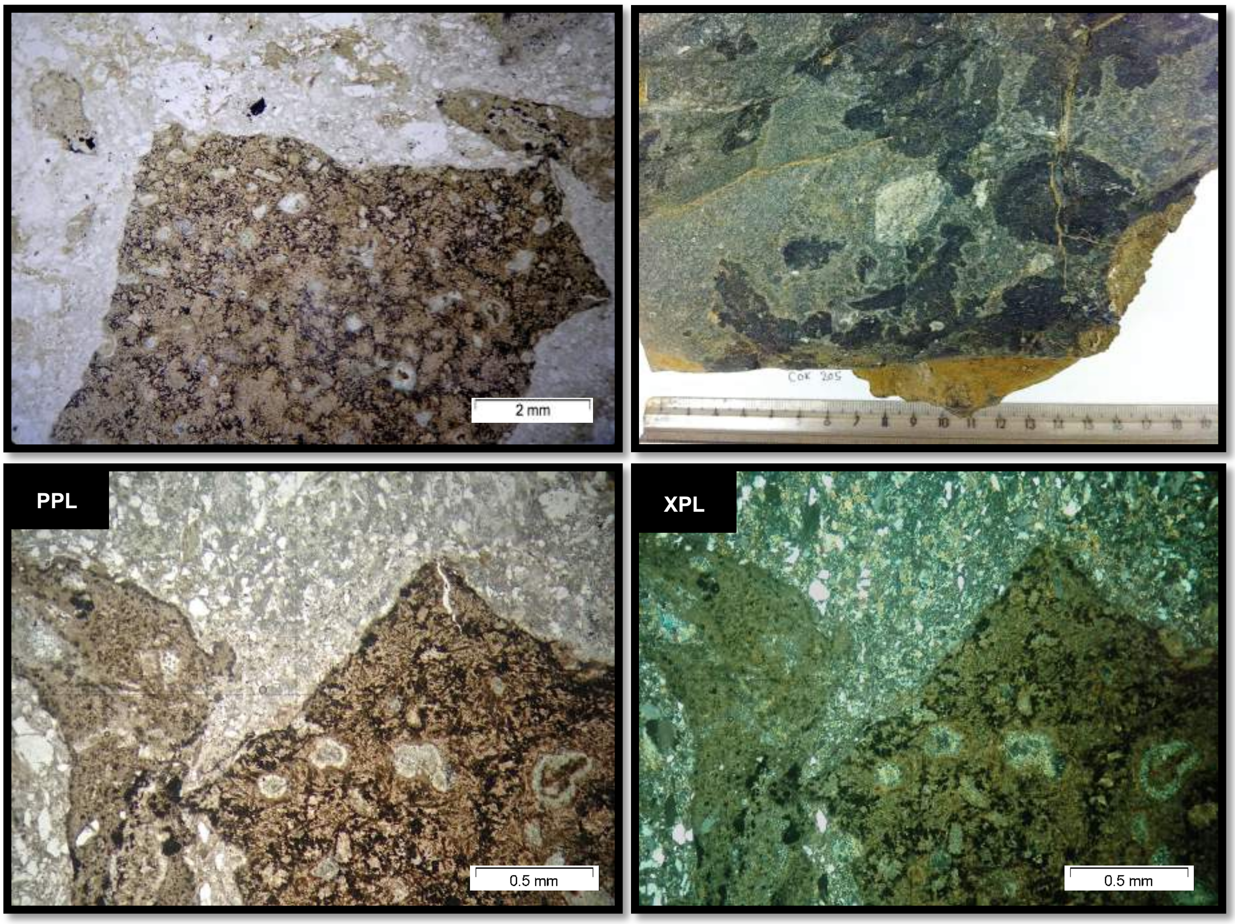

Sample COK205 consists of ~45% of matrix, which is made of a mixture of groundmass (B) and matrix (A). The phenocryst assemblage makes up ~10% of the rock, and is found in groundmass (B). The phenocrysts are made of feldspar. Less than 2% of the feldspar phenocrysts are relict. The relict feldspar is replaced by a fine-grained groundmass, which is too fine to identify. About 45% of the rock consists of xenoliths made of groundmass (B), granoblastic quartz, and disseminated quartz xenocrysts. The xenoliths of groundmass (B) are well-defined, round or angular inclusions.

Both matrices are strongly altered. Fine- to medium-grained epidote and chlorite replace matrix (A). A brown (PPL, XPL) mineral coats groundmass (B). Groundmass (B) xenoliths have coronas of opaque minerals and chlorite. The feldspar is turbid, embayed, and shows perthitic and sieve textures. Feldspar phenocrysts are chloritised.

A.4 Breccia with a trachytic texture - sample COK178

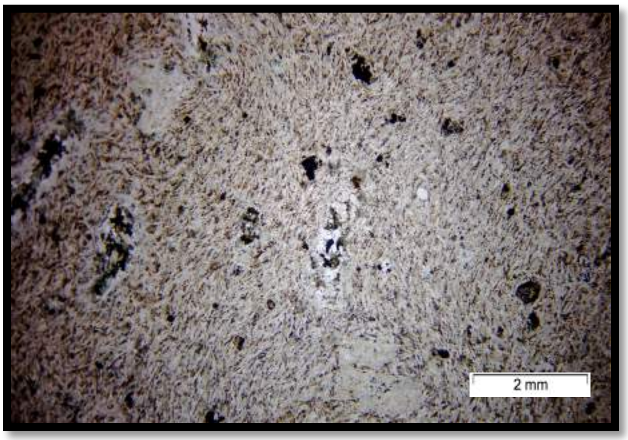

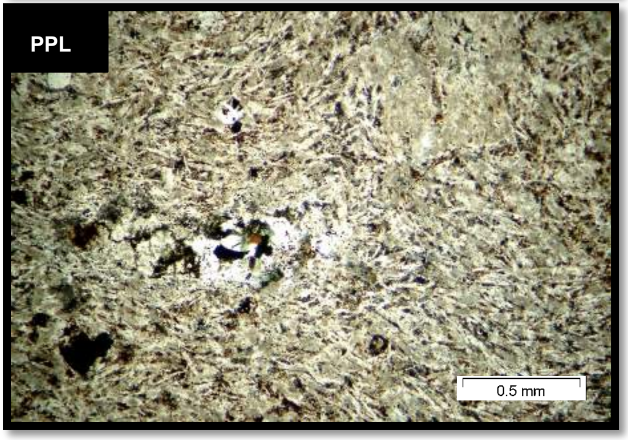

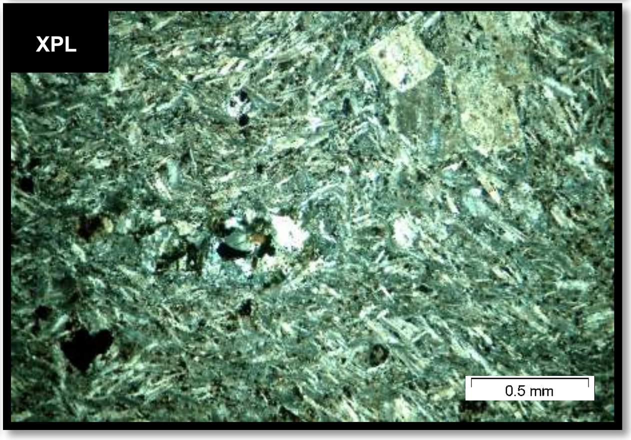

Sample COK178 consists of ~95% matrix, which is described as groundmass (C), and opaque minerals. Groundmass (C) is fine-grained with a trachytic texture made of oriented, elongate crystals of alkali feldspar. The phenocryst assemblage makes up ~5% of the rock. The phenocrysts are medium- to coarse-grained alkali feldspar showing Carlsbad twinning. Less than 1% feldspar phenocrysts are relict phenocrysts, which are phenocrysts recrystallised by a fine-grained matrix too fine to identify any constituents. Relict phenocrysts show intergrowth textures. There are no visible xenoliths.

An abundant brown (PPL) mineral coats the alkali feldspar that makes up groundmass (C). The phenocrysts and groundmass (C) are strongly altered by fine-grained epidote. Phenocrysts are embayed and partially to entirely replaced by epidote.

A.4 **Breccia with a trachytic texture** - sample COK198

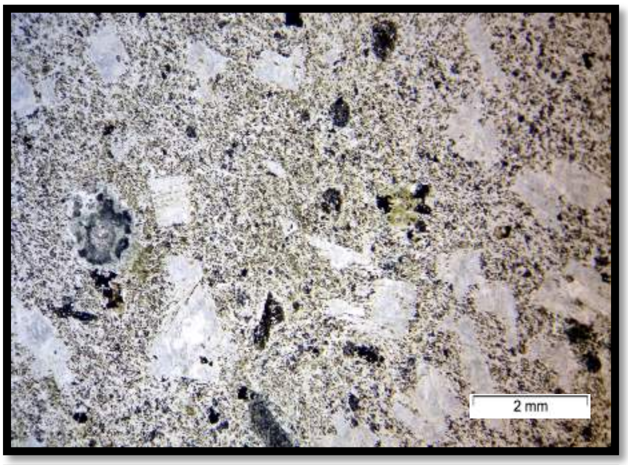

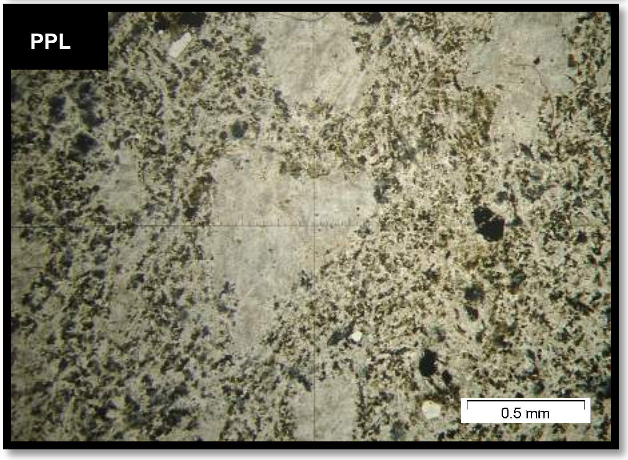

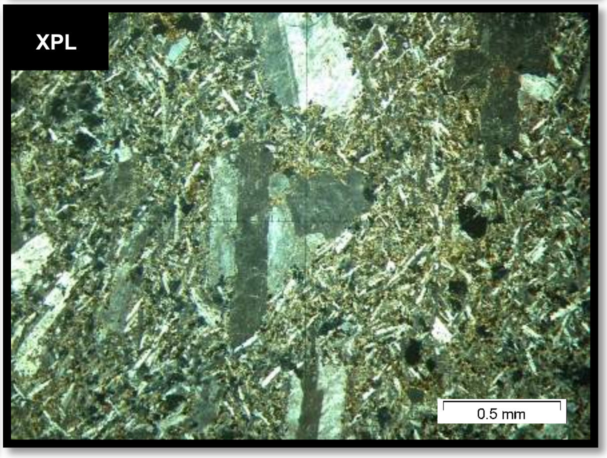

Sample COK198 consists of ~75% matrix, which is described as groundmass (C), and opaque minerals. The groundmass is fine-grained with a trachytic texture made of oriented, elongate crystals of alkali feldspar. The phenocryst assemblage makes up ~20% of the rock. The phenocrysts are coarse-grained alkali feldspar showing Carlsbad twinning. About 5% of the rock is made of groundmass (B) xenoliths.

An abundant brown (PPL) mineral coats groundmass (C) and groundmass (B) xenoliths. The phenocrysts and groundmass (C) are altered by fine-grained epidote. Phenocrysts are embayed and partially to entirely replaced by epidote. Phenocrysts show resorption textures and have a dusty alteration.

A.5 Breccia with a basaltic texture - sample COK172

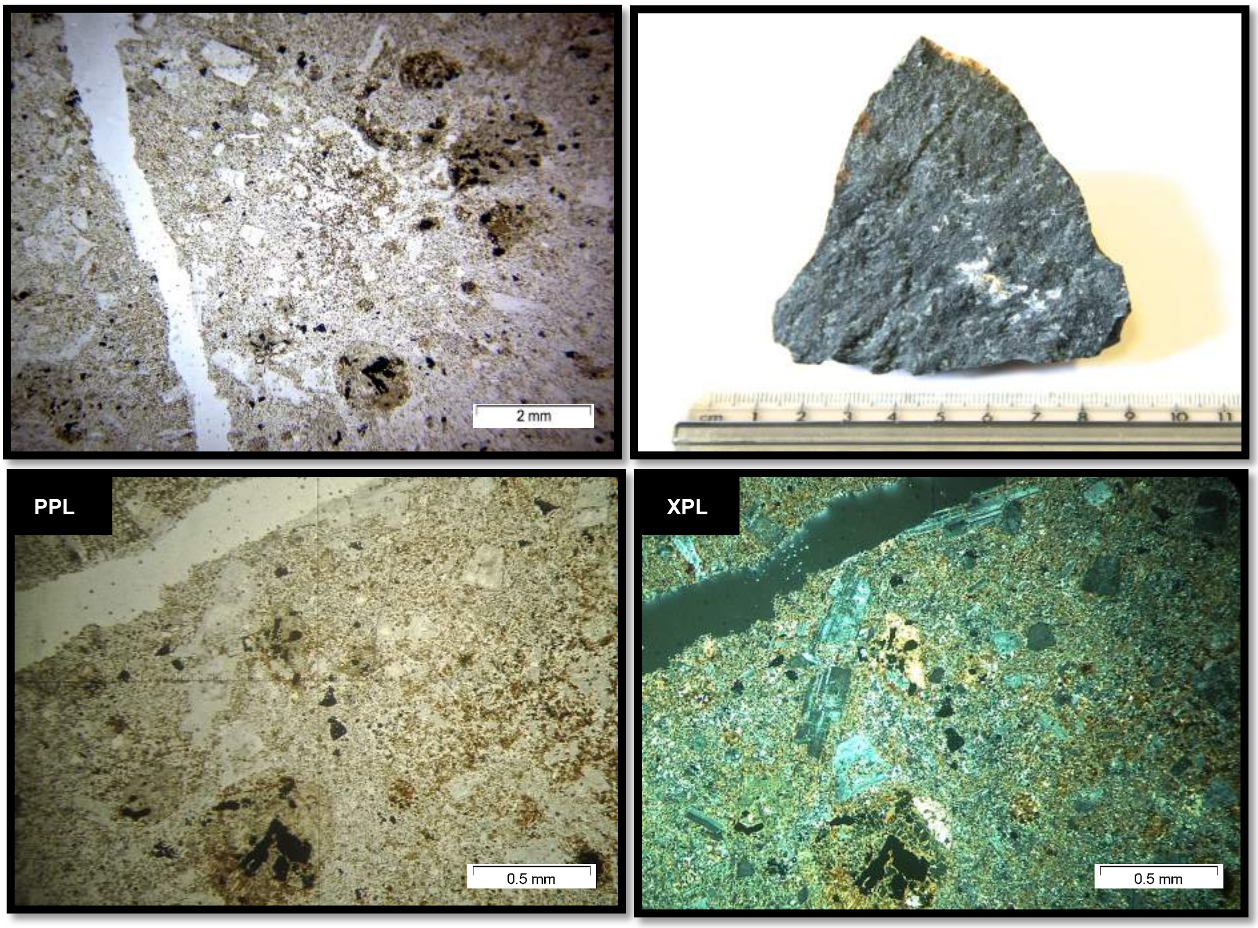

Sample COK172 consists of ~85%, which is described as groundmass (D), and opaque minerals. The groundmass is fine-grained with a basaltic texture. The phenocryst assemblage makes up ~13% of the rock. The phenocrysts include fine- to medium-grained plagioclase showing polysynthetic twinning. Plagioclase laths are euhedral to subhedral and clustered in glomeroporphyritic masses. Phenocrysts of amphibole and pyroxene are recognised by their perfect cleavage intersecting at 60°/120° and right angles respectively. About 2% of the rock consists of gneiss xenoliths made of fine-grained, granoblastic quartz.

Elongate brown pleochroic (PPL) biotite coats groundmass (D). The phenocrysts and xenoliths are altered by fine-grained epidote. Phenocrysts are embayed and partially to entirely replaced by epidote. Phenocrysts show resorption textures. Plagioclase has a dusty alteration.

A.5 **Breccia with a basaltic texture -** sample COK195

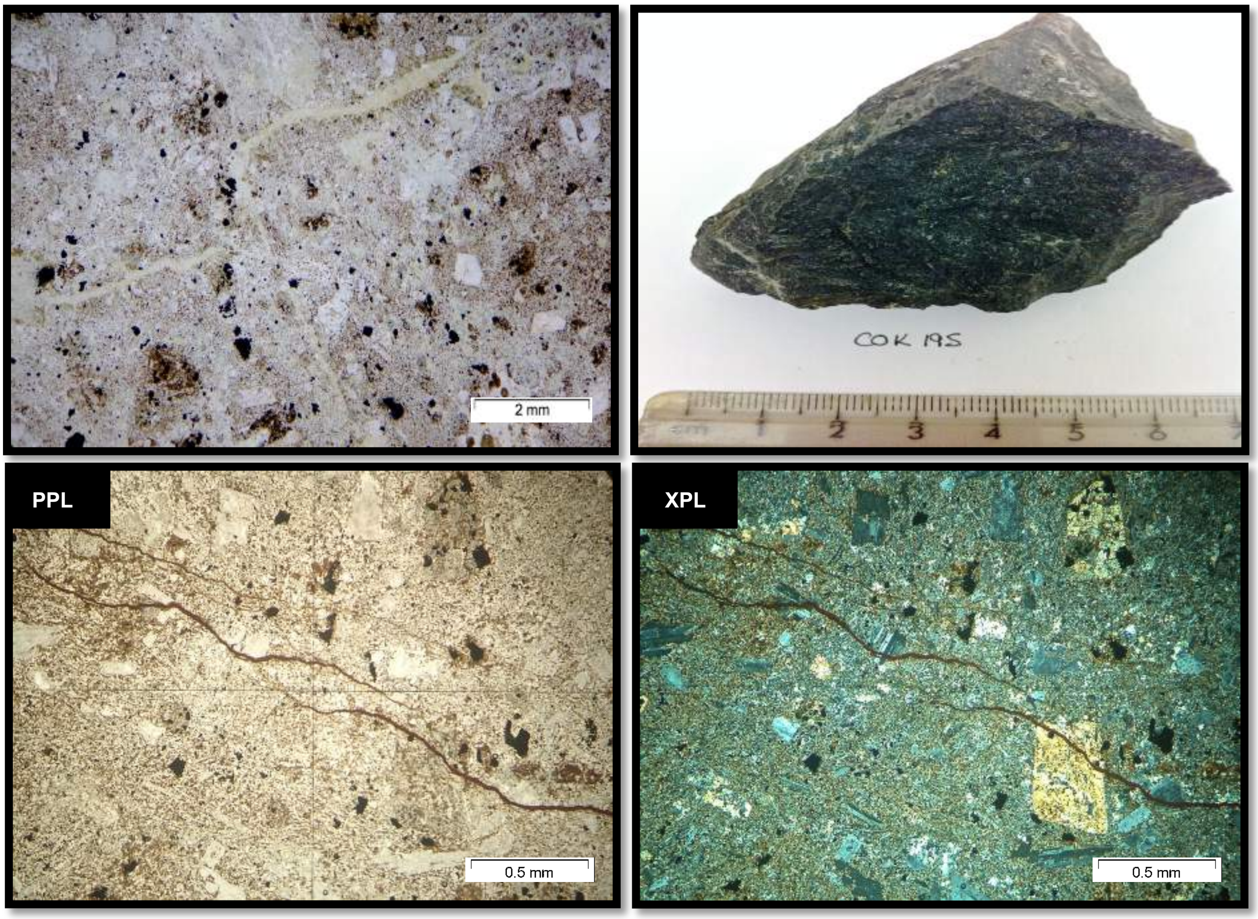

Sample COK195 consists of ~85% matrix, which is described as groundmass (D), and opaque minerals. The groundmass is fine-grained with a basaltic texture. The phenocryst assemblage makes up ~15% of the rock. The phenocrysts include fine- to medium-grained plagioclase showing polysynthetic twinning. Plagioclase laths are euhedral to subhedral and clustered in glomeroporphyritic masses. There are sparse phenocrysts of amphibole and pyroxene with their perfect cleavage intersecting respectively at 60°/120° and right angles. No xenoliths are visible.

Elongate, brown pleochroic (PPL) biotite coats groundmass (D). Epidote and biotite fill fissures in phenocrysts and the groundmass. Phenocrysts are embayed, and show resorption textures. Plagioclase is partially replaced by fine-grained epidote. Plagioclase has a dusty alteration.

A.6 **Phonolite rock** - sample COK192

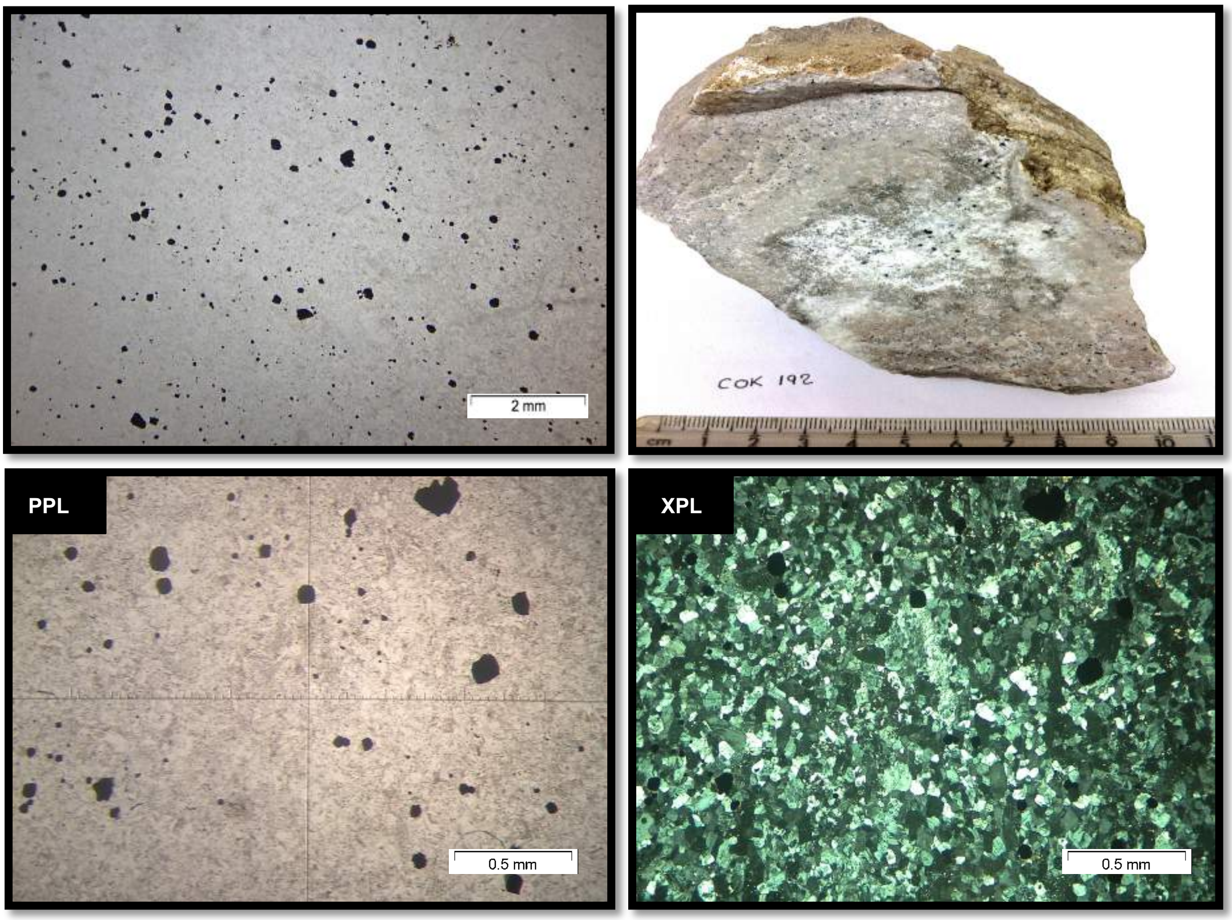

Sample COK192 consists of ~95% matrix, which is described groundmass (E). The groundmass is fine-grained and mostly made of alkali feldspar (>90 volume %). The phenocryst assemblage makes up ~5% of the rock. The phenocrysts are opaque minerals and alkali feldspar. No xenoliths are visible.

Fine-grained epidote has replaced parts of groundmass (E). The alkali feldspar that makes up the groundmass has a dusty alteration. The feldspar phenocrysts are strongly altered, and show perthitic textures. Opaque minerals have coronas of epidote.

A.7 **Gneiss** - sample COK167

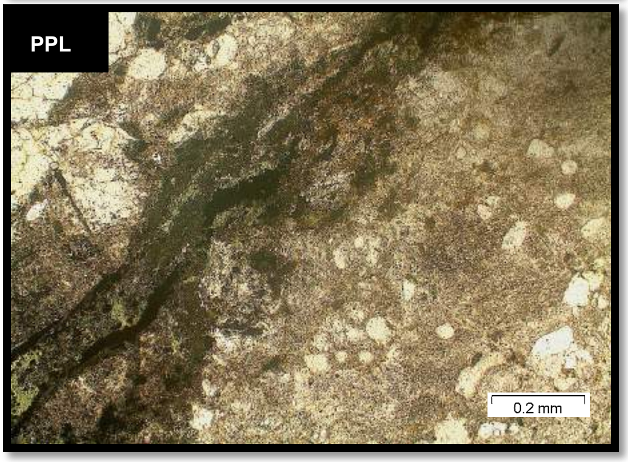

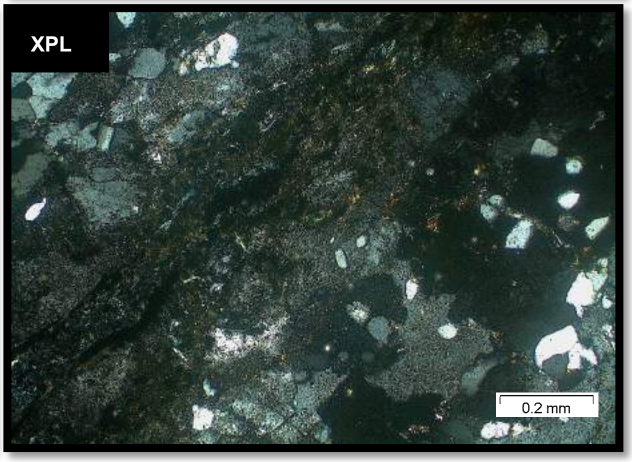

Sample COK167 consists of alkali feldspar (~50%), granoblastic quartz (~40%), fine-grained mafic minerals (~9%), and minor opaque minerals and zircon. The texture is medium- to coarse-grained with sutured grain boundaries. Quartz and feldspar are elongate, showing preferred orientation towards shearing. Biotite is sheared.

There is evidence of recrystallization with fine-grained quartz showing 120° grain boundaries. Quartz and feldspar have altered rims, and are embayed. The feldspar rims and biotite grains are chloritised. Alkali feldspar and plagioclase are perthitic, embayed, and turbid.

A.7 **Gneiss** - sample COK169

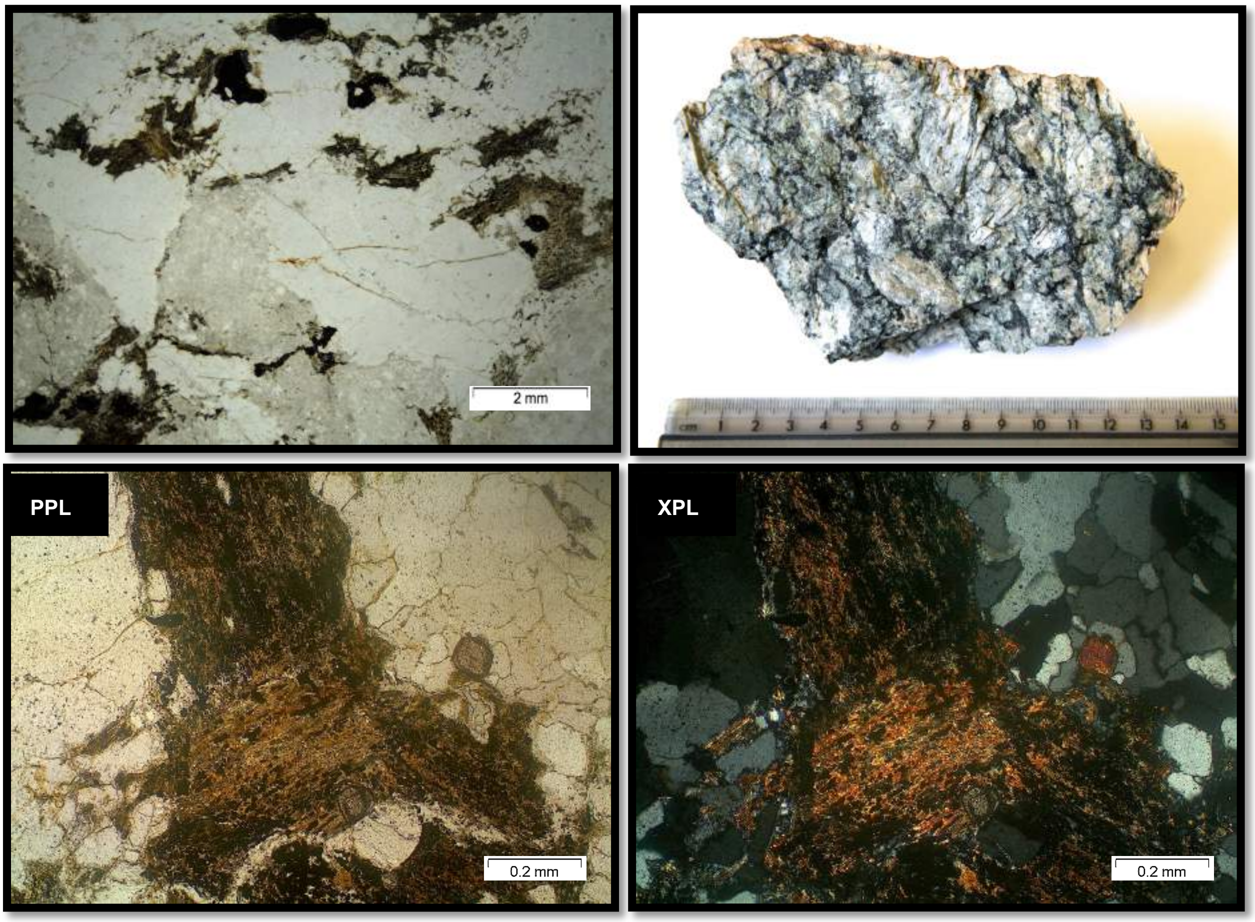

Sample COK169 consists of porphyroblastic alkali feldspar (~50%), quartz (~35%), biotite (~20%), and minor opaque minerals, and zircon. The texture is medium- to coarse-grained with abundant porphyroblastic alkali feldspar showing simple twinning. The alkali feldspar is inequigranular and anhedral to subhedral.

Alkali feldspar rims are chloritised. Alkali feldspar is perthitic, and embayed. Biotite is strongly altered by epidote and chlorite.

APPENDIX B THIN SECTION PETROGRAPHY

Table B.1 Summarised petrography of all the breccia rocks, phonolite rocks, and gneisses sampled in this work.

Size classification: <0.5mm=fine-grained; 0.5-2mm=medium-grained; >2mm=coarse-grained

1) Igneous texture

Breccia rock - bostonite

Sample name	Comment	Rock type	Matrix	Phenocryst	Xenolith / xenocryst	1ry mineralogy	2ry mineralogy	Description	Alteration
COK178	Trachytic texture	Igneous (bostonite)	95%	5%	0%	**Matrix:** groundmass (C); opaque minerals **Phenocryst:** alkali feldspar; relict feldspar	Epidote, brown mineral	Groundmass (C) is fine-grained, with a trachytic texture made of oriented, elongate crystals of alkali feldspar. Alkali feldspar phenocrysts are medium- to coarse-grained, and show Carlsbad twinning. Some feldspars are relict phenocrysts, recrystallised by a fine-grained matrix, too fine to identify. Relict phenocrysts show intergrowth textures. There are no visible xenoliths.	There is an abundant fine-grained, brown (PPL) mineral in between aligned alkali feldspar crystals. The groundmass is strongly altered by epidote. Phenocrysts are embayed, and partially to entirely replaced by epidote.
COK198	Trachytic texture	Igneous (bostonite)	75%	20%	5%	**Matrix:** groundmass (C); opaque minerals **Phenocryst:** alkali feldspar **Xenolith:** groundmass (B)	Epidote, brown mineral	The groundmass is fine-grained, with a trachytic texture made of oriented, elongate crystals of alkali feldspar. Alkali feldspar phenocrysts are coarse-grained, and show Carlsbad twinning.	Fissures are filled with epidote. A moderate amount of a brown (PPL, XPL), round mineral spreads over the groundmass. Xenoliths are coated by a fine-grained, brown (PPL, XPL) mineral. Phenocrysts show resorption textures, and have a dusty alteration. Epidote partially replaces the xenoliths.
COK199	Trachytic texture	Igneous (bostonite)	84%	15%	1%	**Matrix:** groundmass (C); opaque minerals **Phenocryst:** alkali feldspar **Xenolith:** quartz	Epidote, brown mineral	Groundmass (C) is fine-grained, with a trachytic texture made of oriented, elongate crystals of alkali feldspar. Alkali feldspar phenocrysts are medium- to coarse-grained, and show Carlsbad twinning. Feldspar phenocrysts are euhedral to subhedral laths, some clustered in glomeroporphyritic masses. <2% of the phenocrysts are relict feldspar phenocrysts. Gneiss xenoliths consist of granoblastic quartz.	A 1mm wide fissure is filled with fine-grained epidote. There is an abundant fine-grained, brown (PPL) mineral in between the trachytic alkali feldspar crystals. Phenocrysts are strongly altered, and show resorption textures. Alkali feldspar has a dusty alteration, and contains small cracks filled with epidote.

Breccia rock - basalt

Sample name	Comments	Rock type	Matrix	Phenocryst	Xenolith / xenocryst	1ry mineralogy	2ry mineralogy	Description	Alteration
COK172	Basaltic texture	Igneous (basalt)	85%	13%	2%	**Matrix:** groundmass (D) coated by biotite; opaque minerals **Phenocryst:** plagioclase; amphibole; pyroxene **Xenolith:** quartz	Epidote, biotite	The groundmass is fine-grained, with elongate microcrystals of plagioclase. Plagioclase phenocrysts are fine- to medium-grained, and show polysynthetic twinning. Plagioclase laths are euhedral to subhedral, clustered in glomeroporphyritic masses. There are sparse amphibole and pyroxene, with their perfect cleavage intersecting respectively at 60°/120° and right angles. Gneiss xenoliths show fine-grained, granoblastic quartz.	Groundmass (D) is coated by elongate, brown pleochroic (PPL) biotite. The phenocrysts and xenoliths are altered by fine-grained epidote. Amphiboles and pyroxenes show poikilitic and resorption textures. Plagioclase has a dusty alteration.
COK195	Basaltic texture	Igneous (basalt)	85%	15%	0%	**Matrix:** groundmass (D) coated by biotite; opaque minerals **Phenocryst:** plagioclase; pyroxene; amphibole; alkali feldspar	Epidote, biotite	The groundmass is too fine-grained to identify. There are abundant medium- to fine-grained plagioclase phenocrysts. There are pyroxene and amphibole phenocrysts with their perfect cleavage intersecting respectively at right angles and at 60°/120°. There are no visible xenoliths.	The groundmass is coated by biotite. Epidote and biotite fill fissures in phenocrysts. Plagioclase is partially replaced by epidote. Phenocrysts show resorption textures.

Phonolite rock

Sample name	Comments	Rock type	Matrix	Phenocryst	Xenolith / xenocryst	1ry mineralogy	2ry mineralogy	Description	Alteration
COK191	Grey rock	Igneous	93%	3%	0%	**Matrix:** groundmass (E) **Phenocryst:** opaque minerals; alkali feldspar	Epidote, chlorite, brown mineral	Groundmass (E) is fine-grained, mostly made of alkali feldspar. Opaque minerals are round, fine-grained phenocrysts. Feldspar phenocrysts are medium-grained, subhedral, and show intergrowth textures. There are no visible xenoliths.	The groundmass is partly altered by epidote, and chlorite. The groundmass (E) is coated by a brown (PPL, XPL) mineral product. Alkali feldspar has a dusty alteration. Feldspar phenocrysts show perthitic and resorption textures.
COK192	Pink rock	Igneous	95%	5%	0%	**Matrix:** groundmass (E) **Phenocryst:** opaque minerals; alkali feldspar	Epidote, chlorite	The groundmass is fine-grained (coarser-grained than COK191), and mostly made of alkali feldspar (>90 volume %). Opaque minerals are round, fine-grained phenocrysts. Alkali feldspar phenocrysts are medium-grained. There are no visible xenoliths.	Parts of the groundmass (E) is altered by fine-grained epidote. Alkali feldspar in groundmass (E) has a dusty alteration. Feldspar phenocrysts are strongly altered by epidote, and show perthitic textures. Opaque minerals have coronas of epidote.

Continued…

2) Mixture of igneous and metamorphic texture

Breccia rock

Sample name	Comments	Rock type	Matrix	Phenocryst	Xenolith / xenocryst	1ry mineralogy	2ry mineralogy	Description	Alteration
COK162	Flow texture in two quartz xenocrysts	Igneous and metamorphic	39%	0%	60%	**Matrix:** matrix (A) **Xenolith:** groundmass (B) with abundant opaque minerals; quartz	Epidote, brown mineral	Xenoliths are mostly made of groundmass (B). There are sparse, fine- to medium-grained disseminated quartz xenocrysts. Gneiss xenoliths consist of granoblastic quartz. The xenoliths and xenocrysts are round, or angular, and found in matrix (A). Two quartz xenocrysts show a flow texture. Quartz has a wavy extinction. There are no visible phenocrysts.	Matrix (A) is strongly altered by fine-grained epidote. Groundmass (B) xenoliths are coated by a brown (PPL, XPL) alteration product.
COK164	-	Igneous and metamorphic	85%	0%	15%	**Matrix:** groundmass (B); matrix (A); opaque minerals **Xenolith:** groundmass (B) with abundant fine-grained opaque minerals; quartz	Chlorite, epidote, brown mineral	Matrix (A) contains abundant medium- to fine-grained, disseminated quartz xenocrysts, and gneiss xenoliths made of granoblastic quartz. There is a >4mm gneiss xenoliths. There are no visible phenocrysts.	The matrices and xenoliths are strongly altered by chlorite and epidote. There is a fine-grained, brown (PPL, XPL) mineral coating groundmass (B) xenoliths.
COK165	Xenolith with the lowest $\delta^{18}O$ value (-5.6‰)	Igneous and metamorphic	85%	10%	5%	**Matrix:** groundmass (B); matrix (A); opaque minerals **Phenocryst:** feldspar in groundmass (B) **Xenolith:** groundmass (B); quartz	Epidote, chlorite, brown mineral	Groundmass (B) and matrix (A) are mixed together. Relict phenocrysts of feldspar are fine- to medium-grained, and strictly found in groundmass (B). Groundmass (B) xenoliths, and gneiss xenolith made of granoblastic quartz are found in matrix (A).	The matrices and the phenocrysts are strongly altered. Matrix (A) is replaced by fine- to medium-grained epidote, and chlorite. Groundmass (B) is coated by a fine-grained, brown (PPL, XPL) mineral. Feldspar phenocrysts are strongly altered by epidote. The phenocrysts are embayed, and show sieve textures.
COK166	Gneiss xenolith with mafic mineral layer between quartz	Igneous and metamorphic	85%	0%	15%	**Matrix:** groundmass (B); matrix (A); opaque minerals **Xenolith:** groundmass (B) with abundant fine-grained opaque minerals; quartz	Chlorite, epidote, brown mineral	The medium- to fine-grained, disseminated quartz xenocrysts, and the gneiss xenoliths made of granoblastic quartz are only in matrix (A). There is a >4mm gneiss xenoliths made of layers of mafic minerals between quartz and alkali feldspar. There are no visible phenocrysts.	The matrices and xenoliths are strongly altered by chlorite and epidote. There is a fine-grained brown (PPL, XPL) mineral coating groundmass (B) xenoliths.
COK168	Lowest $\delta^{18}O$ value (-5.2‰)	Igneous and metamorphic	85%	10%	5%	**Matrix:** groundmass (B); matrix (A); zircon **Phenocryst:** plagioclase and alkali feldspar in groundmass (B); opaque minerals **Xenolith:** groundmass (B)	Epidote, chlorite, brown mineral, calcite	Plagioclase and alkali feldspar phenocrysts are fine- to medium-grained, and subhedral. Xenoliths of groundmass (B) in matrix (A) contain abundant medium-grained opaque minerals.	Fine- to medium-grained epidote and chlorite replace matrix (A). Sparse calcite is found in matrix (A). Groundmass (B) is partly coated by a fine-grained, brown (PPL and XPL) mineral. Phenocrysts show sieve and resorption textures, and have altered rims.
COK170	Lowest $\delta^{18}O$ value (-5.2‰)	Igneous and metamorphic	86%	0%	15%	**Matrix:** groundmass (B); matrix (A); opaque minerals **Xenolith:** quartz; groundmass (B)	Epidote, brown mineral	Groundmass (B) and matrix (A) are mixed together. The gneiss xenoliths consist of granoblastic quartz. There are no visible phenocrysts.	Matrix (A) is strongly altered by epidote. Parts of granoblastic quartz and groundmass (B) xenoliths are replaced by epidote.
COK174	-	Igneous and metamorphic	55%	15%	30%	**Matrix:** groundmass (B); matrix (A) **Phenocryst:** alkali feldspar and plagioclase mostly in groundmass (B); opaque minerals **Xenolith:** groundmass (B); quartz	Epidote, brown mineral	Parts of groundmass (B) have a trachytic texture. Phenocrysts of alkali feldspar and plagioclase are mostly in groundmass (B), but also found disseminated in matrix (A). Plagioclase phenocrysts are fine- to medium-grained, and show polysynthetic twinning. Groundmass (B) and gneiss xenoliths are in matrix (A). Opaque minerals are medium-grained.	The matrices and the phenocrysts are strongly altered by epidote. Epidote shows glomeroporphyritic textures. Groundmass (B) is coated by fine-grained, brown (PPL, XPL) mineral. Feldspar phenocrysts are turbid, and have perthitic textures.
COK175	Contains the most xenoliths	Igneous and metamorphic	20%	1%	79%	**Matrix:** groundmass (B) **Phenocryst:** alkali feldspar **Xenolith:** quartz; groundmass (B)	Brown mineral, epidote	Groundmass (B) contains sparse phenocrysts of alkali feldspar. There are abundant gneiss xenoliths made of granoblastic quartz, and disseminated, quartz xenocrysts. Groundmass (B) xenoliths have abundant fine-grained, opaque minerals in them.	The groundmass is coated by a brown (PPL, XPL) mineral. The xenoliths and xenocrysts of quartz are strained, and show trails of fluid inclusions. Phenocrysts are turbid, with altered rims. The alkali feldspar shows perthitic and sieve textures.
COK176	Contains volcanic quenched melt crystals	Igneous and metamorphic	75%	0%	25%	**Matrix:** groundmass (B) **Xenolith:** quartz	Brown mineral, epidote	There are no visible phenocrysts. The gneiss xenoliths are made of fine- to medium-grained, granoblastic quartz. Quartz xenocrysts are disseminated. Quartz has a wavy extinction. There are two amygdaloidal minerals with spherulitic crystals.	The groundmass is strongly altered by a brown (PPL, XPL) mineral. Xenoliths have coronas made of opaque minerals. The quartz is dusty.

Continued…

COK193	-	Igneous and metamorphic	70%	10%	20%	**Matrix:** groundmass (B); matrix (A) **Phenocryst:** relict feldspar **Xenolith:** groundmass (B); quartz	Biotite, chlorite	Groundmass (B) includes abundant opaque minerals. Relict feldspar phenocrysts are filled with a fine-grained matrix, too fine to identify. Relict phenocrysts are only in groundmass (B). There are abundant disseminated quartz xenocrysts in matrix (A). Quartz has a wavy extinction.	Groundmass (B) is partly coated by biotite. Matrix (A) is altered by chlorite. Feldspar phenocrysts are too altered to identify their nature. The xenoliths have coronas of opaque minerals.
COK197	-	Igneous and metamorphic	98%	0%	2%	**Matrix:** groundmass (B)	Epidote, chlorite, brown mineral, quartz	The groundmass is made of elongate, microcrystals of feldspar randomly oriented. Feldspar microcrystals are too fine to identify. Groundmass (B) is cracked, and has numerous cavities. There are no visible phenocrysts, and xenoliths.	The fissures and cavities are filled with epidote, opaque minerals, the brown mineral (PPL, XPL), and chlorite. There is recrystallised quartz in the interstitial space.
COK200	-	Igneous and metamorphic	85%	0%	15%	**Matrix:** groundmass (B); matrix (A) **Xenolith:** groundmass (B); quartz	Epidote, brown mineral	Groundmass (B) includes opaque minerals. There are no visible phenocrysts. Xenoliths are either made of groundmass (B), or granoblastic quartz. There are quartz xenocrysts disseminated in matrix (A).	Groundmass (B) is partly coated by a brown (PPL, XPL) mineral. Matrix (A) is partly replaced by epidote.
COK201	-	Igneous and metamorphic	90%	5%	5%	**Matrix:** groundmass (B); opaque minerals **Phenocryst:** plagioclase **Xenolith:** replaced by 2ry minerals	Epidote, chlorite, brown mineral	Phenocrysts of plagioclase are fine-grained, and show polysynthetic twinning. The xenoliths are replaced by secondary minerals.	Xenoliths are entirely replaced by epidote and chlorite. The groundmass is coated by fine-grained, brown (PPL, XPL) mineral. Phenocrysts have a dusty alteration, and are partially replaced by epidote. Opaque minerals have fine-grained coronas of epidote.
COK202	-	Igneous and metamorphic	90%	0%	10%	**Matrix:** matrix (A) **Xenolith:** groundmass (B)	Chlorite, epidote	Groundmass (B) xenoliths are fine-grained. There are no visible phenocrysts.	Chlorite and epidote have replaced matrix (A).
COK205	Mixture of green matrix and black groundmass	Igneous and metamorphic	45%	10%	45%	**Matrix:** groundmass (B); matrix (A) **Phenocryst:** feldspar; relict feldspar **Xenolith:** groundmass (B); quartz	Epidote, chlorite, brown mineral	Groundmass (B) and matrix (A) are mixed together. Groundmass (B) contains the feldspar phenocrysts. Matrix (A) has abundant disseminated quartz xenocrysts and granoblastic quartz xenoliths. The xenoliths of groundmass (B) are well-defined, round or angular, and fine- to coarse-grained. <2% of the feldspar phenocrysts are relict, replaced by a groundmass that is too fine-grained to identify.	Both matrices are strongly altered. Matrix (A) is replaced by abundant epidote, and chlorite. Groundmass (B) is coated by a brown (PPL, XPL) mineral. Groundmass (B) xenoliths have coronas of opaque minerals, and chlorite.
COK207	-	Igneous and metamorphic	80%	1%	19%	**Matrix:** groundmass (B); matrix (A) **Phenocryst:** relict feldspar **Xenolith:** quartz	Epidote, chlorite, brown mineral	Groundmass (B) contains relict feldspar phenocrysts. Relict feldspar phenocrysts are recrystallised by a fine-grained matrix, too fine to identify. Fine- to medium-grained quartz xenocrysts, and granoblastic quartz are in matrix (A).	Groundmass (B) is coated by a brown (PPL, XPL) mineral. Matrix (A) is altered by epidote, and chlorite.
COK208	-	Igneous and metamorphic	90%	1%	9%	**Matrix:** groundmass (B); matrix (A) **Phenocryst:** relict feldspar **Xenolith:** groundmass (B); quartz	Chlorite, epidote, brown mineral	Groundmass (B) shows relict feldspar phenocrysts. Relict feldspar phenocrysts are recrystallised by a fine-grained matrix, too fine to identify. Matrix (A) has disseminated quartz xenocrysts, and granoblastic quartz. The groundmass (B) xenoliths are fine- to coarse-grained.	Groundmass (B) is coated by a brown (PPL, XPL) mineral. Matrix (A) is replaced by fine-grained chlorite and epidote. Groundmass (B) xenoliths have coronas of opaque minerals, and chlorite.

3) Metamorphic rock

Gneiss

Sample name	Comments	Rock type	Matrix	Phenocryst	Xenolith / xenocryst	1ry mineralogy	2ry mineralogy	Description	Alteration
COK163	-	Augen gneiss	-	-	-	Alkali feldspar, quartz, biotite, amphibole, opaque minerals, zircon	Chlorite, epidote	The texture is medium- to coarse-grained, with abundant coarse-grained porphyroblastic alkali feldspar. Feldspar and quartz are inequigranular grains, anhedral to subhedral. There is evidence of shearing. Elongate minerals have a lineation.	Feldspar is perthitic, and highly altered. Biotite is chloritised. Epidote alters the sheared mafic minerals.

Continued…

COK167	Sheared	Augen gneiss	-	-	-	Alkali feldspar, quartz, biotite, opaque minerals, zircon	Chlorite	The texture is medium- to coarse-grained, with sutured grain boundaries. Quartz and feldspar are elongate, showing preferred orientation towards shearing. Biotite is sheared. There is evidence of recrystallization by fine-grained quartz showing 120° grain boundaries.	Quartz and feldspar have altered rims, and are embayed. The feldspar rims and biotite grains are chloritised.
COK169	Greenish rock	Augen gneiss	-	-	-	Alkali feldspar, quartz, biotite, opaque minerals, zircon	Chlorite, epidote	The texture is medium- to coarse-grained, with abundant coarse-grained porphyroblastic alkali feldspar. Feldspar is inequigranular, anhedral to subhedral.	Alkali feldspar rims are chloritised. Alkali feldspar is perthitic, and embayed. Biotite is replaced by epidote and chlorite.
COK171	Black coloured rock	Augen gneiss	-	-	-	Quartz, biotite, feldspar, opaque minerals	Chlorite	The texture is fine-grained and made of quartz and biotite. There is fine-grained feldspar that has been intensely sheared.	Mafic minerals are altered by chlorite.
COK173	-	Augen gneiss	-	-	-	Alkali feldspar, quartz, plagioclase, biotite, opaque minerals, zircon	Chlorite	The texture is medium- to coarse-grained with coarse-grained porphyroblastic feldspar, and quartz. Feldspar and quartz are inequigranular and anhedral. Plagioclase feldspar shows polysynthetic twinning or Carlsbad twinning.	Feldspar generally has a perthitic texture. Feldspar is altered, turbid, and embayed. Biotite and feldspar rims are occasionally chloritised.
COK177	-	Augen gneiss	-	-	-	Alkali feldspar, quartz, biotite, opaque minerals, zircon	Chlorite, epidote	The texture is medium- to coarse-grained with sutured grain boundaries. Feldspar and quartz are coarse-grained porphyroblastic grains, and are inequigranular, and anhedral. Some of the feldspar is fine-grained and shows a preferred orientation towards shearing direction.	Feldspar generally has a perthitic texture. Feldspar is turbid, and embayed. The fine-grained feldspar is chloritised. Biotite is chloritised. Sparse epidote is found in the interstice with the biotite.
COK189	-	Augen gneiss	-	-	-	Alkali feldspar, quartz, biotite, opaque minerals, zircon	Chlorite, epidote	Texture is medium- to coarse-grained with coarse-grained porphyroblastic alkali feldspar, and quartz. Feldspar and quartz are inequigranular and anhedral to subhedral.	Feldspar generally has a perthitic texture. Feldspar and quartz are embayed. Biotite is chloritised. Feldspar is commonly replaced by epidote.
COK190	-	Augen gneiss	-	-	-	Quartz, alkali feldspar, biotite, opaque minerals, zircon	Epidote, chlorite	The texture is fine- to coarse-grained with medium-grained porphyroblastic alkali feldspar. Feldspar and quartz are inequigranular, anhedral to subhedral. Quartz and feldspar are elongate. There is evidence of recrystallization with fine-grained quartz showing 120° grain boundaries. Quartz has a wavy extinction.	Feldspar and quartz are strongly altered. There is abundant interstitial epidote. Biotite and feldspar rims are chloritised.
COK194	-	Augen gneiss	-	-	-	Quartz, alkali feldspar, biotite, opaque minerals, zircon	Epidote, chlorite	The texture is medium- to coarse-grained with coarse-grained porphyroblastic alkali feldspar. Feldspar and quartz are inequigranular and anhedral to subhedral. Quartz and feldspar are elongate. There is evidence of recrystallization with fine-grained quartz showing 120° grain boundaries.	Feldspar and quartz are strongly altered. There is abundant fine-grained interstitial epidote and chlorite. Biotite is chloritised.
COK209	-	Augen gneiss	-	-	-	Quartz, alkali feldspar, biotite, plagioclase, opaque minerals, zircon	Chlorite, epidote	The texture is mostly coarse-grained with sutured grain boundaries. Feldspar is inequigranular, anhedral to subhedral. Biotite is found in patches rather than along a shearing direction. Quartz has a wavy extinction.	Feldspar is strongly altered. Feldspar has a perthitic texture, and is embayed. Chlorite replaces biotite and parts of feldspar.
COK210	-	Augen gneiss	-	-	-	Quartz, biotite, alkali feldspar, opaque minerals, zircon	Epidote, chlorite	The texture is fine- to medium-grained mostly made of quartz and biotite. Quartz is inequigranular and anhedral to subhedral. There is evidence of shearing, and elongate minerals have a lineation. Quartz has a wavy extinction.	Quartz is altered and embayed. Biotite and fine-grained feldspar are chloritised. Epidote is very fine-grained and found in between grains.